Search for the Standard Model Higgs Boson in the $ZH \to \mu^+\mu^- + b\bar{b}$ Channel in $p\bar{p}$ Collisions at $\sqrt{s} = 1.96$ TeV

A Dissertation Presented

by

Huishi Dong

to

The Graduate School

in Partial Fulfillment of the Requirements

for the Degree of

Doctor of Philosophy

in

Physics

Stony Brook University

August 2007

Stony Brook University

The Graduate School

Huishi Dong

We, the dissertation committee for the above candidate for the Doctor of Philosophy degree, hereby recommend acceptance of this dissertation.

John D. Hobbs – Dissertation Advisor
Professor, Department of Physics and Astronomy

John Smith – Chairperson of Defense
Professor, Department of Physics and Astronomy

Axel K. Drees
Professor, Department of Physics and Astronomy

Gregorio Bernadi
Dr, Directeur de Recherches, CNRS/France, University of Paris

Serban Protopopescu
Physicist, Omega Group, Brookhaven National Laboratory

This dissertation is accepted by the Graduate School.

Lawrence Martin
Dean of the Graduate School

Abstract of the Dissertation

Search for the Standard Model Higgs Boson in the $ZH \to \mu^+\mu^- + b\bar{b}$ Channel in $p\bar{p}$ Collisions at $\sqrt{s} = 1.96$ TeV

by

Huishi Dong

Doctor of Philosophy

in

Physics

Stony Brook University

2007

This dissertation describes a search for the standard model Higgs boson (H) produced in association with a Z boson at the DØ experiment. This analysis is based on an integrated luminosity of $L = 370$ pb^{-1}of data. The $p\bar{p} \to ZH \to \mu^+\mu^- + b\bar{b}$ channel is studied where the Z boson decays to $\mu^+\mu^-$ and the H decays to $b\bar{b}$. In order to boost the the signal rate we first introduce the optimized di-muon isolation probability for separating the $Z + 2j$ signal from the multi-jet background, then use the optimized b-jet identifier to enhance the double b-tag signal significance. The upper limits on the $\sigma(p\bar{p} \to ZH) \times \mathrm{Br}(H \to b\bar{b})$ for Higgs masses between 105 GeV and 145 GeV are set at 95% C.L.

Dedicated to my loving family.

Red: Let me tell you something my friend. Hope is a dangerous thing. Hope can drive a man insane.

Andy Dufresne: Remember Red, hope is a good thing, maybe the best of things, and no good thing ever dies.

– Stephen King, *The Shawshank Redemption*

Contents

List of Figures

List of Tables

Acknowledgements

First, my greatest appreciation goes to my advisor, Prof. John Hobbs, who gave me this precious opportunity to conduct useful physics researches at the DØ experiment. I got enormous help from John in countless aspects of the experiments, the analyses and the dissertations, meanwhile I had the greatest freedom of researching whatever I like. The seven years of Ph.D study with John is the most valuable academic experience in my life.

I would also thank Prof. Wendy Taylor, who is one of my best friends, my "effective" supervisor, my mentor and my colleague. I enjoyed our work on the STT crates in the freezing MCH2. I am grateful to your support of me when unhappy things happened. And I really hope I could write better so that you (and John) could spend less time on reading and correcting my poor english.

I own a debt of gratitude to the Stony Brook group and the DØ Higgs group for spending time hearing my talks and giving me useful suggestions. I would especially thank Dr. Yildirim D. Mutaf who inspired me on the dissertation research, Dr. James Heinmiller and Dr. Kazu Hanagaki who provided important information used in this analysis.

My obligation also goes to the DØ EB'04, the DØ collaboration, the beam division of the Tevatron, and the funding agencies. It was a privilege to work with so many diligent, dedicated and bright people. Without their selfless service works, the DØ experiment could not have been so successful, I could not so effortlessly pick up any data set I want to analyze, and my paper would not reach to the publishing stage.

My work and life in Fermilab was made much more easier by the staff of the Stony Brook high energy physics group, Joan Napolitano and Alice Cichanowitz-Dugan, the department secretaries, Patricia Peiliker, *et. al.* My appreciations extend to them.

I would also express my thanks to my friends: Shaohua Fu, Yuan Hu, Feng Guo, Jun Guo, Yanjun Tu, Zongru Wan, Ming Yan, Tingjun Yang, Junjie Zhu, Rui Zhang Xiaojian Zhang. It is they who helped me when a friend is in need, who make the life in Fermilab much more enjoyable.

The members of my dissertation committee, John Smith, Gregorio Bernadi, Axel K. Drees, John Hobbs, Serban Protopopescu, have generously given their time and expertise to better my work. I thank them for their contribution.

And last but never the least I want to thank my family: my father Wankui Dong, my mother Ying Zhang, my sister Huiqian Dong and my wife Wenqun Tang. Thank you for always understanding and supporting me. Thank you for always believe in me when I am down. You teach me love and responsibility. Without you, I could have never survived the test of life.

Thank you all!

Chapter 1

Introduction

This dissertation presents a search for the Standard Model Higgs boson H at the DØ experiment. The Higgs boson is assumed to be produced in association with a Z boson. The Z boson is required to decay into a pair of muons, and the H boson is required to decay into two b- flavored jets. The whole process can described as

$$p\bar{p} \rightarrow ZH \rightarrow \mu^+\mu^- + b\bar{b}$$

For the Standard Model searches this channel has among the best signal to noise ratio because of the cleanliness of the $Z \rightarrow \mu\mu$ process.[1]

The theoretical expectation of the total cross section times branching ratio for the signal is 0.0028 pb for the Standard Model Higgs mass of 115 GeV. With about 300 pb^{-1}data, only about one event should be produced. With various inefficiencies in the detector, the event reconstruction algorithm and the signal selection criteria, the typical signal efficiency is as low as approximately 1%, which makes the observation of the Higgs boson with the current data set seem to be hopeless.

Yet we introduce a set of optimized event selection algorithms to boost the signal efficiency so that we can still try to improve the signal sensitivity, and more importantly lay the ground work for analyses with significantly larger data sets. These optimized algorithms are the definition of muon isolation probability, the subsequent topological analysis method on the di-muon system, and the optimized working point for the b-jet identifier. Compared with the traditional analysis methods which utilize the standard muon isolation requirement and the standard b-tag operating point for selecting the Z signal and b-jets respectively, the combined optimizations could give about 2-5 times more signals [2].

The dissertation is organized as the following: Chapter 2, *Quantum Field Theory of Particles* introduces the Standard Model of particle physics. The motivation of this dissertation is to search for the only undiscovered particle–the Higgs boson–in this theory; Chapter 3, *Particle Accelerator and Detector*, is a description of Tevatron

and the DØ experiment which produces the data used in the analysis; Chapter 4, *Trigger and Data Acquisition System*, discusses briefly how the massive data sets produced in our experiment are collected by the trigger system and data acquisition system; Chapter 5, *Offline Event Reconstruction*, shows the methods to reconstruct the physics properties of the recorded events in the raw data in each detector; Chapter 6, *Monte Carlo Simulation*, is a brief account of the production and the correction of the Monte Carlo data samples used in this analysis; Chapter 7, *Special Object ID*, deals with the identifications of the physics objects in an event, especially the b-jets, the muons and the di-muon pair from the Z boson decay; after the above preparation we go into the Higgs search analysis details in Chapter 8, *ZH Analysis*; finally we conclude the dissertation in Chapter 9, *Conclusion*. The Higgs searches in the other channels and the combinations of the results are discussed, and the impact of the analysis technique developed is also summarized.

Through out the dissertation we will employ the natural unit convention, in which $\hbar = c = 1$, and the rationalized electric charge e is related to the fine structure constant α by $\alpha = e^2/4\pi \approx 1/137$. This convention is widely used in high energy physics references. In this convention the mass and momentum have the same unit as energy: GeV (1 GeV $= 10^9$ eV $= 1.60219 \times 10^{-10}$ J). In order to convert back to the MKS system, one just needs to multiply the mass by c^2 and momentum by c.

The 4 vector is always expressed as $x^\mu = (\mathbf{x}, t)$, and $x^2 = x^\mu x_\mu = \mathbf{x} \cdot \mathbf{x} - t^2$.

Chapter 2

Quantum Field Theory of Particles

Everyone sees and talks about things that are happening, or even not happening, around him or her, in his or her own language; physicists (along with other scientists) observe, describe and explain the world in the plainest and easiest way to the last detail. In this chapter we will take a brief look at the way the physicist describes the world in the content of a quantum field theory of particles: how did it evolve, what is the current status, what are the problems and what we can do to fix them?

2.1 A Little Bit of History

Ever since the start of civilization, the intriguing question of what this world is composed of has puzzled the brightest souls. The earliest answers to this question are that the world was created through the myths of anthropomorphic gods and heroes. As soon as philosophy was developed and human beings could think logically, the myth was replaced by more practical theories, such as the solution proposed by the Greek philosopher Anaximenes of Miletus, or the *Tai-Chi* theory of ancient China. The two theories share a very important belief, that is, the countless types of matter of the world should be composed of only a few simple elements, for example air, water, fire and earth. With this first principle deep in mind, human beings began to prepare for their biggest achievement — science. Indeed, the words "physics" (*phuein* in Greek, to grow) and "nature" (*natura* in Latin, born) bear the very stamp of this ever lasting question of how this world is built.

Twenty five centuries after the atomic theory of the great philosophers of Greece, Mendeleev came up with a more complicated answer, the periodic table of the elements. Despite of its much larger number of building blocks, Mendeleev's answer was proved to be quantitatively precise, yet we now know it is far from the ultimate answer. The proliferation of elements and the organization of the table strongly suggested a substructure within atoms.

Only about thirty years later, J. J. Thomson discovered the electron in 1897, and the electron is still considered as a fundamental particle. This discovery marks the beginning of particle physics. Soon after the electron was discovered, Ernest Rutherford performed his famous Rutherford Scattering experiment in 1911. The experiment showed not only that there is a new kind of particle, the "proton", within the atom but also showed a way of exploring the sub-atomic world, in which we are still using even after a century has passed. In 1930 Wolfgang Pauli suggested a new very light neutral particle, the "neutron", to solve problems in both energy conservation of $\beta-$decay and the spin of Rutherford atomic model. In fact, there are two particles to account for the two problems. In 1932 Chadwick discovered the neutral but heavy component of the atom – the "neutron". The near massless neutral particle needed to understand the kinematics of $\beta-$decay, the "neutrino", was not found until 1956.

During the same period, two of the most important breakthroughs in science occurred: relativity theory and quantum theory. Together, these two new theories laid the foundation of modern particle physics and quantum field theory. In 1905 Albert Einstein's photoelectric theory proposed the existence of a particle, the "photon", as the quanta of electromagnetic field. In 1923 Arthur Holly Compton proved the existence of photon and its particle characteristics by his famous Compton Scattering experiment. The next year Louis de Broglie extended particle-wave duality to matter. Then a new way of describing particles and physical observables using wave functions and operators was developed by Erwin Schrodinger and Werner Heisenberg. In 1927, Paul Dirac began the process of unifying quantum mechanics with special relativity by proposing the Dirac equation for the electron. As a result of the solutions of the Dirac equation, the concept of anti-matter was first developed. Attempts were also made to extend the quantization of a single particle to the wave function itself in order to describe the creation and decay of particles. In 1932 Carl D. Anderson discovered the "positron", the first anti-particle, in cosmic ray experiments. The quantum electromagnetic field theory (QED) was also fully developed in the following years. In 1934, Hideki Yukawa extended the QED to describe a strong interaction that binds the nucleus together. In his theory a new particle pion (π) was introduced which is the counter-piece of photon in EM theory. In the same year Enrico Fermi also established his 4-fermion weak interaction theory for $\beta-$decay and the neutrino. In searching for the π, a new particle, the muon (μ), which is very similar to electron except for its heavier mass was discovered in 1936 again by C. Anderson, *et al.* in cosmic rays. The π was also discovered shortly later.

After WWII, particle experiments and quantum field theory development boomed. In 1947 a "strange" particle, the K^+ caught much attention due to its slow decay pattern. A new conserved observable and new conservation laws were revealed. With the progress of the particle accelerator technique, more and more new particles (so

called hadrons and mesons) were found during the following years. Again the proliferation of particles pointed out substructure waiting to be unveiled, and led to the Gell-man and Zweig quark model in 1964 and later the quantum chromodynamic (QCD) theory of the strong interaction. The QCD theory was later proved to be correct with the discovery of partons, the Bjorken scaling rule, and asymptotic freedom. In the mean time the theory for the weak interaction also developed rapidly. In 1954 C. N. Yang and Mills laid the mathematical foundation with the concept of gauged Yang-Mills fields. In 1956 Wu and Alder proved T. D. Lee and C. N. Yang's suggestion that the weak interaction does not preserve parity. This revolutionary discovery led to the $V - A$ structure of the weak interaction. With the advance of renormalization theory, physicists realized that in order to make Fermi's weak interaction theory renormalizable, new boson particles must be introduced to mediate the weak interaction. Finally around 1968 Sheldon Glashow, Abdus Salam and Steven Weinberg developed a theory to unify the weak interaction and electromagnetic interaction as two different aspect of one electro-weak interaction, and the Higgs boson and spontaneous symmetry breaking were purposed to solve the mass problem of the theory.

The electro-weak interaction model together with the quark-gluon strong interaction was proved to be so successful by later experiments that it is now called the Standard Model (SM) of particle physics. The first proof of the SM was the observation of the weak neutral current in 1973. Then in 1974, the J/Ψ meson was discovered which proved the existence of the c quark. A third charged lepton τ after the electron and the muon was discovered unexpectedly in 1976. The corresponding third generation quarks – b quark and t quark were predicted by Kobayashi and Maskawa to account for the CP violation in the SM and were discovered consequently in 1977 and in 1995 respectively. Perhaps the most important proof of the SM up to now is the discovery in 1983 of the W and the Z bosons.

Recently one of the most significant particle physics discoveries is the non-zero mass of neutrinos. This introduced 10 more free parameters into the SM theory. Yet this discovery does not conflict with the SM. The SM is still the best experimentally proven theory that physicists have come up with to answer the question. The *status quo* of the development of particle physics experiment and quantum field theory is that the theories have overrun the experiments. The SM is known not to be the ultimate fundamental theory. There are numbers of attempts to extend the SM in theory, yet all of them are waiting for the test of experiments. Even for the SM itself, the Higgs boson is still missing. So in this dissertation, the scope of theory will be confined to the SM, and we will try to search for this last missing particle in the theory experimentally. For a more detailed account of experiment and theory history and recent advances, the reader is referred to [3].

2.2 Particles and Relativistic Quantum Fields

Particle physics experiments have shown that the particles should be described by relativistic quantum theory, *eg.*

$$|(\Phi, \Psi)|^2 = |(\Phi', \Psi')|^2 \tag{2.1}$$

where Φ (or Ψ) is the quantum state of the particle system in the experiment, and $\Phi' \equiv U\ \Phi$ is the same physics state in another inertial frame. The two states are connected by the state transformation operator U. It's easy to prove that the operator U is either linear and unitary or anti-linear and anti-unitary:

$$U^\dagger = U^{-1} \tag{2.2}$$

On the one hand, the physics state vector is just a collection of physics quantities that describe the state, we do not have any *a priori* knowledge about what quantities are needed, so there is not much to say about it; on the other hand, the operator U should reflect all the properties of the physics state because different physics states should generally undergo different transformations. So we start building the theory model of the quantum particle system by studying the properties of the operator U.

Once the transformation operator U is determined, the quantum numbers that are needed to define the state of the particle systems can be determined. Thus the quantum state Φ and its transformation properties are defined. This means the theory for the quantum particle system is fully solved. We describe this below and roughly follow the method described in [4].

2.2.1 Relativistic Quantum Theory and Perturbative Method

U is induced by an inhomogeneous Lorentz transformation $L(\Lambda, a)$,

$$L(\Lambda, a) : x \to x'^\mu = \Lambda^\mu_\nu x^\nu + a^\mu \tag{2.3}$$

where x is a space-time 4-vector. We can denote U as $U(\Lambda, a)$. Eq-2.1 states that U furnishes a representation of the inhomogeneous Lorentz group. The Lorentz group can be decomposed into the multiplication of its subgroup—the continuous proper orthochronous inhomogeneous Lorentz group— with a discrete symmetry transformation group $\{1, \mathcal{P}, \mathcal{T}, \mathcal{PT}\}$, where $\mathcal{P}$ and $\mathcal{T}$ are space and time inversions. Thus the Lorentz transformation properties of U are reduced to its properties under the proper orthochronous Lorentz transformation and the time or space inversion.

We will start with U under a proper orthochronous inhomogeneous Lorentz transformation $L(\Lambda, a)$. This subgroup is a connected Lie group, thus any $U(L)$ can be expanded around 1 (corresponding to $L(1, 0)$). U under an infinitesimal Lorentz

transformation $L(1+\omega,\epsilon)$ around $L(1,0)$ can be expanded as:

$$U(1+\omega,\epsilon) = 1 + \frac{1}{2} i\omega_{\mu\nu} J^{\mu\nu} - i\epsilon_\mu P^\mu \tag{2.4}$$

where $\omega_{\mu\nu} = -\omega_{\nu\mu} \ll 1, \epsilon \ll 1$, $J^{\mu\nu} = -J^{\nu\mu}$ and P^μ are the Lie group's generator.

In order to satisfy Eq-2.2 the 10 generators J and P must be Hermitian operators:

$$J^{\mu\nu\dagger} = J^{\mu\nu}, P^{\mu\dagger} = P^\mu \tag{2.5}$$

Since $U(1,0) = 1$ is a linear operator and U is a connected Lie group, J and P must be linear operators, too, so these generators could be physics observables according to quantum theory.

Eq-2.4 shows that ωJ and ϵP are Lorentz invariant, so J and P are Lorentz tensor and vector, respectively. Obviously P has the inverse dimension of length, so it must be proportional to the total 4-momentum operator of the particle state (not necessarily for single particle or free particle states). It can be shown that with the chosen convention in Eq-2.4, $H = P^0$ is the energy operator, or Hamiltonian, of the physics state, and $\mathbf{P} \equiv \{P^1, P^2, P^3\}$ is the 3-momentum operator. With the same argument, $\mathbf{J} \equiv \{J^{23}, J^{31}, J^{12}\}$ is the total angular momentum[1] of the state. The remaining 3 operators $\mathbf{K} \equiv \{J^{10}, J^{20}, J^{30}\}$ are called the boost 3-vector. Simple calculation shows that $[H, H] = [\mathbf{P}, H] = [\mathbf{J}, H] = 0$, so energy, 3-momentum and angular momentum are conserved (unchanging with U of time translation, or in more ordinary language with time evolution) and can be used to describe the particle states; $[\mathbf{K}, H] \neq 0$, so it is not related with any physics observable.

Direct calculation indicates the Lie groups induced by Lorentz transformation that contains only H (time evolution), or $\mathbf{P}$ (space translation), or $\mathbf{J}$ (space rotation) are Abelian, so energy, 3-momentum and angular momentum are additive observables. For an arbitrary general proper orthochronous inhomogeneous Lorentz transformation, the Lie algebra of the connected Lie group provides the exact solution for U. So the relativistic quantum theory of particle is partially exact solvable.

Now let's finish the solution of U by looking at the remaining transformations P and T of the general inhomogeneous Lorentz group. They are induced by Lorentz transformations space inversion $\mathcal{P}$ and time inversion $\mathcal{T}$, respectively,

$$\mathcal{P} \equiv \begin{pmatrix} -1 & 0 & 0 & 0 \\ 0 & -1 & 0 & 0 \\ 0 & 0 & -1 & 0 \\ 0 & 0 & 0 & 1 \end{pmatrix}, \ \mathcal{T} \equiv \begin{pmatrix} 1 & 0 & 0 & 0 \\ 0 & 1 & 0 & 0 \\ 0 & 0 & 1 & 0 \\ 0 & 0 & 0 & -1 \end{pmatrix} \tag{2.6}$$

[1]Experiments show particle could have a kind of intrinsic symmetry that has the same structure as rotation group, so it is called the spin S of the particle, total angular momentum J is the "vector" sum of orbital angular momentum L and spin S.

Since P and T are not connected to the Lie group that has unit element 1, a physics system is not guaranteed to be symmetric under these transformation, and experiments indeed show that for some physics systems Eq-2.1 is not valid under these discrete Lorentz transformation, so there is no such unitary or anti-unitary operator U that can act on these physics systems to induce these discrete Lorentz transformation. This is one of the reasons we need to introduce quantum fields to account for this kind of broken symmetry system; otherwise relativistic quantum theory alone is enough to be the foundation of the whole of particle physics. We will talk about this issue in the next section. For the time being let's assume the physics system we are considering does maintain the symmetry under $\mathcal{P}$ and $\mathcal{T}$, so the existence of P and T is ensured and they satisfy

$$[P, H] = [T, H] = 0. \tag{2.7}$$

Since the $U(\Lambda, a)$ of a proper orthochronous Lorentz transformation and P, T together furnish a representation of general inhomogeneous Lorentz group, we have:

$$PU(\Lambda, a)P^{-1} = U(\mathcal{P}\Lambda\mathcal{P}^{-1}, \mathcal{P}a) \tag{2.8}$$
$$TU(\Lambda, a)T^{-1} = U(\mathcal{T}\Lambda\mathcal{T}^{-1}, \mathcal{T}a) \tag{2.9}$$

Using Eq-2.6, Eq-2.8 and 2.9 implies[2]

$$PiHP^{-1} = iH \tag{2.10}$$
$$TiHT^{-1} = -iH \tag{2.11}$$

Combined with Eq-2.7, these relations obviously show that P is linear and unitary and T is anti-linear and anti-unitary, so P can be used as a physics observable, while T can not. The physics observable associated with P is called intrinsic parity, since it generated from the discrete symmetry transformation. It is a discrete multiplicative quantum number instead of additive, and it can be determined for each particle from experiments.[3]

Clearly Eq-2.8, 2.9 also provide the extended Lie algebra between P, T and $\mathbf{P}$, $\mathbf{J}$ and $\mathbf{K}$ which reads:

$$P\mathbf{P}P^{-1} = -\mathbf{P},\ P\mathbf{J}P^{-1} = \mathbf{J},\ P\mathbf{K}P^{-1} = -\mathbf{K}, \tag{2.12}$$
$$T\mathbf{P}T^{-1} = -\mathbf{P},\ T\mathbf{J}T^{-1} = -\mathbf{J},\ T\mathbf{K}T^{-1} = \mathbf{K} \tag{2.13}$$

The physics meaning of the above equations is obvious.

So we have defined all the necessary quantum numbers to describe a physics state

[2]The i on the LHS is kept in position because we do not know whether P and T are linear or anti-linear operators.

[3]For mass zero particle, there is a complication[4].

by studying the Lorentz transformation operator U. Given the 3-momentum $\mathbf{p}_i$ [4], the spin $\mathbf{s}_i$ and the specie number r_i (which may include the parity and any other possible intrinsic quantum numbers that differ the particle from the other species.) of the $i-$th particle the quantum state Φ of an n-particle state can be denoted as:

$$\Phi = \Phi(\mathbf{p}_1, \mathbf{s}_1, r_1; \mathbf{p}_2, \mathbf{s}_2, r_2; ...\mathbf{p}_n, \mathbf{s}_n, r_n) \equiv \Phi_\alpha. \tag{2.14}$$

Using the Lie algebra of the proper orthochronous inhomogeneous Lorentz group plus the relations in Eqs-2.12 and 2.13, an arbitrary transformation operator $U(\Lambda, a)$ can be determined for a given particle system Φ_α. Thus in principle the relativistic quantum theory of particles is formally solvable. A simple but very useful example is the time translation operator $U(1, -t)$:

$$U(1, -t) = e^{-iHt} \tag{2.15}$$

by requiring $\omega = 0,\ \epsilon = (0, -dt)$ and integrating Eq-2.4. $U(1, -t)$ transforms a state Φ_α from time 0 to time t[5].

If the state is a eigenstate of H then Eq-2.15 is reduced to $U(1, -t) = e^{-iEt}$ where E is the energy (the eigenvalue) of the system. An example of this case is the non-interactive Hamiltonian H_0 for a free particle system.

For realistic processes, H contains interactions between different particles. The full Hamiltonian operator H can be decomposed as:

$$H = H_0 + H_i. \tag{2.16}$$

H_0 is the free Hamiltonian; H_i, the interaction Hamiltonian. H_0 and H_i describe the energies of free elementary particle states and the transition probabilities between these states, respectively. In this case Eq-2.15 is generally not analytically solvable. Fortunately we usually do not need the full knowledge of U to calculate the experimental measurements. The solution is to use the perturbative method sketched below.

For an interacting particle system, the experimentally observable quantum states are the asymptotically free particle states. This means if we define the initial (in) and final (out) states of an experiment (an interaction) as $\Psi^+_\alpha(t_i = 0 - \delta)$ and $\Psi^-_\alpha(t_i = 0 + \delta)$, respectively, where the interaction happens at $t_i = 0$ and 2δ is the interaction

[4]Unlike a virtual state in which the energy is arbitrary, the energies of a system's physical states is fully determined by the other quantum numbers, for example, a free particle $p_0 = \sqrt{\mathbf{p}^2 + m^2}$. So we will not write p_0 explicitly.

[5]Note the Schröedinger picture is used, so the state vector Φ_α is time dependent and the operator H is time-independent.

duration, we can always choose a free particle state Φ so that:

$$\lim_{t\to\mp\infty} U(1,-t)\Psi_\alpha^\pm(\mp\delta) = \lim_{t\to\mp\infty} U_0(1,-t)\Phi_\alpha(\mp\delta) \tag{2.17}$$

where U and U_0 are for the interactive and free particle, respectively. So we have

$$\Psi_\alpha^\pm = \Omega(\mp)\Phi_\alpha \tag{2.18}$$

where

$$\Omega(\tau) \equiv e^{iH\tau}e^{-iH_0\tau} \tag{2.19}$$

To describe the particle experiments, we only need to calculate the transition probability amplitude $S_{\beta,\alpha}$ between two asymptotic free states Ψ_α^+ and Ψ_β^-:

$$S_{\beta,\alpha} = \lim_{\delta\to 0}(e^{iH\delta}\Psi_\beta^-, e^{-iH\delta}\Psi_\alpha^+) = (\Phi_\beta(0), \mathcal{S}\Phi_\alpha(0)). \tag{2.20}$$

where the operator $\mathcal{S}$ is defined as:

$$\mathcal{S} = \Omega^\dagger(+\infty)\Omega(-\infty) = S(+\infty,-\infty), \tag{2.21}$$

and $S(t,t_0)$ is defined as:

$$S(t,t_0) = e^{iH_0t}e^{-iH(t-t_0)}e^{-iH_0t_0}. \tag{2.22}$$

From the definition of $\mathcal{S}$ in Eq. 2.21, it is obvious that $\mathcal{S}$ is Lorentz invariant.

In deriving Eq-2.20, the interaction duration is assumed to be infinitesimal, and H does not contain singularities. This is not true when there are the intermediate states between the in and out state (there will be finite interaction time), plus for a intermediate state that is a resonant state (on the mass shell), the H_i contains singularity (besides the momentum conservation δ function) so $\lim_{\delta\to 0} e^{-iH_i\delta} \neq 1$. Note that the existence of a intermediate state means there are multi-interactions between the in and out states. We can split the duration between the in and out state so that in each new time span there is only interaction, we assume the intermediate virtual states are the "in" and "out" states and consider only one of the spans in deriving the above Eqs-2.20–2.22. It can be shown that these intermediate virtual states will be automatically accounted for by the so called particle propagators.

In order to obtain an analytical expression of $S(t,t_0)$, we rewrite it using an integral equation:

$$S(t,t_0) = 1 - i\int_{t_0}^{t} d\tau V(\tau)S(\tau,t_0), \tag{2.23}$$

where $V(t)$ is defined as:

$$V(t) = e^{iH_0t}H_ie^{-iH_0t} \tag{2.24}$$

is the H_i expressed in a so called interaction picture. In this form $S(t,t_0)$ and $\mathcal{S}$ can be solved recursively:

$$\mathcal{S} = 1 + \sum_{n=1}^{\infty} \frac{(-i)^n}{n!} \int_{-\infty}^{\infty} dt_1 \cdots dt_n T\left\{V(t_1)\cdots V(t_n)\right\} \equiv T\left\{e^{-i\int_{-\infty}^{\infty} dt V(t)}\right\}. \quad (2.25)$$

where $T\{\cdots\}$ is the time ordered product. Using Eq-2.25 the transition probability amplitude $S_{\beta,\alpha}$ can be calculated perturbatively.

From Eq-2.20 we can see that $\mathcal{S}$ is a Lorentz scalar:

$$U(\Lambda,a)^{-1}\mathcal{S}U(\Lambda,a) = \mathcal{S}, \quad (2.26)$$

in order to make $\mathcal{S}$ explicitly Lorentz invariant, we introduce a interaction Hamiltonian density:

$$V(t) = \int d^3\mathbf{x}\mathcal{H}(\mathbf{x},t), \quad (2.27)$$

thus $\mathcal{S}$ can be rewritten as:

$$\mathcal{S} = 1 + \sum_{n=1}^{\infty} \frac{(-i)^n}{n!} \int_{-\infty}^{\infty} d^4x_1 \cdots d^4x_n T\left\{\mathcal{H}(x_1)\cdots\mathcal{H}(x_n)\right\} \quad (2.28)$$

if we require $\mathcal{H}(x)$ satisfy

$$U_0(\Lambda,a)\mathcal{H}(x)U_0^{-1}(\Lambda,a) = \mathcal{H}(\Lambda x + a) \quad (2.29)$$

$$[\mathcal{H}(x),\mathcal{H}(x')] = 0 \quad \text{for} \quad (x-x')^2 \geq 0 \quad (2.30)$$

then $\mathcal{S}$ is explicitly Lorentz invariant. Eq-2.30 is called the causality condition, it basically states that two space-like points can not be correlated by any interaction[6].

At this point it seems that by studying the Lorentz symmetry properties of the general quantum states we have fully solved the problem of describing the particle physics experiment. Yet this is not true. For a simple quantum system in which there are only a few quantum states, $\mathcal{H}$ is easy to construct. But for a particle system, the construction of $\mathcal{H}$ is far from easy since there are infinite number of quantum states. We will see in Sections 2.2.3 and 2.3 that by introducing a quantum field $\mathcal{H}$ can be easily constructed. Also many questions that are not answered by the relativistic quantum theory can be naturally explained: why anti-particles exist, why boson-fermion statistics is connected with the spin of the particle, why the electric charge is conserved, or why there are so many other symmetry rules.

[6]The causality condition is not based on perturbative method, and it is not a necessory condition for the Lorentz invariance of $\mathcal{H}$.

2.2.2 Elementary Particles and Interactions

Having established the first theory of particles, let's have a look at the experimental results. There are 16 types of elementary particles (plus their anti-particles), *ie.* particles with no observed substructures. These particles and the interactions in which they are involved are shown in Figure-2.1.

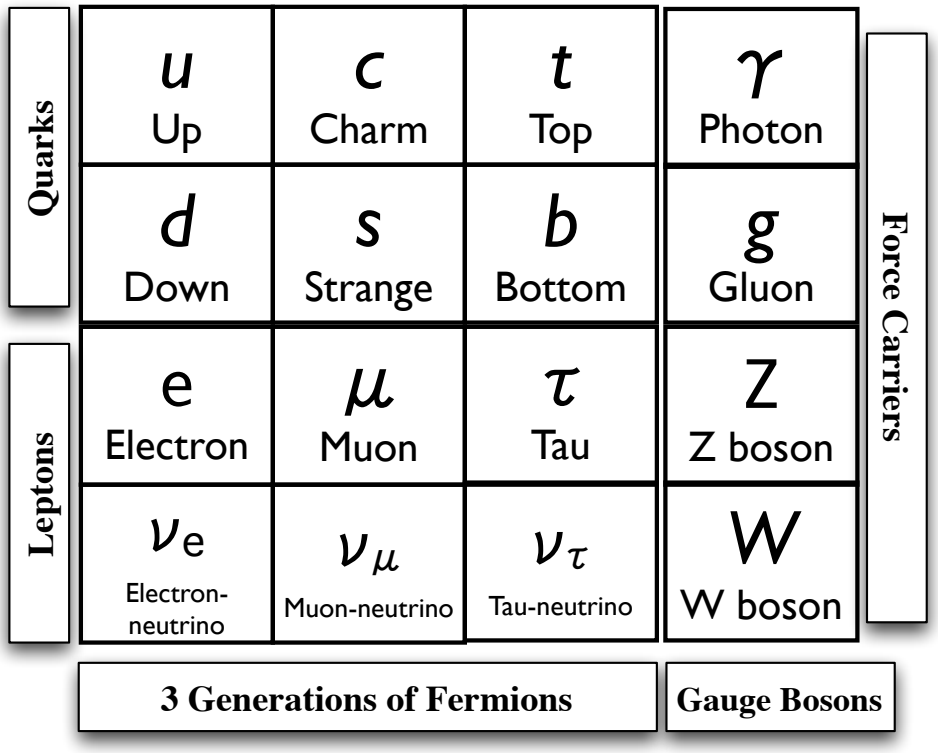

Figure 2.1: The elementary particles that have been discovered in the experiments up to 2006. Each particle in the three generations of fermions has its anti-particle. For the neutral gauge bosons, *ie.* photon, gluon and Z boson, their anti-particles are themselves. The W boson contains W^+ and W^-, and they are each other's anti-particle. The gluon, W/Z bosons and photon only participate in strong, weak and electromagnetic (EM) interactions, respectively. Quarks participate in all three kinds of interactions. Leptons participate in weak and EM interactions.

The properties of these elementary particles are listed in Table-2.1. As shown in the table, there are many more quantum numbers besides the spin J and parity P. The charge conjugation parity C is introduced to connect the particles with their anti-particles. The other quantum numbers are introduced to describe various conservation rules established by particle experiment results: the isospin I reflects the symmetry

between proton and neutron (or u and d quark) in the strong interactions, the quark flavor numbers S, C, B, T are introduced to reflect the corresponding conservation rules in the strong interactions[7], the lepton number $\mathbf{L}$ and the baryon number $\mathbf{B}$ are conserved due to a more subtle reason—the anomaly cancellation in the Standard Model. Last, the weak isospin I_3^w is purely a result of the Standard Model with the aim to unify the weak and the electromagnetic (EM) interactions. For fermions it is related to the electric charge Q by:

$$Y_w = 2(Q - I_3^w) \tag{2.31}$$

where Y_w is called the weak hypercharge. This relation will be derived in Section 2.3.1. For the left-handed fermions, there is another relation $Y_w = \mathbf{B}-\mathbf{L}$. The hypercharge is related to the $U(1)$ symmetry transformation of the electroweak interaction. We will get back to these relations in Section 2.3. It is worth noting that these conservation rules do not stem from the Lorentz invariance of the relativistic quantum theory in Eq-2.1, they are model dependent, and can be broken. For example, the $\mathbf{B}$ and $\mathbf{L}$ can be non-conservative in some supersymmetric models (but then $\mathbf{B}-\mathbf{L}$ is another candidate for the conservation law), the isospin is not conserved in the EM and weak interactions, and the baryon family numbers S, C, B, T are not conserved in the weak interaction.

Four kinds of interactions are known to exist between these elementary particles: gravity, weak, strong, and electro-magnetic. In classical theory, interaction is due to the potential; in the quantum theory, the interaction is due to the exchange of particles. These exchanged particles carry the transferred momentum, angular momentum and other quantum numbers. Interactions that involve photon, gluon, W/Z boson are the EM, strong, and weak interactions, respectively. Another particle called the *graviton* is believed to be the exchanged particle of gravitation, but there is no experiment evidence of its existence yet. The characteristic interaction lengths and strengths of these four interactions are list in Table-2.2.

As mentioned in Section 2.2.1, not all physics system's Hamiltonians H satisfy Eq-2.7. These four kinds of interactions' properties under various discrete symmetry transformations are listed in Table-2.3. Besides the Lorentz transformation invariance, these symmetry properties play important roles in building the theoretical models for the elementary particles and their interactions.

A very important concept that differentiates the quantum theory from the classical theory is that of an *identical particle*. A quantum particle can not be fully localized if it should be described by the quantum numbers discussed above, so two of the same kind of particles can not be distinguished by their space coordinates. A multi-particle

[7]We may also introduced the lepton flavor numbers as S, C, B, T. In fact the experiments have not shown direct evidence for the lepton family violating process yet, but due to the neutrino mixing, the lepton flavor number is expected not to be fully conservative.

N(Q)	$I_3(J)^{PC}$	**B**	**L**	S	C	B	T	$(I_3^w)_{L,R}$	M (GeV)	Γ (GeV)
$u(\frac{2}{3})$	$\frac{1}{2}(\frac{1}{2})^{+*}$	$\frac{1}{3}$	0	0	0	0	0	$\frac{1}{2}, 0$	$\approx 3 \times 10^{-3}$	N/A
$d(-\frac{1}{3})$	$-\frac{1}{2}(\frac{1}{2})^{+*}$	$\frac{1}{3}$	0	0	0	0	0	$-\frac{1}{2}, 0$	$\approx 5 \times 10^{-3}$	N/A
$c(\frac{2}{3})$	$0(\frac{1}{2})^{+*}$	$\frac{1}{3}$	0	0	1	0	0	$\frac{1}{2}, 0$	1.25 ± 0.09	N/A
$s(-\frac{1}{3})$	$0(\frac{1}{2})^{+*}$	$\frac{1}{3}$	0	-1	0	0	0	$-\frac{1}{2}, 0$	$\approx 95 \times 10^{-3}$	N/A
$t(\frac{2}{3})$	$0(\frac{1}{2})^{+*}$	$\frac{1}{3}$	0	0	0	0	1	$\frac{1}{2}, 0$	174.2 ± 3.3	N/A
$b(-\frac{1}{3})$	$0(\frac{1}{2})^{+*}$	$\frac{1}{3}$	0	0	0	-1	0	$-\frac{1}{2}, 0$	4.2 ± 0.07	N/A
$e(-1)$	$*(\frac{1}{2})^{**}$	0	1	0	0	0	0	$-\frac{1}{2}, 0$	0.51×10^{-3}	$> 4.6 \times 10^{26}$ yr
$\nu_e(0)$	$*(\frac{1}{2})^{**}$	0	1	0	0	0	0	$\frac{1}{2}, 0$	$< 2.2 \times 10^{-9}$	various
$\mu(-1)$	$*(\frac{1}{2})^{**}$	0	1	0	0	0	0	$-\frac{1}{2}, 0$	105.7×10^{-3}	2.2×10^{-6} s
$\nu_\mu(0)$	$*(\frac{1}{2})^{**}$	0	1	0	0	0	0	$\frac{1}{2}, 0$	$< 170 \times 10^{-6}$	various
$\tau(-1)$	$*(\frac{1}{2})^{**}$	0	1	0	0	0	0	$-\frac{1}{2}, 0$	1.777	290.6×10^{-15} s
$\nu_\tau(0)$	$*(\frac{1}{2})^{**}$	0	1	0	0	0	0	$\frac{1}{2}, 0$	$< 15.5 \times 10^{-3}$	various
$W^+(+1)$	$*(1)^{**}$	0	0	0	0	0	0	1	80.4	2.14
$Z(0)$	$*(1)^{**}$	0	0	0	0	0	0	0	91.2	2.5
$\gamma(0)$	$0, 1(1)^{--}$	0	0	0	0	0	0	0	$< 6 \times 10^{-23}$	stable
$g(0)$	$0(1)^{-*}$	0	0	0	0	0	0	0	0	N/A

Table 2.1: Properties of the observed elementary particles[20]. To save space, the precisions quoted here are reduced. Each specie of fermion has two types according to its helicity: left-handed and right-handed. The eigenstate states of the down type quarks (d, s, b quarks) in the strong interaction are different from those of the weak interactions, these two set of eigenstates are related by the Cabibo-Kobyashi-Maskawa matrix. Experiments have shown that the three flavors of neutrinos also have mixing, but the mixing the not determined yet. I_3 is the third component of the isospin; J^{PC} are the spin J with intrinsic parity P and the charge conjugation parity C; **B** and **L** are baryon number and lepton number, respectively; S, C, B, T are the strangeness, charm, bottomness and topness respectively; I_3^w is the third component of the weak isospin, for left-handed fermions, $I^w = \frac{1}{2}$, and $I_3^w = \pm\frac{1}{2}$, for the right handed fermions, $I^w = I_3^w = 0$; M is the rest mass in GeV; Γ is the decay width in GeV. Notice not all the particles have defined isospin or parities, in this case an asterisk is put in place. Due to color confinement, the quarks and gluon decay widths are not determined. The masses and the decay widths of neutrinos are not determined yet. Anti-particles have the same mass and life time as particles, carry the same additive quantum numbers with the opposite sign, the multiplicative quantum numbers are to be determined from experiment.

Interaction	Range (m)	Strength
Strong	$\sim 10^{-15}$	1
EM	Infinite	$\frac{1}{137}$
Weak	$\sim 10^{-18}$	10^{-6}
Gravity	Infinite	6×10^{-39}

Table 2.2: The four kinds of observed interactions. The stong interaction is short range because of the color confinement effect. The weak interaction is also short range since the mediator bosons have enormous masses (compared to electrons) which prevent them from propagating through long distances. The EM interaction and gravity have infinite interaction cross sections, so they are long range interactions. While the EM interaction is important for the both microscopic and macroscopic world, gravity is only manifest at stellar and galactic scales, and it is so weak compared to the other interactions that generally it is ignored (as is true for the Standard Model used in this dissertation) in the particle physics experiments. Also it turns out the quantization of gravity needs special theory frameworks (supergravity or superstring theories), and it is beyond the scope in this dissertation. The strengths of the different interactions are in fact not constants due to the quantum corrections, they depends on the observation energy scale. The value quoted in the table are measured in the GeV energy range, at the very high energy scale (Plank scale, $\sim 10^{19}$ GeV), the strengths of the four are supposed to be the same and the grand unification is achieved.

Interaction	C	P	T	CP	CPT
Strong	◯	◯	◯	◯	◯
Weak	×	×	×	×	◯
EM	◯	◯	◯	◯	◯
Gravity	◯	◯	◯	◯	◯

Table 2.3: Properties of the 4 kinds of interactions under various discrete symmetry transformations: C is the charge conjugation, P and T are space and time reverse, CP and CPT are the combination of C, P and T. ◯ means the symmetry is preserved, × means the symmetry is broken. The CPT can be proven to be conserved in quantum field theory. The weak interaction breaks the P symmetry maximally, on the contrary, the CP is only slightly broken. A broken CP symmetry in the theory is required in the theory in order to explain the observed baryogenesis, the CP violation in the Standard Model is not strong enough for the observed baryongenesis, and it is called the weak CP violation.

state Φ_α in Eq-2.14 is either symmetric or anti-symmetric under the transformation of exchanging two identical particles. Experiments show that all the bosons have integer spin and are symmetric while all the fermions have half integer spin and are anti-symmetric. That identical fermions' physics state must be anti-symmetric is also called Pauli exclusive principle.

All observed matter is built from the bound states of elementary fermions because only fermions can form stable bound states with non-zero energy eigenstate due to the Pauli exclusive principle. The bosons act as the "binding agent" of these fermion bound states.

A few examples of fermion bound states: the proton is made of (uud) and neutron is made of (udd), see Figure 2.1. This kind of three quark bound state is called a baryon, and a baryon itself is fermion, too. The common baryons, proton and neutron, make nuclei. A nucleus and electrons make an atom, and atoms are the building block of the world according to Mendeleev's period table. A pair of quark and anti-quark $q\bar{q}'$ can form another bound state called a meson. The lightest meson π is responsible for the binding of proton and neutron. The π is also abundant in cosmic rays and is the main source of the so-called showering in particle detectors.

2.2.3 Quantum Field Theory of Particles

One practical difficulty of using the relativistic quantum theory in Section 2.2.1 to describe the elementary particles listed in the Table-2.1 is that the time translation operator $U(1, -t)$ is not analytically solvable[8] for two reasons: these observed elementary particles are not the eigenstates of the full Hamiltonian H which contains the strong, weak and EM interactions[9], and the particles have infinite numbers of states.

Yet it is desirable to build the theory from these fundamental particles, because it is these asymptotically free particles that are directly observable in particle experiments. We will show in this section that by using quantum fields to describe the particles instead of the simple quantum state vectors Φ_α, these problems can be solved. We will start with the matrix elements of the full Hamiltonian $H = H_0 + H_i$ under the basis of asymptotically free particles.

The matrix element of H_0 is the total energy of the asymptotically free particle system multiplied by a δ functions that ensure the number of each specie of particles and their quantum numbers are preserved. The energy E of a asymptotically free particle with 3-momentum $\mathbf{p}$ is given by $E = \sqrt{\mathbf{p}^2 + m_0^2}$ where m_0 is the measured rest

[8] A Lorentz transformation without time translation $U(\Lambda, \mathbf{a})$ is solvable because the state 3-vector $\mathbf{p}$ and spin σ are still "good" quantum numbers for interactive particles.

[9] Except for e and γ, since the kinematics forbids them from decaying. The proton, with life time $\Gamma > 10^{32}$ yr could be a candidate for the eigenstate of the full H.

mass of the *asymptotically* free particle (not the "bare" mass of a true free particle), so H_0 is a diagonal matrix:

$$H_0 = \sum_{\alpha';\alpha} E_\alpha \delta(\alpha' - \alpha_1) \tag{2.32}$$

$$E_\alpha = \sum_i E_i \tag{2.33}$$

where the sum over i run through all the particles in the state.

It is obvious from Eqs-2.32 and 2.33 that the operator $U(1, -t)$ of asymptotically free multi-particle system has the simple form of $e^{-i\sum_j E_j t} = \prod_j e^{-iE_j t}$. Thus the state Φ_α is the product of each asymptotically free single particle state with proper symmetry requirement for the identical bosons and fermions:

$$\Phi_\alpha = \mathcal{S}\left\{\prod_i \Phi_i(\mathbf{p}_i, \mathbf{s}_i, r_i)\right\} \tag{2.34}$$

where $\mathcal{S}$ denoted the symmetry requirement for the identical particles, and Φ_i stands for a state of a single asymptotically free particle.

Now we study the properties of the H_i, or equivalently $V(t)$. As shown in Eq. 2.4, H describes the change of a quantum state under infinitesimal time translation. Within an infinitesimal time interval, only one interaction could take place. The 3-momentum must be preserved by any interaction, so the matrix element of H_i contains a single 3-momentum conservation delta function $\delta^3(\mathbf{P} - \mathbf{Q})$, where $\mathbf{P}$ and $\mathbf{Q}$ are the initial state and the final state 3-momenta, respectively.

In order for H_i to describe the transitions between the initial and final particle states, it must be able to destroy the initial particle state and create the final particle state which in general is different from the initial state. For this purpose we introduce a special kind of creation operator $a^\dagger_{\mathbf{p},\mathbf{s}}$ which creates a free particle with 3-momentum $\mathbf{p}$ and spin $\mathbf{s}$:

$$\Phi_{\mathbf{p},\mathbf{s}} = [(2\pi)^3 p_0]^{1/2} a^\dagger(\mathbf{p}, \mathbf{s})\Phi_0 \tag{2.35}$$

where $\Phi_{\mathbf{p},\mathbf{s}}$ is a single free particle state with momentum $\mathbf{p}$ and spin $\mathbf{s}$, Ψ_0 is the vacuum state, the normalization factor $(2\pi^3 p_0)^{1/2}$ is chosen so that the normalization condition $(\Phi_{\mathbf{p}',\mathbf{s}'}, \Phi_{\mathbf{p},\mathbf{s}}) = \delta(\mathbf{p}' - \mathbf{p})\delta(\mathbf{s}' - \mathbf{s})$ is Lorentz invariant. Thus a multi-particle state Φ_α in Eq-2.34 can be expressed using $a^\dagger$ as:

$$\Phi_\alpha = \mathcal{S}\left\{\prod_i a^\dagger_i(\mathbf{p}_i, \mathbf{s}_i)\right\}\Phi_0. \tag{2.36}$$

The time dependence of $a^\dagger$ is derived from Eq-2.35 as:

$$a^\dagger(t) = U_0^{-1}(1,-t)a^\dagger U_0(1,-t) = e^{iEt}a^\dagger \tag{2.37}$$

By the definition of the adjoint of an operator, it is easy to show that the adjoint of $a^\dagger$, denoted as a, destroys a free particle, so we call a the annihilation operator. With $a^\dagger$ and a, we can model H_i as proportional to product of a series of creation and annihilation operators.

$$V(t) = \sum_{N,M} C_{N.M}\delta^3(\mathbf{P}_M - \mathbf{Q}_N)\prod_N a^\dagger_{\mathbf{p}_j,\mathbf{s}_j,n_j}(t)\prod_M a_{\mathbf{q}_k,\mathbf{s}_k,n_j}(t) \tag{2.38}$$

where $C_{N,M}$ is the transition rate from initial state M to final state N, $\mathbf{P}_M = \sum_i^M \mathbf{p}_i$ and $\mathbf{Q}_N = \sum_i^N \mathbf{q}_i$ are the total momenta summed over all the initial and final state particles, respectively.

Notice that

$$\delta^3(\sum_i^M \mathbf{p}_i - \sum_j^N \mathbf{q}_j) = \int \frac{d^3x}{(2\pi)^3}\left(e^{if(x)}\prod_i^N e^{-i\mathbf{p}_i\cdot\mathbf{x}}\right)\left(e^{-if(x)}\prod_j^M e^{i\mathbf{q}_j\cdot\mathbf{x}}\right) \tag{2.39}$$

where $f(x)$, an arbitrary real (scalar) function of x, is called the *gauge*. For now we only consider $f \equiv 1$. Combining Eqs-2.27, 2.38, 2.39, $\mathcal{H}$ can be expanded by the product of a series of creation field operator $\phi^-(x)$

$$\mathcal{H}(x) = \sum_{N,M}\sum_{l'_1\cdots l'_N}\sum_{l_1\cdots l_M} g_{l';l}\phi^-_{l'_1}(x)\cdots\phi^-_{l'_N}(x)\phi^+_{l_1}(x)\cdots\phi^+_{l_M}(x) \tag{2.40}$$

here the sum $\sum_{N,M}$ does not include the integrations over momenta, $g_{l';l}$ is the interaction coefficient, for different particles there are different annihilation and creation field operators $\phi^+_l(x)$, $\phi_l(x)$, respectively. These field operators are defined as:

$$\phi^+_l(x) = \sum_\sigma \int \frac{d^3\mathbf{p}}{(2\pi)^3(2p_0)^{1/2}} u_l(\mathbf{p},\sigma)a(\mathbf{p},\sigma)e^{ipx} \tag{2.41}$$

$$\phi^-_l(x) = \sum_\sigma \int \frac{d^3\mathbf{p}}{(2\pi)^3(2p_0)^{1/2}} v_l(\mathbf{p},\sigma)a^\dagger(\mathbf{p},\sigma)e^{-ipx} \tag{2.42}$$

where the coefficients u, v are called the wave function of the particle in the momentum space. The factor $(2p_0)^{-1/2}$ is added since $d^3\mathbf{p}/(2p_0)^{-1/2}$ is the Lorentz invariant integration volume element. The subscript l denotes the internal components of the field operator since that the particle it describes may have Lorentz structure, such as scalar, vector or spinor particle depending on the spin of the particle.

As discussed in Section 2.2.1, the $\mathcal{H}(x)$ constructed from these field operators

must satisfy Lorentz invariance Eq-2.29 and causality condition Eq-2.30. These two conditions put strong constraints on the field operators as well as on the structure of the constructed $\mathcal{H}$.

Based on a sounded physical assumption, we can choose the field operators to be Lorentz covariant:

$$U_0(\Lambda, a)\phi_l^{\pm}(x)U_0^{-1}(\Lambda, a) = \sum_{\bar{l}} D_{l\bar{l}}(\Lambda^{-1})\phi_{\bar{l}}^{\pm}(\Lambda x + a) \tag{2.43}$$

where $D_{l\bar{l}}(\Lambda^{-1})$ represents the covariance of the field operator. Clearly $D_{l\bar{l}}(\Lambda^{-1})$ furnishes a representation of the homogeneous Lorentz group.[10] For example, $D = 1$ represents a scalar field, and $D = \Lambda$ represents a vector field. In order for $\mathcal{H}$ to satisfy Eq-2.29, $g_{l;l'}$ should also be Lorentz covariant so that $\mathcal{H}$ in Eq-2.40 is Lorentz invariant. It can be shown that using Eq-2.43, u, v can be fully determined (with some chosen conventions) for a particle with given spin, so the field operators are fully determined. Also the dynamic equations that the field of this particle satisfy can also be derived.

Simple calculation shows that $[\phi_l^+(x), \phi_{\bar{l}}^-(y)] \neq 0$, so the $\mathcal{H}$ constructed in Eq-2.40 can not satisfy Eq-2.30. In order to solve this problem, we expand $\mathcal{H}$ with the linear combination of $\phi^{\pm}(x)$:

$$\phi_l(x) = a\phi_l^+(x) + b\phi_l^-(x) \tag{2.44}$$

With properly chosen a and b, it can be shown that for two space-like separated points x, y:

$$[\phi_l(x), \phi_{\bar{l}}(y),]_{\pm} = [\phi_l(x), \phi_{\bar{l}}^{\dagger}(y),]_{\pm} = 0. \tag{2.45}$$

this linear combination $\phi_l(x)$ is called the quantum field operator of the particle, or simply, the quantum field.

So by introducing the relativistic quantum field, we have completed the task of constructing a general theory for a quantum particle system. Our theory satisfies the most fundamental requirements of Lorentz invariance and causality, and it is calculable perturbatively.

With the relativistic quantum field theory, the un-solved questions mentioned at the end of the Section 2.2.1 can also be answered. The outline of the arguments are listed below:

- **Anti-particles.** This is basically a requirement of the causality condition. If a particle's charge conjugate is not the same as itself, the conjugate of the corresponding field is not the same, either, which implies the creation and annihilation operators in the $\Phi^{\pm}$ are not charge conjugate with each other. Further calculation indicates that they correspond to two particles with the same mass,

[10] We choose $D_{l\bar{l}}(\Lambda^{-1})$ instead of $D_{l\bar{l}}(\Lambda)$ due to the simplification of the further calculation.

but opposite internal symmetric quantum numbers, such as the electric charge, parity (if it exists), handedness (helicity), lepton number, baryon number, *etc.*

- **Boson and fermion statistics.** The spin of the particles determines the form of the momentum space field functions u, v. Whether the causality condition Eq-2.45 should commute or anti-commute is basically determined by the field functions. It can be shown for an integer spin particle, the commutation relation is always assumed, yet for a half-integer spin particle, the anti-commutation relation should be used. This is just the experimentally observed relation between spin and statistics.

- **CPT theorem.** Based on Lorentz invariance and the causality condition, the operator $\mathcal{H}$ constructed using the relativistic quantum field always satisfies $CPT\mathcal{H}(x)(CPT)^{-1} = \mathcal{H}(-x)$, as has shown in Table 2.3.

- **General interaction structure.** Because of the Lorentz invariance properties of $\mathcal{H}$, there must be even numbers of fermion fields appearing in the interaction. This is why fermions are usually called the matter—unlike bosons (for example, photon) they can not be created or destroyed "freely". By counting the dimension of the fermion and boson field, for a theory that can be renormalized in 4-D, the interaction can only contain zero or two fermions, and the fermion pair always couples with a boson field. Since all the observed boson fields are Lorentz vector fields, the two fermion fields must also be combined to form a Lorentz vector, this vector is called the current J_μ. The Lorentz invariant requirements on $\mathcal{H}$ implies that the fermion current is a conserved current at the tree level, *eg.* $p^\mu J_\mu = 0$.[11] That is the origin of the lepton number and baryon number conservation. Since gravity can mix the baryon and lepton, the lepton or baryon number will not be conserved for gravity, thus the graviton can not be a vector boson field, it must be at least spin 2.

- **Gauge symmetries and conserved charges.** As implied from Eq-2.39 and the argument above, the $\mathcal{H}$ has an exact symmetry—the *gauge symmetry*, in which the phase of the fermion fields can be changed locally by an arbitrary gauge function. The gauge symmetry, like the Lorentz invariance (symmetry), is unbroken and exact, which is why the gauge symmetry is such a strong and important property that almost all quantum particle theories are based on it. It is a physically sound symmetry because the phase of the wave function is not a measurable physical quantity, so it should be defined freely. Since $\mathcal{H}$ alone describes the time evolution of the whole quantum system, the gauge symmetry should be an exact symmetry observed by the elementary particles.

[11] For the current to be conserved with the quantum correction, the anomaly in the theory must be exactly canceled.

Yet the local change in the phase of the fermion field means the change of the fermion's momentum spectrum, thus the energy H_0 of the fermion which the field represents. In order to preserve H_0 for the fermions, the boson fields must also undergo some corresponding gauge symmetry transformations so that the extra terms from the boson field gauge transformations can cancel the change in the fermion field H_0. That is the reason the bosons are called the gauge bosons. It can be shown that all the gauge transformations form a group. The gauge transformation in Eq-2.39 is just a illustration of the simplest gauge symmetry group, the $U(1)$ group, where the generator of the transformation is $\mathbf{I}$. The EM interaction, in which the fermion current has the form $(e\mathcal{O}_\mu e)$, satisfies the $U(1)$ symmetry. For the weak interactions where a lepton field ℓ and a neutrino field ν_ℓ form a current $(\nu_\ell \mathcal{O}_\mu \ell)$, the gauge symmetry implies that the two different fields ℓ and ν_{ell} belong to a doublet $(\nu_\ell, \ell)^T$ that transforms under the $SU(2)$ symmetry group (the same argument is applicable to quark doublets, too.). For the strong interaction where three colors of quarks form the current, the symmetry group is $SU(3)$ since the transformation is on a triplet $(q_R, q_B, q_G)^T$. The various charges can be shown to be closely related with the generators of the gauge symmetry group.

At this point we use the Hamiltonian density $\mathcal{H}$ exclusively to construct the quantum gauge field theory of the particles. The Lagrangian density $\mathcal{L}$ is equivalent to $\mathcal{H}$. Either the canonical transformation method or the path integral method can be used to derive the $\mathcal{L}$ from the $\mathcal{H}$. In practice, using $\mathcal{L}$ makes the Lorentz symmetry and the gauge symmetry clearer than using $\mathcal{H}$, so from now on, we will switch to $\mathcal{L}$.

2.3 The Standard Model

To illustrate the gauge symmetry using the Lagrangian density, we will start with the free Lagrangian density $\mathcal{L}_0$ of a massless free fermion field ψ with half spin:

$$\mathcal{L}_0 = \bar{\psi}(i\ \partial\!\!\!/)\psi \tag{2.46}$$

where $\bar{\psi} \equiv \psi^\dagger \gamma^0$, $\partial\!\!\!/ \equiv \gamma^\mu \partial_\mu$ and γ^μ's are the 4×4 γ matrices.

First we consider the EM interaction which has the $U(1)$ symmetry. The interaction Lagrangian density $\mathcal{L}_i^{\text{EM}}$ is:

$$\mathcal{L}_i^{\text{EM}} = -eJ^{\text{EM}} \cdot A \tag{2.47}$$

where e is the electric charge, A_μ is the photon's vector boson field, and the EM current J^{EM} is defined as:

$$J_\mu^{\text{EM}} \equiv \bar{\psi}\gamma^\mu \psi. \tag{2.48}$$

The $U(1)$ gauge symmetry transformation on the fermion field $\psi(x)$ means:

$$\psi(x) \to \psi'(x) = e^{i\mathbf{I}\theta(x)}\psi(x) \tag{2.49}$$

where $\mathbf{I}$ is the generator of $U(1)$ group (a number for this special $U(1)$ symmetry), and $\theta(x)$ is the gauge, an arbitrary real function as in Eq-2.39. Clearly $\mathcal{L}_i$ is unchanged, but $\mathcal{L}_0$ has an extra term from this local gauge transformation:

$$\mathcal{L}_0 \to \mathcal{L}_0 - \bar{\psi}\mathbf{I}\ \partial\!\!\!/\theta\psi \tag{2.50}$$

But if we rewrite the field A in Eq-2.47 as $A \cdot \mathbf{I}$ and transform the photon field A as:

$$A \to A' = A - \frac{1}{e}\partial\theta \tag{2.51}$$

then the second term above will cancel the extra term in Eq-2.50, which leaves $\mathcal{L}_0(\psi') = \mathcal{L}_0(\psi)$ and $\mathcal{L}_i(\psi', A') = \mathcal{L}_i(\psi, A)$. Combining $\mathcal{L}_0$ and $\mathcal{L}_i$, we can get a more concise expression:

$$\mathcal{L} = \mathcal{L}_0 + \mathcal{L}_i = \bar{\psi}\ D\!\!\!/\psi \tag{2.52}$$

where the covariant derivative D_μ is defined as:

$$D_\mu \equiv \partial_\mu + ieA_\mu \cdot \mathbf{I}. \tag{2.53}$$

Similarly, to include the $SU(2)$ and $SU(3)$ gauge symmetry, we only need to add the corresponding gauge fields multiplied with the group generators into Eq-2.53.

The most distinguishing features of the strong interaction are the color confinement and the asymptotic freedom, which are due to its non-Abelian $SU(3)$ symmetry group. Except for the non-Abelian group structure, the strong interaction is very much like the EM interaction: they both preserve most of the symmetry properties, and the gauge bosons of the two kinds of interactions are both massless.

The weak interaction also satisfies a non-Abelian symmetry group, $SU(2)$. The $SU(2)$ group acts on the weak isospin doublets $(\nu_\ell, \ell)^T$, $(\mathcal{U}, \mathcal{D})^T$ and their charge conjugates, where $\ell = \{e, \mu, \tau\}$, $\mathcal{U} = \{u, c, t\}$, $\mathcal{D} = \{d, s, b\}$. The most important feature of the weak interaction is the broken parity symmetry. Notice the interaction in Eq-2.47 is basically the inner product of two vectors: the vector gauge boson fields and the vector fermion current. Under space inversion, $\mathbf{V} \cdot \mathbf{V}$ is invariant. That is the reason why strong and EM interactions conserve parity. For the weak interaction to break parity, the weak gauge bosons (vector particles as shown in Table 2.1) must be coupled to an axial-vector fermion current, *eg.* to have $\mathbf{A} \cdot \mathbf{V}$ structure in the weak interaction Lagrangian $\mathcal{L}^{\text{WEAK}_i}$. So the weak fermion current $\mathbf{J}^{\text{WEAK}}$ has the form:

$$\mathbf{J}_\mu^{\text{WEAK}} = \bar{\psi}' \left(\gamma_\mu(C_1 + C_2\gamma^5)\right) \psi \tag{2.54}$$

where ϕ is a fermion field, $C_1,\ C_2$ are constants. Experiments have proven that for a charged weak current where $\psi' \neq \psi$ the weak interaction maximally breaks the parity symmetry, *eg.* $C_1 = C_2$. So the charged weak current is reduced to $\mathbf{V} + \mathbf{A}$:

$$\mathbf{J}_\mu^\pm = \bar{\psi}'\gamma_\mu \left(\frac{1+\gamma^5}{2}\right)\psi = \bar{\psi}'\gamma_\mu\psi_{\text{L}} = \bar{\psi}'_{\text{L}}\gamma_\mu\psi_{\text{L}}. \tag{2.55}$$

which implies only the left-handed (LH) fermion doublets obey $SU(2)_{\text{L}} \times U(1)$ while the right-handed (RH) fermions obey a different symmetry group $SU(2)_{\text{R}} \times U(1)$ where $SU(2)_{\text{R}} = 1$ is trivial.

The Standard Model combines the three symmetry groups of the three kinds of interactions into $SU(3)_{\text{C}} \times SU(2)_{\text{L}} \times U(1)_{\text{Y}}$. It predicted the existence of the neutral weak current and the Z boson. With the $SU(2)_{\text{L}} \times U(1)_{\text{Y}}$, it provided a way to unify the weak and the EM interactions into one interaction, the electroweak force.

2.3.1 Electroweak Unification

The covariant derivative D_μ that includes the $SU(2) \times U(1)_{\text{Y}}$ can be written as:

$$D_\mu \equiv \partial_\mu \mathbf{I} + ig\mathbf{T}^a W_\mu^a + ig'\frac{\mathbf{Y}}{2}B_\mu \tag{2.56}$$

where W^a $(a = 1, 2, 3)$ and B are the gauge boson fields, g and g' are the coupling constants, the 2×2 matrices $\mathbf{I}$, $\mathbf{T}^a$ and $\mathbf{Y}$ are the unit matrix, the generators of the $SU(2)$ group and the $U(1)$ group, respectively. $\mathbf{T}^3$ is called the weak isospin operator, and $\mathbf{Y}$ is called the weak hypercharge operator. The weak isospin and weak hypercharge of each elementary particles are defined in Table 2.1. Recombining $(\mathbf{T}^1,\ \mathbf{T}^2)$, $(W^1,\ W^2)$ and $(W^3,\ B)$ in the following way:

$$\mathbf{T}^\pm \equiv \mathbf{T}^1 \pm i\mathbf{T}^2 \tag{2.57}$$

$$W^\pm \equiv \frac{1}{\sqrt{2}}(W^1 \pm iW^2) \tag{2.58}$$

$$\begin{pmatrix} B \\ W^3 \end{pmatrix} \equiv \begin{pmatrix} \cos\theta_w & -\sin\theta_w \\ \sin\theta_w & \cos\theta_w \end{pmatrix} \begin{pmatrix} A \\ Z \end{pmatrix} \tag{2.59}$$

where A and Z are the observed EM field and the neutral weak gauge boson, $W^\pm$ are the charged weak gauge bosons, and θ_w is called the weak mixing angle. If we further require:

$$g\sin\theta_w = g'\cos\theta_w = e \tag{2.60}$$

$$\mathbf{Q} = \mathbf{T}^3 + \frac{\mathbf{Y}}{2} \tag{2.61}$$

where e is the electric charge and $\mathbf{Q}$ is the charge operator (in the unit of the electron charge e), then Eq-2.56 can be rewritten as:

$$\begin{aligned} D &= \partial + i\frac{g}{\sqrt{2}}(\mathbf{T}^+W^- + \mathbf{T}^-W^+) \\ &\quad +i(g\mathbf{T}^3\cos\theta_w - g'\frac{\mathbf{Y}}{2}\sin\theta_w)Z + i(g\mathbf{T}^3\sin\theta_w + g'\frac{\mathbf{Y}}{2}\cos\theta_w)A \\ &= \partial + i\frac{g}{\sqrt{2}}(\mathbf{T}^+W^- + \mathbf{T}^-W^+) \\ &\quad +i\frac{g}{\cos\theta_w}\left[\mathbf{T}^3 - \sin^2\theta_w\left(\mathbf{T}^3 + \frac{\mathbf{Y}}{2}\right)\right]Z + ie\left(\mathbf{T}^3 + \frac{\mathbf{Y}}{2}\right)A. \end{aligned} \tag{2.62}$$

We know the broken parity of the weak force means the left handed (LH) and right handed (RH) fermions have different $SU(2)$ gauge symmetry properties. Notice that

$$\bar{\psi}\not{D}\psi = \bar{\psi_{\rm L}}\not{D}\psi_{\rm L} + \bar{\psi_{\rm R}}\not{D}\psi_{\rm R} \tag{2.63}$$

where $\psi = (\nu_\ell, \ell)^T, (\mathcal{U}, \mathcal{D})^T$ represents the fermion fields doublets, we can consider the LH and RH fermions separately.

The LH fermion Lagrangian density $\mathcal{L}^{\rm L}$ can be written as:

$$\begin{aligned} \mathcal{L}^{\rm L} &= \bar{\psi_{\rm L}}\not{D}\psi_{\rm L} + \text{h.c.} \\ &= \mathcal{L}_0^{\rm L} + i\frac{g}{\sqrt{2}}(J^+W^- + J^-W^+) \\ &\quad +i\frac{g}{\cos\theta_w}\left[J^3 - \sin^2\theta_w J_{\rm L}^{\rm EM}\right]Z + ieJ^{\rm EM}A + \text{h.c.} \\ &= \mathcal{L}_0^{\rm L} + i\frac{g}{\sqrt{2}}(J^+W^- + J^-W^+) + i\frac{g}{\cos\theta_w}J_{\rm L}^0 Z + ieJ_{\rm L}^{\rm EM}A + \text{h.c.} \end{aligned} \tag{2.64}$$

where h.c. means the hermitian conjugate (to account for the anti-particles), the $J^\pm$, $J_{\rm L}^0$ and $J_{\rm L}^{\rm EM}$ are the charged weak current (LH), the LH neutral weak current and the LH EM current, respectively.

For the RH fermions doublets, on the one hand they should not change under the $SU(2)_{\rm R}$ gauge symmetry transformation since they do not participate in the charged weak interactions, on the other hand they should satisfy the same $U(1)_{\rm Y}$ symmetry as the LH fermions since they experience the same kind of EM force. So for the RH fermions, the $SU(2)$ group generators $\mathbf{T}$ are trivial, *eg.* 0, and the $U(1)_{\rm Y}$ group generator is now $\frac{\mathbf{Y}}{2} = \mathbf{Q}$ according to Eq-2.61, the RH fermion Lagrangian density $\mathcal{L}^{\rm R}$ is then:

$$\mathcal{L}^{\rm R} = \bar{\psi_{\rm R}}\not{D}\psi_{\rm R} + \text{h.c.}$$

$$= \mathcal{L}_0^{\rm R} - i\frac{g\sin^2\theta_w}{\cos\theta_w} J_{\rm R}^{\rm EM} Z + ieJ_{\rm R}^{\rm EM} A + \text{h.c.} \tag{2.65}$$

where $J_{\rm R}^{\rm EM}$ is the RH EM current.

With the quantum numbers of the elementary particles defined as in Table 2.1, $J_{\rm L}^{\rm EM}$ and $J_{\rm R}^{\rm EM}$ are identical except for their handedness, so the EM interaction terms in Eqs-2.64 and 2.65 can be recombined into $J_\mu^{\rm EM} = \bar{\psi}\gamma_\mu \mathbf{Q}\psi$, which is the same as Eq-2.48 after replacing $\mathbf{Q}$ with the corresponding EM charge. Also the charged weak current $J_\mu^\pm \equiv \bar{\psi}\gamma_\mu \mathbf{T}^\pm \psi$ in Eqs-2.64 is the same as Eq-2.55. The neutral weak current J^0 that couples with the Z boson can be defined as:

$$\begin{aligned} J^0 &= J_{\rm L}^0 - \sin^2\theta_w J_{\rm R}^{\rm EM} \\ &= J_{\rm L}^3 - \sin^2\theta_w J^{\rm EM} \\ &\sim \bar{\psi}\gamma^\mu \frac{\left(\mathbf{T}^3 - 2\sin^2\theta_w \mathbf{Q}\right) + \mathbf{T}^3\gamma^5}{2}\psi \end{aligned} \tag{2.66}$$

clearly the neutral weak current does not have the maximum parity violation property as the charged weak current.

Thus we have unified the EM interaction with the weak interaction into a electroweak interaction. The weak mixing angle is measured to be $\sin^2\theta_w \approx 0.23$. With low energy approximation, the W mass can be related with the Fermi coupling constant G_F, the EM charge e and the weak mixing angle θ_w by relation $m_W = (\sqrt{2}e^2/8G_F\sin^2\theta_w)^{1/2} \approx 80.4$ GeV. From Eq-2.59, the mass of Z boson can be implied by the facts that $m_\gamma = 0$ and $(Z,\ A)$ are orthogonal fields, the relation between m_W, m_Z and θ_w is $m_W = m_Z\cos\theta_w$, the direct measurement shows that $m_Z \approx 91.2$ GeV.

Although the experiments show the W and the Z bosons have large masses, in the above $SU(2)\times U(1)$ theory, the gauge boson fields can not explicitly have mass terms because bilinear terms such as WW, BB would break the gauge symmetry. Also, the fermion fields in the above theory can not have mass terms, either, because the fermion field mass term $m\bar{\psi}\psi = m\bar{\psi}_{\rm L}\psi_{\rm R} + m\bar{\psi}_{\rm R}\psi_{\rm L}$ will mix the LH and RH fermion fields, so they breaks the gauge symmetry, too. The mass problem is solved by the Higgs mechanism.

2.3.2 The Higgs Mechanism

Consider a scalar field doublet Φ which has weak isospin $I^w = 1/2$ and weak hypercharge $Y^w = 1$:

$$\Phi = \begin{pmatrix} \Phi^+ \\ \Phi^0 \end{pmatrix} \tag{2.67}$$

Since Φ^+ is a charged field, Φ is a complex field doublet.

We write a self-coupling Lagrangian of Φ as the following:

$$\mathcal{L} = (D_\mu \Phi)^\dagger (D^\mu \Phi) - \mu^2 \Phi^\dagger \Phi - \lambda (\Phi^\dagger \Phi)^2. \tag{2.68}$$

We would like to obtain the vacuum expectation value (VEV) of the field $< \Phi > \equiv < 0|\Phi|0 >$. Notice that in the vacuum, the field should not have space structure otherwise it will have momentum, so $\partial_{\mathbf{x}} < \Psi >= 0$. Also the field should not be time dependent, so $\partial_t < \Psi >= 0$. We know a stable physical state should satisfy $\delta \int dt \mathcal{L}(\Phi) = 0$ and $\delta^2 \int dt \mathcal{L}(\Phi) > 0$, so by finding the minimum of $\mathcal{L}^{\text{VAC}}(< \Phi >) = -\mu^2 < \Phi^\dagger \Phi > -\lambda(< \Phi^\dagger \Phi >)^2$ we will be able to calculate the VEV. Clearly for the mass term, $\mu^2 > 0$, if we require $\lambda < 0$, then a global minimum can be achieved at $| < \Phi > | = (< \Phi^\dagger \Phi >)^{1/2} = \sqrt{-\mu^2/2\lambda} \equiv \nu/\sqrt{2}$. The vacuum state of Φ is degenerate. Assume the true vacuum state is:

$$\Phi_{\text{VAC}} = \begin{pmatrix} 0 \\ \frac{\nu}{\sqrt{2}} \end{pmatrix} \tag{2.69}$$

then the symmetry (degeneracy) of the vacuum state is broken. With this broken vacuum symmetry, the scalar field Φ, which couples to all the other elementary particles, will produce the necessary mass terms in the Lagrangian and preserve the gauge symmetry in our theory implicitly. This mechanism is called Spontaneous Symmetry Breaking (SSB).

The scalar field Φ can be expanded around Φ_{VAC}:

$$\Phi = \begin{pmatrix} f_1(x) + f_2(x) \\ f_3(x) \end{pmatrix} = e^{-i\mathbf{T}\cdot\zeta(x)} \begin{pmatrix} 0 \\ \frac{\nu}{\sqrt{2}} + h(x) \end{pmatrix} \tag{2.70}$$

where $f_i(x), (i = 1, 2)$ are complex fields (since Φ^+ is a charged boson), f_3 is a real field (Φ^0 is a neutral boson), $\zeta_i(x)$ are real fields determined by f_i, $\mathbf{T}_i$ are the $SU(2)$ group generators, and $h(x)$ is a real field[12], which is called the Standard Model Higgs boson, the particle we are trying to search in this dissertation. In the last equation we use the fact that the complex field Φ can be spanned by the $SU(2)$ transformation. If we choose a so called unitary $SU(2)$ gauge where $\Phi \to e^{i\mathbf{T}\cdot\zeta(x)}\Phi$, then Φ can be simplified as:

$$\Phi = \begin{pmatrix} 0 \\ \frac{\nu}{\sqrt{2}} + h(x) \end{pmatrix}. \tag{2.71}$$

Inserting Eq-2.71 into Eq-2.68 and expanding Φ, we can get mass terms for the W/Z bosons due to the VEV, and retain the massless photon field since the *explicit*

[12]It is also defined as $h(x)/\sqrt{2}$ in some literature, which leads to a artificial scale factor $\sqrt{2}$ to the field, thus the mass of the Higgs boson is scaled by $\sqrt{2}$, too.

$SU(2)$ gauge invariance is only in the $\Phi_{\rm VAC}$ direction (this is the so called Goldstone Theorem):

$$m_{\rm W} = \frac{g\nu}{2} \tag{2.72}$$

$$m_{\rm Z} = \frac{g\nu}{2\cos\theta_w} \tag{2.73}$$

$$m_{\rm H} = \mu \tag{2.74}$$

Clearly $m_{\rm Z}$ and $m_{\rm W}$ satisfy the relationship derived in Section 2.3.1.

In order for the Higgs boson to produce the lepton mass, we introduce the Yukawa coupling:

$$\mathcal{L}_{\rm Yukawa} = -f_\ell \bar{\phi_{\rm L}} \Psi \ell_{\rm R} + {\rm h.c.} \tag{2.75}$$

where $f_\ell (\ell = \{e, \mu, \tau\})$ are the lepton-Higgs coupling constants introduced in the Standard Model. Note that in the Standard Model the neutrinos are massless. By counting the weak isospin and the weak hypercharge, it is easy to see that under $SU(2)_{\rm L} \times U(1)_{\rm Y}$, with proper chosen transformations for the Higgs boson, the leptonic Yukawa coupling is gauge invariant. The lepton masses produced from these couplings are:

$$m_\ell = \frac{f_\ell \nu}{\sqrt{2}} \tag{2.76}$$

so the lepton mass is proportional to their coupling to the Higgs boson.

To produce the quark masses, the Yukawa coupling needs some manipulations[5]:

$$\mathcal{L}_{\rm Yukawa} = -f_{\mathcal{D}} \bar{\phi_{\rm L}} \Psi \mathcal{D}_{\rm R} - f_{\mathcal{U}} \bar{\phi_{\rm L}} \tilde{\Psi} \mathcal{U}_{\rm R} + {\rm h.c.} \tag{2.77}$$

where $\tilde{\Psi} = i\mathbf{T}^2 \Psi^\dagger$ has $Y^w = -1$, $f_{\mathcal{U}}, f_{\mathcal{D}}$ are the up and down type quark-Higgs boson coupling constants. Again, in each term, the sum of weak isospin and weak hypercharge are zero, respectively, so they are $SU(2)_{\rm L} \times U(1)_{\rm Y}$ invariant. The masses of quarks are:

$$m_{\mathcal{U}} = \frac{f_{\mathcal{U}} \nu}{\sqrt{2}} \tag{2.78}$$

$$m_{\mathcal{D}} = \frac{f_{\mathcal{D}} \nu}{\sqrt{2}} \tag{2.79}$$

The quark mixing can also be accounted for by the Yukawa coupling by adding more coupling terms in Eq-2.77.

From Eqs-2.72 and 2.73, we can determine $\nu = (\sqrt{2} G_F)^{-1/2} \approx 245$ GeV, but no experiment has been able to observe and measure the Higgs boson mass $m_{\rm H}$ (or equivalently the Higgs self-coupling constant λ) yet.

2.3.3 Higgs Boson Phenomenology

Higgs mass m_{H} is one of the undetermined parameters in the Standard Model (the others are the neutrino masses). Searching for the Higgs boson is now the biggest challenge of particle experiments. Although it has not been discovered yet, and its existence is only a hypothesis, there are various constraints on the range of the mass from the theory and experiments.

A Higgs boson is required not only for the SSB to generate the mass spectrum, but also for the unitary conditions at high energy in the $VV \to VV$ and $VV \to f\bar{f}$ scattering, where V stands for the vector gauge bosons and f stands for a fermion. Using these constraints the Higgs mass has a upper bound of $\sim$ 700 GeV. Much more stringent limits are derived when considering the running Higgs self-coupling constant λ as a function of the energy scale Λ as shown in Figure 2.2 (a). The quantum correction from the Higgs loop to the coupling constant is a function of the Higgs mass. Thus the upper limit on m_{H} is set by requiring $\lambda(\Lambda) < \infty$. The lower limit on m_{H} is set by requiring vacuum stability. If λ is too small, the quantum correction from the top quark loops can drive λ to a positive value, thus causing a zero VEV. The resulting m_{H} bounds are shown in Figure 2.2 (b).

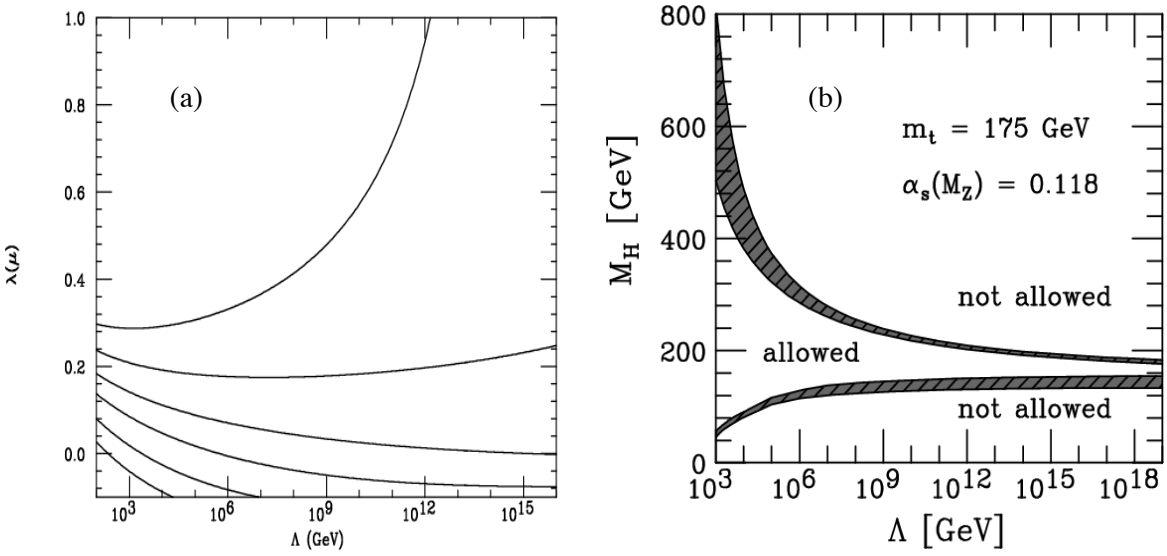

Figure 2.2: The limit on the m_{H} set by the running Higgs self-coupling constant: (a) the running coupling constant as a function of the energy scale[6]; (b) the upper and lower bound on the m_{H} as a function of the energy scale[7]. It is interesting to note that figure (b) does not rule out the possibility that the Standard Model is valid up to the Planck scale. If that were the case the Higgs mass would have to be between 130 GeV and 190 GeV.

Although the Higgs boson is not observed yet, its quantum correction effects on the heavy particles (namely top quark, W/Z bosons) are accessible in very precise EW experiments. For example, the W mass corrections depend logarithmically on the Higgs mass and quadratically on the top-quark mass. Constraints on $m_{\rm H}$ can be derived from precision measurements as shown in Figure 2.3. The current best constraint on the Higgs mass is $m_{\rm H} > 114.4$ GeV at 95% CL and < 199 GeV at 95% CL.[8]

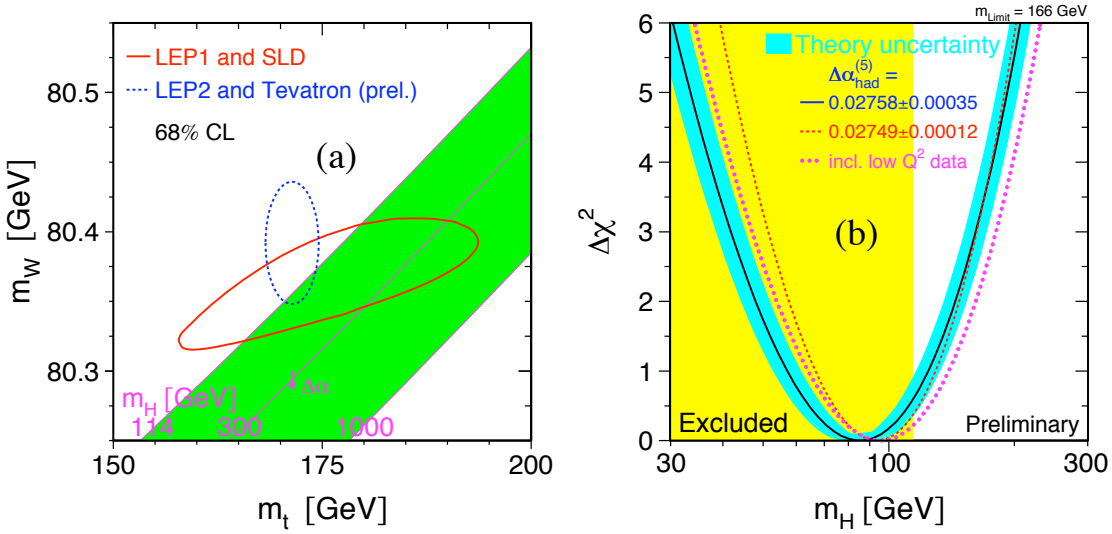

Figure 2.3: The limits on the $m_{\rm H}$ set by the precision EW measurements[9]: (a)Regions of allowed Higgs boson mass consistent with the measurements for the mass of the W boson and the top quark. The red solid circle shows the limit from the indirect measurements of LEP-I and SLD and the green dashed circle shows the direct measurements from proton-antiproton colliders and LEP-II experiments. In both cases the 68 % C.L. curves are plotted [6]; (b) Goodness of the electroweak precision data fit ($\Delta\chi^2 \equiv \chi^2 - \chi^2_{min}$) versus the mass of the Higgs boson m_H. The line shows the fit using all available data and the band shows the estimate of the theoretical uncertainty. The yellow vertical band covering the low mass regions shows the 95 % C.L. exclusion limit on the mass of the Higgs boson from direct searches at LEP.

The unitary conditions in the $VV \to VV$ and $VV \to f\bar{f}$ scattering require that the coupling constants of the Higgs boson (or whatever the new particle there should be) to the vector bosons and fermions are proportional to their masses. So the Higgs boson is dominantly produced by or in association with massive particles and prefers decays to the most massive particles kinematically allowed [10]. The main Standard Model Higgs production channel Feynman diagrams and their cross sections at the Tevatron Run II are shown in Figure 2.4 [11, 12]. Various Higgs decay channel widths

and their branching ratios (BR) are shown in Figure 2.5 [13].

Considering the background, the most promising channels are the WH and ZH associated Higgs production processes followed by Higgs decaying to $b\bar{b}$ (for $m_{\rm H} <\sim$ 140 GeV) or WW (for $m_{\rm H} >\sim$ 140 GeV). A general rule of thumb for experiments at hadron colliders to reduce the multiple jet background produced by pure strong interactions (QCD) is to include high energy leptons in the analyzed final states. As such, this dissertation describes the Higgs search in the following channel:

$$p\bar{p} \rightarrow Z + H \rightarrow \mu^+\mu^- + b\bar{b}. \tag{2.80}$$

where the Z decays to a pair of muons, and the H decays to two b flavor jets.

2.3.4 Challenges to the Standard Model

The gauge field theory of the Standard Model has been tested for decades and has been proven to be extremely successful. Now with the improved Tevatron luminosity and the approaching LHC era, we are almost sure to find the last missing piece of the theory—the Higgs boson, or rule out the Standard Model (and other models). Despite the glory of the Standard Model, it is well believed that it is not the complete or the final theory [14]. There are various extensions and modifications to the Standard Model hoping to achieve the grand unification (GUT, the unification of the strong interaction and gravity with the EW interaction). Even without such a big ambition as the GUT in mind, there are Standard Model criticisms that are based on sound but purely conceptual considerations. Among them, the most famous is the hierarchy problem which states that the large barren gap between the Higgs boson mass and the Plank scale is unnatural. Also the Standard Model does not provide a clear picture about how the vacuum condensate is produced. So there are theories in which the fermions and quarks can achieve masses without the Higgs bosons. Also there are models in which Higgs bosons are not fundamental particles but composed of other particles.

Attempts of applying the Standard Model to cosmology also raised some interesting questions that seem to be beyond the capability of the Standard Model. For example, the baryon and lepton genesis problem in which the Standard Model seems not to be able to provide enough CP violation. The Standard Model does not provide explanations for various neutrino problems, for example, the massive neutrino is not simply produced by the Yukawa coupling of the Standard Model Higgs boson since the RH neutrinos have no weak isospin or weak hypercharge, thus its coupling to the Higgs boson is not allowed (at least in a simple way as the other leptons) since the Higgs boson has weak hypercharge of one. This leads to the search for the sterile neutrino and Marjorana neutrino which are not Standard Model neutrinos but which are good candidates for dark matter. Also the observed neutrino mixing and

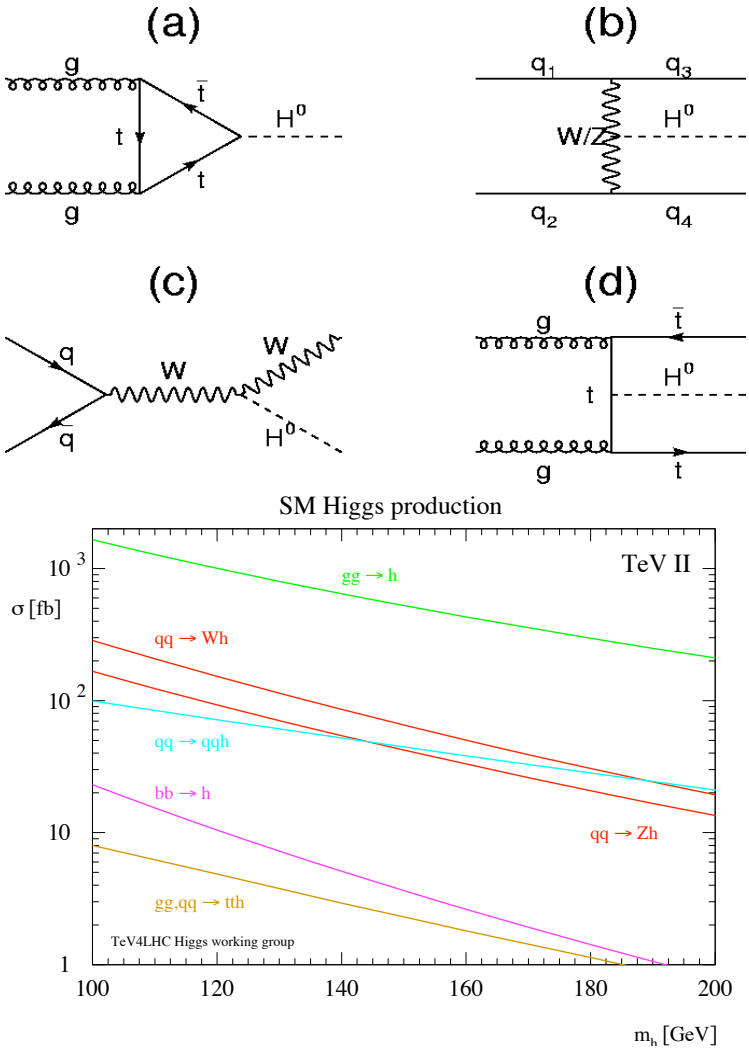

Figure 2.4: Various Standard Model Higgs boson production channel's Feynman diagrams and their cross sections at the Tevatron. The most probable channel is the gluon fusion process followed by the associated production with W and Z bosons and quark pair. The gluon fusion process and the qqh processes are experimentally uniteresting due to the large background from the QCD multi-jet process (9 orders of magnitude larger w/o the detector effects). Thus the most promising processes are the WH and ZH processes.

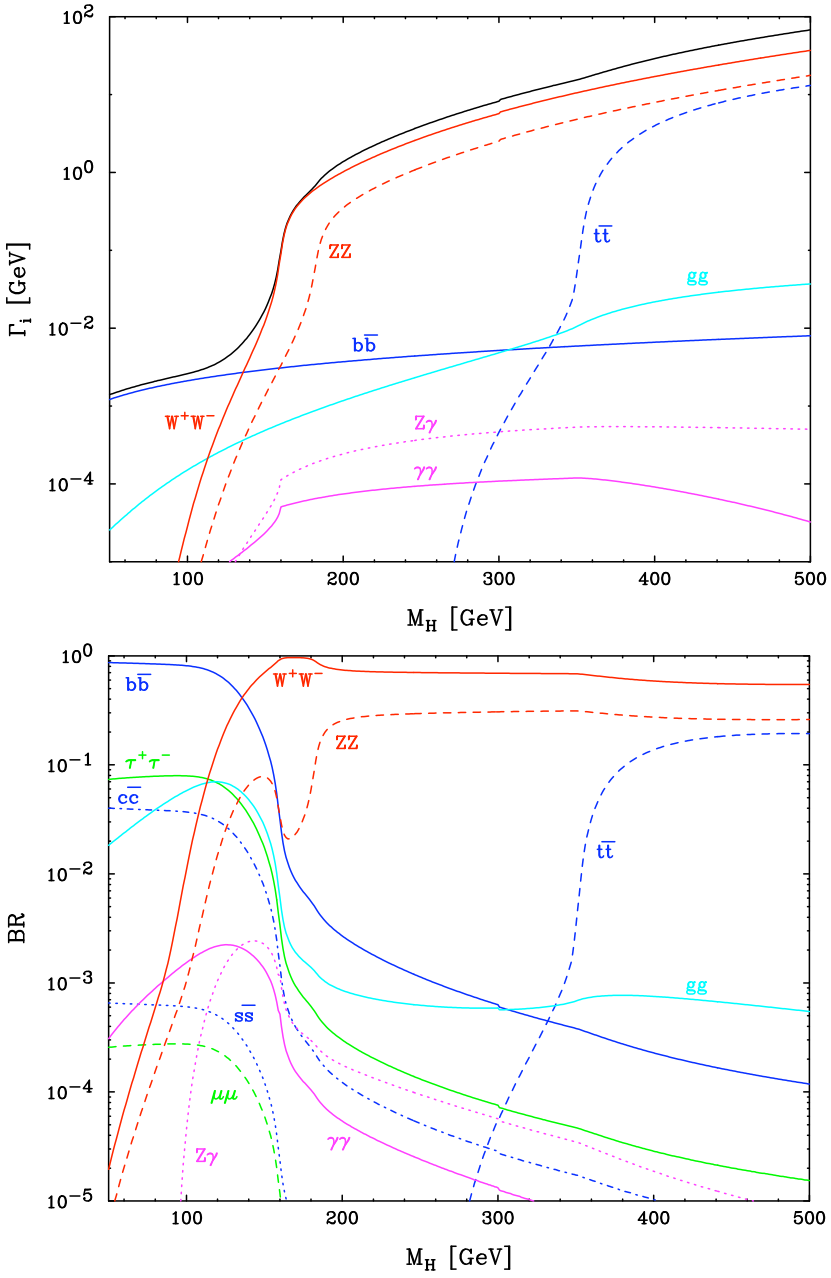

Figure 2.5: Various Standard Model Higgs boson decay modes' decay widths and their branching ratios as functions of Higgs mass [13].

oscillation is not explained in the Standard Model. Perhaps the most direct threat to the Standard Model is that the VEV in the Standard Model is many orders of magnitude larger than that expected from the cosmological constant of the general relativity [15].

From our own construction of the field theory and the origin of the gauge symmetry, we can see immediately a few questions about the Standard Model Higgs boson:

- **Unnatural Interaction Properties.** According to gauge theory, all the interactions (at least for the three stronger interactions) are naturally needed due to the requirement of the gauge invariance of the free particle Hamiltonian H_0. Yet, the introduction of the Higgs boson actually violates this natural rule. On the one hand, Higgs boson is not a gauge boson, so it is not a force mediator, yet it must interact with all the other particles, just like a companion to all kinds of the gauge bosons, in order to produce the mass term. This puts it in a rather suspicious and awkward position. On the other hand, the coupling constants of the Higgs boson to the other particles are not the same as the strong or electroweak coupling constants, so effectively the Higgs boson invokes 13 more *new* kinds of interactions (including the Higgs self-coupling constant) besides the strong, weak and EM interactions! This is a steep price to pay to generate the mass term in the Standard Model.

- **Abnormal Gauge Symmetry Properties.** From the way we introduced the gauge symmetry, we can see that different particles (with respect to the symmetry group, and the particle family) should be able to undergo gauge symmetry transformations independently, *eg.* the $SU(2)_{\rm L}$ doublets $(u,d)^T_{\rm L}$, $(t,b)^T_{\rm L}$ and $(\nu_e,e)^T_{\rm L}$ should be able to transform independently, and this independence is very agreeable to our physics intuitions. Yet the Higgs boson bluntly breaks this independence, as we can see from the Yukawa terms. It shackles all the LH particles together under the same $SU(2)_{\rm L}$ symmetry transformation, which is very surprising, if not at all unnatural. Also, although a boson, it strangely behaves like a fermion under $SU(2)_{\rm L}\times U(1)_{\rm Y}$, which also sounds not very appealing.

- **Trivial Charged Field.** The structure of the Φ field is rather strange. It is a doublet of a charged field Φ^+ and a neutral field Φ^0, and in the Standard Model the neutral field–Higgs boson–is its own anti-particle. So by expanding the two fields with the creation and annihilation operators, Φ should be written in the following form:

$$\Phi = \begin{pmatrix} a(\mathbf{p},\mathbf{s}) + b^\dagger(\mathbf{p},\mathbf{s}) \\ c(\mathbf{p},\mathbf{s}) + c^\dagger(\mathbf{p},\mathbf{s}) \end{pmatrix} \tag{2.81}$$

where $a \neq b$ are the annihilation operators of the particle and anti-particle of the charged field Φ^+, c is the annihilation operator of the Φ^0. It is natural to require the Φ^0 field to be its own anti-particle, otherwise there would not be a clear separation between particle and anti-particles. Clearly, only by requiring $\Phi^+ \equiv 0$ can the Φ^0 preserve this property under the $SU(2)_{\rm L}$ transformation. The choice of the unitary gauge seems to hide this problem, but at the cost of the $SU(2)_{\rm L}$ gauge freedom of all the LH fermions and the EW gauge bosons, this means the $SU(2)_{\rm L}$ gauge symmetry is totally lost. In another word, the necessity of introducing a field that is trivial is not a natural thing in the theory. The workaround to this problem is to require the $\Phi^0 \neq (\Phi^0)^\dagger$, but the complication is that we now have two Higgs boson with exactly the same set quantum numbers yet they are each other's anti-particles, which implies a hidden symmetry and quantum number.

So despite its success and beauty, the Standard Model of the quantum gauge field theory has a lot of unsolved problems. Indeed, it is just one of the many methods to describe the relativistic quantum particle system. Another example is the string theory. Instead of using the 4-D fields, it switches to higher dimension strings to describe the particles. In my own opinion, field theory is far from fully understood. The three problems of the Higgs boson discussed above indicates that the Standard Model Higgs boson is in many way acting like a graviton if the gravity can be described by the gauge field theory at all. In fact, the gravity experiments have only been performed in the scale of $\sim 10^{12}$ fm, while the collider has tested the Standard Model down to $\sim 10^{-3}$ fm. If gravity became abnormally as strong as the weak interaction, then the graviton may well replace the Higgs boson. After all the mass is more directly related to the gravity than to the singularities of the quantum field propagators that are produced by the mass terms in the Lagrangian. And it is very probable that quantum gravity requires super-symmetry, and those super-symmetry particles may well be in the reach of the energy scale of the current and next generation of the collider physics.

To summary, the Higgs boson, be it real or not, is the starting point to a exciting new physics. So searching for the Higgs boson and the possible new physics is a crucial goal of the modern particle physics.

2.4 Collider Experiment Analyses

2.4.1 Decay Rate and Cross Section

Particle searches are essentially counting experiments in which the interesting event signals are selected, analyzed, and counted. What a theory can provide is the probability of the quantum state transition. In order to relate the event counting and

the probability so that the theory can be tested by experiments, the decay rate and the cross section are introduced.

Consider a quantum particle system enclosed in a box with volume V. The system is supposed to exist only during time period $-T/2 \sim T/2$. The 3-momentum phase space integral element is now

$$dN = \frac{V}{(2\pi)^3} d\beta \tag{2.82}$$

where dN is the number is possible quantum state in momentum interval $d\beta$ (including the 3-momentum, spin, *etc.*). The momentum space δ functions is now:

$$\begin{aligned} \delta^3(\mathbf{p}' - \mathbf{p}) &= \frac{1}{(2\pi)^3} \int_V d^3\mathbf{x} e^{i(\mathbf{p}'-\mathbf{p})\cdot\mathbf{x}} = \frac{V}{(2\pi)^3} \delta_{\mathbf{p}',\mathbf{p}} \\ \delta(E_\alpha - E_\beta) &= \frac{1}{2\pi} \int_{-T/2}^{T/2} dt e^{i(E_\alpha - E_\beta)t} = \frac{T}{2\pi} \delta_{E_\alpha, E_\beta} \end{aligned} \tag{2.83}$$

where $\delta_{\mathbf{p}',\mathbf{p}}$ is the Kronecker delta. Consequently, the norm of the state vector Ψ_α in Eqs-2.35 and 2.36 is also changed:

$$\Psi_\alpha^{\text{Box}} = \left[\frac{(2\pi)^3}{V}\right]^{N_\alpha/2} \Psi_\alpha \tag{2.84}$$

where N_α is the number of particle in the state α, Ψ_α^{Box} is the state vector in the box, and it satisfies the normal condition $(\Psi_\alpha^{\text{Box}}, \Psi_\beta^{\text{Box}}) = \delta_{\alpha,\beta}$. The transition probability amplitude in Eq-2.20 is also changed according to this new norm:

$$S_{\beta,\alpha}^{\text{Box}} = \left[\frac{(2\pi)^3}{V}\right]^{(N_\alpha+N_\beta)/2} S_{\beta,\alpha} \tag{2.85}$$

$S_{\beta,\alpha}$ can be shown to contain a 4-momentum conservation δ function, so it is usually written as:

$$S_{\beta,\alpha} = \delta(\alpha - \beta) - 2i\pi\delta^3(\mathbf{p}_\alpha - \mathbf{p}_\beta)\delta(E_\alpha - E_\beta) M_{\beta,\alpha} \tag{2.86}$$

where $M_{\beta,\alpha}$ is called the matrix element, thus the differential transition probability (in the box) is:

$$\begin{aligned} dP(\alpha \to \beta) &= |S_{\beta,\alpha}^{\text{Box}}|^2 (dN)^\beta \\ &= \left[\frac{(2\pi)^3}{V}\right]^{N_\alpha} |S_{\beta,\alpha}|^2 d\beta \\ &= (2\pi)^2 \left[\frac{(2\pi)^3}{V}\right]^{N_\alpha - 1} \left(\frac{T}{2\pi}\right) |M_{\beta,\alpha}|^2 \delta^4(p_\alpha - p_\beta) d\beta \end{aligned} \tag{2.87}$$

In the last equation we used $(\delta^4(p_\alpha - p_\beta))^2 = (\delta^4(p_\alpha - p_\beta))(\delta^4(0))$ and $\delta^4(0) = V \cdot T/(2\pi)^4$ due to Eq-2.83, also we assumed $\alpha \neq \beta$.

We can define the differential transition rate as:

$$d\Gamma(\alpha \to \beta) = \frac{dP(\alpha \to \beta)}{T} = (2\pi)^{3N_\alpha - 2} V^{1-N_\alpha} |M_{\beta,\alpha}|^2 \delta^4(p_\alpha - p_\beta) d\beta \tag{2.88}$$

When the initial state contains only one particle, *eg.* $N_\alpha = 1$, Eq-2.88 is reduced to the decay rate of the particle. For an unstable particle, different decay channels have different Γ_i, the ratio Γ_i/Γ is called the branching ratio (BR). The sum $\Gamma = \sum_i \Gamma_i$ equals to the width of the resonant peak of the invariant mass distribution for the final state of the unstable particle, so it is also called the decay width (Γ has dimension 1 as mass in the natural unit.). $\Gamma = \tau^{-1}$ where τ is the life time of the unstable particle.[13]

When the initial state contains two particles, like in the $p\bar{p}$ collisions of the Tevatron or the e^+e^- collisions of the LEP, Eq-2.88 has an extra factor V^{-1}. We can define a flux Φ_α of the initial state and a differential cross section $d\sigma$ [14] as:

$$d\sigma \equiv d\Gamma(\alpha \to \beta)/\Phi_\alpha = (2\pi)^4 u_\alpha^{-1} |M_{\beta,\alpha}|^2 \delta^4(p_\beta - p_\alpha) d\beta \tag{2.89}$$

$$\Phi_\alpha \equiv u_\alpha / V \tag{2.90}$$

where the u_α is defined as:

$$u_\alpha \equiv \sqrt{(p_1 p_2)^2 - m_1^2 m_2^2}/E_1 E_2 \tag{2.91}$$

In the inertial frame where one of the particles is at rest, u_α is just the speed of the other particle, thus Φ_α is called the flux. The meaning of σ is the transition rate per unit incident flux per target particle, and the usual unit of σ is picobarn (pb), or 10^{-12} barn. 1 barn = 10^{-28} m^{-2}. For collider experiments, given the cross section σ of a process, the event rate of the process can be derived:

$$\frac{dN}{dt} = \sigma \mathcal{L} \tag{2.92}$$

where the flux of the colliding beams $\mathcal{L}$ is called the instantaneous luminosity. The definition of $\mathcal{L}$ is [20]:

$$\mathcal{L} = f \frac{N_a N_b}{4\pi \sigma_x \sigma_y} \tag{2.93}$$

where f is the bunch revolution frequency, N's are the number of particles in the

[13] Notice $|M_{\beta,\alpha}|^2 \prod_\alpha E_i \prod_\beta$ is a Lorentz scalar, so the decay width Γ is not Lorentz invariant. This makes sense since the life-time τ is not Lorentz invariant.

[14] With the same argument for the decay rate, it can be seen the cross section is Lorentz invariant.

colliding bunches, and $\sigma_{x/y}$'s are the characteristic transverse beam profile.

2.4.2 The Parton Model and Factorization Theory

The experiments performed at Tevatron involve collisions of protons and anti-protons at high energy. Because the perturbation method breaks down for the strong interaction that binds the quark and gluons together into a hadron, we can not use the states of free quark and gluon to describe a bound state of a hadron. Fortunately, due to the special feature of the asymptotic freedom of the strong interaction, the problem can be solved.

From deep inelastic scattering (DIS) experiments, we know that the proton (anti-proton) consists of nearly free constituents (called the partons) when probed with high energy (above a few GeV). This important result implies that the non-perturbative aspect of the strong interactions that are responsible for the color confinement are relatively "slow", compared to the hard scattering processes. Thus the hard inelastic collisions at the hadron collider can be separated into three phases, as shown in Figure 2.6. Within the time scale when the high energy hard scattering processes occurs, the initial state partons and the final state products can be deemed as free, thus our perturbation method can be used to calculate the transition matrix element for this short time scale process. For the time period before the hard process, the parton distribution functions (PDF) are used to describe the partons. The PDF's are measured from DIS experiments (at HERA as well as the Tevatron). For the time period after the hard process, the final state quarks and gluons are evolved through a fragmentation (gluon emission and gluon splitting) and hadronization (quark and gluon binding) processes, hadronic jets are formed around them. Since the evolution of the final state partons involves mostly low momentum transfer process (soft or collinear gluon emissions, *etc.*), a jet is basically a collection of nearly collinear hadrons [16]. There are several techniques, for example resummation [17], to calculate the evolution process. It is also widely calculated using Monte Carlo simulations.

The intuitive picture described above can be proved by the factorization theorem. [18]. Using the PDFs, the cross section of the hadron collider processes can be expressed as:

$$\sigma(Q^2) = \sum_{i,j} \int dx_i dx_j \hat{\sigma_{i,j}}(x_i p_A, x_j p_B, \mu_R, \mu_F, \alpha_s(\mu_R)) f_i^A(x_i, \mu_F) f_i^B(x_j, \mu_F) \qquad (2.94)$$

where the sum runs over all the possible partons, f_i is the parton distribution, x_i is the portion of the hadron momentum carried by the parton, $\hat{\sigma}$ is the hard scattering cross section (hadronization may included), and Q^2 is the typical momentum transfer of the process. There are two energy scales introduced, μ_R the renormalization energy scale, and μ_F the factorization scale. A common practice is the set them equal

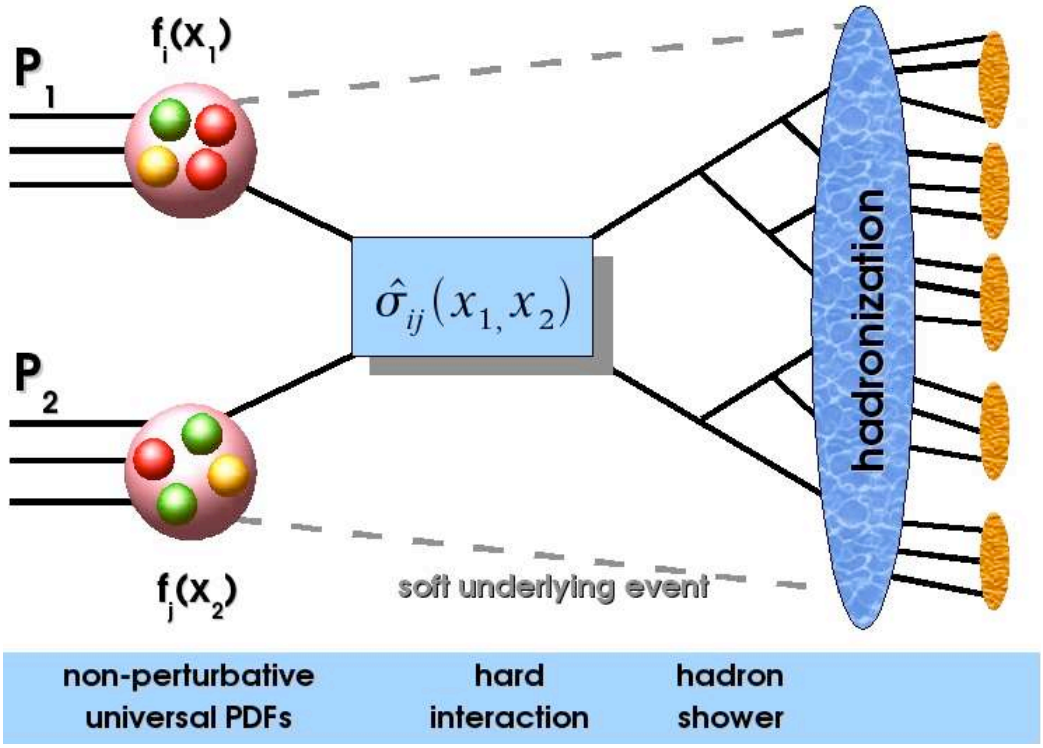

Figure 2.6: The three phases of a hard $p\bar{p}$ inelastic collision. $f_{1,2}(x)$ are the PDF of the two interacting partons, $\sigma_{i,j}$ is the hard scattering matrix element. For hard scattering processes, the final products usually have very large transverse momentum ($>$ a few GeV) due to the large momentum transfer Q^2. The soft underlying event is due to the remnant of the proton and anti-proton that do not participate in the hard scattering. They can also be generated from the multiple parton interactions between the beam and the hard scattering product. The underlying events usually have very small transverse momentum, and are nearly collinear with the incident beams.

$\mu_R = \mu_F = |Q^2|$. Typical parton distribution functions for different partons in a proton is shown in Figure 2.7.

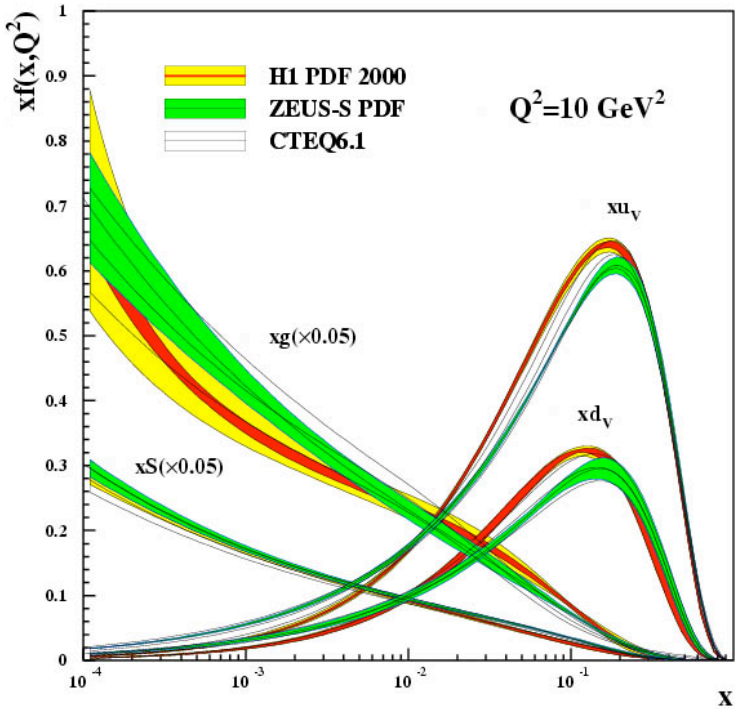

Figure 2.7: Typical parton distribution functions $xf(x, Q^2)$ for partons of a proton. u_v, d_v, g, s stands for the valence up and down quarks, sea gluon and sea strange quark, respectively. PDFs $f(x, Q^2)$ are usually shown in the form of $x^n f(x, Q^2)$ since typical cross section calculations involve such kind of momenta terms [19].

2.4.3 ZH Signal and Backgrounds

In this analysis, the Higgs boson will be searched for in the process of Eq-2.80. The leading order (LO) contribution is shown in Figure 2.8. The signal is characterized by two muons and two b quarks.

There are many other processes that can have the similar final state. The biggest background is QCD heavy flavor jet production where two heavy quarks (b or c, collectively denoted as Q) decay to light quarks and produce two muons. The LO and tree-level next-to-LO (NLO) Feynman diagrams are shown in Figure 2.9, and the cross sections as a function of $b-$jet E_{T} is shown in Figure 2.10. Since the muons from the $b-$quark decays are mostly close to the jet while the muons from Z are not correlated to any jets, with proper requirements on the muon-jet separation, the QCD multi-jet background can be greatly reduced.

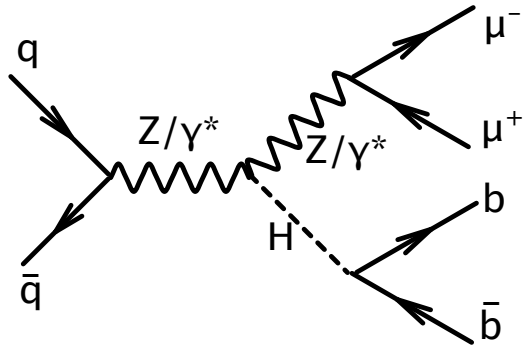

Figure 2.8: The LO Feynman diagrams of the $ZH \to \mu\mu b\bar{b}$ signal.

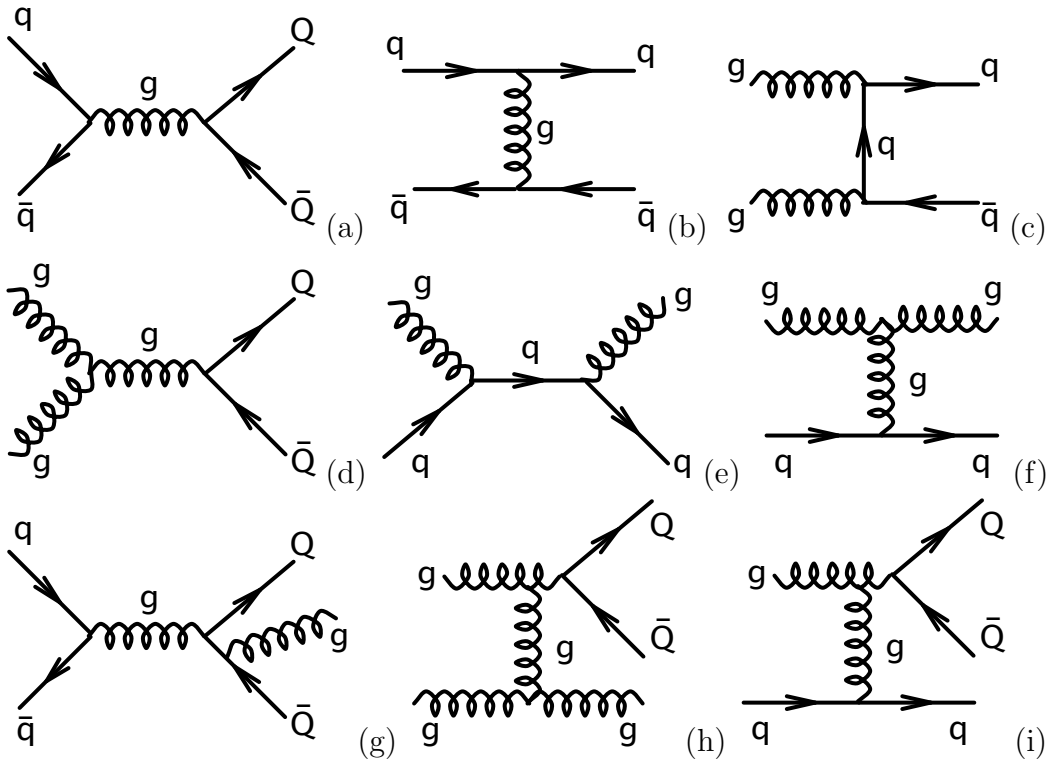

Figure 2.9: The LO and the tree level NLO representative Feynman diagrams of the b quark production in the QCD multi-jet events. (a, b) $q\bar{q}$ LO contributions; (c, d) gg LO contributions; (e, f) gq LO contributions, notice that LO gq has no contribution if requiring two muons in the final state; (g) $q\bar{q}$ NLO contribution; (h) gg NLO contribution; (i) gq NLO contribution.

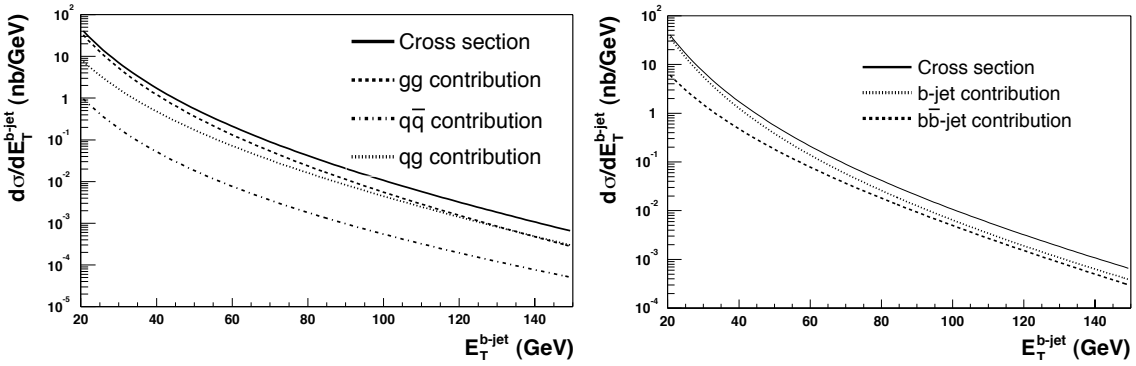

Figure 2.10: Theoretical b jet production cross sections as a function of $b-$jet E_{T} in QCD multi-jet events. $b-$jet $|\eta| < 0.6$, jet cone size (see Section 5.3) $\Delta R = 0.5$. In the case of two partons within a cone of radius 0.5, they are merged into a single jet with four-momentum equal to the sum of the two partons four-momenta. The PDF used is CTEQ6M. [21]

The other background includes $Z+2q$ production which is basically QCD multiple jet production with a Z boson radiating from a initial/final/intermediate quark in Figure 2.9. Now the quarks in Figure 2.9 can be either heavy quarks or any light flavor quarks and gluons (collectively denoted as j) since the light flavor jets may fake b-jets due to the mis-identification. The results of various $Z + nq$ cross sections are listed in Table 2.4.

Combining the cross sections in Table 2.4, we can estimate the contributions of various $Z + nq$ processes to the final state of Z boson plus zero, single and double b-tagged jets (2 jets are required to present in the final state). The results are listed in Table 2.5. From the estimation we can see $Z + bc$ can be ignored, the contribution of $Z + jc$ and $Z + jb$ are small compared to $Z + 2j$ but are comparable to $Z + bb$ and $Z + cc$ in the zero and single b-tagged events (see Section 7.2). In the double b-tagged events, their contributions are even more important and comparable to $Z + 2j$ and $Z + 2c$. Since no Zjb or Zjc Monte Carlo samples are available, correction factors on the number of Zjj events are used to account for these mixed-flavor-jet events:

$$0 \text{ b-tag} : m_0 = \frac{137 + 3.22 + 2.19}{137} = 1.04 \tag{2.95}$$

$$1 \text{ b-tag} : m_1 = \frac{10.7 + 0.75 + 1.77}{10.7} = 1.24 \tag{2.96}$$

$$2 \text{ b-tag} : m_2 = \frac{0.22 + 0.03 + 0.07}{0.22} = 1.45 \tag{2.97}$$

Besides the $Z + 2q$ events, there are also di-boson production ZZ, WZ and WW events and top-pair production events as shown in 2.11. These events are important

	ZQ	$Z(Q\bar{Q})$	ZQj	ZQQ	ZQ inclusive
$gb \to Zb$	10.4	0.169	2.19	0.631	13.4
$q\bar{q} \to Zb\bar{b}$	3.32	1.92	—	1.59	6.83
$gc \to Zc$	16.5	0.130	3.22	0.49	20.3
$q\bar{q} \to Zc\bar{c}$	5.66	6.45	—	1.70	13.8
	Zj		Zjj		Zj inclusive
$q\bar{q} \to Zg$ and $gq \to Zq$	870		137		1010

Table 2.4: NLO cross section theoretical results for Z production in association with heavy flavor jets at the Tevatron. The unit is pb. The jets are required to have $p_{\rm T}>$ 15 GeV and $|\eta| < 2$, jet cone of $\Delta R = 0.7$ is used. In the case of two partons within a cone of radius 0.7, they are merged into a single jet with four-momentum equal to the sum of the two partons four-momenta. The kinematic requirements are applied after any merging is performed. ZQ refers to the final state of exactly one heavy quark; $Z(Q\bar{Q})$ refers to exactly one jet, which contains a merged heavy quark pair; ZQj refers to exactly two jets, one of which contains a heavy quark; $ZQ\bar{Q}$ refers to the final state of two jets, both of which contains a heavy quark. [22, 23]

# b-tagged jet	Zjj	Zjc	Zjb	Zcc	Zbb	Zcb
0	137	3.22	2.19	2.19	2.22	0.08
1+	10.7	0.75	1.77	0.8	2.13	0.06
2+	0.22	0.03	0.07	0.09	1.02	0.01

Table 2.5: Estimated cross sections of the $Z + nq$ contribution in the Z+2 jets events with 0,1,2 b-tagged jets. The unit is pb. In this table it is assumed that the $b-$jet tag efficiency is 80%, the $c-$jet mis-tag rate is 20%, the light flavor jet mis-tag rate is 4%. The Zcb cross section is estimated by $\sigma(Zjc)\frac{\sigma(Zcc)}{\sigma(Zjj)} + \sigma(Zjb)\frac{\sigma(Zbb)}{\sigma(Zjj)}$.

in the double b-tagged events.

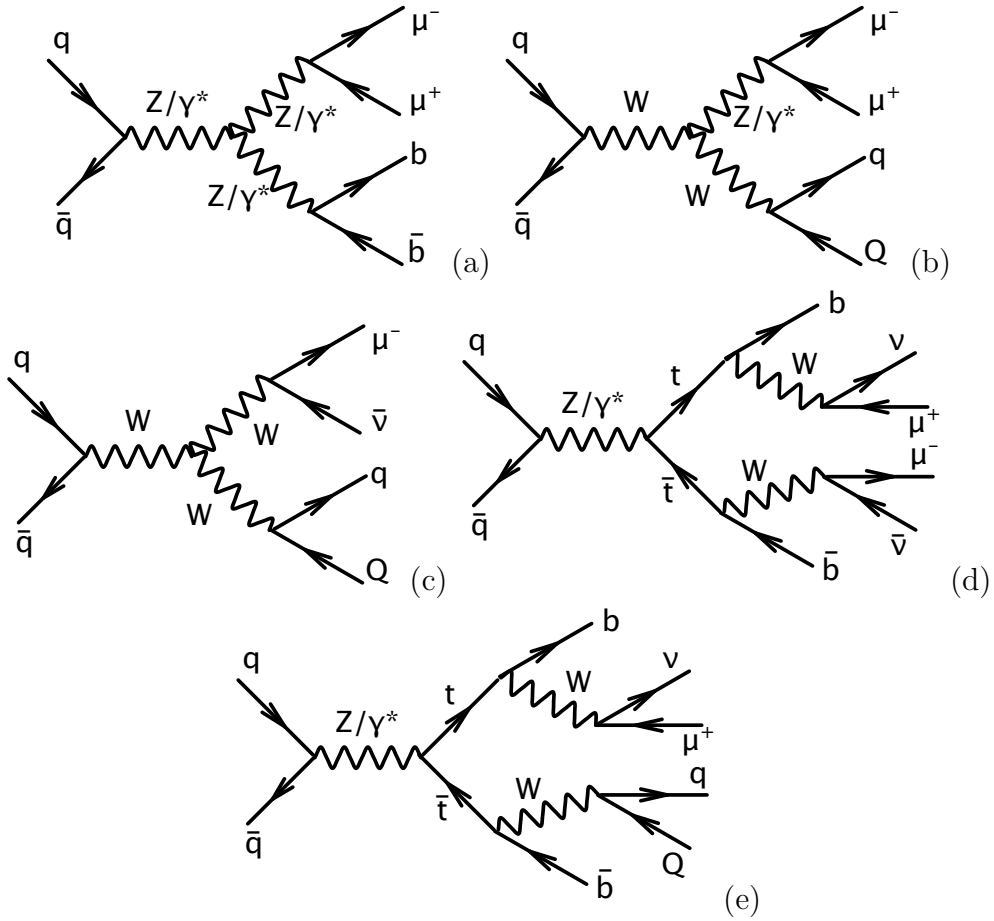

Figure 2.11: (a, b, c) Di-boson production; (d, e) top pair production, single leptonic and di-leptonic decay modes. WZ events can fake the signal by Z decays to two muons and W decays into jets, WW events can also have additional muon from a jet. As shown in Section 8.8, the WZ/WW contributions to the final Higgs signals is negligible. WW production can also fake the signal by a leptonically decaying W mimicking a Z, but the contribution is even smaller than the WZ so it is omitted.

Chapter 3

Particle Accelerator and Detector

There are essentially two ways of doing particle physics experiments: (1) using naturally occurring sources such as cosmic rays and (2) particle accelerators. Historically the observation of cosmic rays and natural radioactivities led to the discoveries of many particles. Nowadays cosmic rays are still very useful for probing new particles and new physics [24] since they can be produced by extremely energetic astrophysical processes that are far beyond the capability of current particle accelerator technology. Yet when one wants to get more control of the experiment, especially when searching for new particles in a given energy range, particle accelerators are widely used. Indeed most of the known particles were found using accelerators.

There are over 100 particle accelerators around the world [25]. They can be divided into two main categories: linear and circular. Both kinds of accelerators use radio frequency (RF) EM fields to accelerate charged particles, such as electrons or protons. The next generation accelerators (including the LHC at CERN and the proposed ILC) also use RF EM fields. Their much larger size provides much higher energy.

Generally speaking higher particle energy is desirable because it provides finer resolution of particle substructure, and more importantly it allows new particles (likely to be close to or beyond the current upper limit of particle masses, ~ 200 GeV) to be produced. There is a technological limit on the RF EM driving fields of ~ 0.1 GeV/m. Beyond this limit RF fields will be unstable. In order to achieve higher energy, a new technology called plasma wakefield acceleration is under study, and hopefully it will be able to deliver over 100 GeV/m acceleration [26].

The experiments using accelerators can be classified into two types: fixed target and collider. Recent experiments favor particle colliders because they are more efficient in transferring the kinetic energy of particles into collision energy. For a general discussion of particle accelerators and experiments refer to [27, 28].

Currently the largest and most energetic particle accelerator is the Tevatron of Fermi National Accelerator Laboratory (FNAL, Fermilab). The experiment described

in this dissertation was performed at the Tevatron using the DØ detector system. In this chapter we will first briefly discuss the particle acceleration process at Fermilab, and then describe the the DØ detector system. For a detailed description of the Tevatron and DØ detector the reader should refer to [29, 30].

3.1 The Tevatron

The Tevatron is a synchrotron accelerator. A synchrotron adjusts both the magnetic field and the frequency of the RF driving field so that the particle can be accelerated in a fixed radius circle (the storage ring). To reduce the synchrotron radiation as well as to simplify the construction, the Tevatron accelerates protons p and anti-protons $\bar{p}$ at the same time. $p\bar{p}$ are accelerated to the center of mass energy $\sqrt{s} = 1.96$ TeV and collide at B0 and D0 position of the ring, as shown in Fig.-3.1.

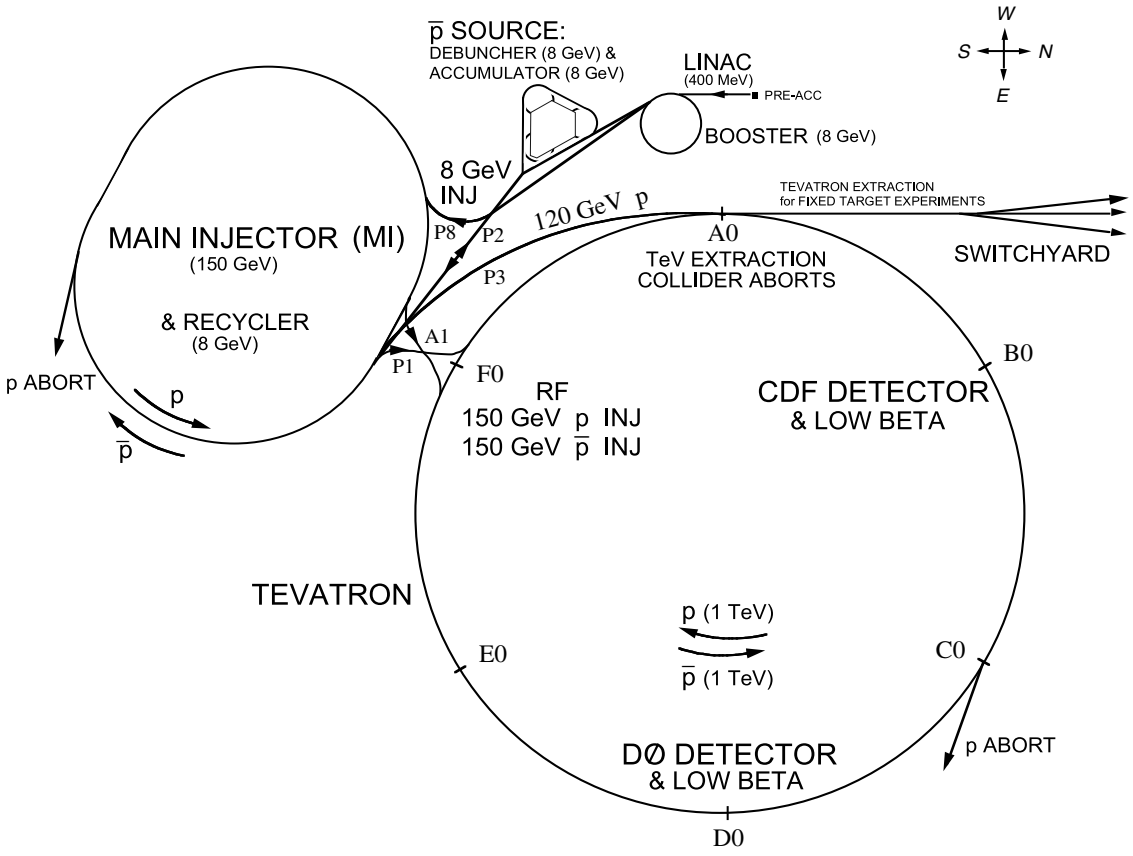

Figure 3.1: A scheme of the Tevatron and the assisting accelerators [31].

The Tevatron is only the finale of a series of six stages which produce the p and

$\bar{p}$ and accelerate them to 0.98 TeV [32]:

1. **Pre-accelerator.** At this very first stage hydrogen gas enters a magnetron surface-plasma source. The produced H^- ions are accelerated by a commercial Cockcroft-Walton accelerator to 750 keV. These ions pass through a RF cavity with a single gap to produce H^- bunches. The bunches then enter the next stage.

2. **Linac.** This is a 500 foot long linear accelerator which accelerates bunches of H^- ions to 400 MeV.

3. **Booster.** This is a synchrotron with a storage ring of 151 m diameter. Before H^- ions from the linac enter the booster, they pass through a thin carbon foil which strips the electrons off, leaving bunches of protons. The bunches initially travel in the booster without acceleration until about 5×10^{12} protons have been collected. This take six revolutions (84 bunches). The linac then stops feeding the booster to let it boost the proton bunches to 8 GeV.

4. **Main Injector.** The 8 GeV proton bunches are transferred to this bigger synchrotron (1 km in diameter) and accelerated to 150 GeV. The main injector also delivers 120 GeV protons to the anti-proton source.

5. **Debuncher and Accumulator.** This is where anti-protons $\bar{p}$ are produced. Inside this source one bunch of the 120 GeV protons hits a nickel target every 1.47 seconds to produce $\bar{p}$ (among many other secondary particles). The $\bar{p}$ production rate at the target is about 1.5×10^{-5} per proton. A lithium lens of 740 Tesla/m focuses the negative secondary particles and a pulsed dipole bending magnet steers the $\bar{p}$ into the debuncher and accumulator. Since the $\bar{p}$'s are produced with random momenta in all directions, the debuncher uses a process known as stochastic cooling to reduce the wide spread in momentum and space spectrum before a sufficient number of $\bar{p}$'s (a stack) in the form of bunches are stored and accelerated to 8 GeV in the accumulator. Then the $\bar{p}$ bunches are sent back to the main injector to be accelerated to 150 GeV together with protons.

6. **Tevatron.** The p and $\bar{p}$ bunches are accelerated at the same time to 980 GeV in the vacuum storage ring which is 1 km in diameter. In the storage ring there are 1113 RF buckets with a frequency of 53.1 MHz and nearly 1000 superconducing magnets which provide a magnetic field of 4.2 Tesla at a temperature of 4.6 K. The p and $\bar{p}$ beams are squeezed into a small transverse area of about 5×10^{-5} cm^2 by two low β magnets at the colliding points B0 and D0. The beam spot is steered close to the geometrical center of the detectors at the two colliding points (designed to be about 50 μm, but in actual operations the beam spot

position is about 1 mm away from the center at DØ). Besides the colliding mode, the Tevatron can also run fixed target experiments. In this mode, no $\bar{p}$ is needed. Protons are accelerated to 980 GeV and extracted down to the fixed target beam line for meson and neutrino related experiments.

Some of the Tevatron operating parameters are listed in Table 3.1. The beam structure of the Tevatron is shown in Figure 3.2. The basic time unit of Tevatron is marked by ticks. The time interval between two ticks lasts 132 ns. During each tick interval the $p\bar{p}$ bunches are accelerated by 7 RF buckets (two buckets are separated by 21 ns/1113 = 18.8 ns). A full revolution contains 159 tick intervals. The full ring of beam in Run II has 36 bunches which are grouped into three super bunches. Within a super bunch the spacing between adjacent bunches is 3 tick intervals (396 ns, or about 120 m). The spacing between super bunches is 20 tick intervals. This spacing is required for the Tevatron beam abort system, and it is also essential for the experimental data acquisition system to issue internal resets to execute read out reset procedures.

Parameters	Run I	Run II.a	Run II.b
Energy $p, \bar{p}$	900	980	980
Proton Bunch	6	36	36
Anti-proton Bunch	6	36	36
Proton/Bunch	2.3×10^{11}	2.7×10^{11}	2.7×10^{11}
Anti-proton/Bunch	5.5×10^{10}	3.0×10^{10}	7×10^{10}
Bunch Spacing (ns)	3500	396	396
Peak Inst. Luminosity. ($\mathrm{cm^2 s^{-1}}$)	0.16×10^{32}	0.86×10^{32}	3×10^{32}
Inte. Luminosity ($\mathrm{pb^{-1}}$/week)	3.2	17.3	60
Interactions per Crossing	2.5	2.3	4.8

Table 3.1: The Tevatron operating parameters for Run I, Run IIa and Run IIb [33].

Useing Eq.2.93, the instantaneous luminosity of the Tevatron colliding beams can be written as [34]:

$$\mathcal{L} = \frac{N_p N_{\bar{p}} n_B f}{2\pi(\sigma_p^2 + \sigma_{\bar{p}}^2)} F(\sigma_l/\beta^*) \tag{3.1}$$

where n_B is the number of bunches (36 in Run II) in one revolution, f is the bunch revolution frequency(47.7 kHz), N's are the bunch intensities, and $\sigma_p(\sigma_{\bar{p}})$ is the RMS transverse size of the proton (anti-proton) beam at the colliding point, and F is a form factor that depends on the ratio of the bunch length σ_l and the β function β^*. The $\mathcal{L}$ defined in this equation is the Tevatron operating luminosity.

The duration in which proton and anti-proton beams circulate in the Tevatron is called a store. Stores last from several hours to a couple of days. The instantaneous

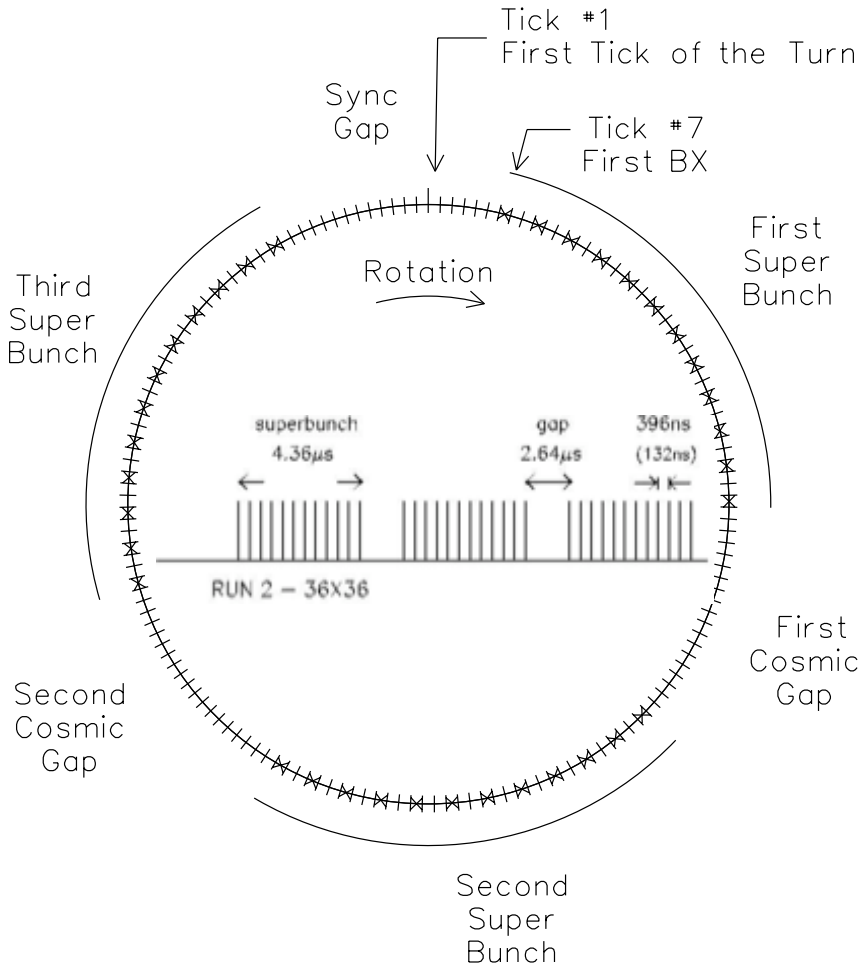

Figure 3.2: The bunch structure of the Tevatron in Run II. The bunch length of $p\bar{p}$ is about 2 ns so it can be ignored here.

luminosity is highest at the beginning of a store and decreases as anti-protons are lost to collisions and beam instabilities.

3.2 Particle Material Interactions

The only directly detectable particles resulting from a $p\bar{p}$ collision are those which can travel as asymptotically free particles a macro-scale distance (ranging from 10^{-2} to 10^{1} m) due to the limit on the size and resolution of particle detectors. These particles include e, μ, γ and some hadrons. (The neutrinos interact with materials too weakly to be detected directly by ordinary detectors.) The main method to detect these particles and to measure their properties is to study the deposited energy as they pass through layers of material. The energy deposition processes for energetic particles (about 0.5 GeV and above) include Coulomb scattering, ionization and excitation (of the charged particles), EM showering (photon pair production and electron *bremsstrahlung*) and hadronic showering.

3.2.1 Ionization and Radiation

All charged particles traversing material experience energy loss via ionization or excitation processes of the material atoms. The energy transferred to atoms will be re-emitted and can be observed as scintillation light, Cerenkov radiation, *etc.* Except for electrons, this process is the dominant mechanism of energy loss for moderately relativistic particles (such as the particles found in the Tevatron collision byproducts). Ionization and excitation can be described as photon exchange with material atomic electrons using the Bethe-Bloch equation. The average energy loss rate along the traveled distance dE/dx depends on the relativistic variable $\beta\gamma$ of the incident particle and on the material properties (excitation energy, atomic number Z, atomic mass A, density, *etc.*) At very high energy (for example cosmic rays or the products of the LHC), the radiative effect becomes more important than the ionization. The radiations can produce *bremsstrahlung*, EM and hadronic showers, and the energy losses can reach up to a few GeV so energy corrections are needed when detecting and measuring very energetic particles [35].

Figure 3.3 shows the ionization energy loss as a function of $\beta\gamma$. Different particles reach the minimum ionization point ($dE/dx \approx 1 - 1.5$ MeV cm^{2}g^{-1}) at different energies. For example, for electrons the energy is a few MeV. For muons, this energy is a few GeV. After the minimum ionization point, dE/dx rises only logarithmically with γ. In high energy particle experiments, such as DØ at the Tevatron, most collision products have energy higher than a few GeV and exceed the minimum ionization point, so they lose energy at about the same minimum rate. By locating the ionization energy loss, the trajectories of particles can determined. On the one hand, the particle

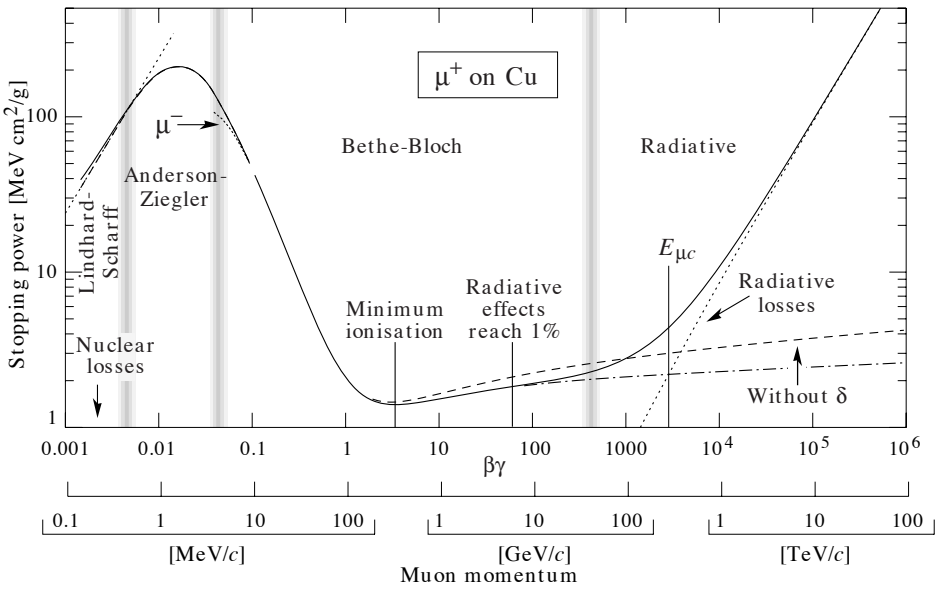

Figure 3.3: Muon energy loss rate in copper. β is the velocity of the particle, $\gamma = (1-\beta^2)^{-1/2}$. The vertical bands separate the energy range where different physics processes dominate the energy loss. For moderately relativistic particles, the energy is lost mainly through the material ionization and excitation [20].

tracks are minimally affected by the detector, so no energy corrections are needed for moderately relativistic particles; on the other hand, the roughly constant energy loss means this mechanism cannot be used for particle ID. In order to have good energy resolution, detection sensitivity and linear characteristics, semiconductors are widely used in modern ionization detectors since they have very low liberation energy (a few eV) compared to other materials (a couple of dozens eV).

3.2.2 Electromagnetic Showering

At low energy, electrons lose energy mainly via ionization processes. At high energy (for example, the Tevatron energy scale), electrons lose energy primarily through *bremsstrahlung*. The mechanism of the electron *bremsstrahlung* is the following: as an electron passes through material, it is deflected by the EM field around the material nucleus and emits a photon which carries away the deflected momentum and energy of the electron. The average loss over traveled distance dE/dx can be written as:

$$\frac{dE}{dx} = \frac{E}{X_0} \tag{3.2}$$

where E is the energy of the electron, and the constant X_0 is called the material radiation length. The deflected electron will continue this process and its energy will decrease exponentially until reaching a critical point where ionization energy loss begins to dominate. This critical energy depends on the material atomic number as well as and the incident particle mass. Typically it is of the order of 100 MeV for electron. For muons and heavier charged particles it is of the order of a few TeV. Thus for Tevatron colliding experiments, we need to consider only the electron bremsstrahlung.

A photon can be absorbed by material via three processes: Compton scattering, photo-electric absorption and pair production. The first two effects dominate for low energy photons. For energetic photons ($\geq$ 100 MeV as in Tevatron experiments) pair production reactions $\gamma + \gamma^* \rightarrow e^+ + e^-$ dominates. The subsequent $e\bar{e}$ pair (if of high enough energy) will start losing their energy via *bremsstrahlung* as discussed above.

As shown in Figure 3.4, the two processes mentioned above will produce a cascading shower of electrons and photons called an EM shower. Clearly the number of particles in the shower depends on the energy of the electron or photon. Detectors called calorimeters essentially measure the number of showering particle (by measuring their ionization energy loss), and thus can be used to measure the energy of the initial electron or photon.

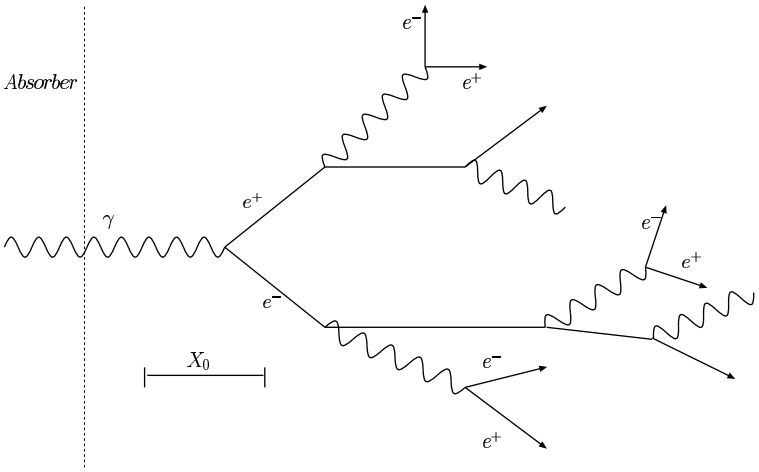

Figure 3.4: Scheme of the EM showering process. Photon pair production $\gamma + \gamma^* \rightarrow e\bar{e}$ (γ^* stands for the EM field of the material) and electron *bremsstrahlung* $e\gamma^* \rightarrow e\gamma$ intermingle and produce a cascading EM shower of lower energy photons and electrons.

3.2.3 Hadronic Showering

In addition to the EM showers from light hadrons such as $\pi^{\pm}$ meson (neutral hadrons such as π^0's mainly also produce EM showers by decaying into two photons), the strong interaction between an incident hadron and the material nuclei also causes energy loss. The inelastic strong interaction results a shower of cascading hadrons called hadronic shower, as shown in Figure 3.5. About 30% energy of the incident hadron is transformed into nuclear binding energy, and this portion of the energy is not detectable. One way to compensate this invisible loss is to use ^{238}U as the material (in sampling calorimeters) because it can release extra energy by the fission processes of ^{238}U and low energy neutrons.

Similar to EM showers, there is a characteristic hadron shower length called nuclear interaction length λ_a [36]. This length is typically an order of magnitude larger than the radiation length for the same material.

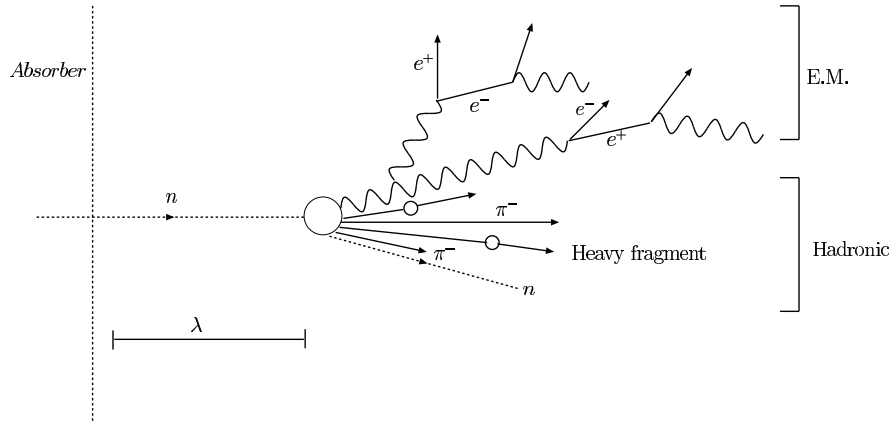

Figure 3.5: Scheme of the hadronic showering process. Most of the particles in the hadronic showers are $\pi^{\pm}$'s which have strong interactions with the material nuclei. A π^0 decays into two photons rapidly (an EM process with life time $\tau \sim 8.4 \times 10^{-17}$ s compared to the weak decays of $\pi^{\pm}$ with life time $\tau \sim 2.6 \times 10^{-8}$ s) and mainly produces EM shower.

3.2.4 Coulomb Scattering

Besides the EM interactions with the electrons and the EM field of the material atoms, a charged particle can also be electromagnetically scattered by the nuclei. This process is called the Coulomb scattering. Due to the small scattering cross section, the effect of Coulomb scattering is generally a small deflection of the particle. A charged particle could experience many Coulomb scatters when passing through materials, so this effect is also called multiple scattering.

The mean scattering angle is inversely proportional to particle momentum. The characteristic length of multiple scattering is the same as the radiation length X_0 of the material. Multiple Coulomb scattering produces no particularly strong observable signals, so it is desirable to reduce its effect as much as possible. This can be achieved by using thin layers of detectors and materials with long radiation length.

3.3 The DØ Detector

As a result of the drastically increased energy of modern accelerators and the corresponding variety of particles emitted in reactions, multipurpose detector systems are indispensable for particle physics experiments because of their capability for detecting and measuring various type of particles over a broad range of momenta. Modern multipurpose detectors, like the DØ detector, have many things in common in their designs:

- **Precise Inner Tracking System.** This is the part closest to where the interactions happen. Thin layers of semiconductors are widely used to prevent showers and multiple scatterings so that precise tracking and the minimum energy loss can be achieved at the same time.

- **Larger Outer Tracking System.** The semiconductor detectors are still too expensive for large scale tracking system (size of meters), so other materials, such as scintillating fibers, are used outside the inner tracker. Magnetic fields can also be added to determine the momentum and charge of the charged particles. Minimum energy loss and multiple scattering are essential to cleanly reconstruct the trajectories.

- **Calorimeter.** In order to measure the energy of particles, to tell apart hadrons from EM particles (electron and photon), and to be able to detect and measure energy of neutral particles such as photons and K^0's, a calorimeter is used. Most of the particles deposit all of their energies in calorimeters and are stopped, so a calorimeter resides outside the tracking system. Calorimeters can also be used to roughly measure the trajectories of particles, which in combination with the information from the tracking system, can provide better particle ID and tracking.

- **Muon System.** Muons are special in that they do not produce showers, so they will pass through the calorimeter. Specialized tracking systems are implemented as the outermost detector elements to provide muon ID and tracking information.

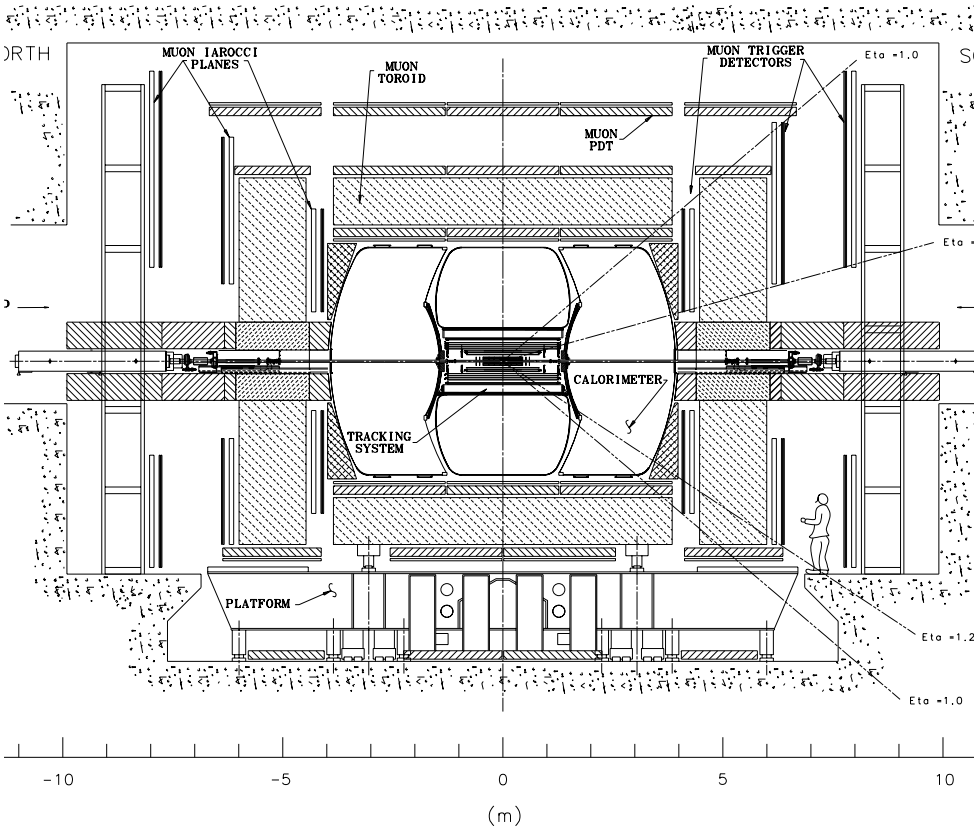

Figure 3.6: Overview of the DØ detector.

A diagram of the DØ detector is show in Figure 3.6. A right-handed coordinate system is used at DØ , with the z-axis along the proton direction, positive y upward, positive x pointing opposite to the center of the Tevatron storage ring. The polar angle $\theta = 0$ coincides with the positive z-axis, and the azimuthal angle $\phi = 0$ with the positive x-axis.

In addition to the common Cartesian and spherical coordinates, the most commonly used coordinate system at DØ is a modified spherical system in which the polar angle θ is replaced with the pseudo-rapidity η, defined as:

$$\eta = -\ln\left(\tan\frac{\theta}{2}\right) \tag{3.3}$$

the pseudo-rapidity is derived from the rapidity y:

$$y = \frac{1}{2}\ln\left(\frac{E+p_z}{E-p_z}\right) \tag{3.4}$$

in the limit of $m/E \to 0$)

The *central region* refers to the detector region with $|\eta| \leq 1.2$, where a particle traveling in this region will pass through nearly all of the important detector system. Close to the beam pipeline (with $|\eta| > 3$) is the *far forward region*. The far forward region has fewer detectors, and it is filled with the remnants of the inelastic collisions and $p\bar{p}$ from the elastic collisions. Since the longitudinal kinematics of the partons in the $p\bar{p}$ collision are not available on an event-to-event basis, it is impossible to study an collision event along the z axis. But the transverse momenta of the partons should be approximately balanced (soft radiation causes corrections to this first order approximation), and for most of the deep inelastic events that are of physics interest for the Standard Model testing, large transverse momentum transfers are involved, consequently, transverse kinematic variables in the $x-y$ plane, such as $E_T = E\sin\theta$ and $p_T = p\sin\theta$, are extensively used at DØ (and at almost any particle experiments) and in this thesis. The contributions from the remnants which are in the forward direction are negligible.

The main advantage of using η or y is that the difference in y between two particles is invariant under Lorentz boost along the z-axis. So a distribution as a function of y is invariant for any boosts along z. An important application of this property is that many physics variables' y distributions for particles produced purely by QCD interactions are flat.

It is normally convenient to choose the origin of the event coordinate system to be the same as the location of the actual interaction point which varies from event to event. The length of the interaction region along $z-$axis is approximately 25 cm (Gaussian distributed) and roughly 35 mm in the $x-y$ plane. However, it is

sometimes also useful to choose the detector center as its origin. These two definitions are referred to as the physics and the detector coordinates, respectively. With the exception of this chapter, physics coordinates are used throughout the thesis.

3.3.1 Central Tracking Detectors

The DØ tracking system resides in the center of the detector. It consists of the inner silicon tracker and outer fiber tracker surrounded by the solenoid magnet as shown in Figure 3.7. The main purpose of the super-conducting solenoid magnet is to bend the charged particle tracks so that their momenta, as well as the signs of their charge can be determined. The central field was initially chosen to be a consistant 2 T as shown in Figure 3.8. Due to an incident in the magnetic cooling system in 2005, the field is now 1.96 T. By measuring the position where charged particles pass each layer of the tracking detectors, the track radius of curvature and vertex (refer to Section 5.2) can be determined.

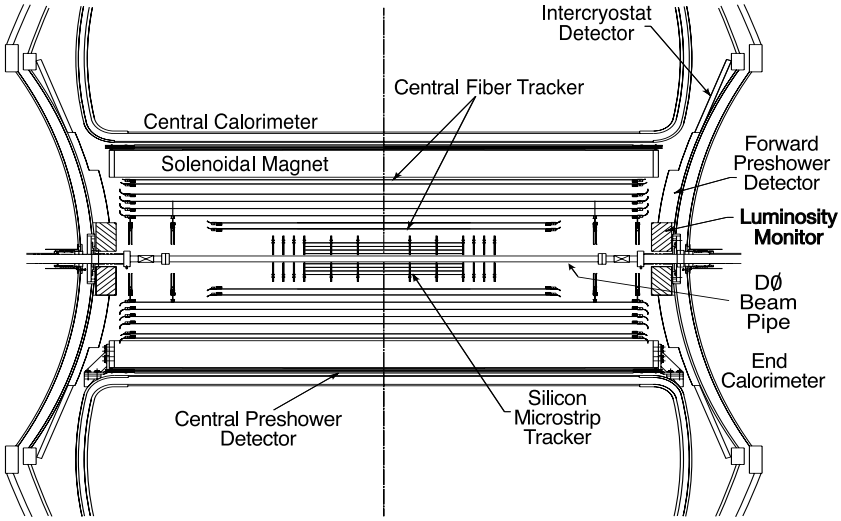

Figure 3.7: The central tracking system of DØ .

Silicon Microstrip Tracker (SMT)

As shown in Figure 3.9(a) the SMT consists of six barrels interspersed with 12 disks (F disks) in the center and four disks (H disks) in the forward regions. Each barrel has four concentric layers of readout units. Silicon detector modules on these units are called ladders. Layers 3 and 4 have 24 ladders each; layers 1 and 2 have 12 ladders each, for a total of 432 ladders (387072 readout channels). A section view of a barrel is shown in Figure 3.9(b). The F and H disks consist of 144 (258048

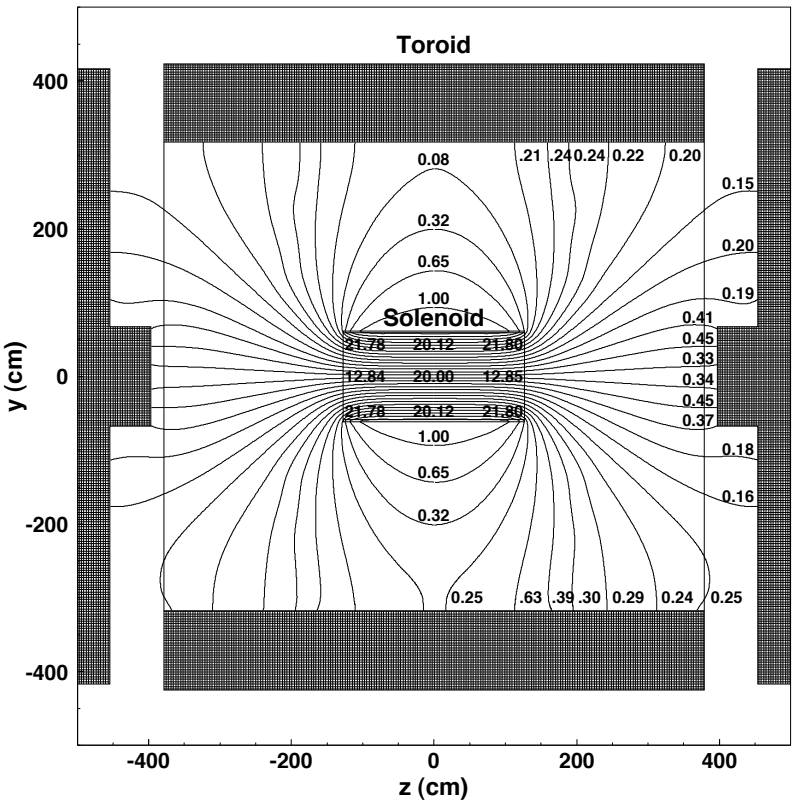

Figure 3.8: The $y - z$ view of the DØ magnetic field (in kG) with both the toroidal and solenoidal magnets at full currents (1500 A and 4749 A, respectively) [30].

channels) and 96 (147456 channels) of readout wedges, respectively. The centers of the H-disks are located at $|z| = 100.4$, and 121.0 cm; the F-disks are at $|z| =$ 12.5, 25.3, 38.2, 43.1, 48.1, and 53.1 cm. The centers of the barrels are at $|z| =$ 6.2, 19.0, and 31.8 cm.

The SMT sensors use a mixture of single and double-sided silicon wafers as shown in Table 3.2. Single-sided sensors have a slightly doped $n-$type (n^-) silicon base with a series of parallel $p-$type silicon microstrips on one side and a heavily doped $n-$type (n^+) silicon surface on the other side. n^+ is positively biased as shown in Figure 3.10. When a charged particle passes through the sensor, ionization will create pairs of electrons and holes. The holes under the positive bias on n^+ will drift to $p-$strips and form a charge signal. Double-sided sensors also have $p-$type wafer with negative bias and $n-$ type strips to collect the electrons. By reading out the position and the pulse height of the signal, the trajectory and dE/dx of the charged particles can be obtained.

Module	Type	Layer	Pitch (μm) p/n	Length (cm)	Inner radius (cm)	Outer radius (cm)	Si Area (m^2)
F-disks	DS	-	50/62.5	7.93	2.57	9.96	0.4
H-disks	SS	-	$\frac{40^i}{40^o}$	$\frac{7.63^i}{6.63^o}$	9.5	26	1.3
Central	DS(DM)	1, 3	50/153.5	12.0	2.715	7.582	1.3
barrels (4)	DS	2, 4	50/62.5	6.0	4.55	10.51	
Outer	SS	1, 3	50	6.0	2.715	7.582	
barrels (2)	DS	2, 4	50/62.5	6.0	4.55	10.51	

Table 3.2: The configurations of sensor on all layer and wedge detectors. SS stands for single-sided, DS for double-sided. An H-disk has two single-side detectors on the inner (i) and outer (o) surface. [30]

All the barrel wafers have axial strips arranged along the $z-$ axis. For the double-sided wafers the strips on the other side have either a 2° or 90° stereo angle depending on the layer and barrel of the ladder. All the trapezoid shape wedge sensors on disks have strips parallel to the long edge. Double-sided wedges have strips with 30° stereo angle. Single-sided wedges consist of two back-to-back half wedges with 15^o stereo angle. The barrel detectors primarily measure the $r - \phi$ coordinate and the disk detectors measure $r - z$ as well as $r - \phi$. Thus the SMT is able to provide both tracking and vertexing with a precision up to 10 μm over nearly the full η coverage of the calorimeter and muon systems.

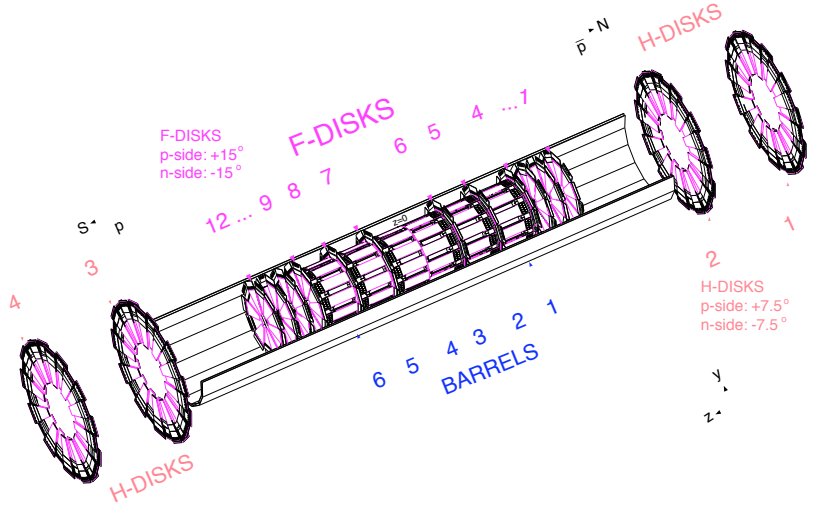

(a)

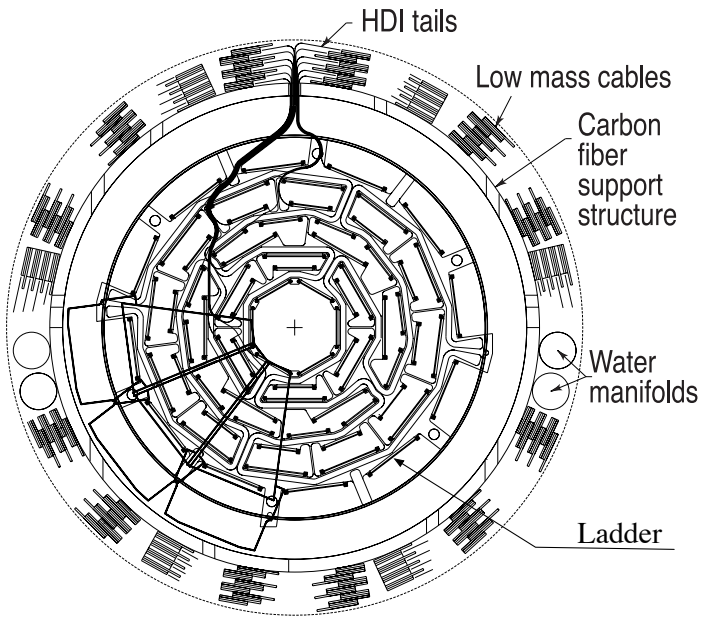

(b)

Figure 3.9: The SMT of DØ . (a) the construction of the SMT barrels and disks; (b) the ladders in a barrel.

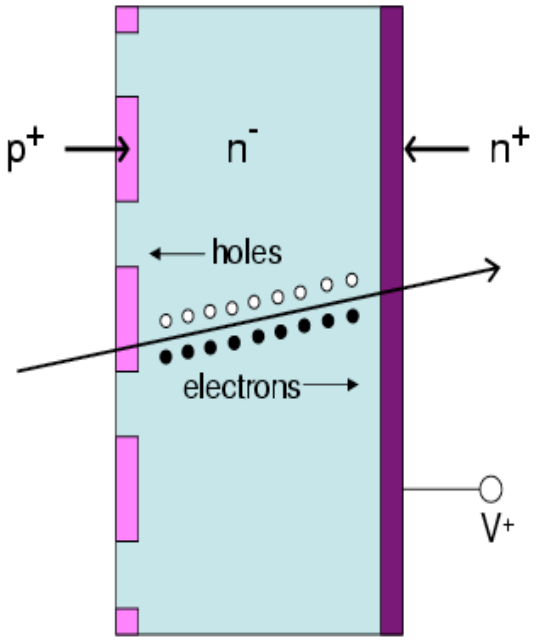

Figure 3.10: The mechanism of the SMT silicon sensor.

Central Fiber Tracker (CFT)

The CFT lies between the solenoid and the SMT. It covers the central region ($|\eta| \leq 1.8$) as shown in Figure 3.11. The CFT consists of eight concentric carbon fiber cylinders. Each cylinder contains two layers of fiber doublets. The inner layer is axial (parallel to the $z-$axis), the outer layer has a $\pm 3^o$ stereo angle with respect to the inner layer, the sign of which alternates with each successive stereo layer. Within each doublet, the two layers are offset by half the fiber radius to improve the angular coverage. The scintillating fibers have a radius of 835 μm and lengths of either 1.66 m (layers A and B) or 2.52 m (layers C–H). The fibers are made of slightly doped polystyrene core that is clad in an inner thin acrylic layer and an outer fluoroacrylate. The CFT are divided evenly into 80 sectors in the ϕ direction. The fibers in each sector are grouped together for readout. The configuration of the CFT is listed in Table 3.3.

The ionization from a charged particle passing through a fiber causes scintillating light (yellow green visible light) that travels towards both ends of the fiber. At one end an aluminum mirror reflects the light back down the fiber. At the other end, the fiber is joined to a wavelength shifting waveguide which transmits the light to a solid state device (Visible Light Photon Counter, VLPC) that converts the light signal into an electronic signal for further processing. The CFT can measure both the $r-\phi$ position and the $r-z$ position. The radius of the fiber determines the position

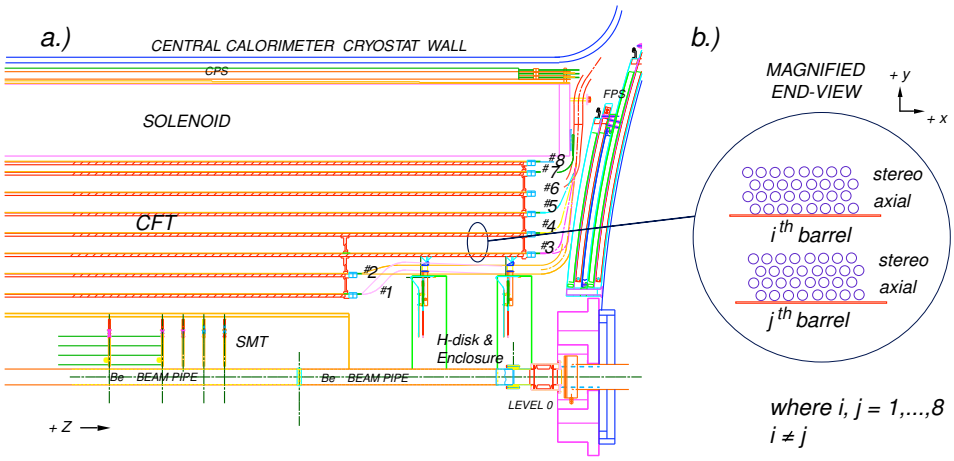

Figure 3.11: A section view of the Central Fiber Tracker.

layer	Radius (cm)	# of fibers	Fiber Pitch (μm)
A	20.1	2560	985.606
B	25.0	3200	981.300
C	29.9	3840	978.105
D	34.8	4480	976.101
E	39.7	5120	974.598
F	44.6	5760	973.429
G	49.5	6400	972.297
H	51.5	7040	919.610

Table 3.3: Summary of the CFT configuration.

resolution of the CFT, which is about 100μm, corresponding to $\sim 2 \times 10^{-4}$ in the ϕ direction and ~ 1 cm in the Z direction.

Momentum Resolution

The curvature κ of a charged particle's track in magnetic field B along the z direction is expressed by the following equation:

$$\kappa = \frac{1}{R} = 0.3B\frac{q}{p_T} \tag{3.5}$$

where R is the radius of the track in meters, q is the charge of the particle in the unit of the electron charge e, p_T is the transverse momentum in GeV and B is in Tesla. The resolution of κ is mainly determined by two factors: the position resolution of the detector and the multiple scattering. The position resolution of the SMT is much better than the CFT, yet the CFT has much larger radial size, so combining them together yields a good overall position resolution. The multiple scattering is anti-correlated with the momentum of the particles. The expected momentum resolution of DØ central tracking system is shown in Figure 3.12 [37]. At $\eta = 0$ it can be parameterized as[38]:

$$\frac{\Delta p_T}{p_T} = \sqrt{0.015^2 + (0.0014 p_T)^2} \tag{3.6}$$

where p_T is in GeV. The first term represents the multiple scattering, the second term reflects the position resolution.

3.3.2 Central/Forward Preshower Detectors (CPS/FPS)

Cables, detector supports and the solenoid magnet with a thickness of about $0.9X_0$ (refer to Eq. 3.2) can cause significant amount of energy losses via multiple scattering and EM showering for EM particles before they enter the calorimeter. In order to correct for their energy losses, the FPS and CPS detectors are installed in the forward $|\eta| \leq 1.3$ and central region $1.5 \leq |\eta| \leq 2.5$, respectively, as shown in Figures 3.6 and 3.7.

The CPS/FPS cause EM particles to produce showers before the calorimeter. The shower multiplicity and position are then measured using scintillating light which provides much better position precision than the calorimeter. This information can be used online as for L1 triggers, or offline to enhance the EM particle ID and energy measurement, and to provide better spatial track matching between the central tracking system and the calorimeter,

The CPS consists of three layers of scintillating strips mounted in concentric cylinders. A layer of lead-stainless-steel radiator, ($\sim X_0$) is installed directly on the

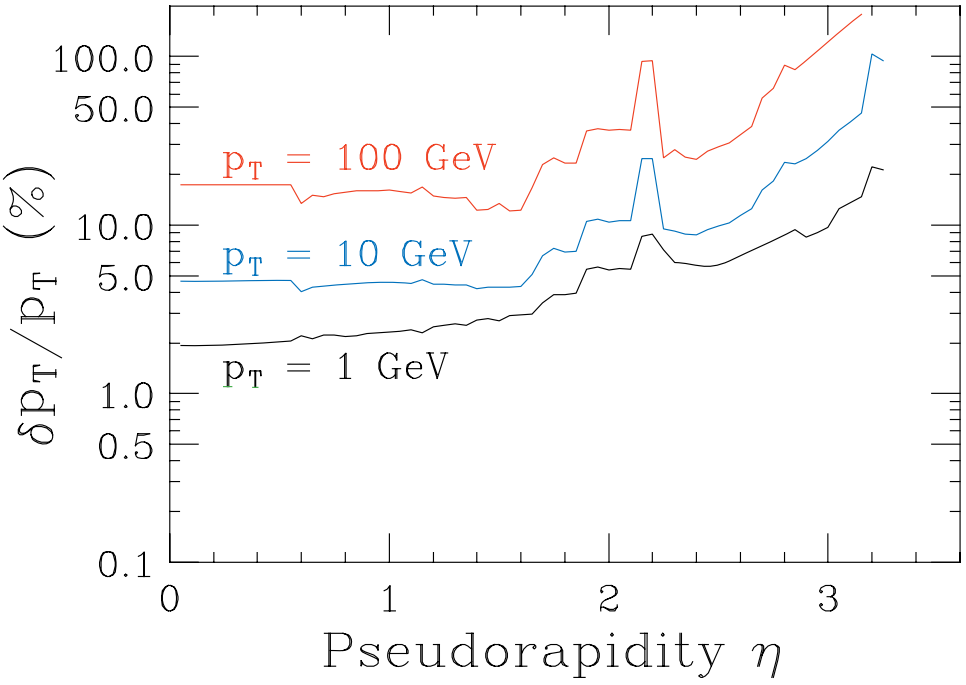

Figure 3.12: The expected fractional p_T resolution of the DØ central tracking system. The increase after $|\eta| = 1.6$ is due to loss of the CFT coverage. When $|\eta| \geq 2.1$ the F and H-disks of the SMT compensate this loss of coverage.

solenoid. EM particles will produce showers after passing the radiator and cause scintillator light in the strips. Heavier particles are less likely to produce showers. Instead they produce signals of a minimum ionization particle (MIP). Each CPS layer contains eight octet modules that can be matched to the CFT's 80 modules. The strips in the innermost layer of the CPS are axial while the outer two (u and v) layers are at stereo angles of about $\pm 24^\circ$ with respect to the innermost layer. This stereo geometry allows the reconstruction of 2-D clusters.

The FPS detectors are round-shaped and mounted on each of the calorimeter endcaps. They consist of two layers of trapezoidal modules separated by a layer of lead-stainless-steel absorber, ($\sim 2X_0$ thick). Each module is composed of two sublayers (u and v) of scintillating strips at a stereo angle of 22.5° and covering 22.5° in azimuth. The upstream module (those nearest the interaction region) are known as the MIP layers while the downstream layers behind the absorber are called the shower layers. Charged particles passing through the detector will register a MIP signal in the MIP layer, allowing measurement of the 2-D location of the track. Electrons will readily shower in the absorber, leading to a cluster of energy, typically on the order of three strips wide, in the shower layer that is spatially matched with the MIP-layer signal. Heavier charged particles are less likely to shower, typically producing a second MIP signal in the shower layer. Photons will not generally interact in the MIP layer, but will produce a shower signal in the shower layer.

The scintillating strips are mode of slightly doped polystyrene triangle-shaped plastic as shown in Figure 3.13. Embedded at the center of the strip is a wavelength shifting fiber that produces yellow green scintillating light and transmits the light signal to a VLPC for further processing. The position resolution of CPS/FPS is about 550 μm in the $r-\phi$ plane (CPS) and $r-z$ plane (FPS) [39].

3.3.3 Calorimeter System

The DØ calorimeter system mainly measures the energy and the shape profile of EM particles and hadronic jets. It consists of a central region calorimeter (CC) covering $|\eta| \leq 1.1$, two forward region calorimeters, one on each end (ECS and ECN), covering $1.3 \leq |\eta| \leq 4$ and intercryostat detectors covering the gap of $1.1 \leq |\eta| \leq 1.4$ between the cryostats, as shown in Figure 3.14.

Calorimeters

The DØ calorimeter is a compensating sampling calorimeter, using liquid argon as the active medium and uranium, copper or stainless steel as the absorber. The calorimeter is composed of many unit cells. The unit cells are grouped into many layers of larger readout units. As shown in Figure 3.14, the readout cells can be

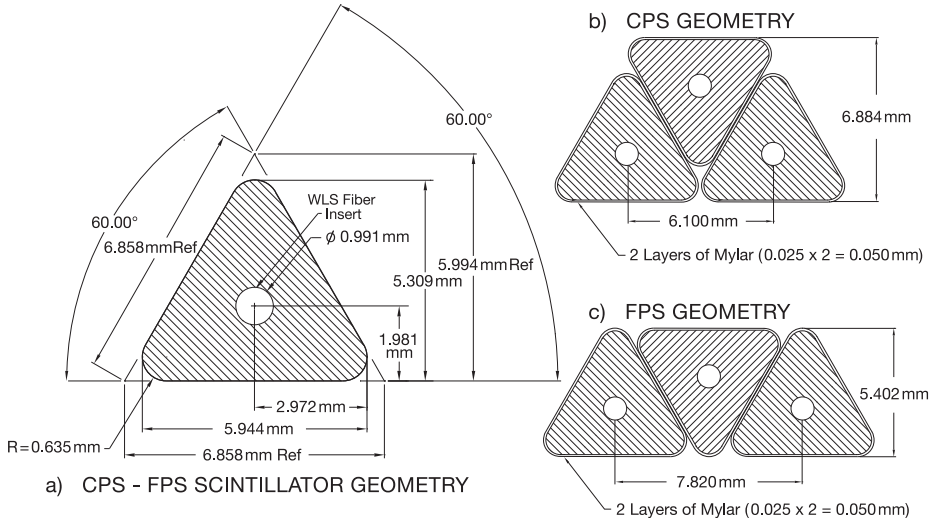

Figure 3.13: The cross section and layout geometry of the CPS and FPS scintillating fibers.

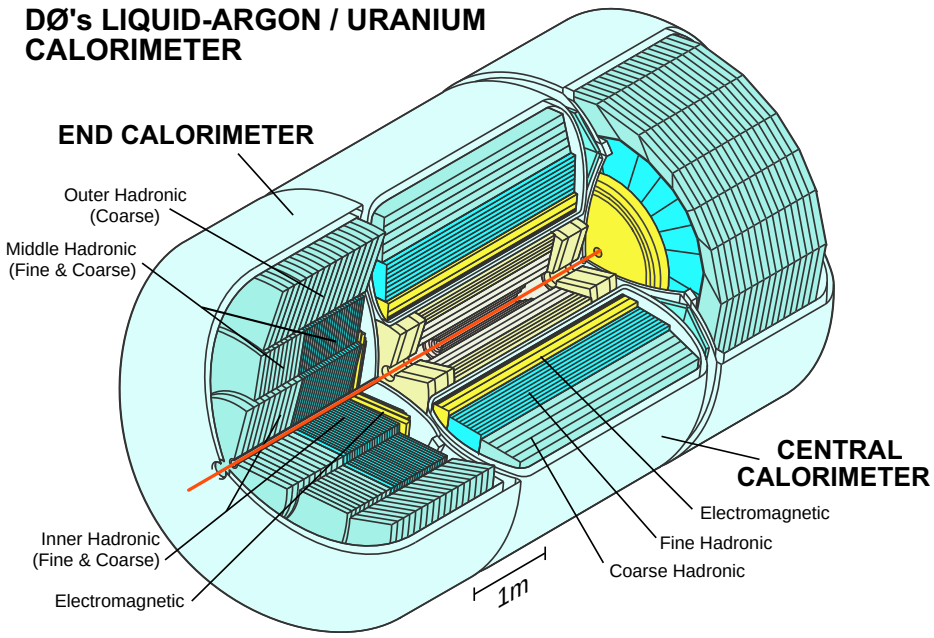

Figure 3.14: The DØ calorimeter.

further grouped into three types: electromagnetic (EM), Fine Hadronic (FH) and Coarse Hadronic (CH).

Longitudinally (*eg.* from the collision point toward outside of the detector), towers are arranged in EM–FH–CH order.[1] This is because hadronic showers have much larger spatial expansion than the EM showers (see Sections 3.2.2 and 3.2.3). Within the energy range of Tevatron, a typical EM shower has a size of $\Delta R \approx 0.2$, where $\Delta R \equiv \sqrt{\Delta\eta^2 + \Delta\phi^2}$, while for a typical hadronic shower, the size is ≈ 0.5. Segments that are finer than 0.2 in the $\eta - \phi$ plane enables us to discern the differences in the shape profile between the EM showers and hadronic showers. So the towers in each layer are arranged into to a consecutive $(\Delta\eta, \Delta\phi)$ segments with intervals of $\Delta\eta_{det} = 0.1$ and $\Delta\phi = \frac{2\pi}{64} \approx 0.1$.[2] The third layer of EM is more finely divided into $(\Delta\eta, \Delta\phi) = (0.05, 0.05)$ since an EM shower maximum is expected in this layer. The EC and CC have different layouts of these segments for EM/FH/CH towers as shown in full detail in Figure 3.15. Tables 3.4 and 3.5 listed the important parameters of the EC and CC layouts.

	EM	FH	CH
Number of Modules	32	16	16
Absorber	Uranium	Uranium	Copper
Absorber Thickness (mm)	3	6	46.5
Argon Gap (mm)	2.3	2.3	2.3
Number of Layers	4	3	1
Cells per Readout Layer	2, 3, 7, 10	20, 16, 14	9
Total Radiation Length (in X_0)	20.5	96.0	32.9
Total Interaction Length (in λ_A)	0.76	3.2	3.2

Table 3.4: Parameters of the tower layout in the CC.

The scheme of a typical calorimeter cell is shown in Figure 3.16. The cell is filled with liquid argon, with an absorber plate connected to ground and a readout plate at +2.0 kV. A charged particle passing through the cell leaves a trail of ionization in the liquid argon, and the electrons drift to the readout plate to form a charge signal. The dense absorber induces showering so all the energy of the incident particle is measured. The liquid argon gaps are 2.3 mm wide, with an electron drift time of about 450 ns, close to the Tevatron bunch crossing time (396 ns). The gap width was

[1] Since the calorimeter system is contained in three separate cryostats, it provides incomplete coverage in the pseudo-rapidity region $0.8 \leq |\eta| \leq 1.4$, as can be seen in Figure 3.15. In addition, there is substantial unsampled material in this region, degrading the energy resolution. To address these problems, additional layers of single-cell units are added within the central and end cryostats. These cells are called massless gaps.

[2] In the very high η region, the EM cell size, as well as those of the FH and CH increases to avoid very small cells.

	EM	IFH	ICH	MFH	MCH	OH
Number of Modules	1	1	1	16	16	16
Absorber	Uranium	UNb	SS	UNb	SS	SS
Absorber Thickness (mm)	4	6	46.5	6	46.5	46.5
Argon Gap (mm)	0.23	0.21	0.21	0.22	0.22	0.22
Number of Layers	4	4	1	4	1	3
Cells per Readout Layer	2, 3, 6, 8	16	14	15	12	8
Total Radiation Length (in X_0)	20.5	121.8	32.8	115.5	37.9	65.1
Total Interaction Length (in λ_A)	0.95	4.9	3.6	4.0	4.1	7.0

Table 3.5: Parameters of the tower layout in the EC. IFH, ICH, MFH, MCH, OH stand for inner fine, inner coarse, middle fine, middle coarse and outer hadronic sections, respectively. UNb and SS stand for Uranium-Nioblum alloy and Stainless Steel.

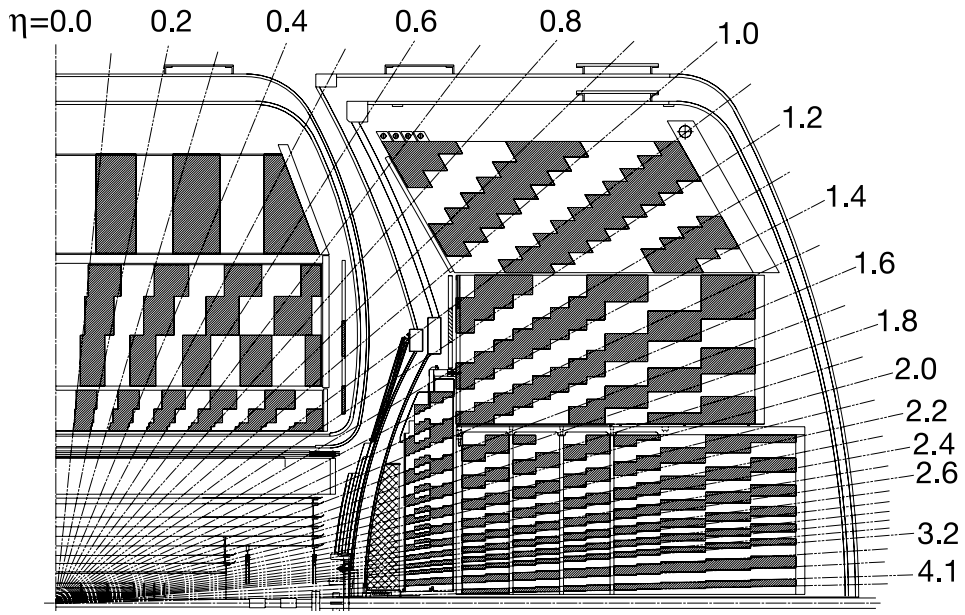

Figure 3.15: The cross section view of a quarter of the DØ calorimeter. The shading pattern indicates the readout unit (towers), each of them contains many unit cells. The rays indicates the η_{det} intervals.

chosen so that the MIP signal can be observed while the construction of cells could avoid excessive difficulty.

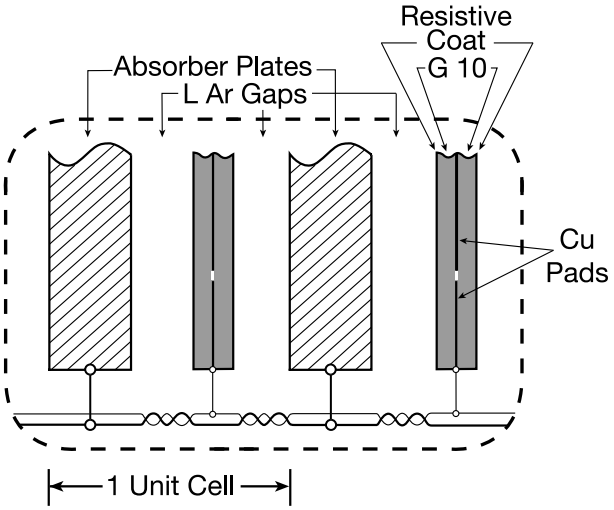

Figure 3.16: The scheme of a typical calorimeter unit cell.

Intercryostat Detector (ICD)

The ICD, shown in Figures 3.7 and 3.15, consists of a single layer of 384 scintillating tiles with a size of 0.1×0.1 in $\eta - \phi$, matching the cell size of the calorimeter. These tiles are optically isolated from each other. The signal on each tile is collected by wavelength shifting fibers embedded in the tiles and transmitted using clear fiber waveguides to photomultiplier tubes (PMTs) located outside of the magnetic field.

Calorimeter Performance

The energy resolution σ_E of the ideal calorimeter is affected mainly by three factors: the uranium noise, the statistical fluctuations of energy deposition in the liquid argon, and the calibration of the calorimeter. The fractional energy resolution can be parameterized as:

$$\frac{\sigma_E}{E} = \sqrt{\left(\frac{N}{E}\right)^2 + \left(\frac{S}{\sqrt{E}}\right)^2 + C^2} \tag{3.7}$$

The first term is the noise term, since noise is independent of the signal; the second term represent the statistical uncertainty which is proportional to $\sqrt{E}$. The third term stands for the calibration uncertainty, which to good approximation is linear in the signal. The values are listed in Table 3.6.

		N	S ($\sqrt{\text{GeV}}$)	C (GeV)
DØ RunI	EM Object	$0.0115^{+0.0027}_{0.0036}$	0.135 ± 0.005	0.43
	Jet	0.032 ± 0.004	0.45 ± 0.04	0.975
DØ RunII	EM Object	~ 0.29	$\sim 21\%$	~ 0.022
	Jet	$\sim 0.0 \pm 0.4$	$\sim 0.8 \pm 0.008$	$\sim 0.06 \pm 0.001$

Table 3.6: The calorimeter resolution constants for the central region detector data during RunI and RunII[40, 41, 42]. For DØ RunI, the parameters of EM objects are measured with electrons: C from the $Z \rightarrow e^+e^-$ mass resolution, S from the test beam and N from $W \rightarrow e\nu$; jet parameters are measured with pions from the test beam. For DØ RunII, the parameters for EM objects are measured using $Z \rightarrow e^+e^-$ events, the parameters for jets are measured using di-jet events. Due to the added material within in RunII, the calorimeter can not be very well modelled as an ideal one. For example, the S for the EM objects is energy dependent. As such the central values are just approximate averages, and the uncertainties are not determined.

3.3.4 Muon Detectors

Almost no particles can penetrate the calorimeter except for muons (and neutrinos which are not directly detectable at DØ). A muon leaves MIP signals in the central tracking, the calorimeter and the muon detectors with little energy loss. The muon system is used to ID and trigger on these muons by measuring the position and the timing of their tracks. The muon detectors consist of proportional drift tubes (PDTs), mini drift tubes (MDTs) and scintillation counters. Each detector has three layers named A, B and C from inside out, with a toroid magnet of 1.8 T installed between A and B layers. With this magnet the muon detectors can also provide a crude measurement of their momenta and charge. The muon detectors are also divided into 3 regions: one central region covering $|\eta| \leq 1.0$ called Wide Angle Muon System (WAMUS) and two forward regions covering $1.0 \leq |\eta| \leq 2.0$ called Forward Angle Muon System (FAMUS). A sketch of the muon detectors is shown in Figure 3.17.

PDTs and MDTs

The PDTs and MDTs are arranged in planes. Both the PDTs and the MDTs have four layers of drift tubes in the A layer[3], and three layers each in the B and C layer. The drift tubes are filled with gas that is ionized by the passage of a charged particle. The charge is collected on high voltage sense wires running through the volume. The liberated electron's drift speed is almost a constant of 10 cm/μs when the voltage on the sense wire is as high as 5.0 kV. By comparing the arrival time of the particle (

[3]The A layer PDT at the bottom of the DØ detector system has only 3 layers of tubes. A hole in ϕ from 225° to 310° exists to allow for the calorimeter support structure.

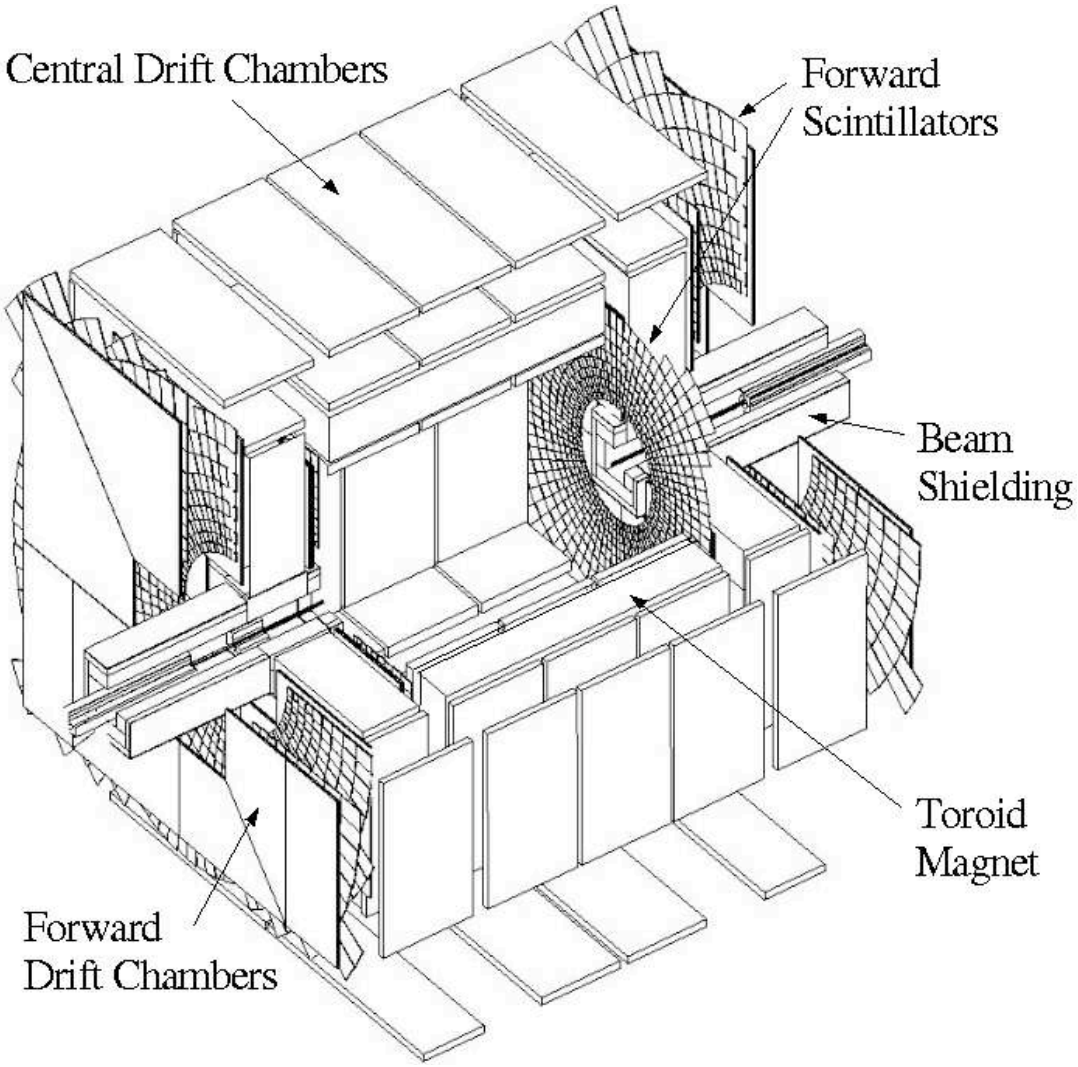

Figure 3.17: Cut-away view of the DØ muon detectors.

provided by the scintillation counters which have very fast response) and the signal time on the sense wire, the radial distance from the sense wire to the particle track can be calculated. The maximum drift time of PDTs and MTDs are 600 ns and 60 ns, respectively. Their position resolution (along $z-$axis) are about 3 mm and 0.7 mm, respectively. The neighboring PDT tubes have connected readout so that the axial time information (corresponding to ϕ) can also be determined.

The PDTs cover the WAMUS while the MDTs cover the FAMUS. The MDTs were chosen for the forward region in consideration of the higher radiation and background due to the proximity to the beam pipeline. Additional shielding is also installed to reduce the beam effect to the MDTs.

Scintillator Counters

In the central muon region two layers of scintillator are added inside the A-layer (called A-Phi layer) and outside of the C-layer (called cosmic cap). In the forward region, all three layers of MDTs are covered with a layer of scintillator pixels each of which covers a surface of 4.5° in ϕ and 0.1 in η. The counters collect scintillation light produced by the passage of a charged particle. Wavelength shifting fibers are embedded onto the scintillators and are connected to PMTs which convert the light to an electronic signal.

The scintillator counters provide additional position measurement (especially in ϕ), and are used for triggering, cosmic ray veto, beam related muon rejection and track reconstruction.

Momentum Resolution

The average energy loss of a muon in the calorimeter is 1.6 GeV, and about 1.7 GeV in the toroid magnet iron. The momentum measurement is corrected for this energy loss. As a comparison to the momentum resolution of the central tracking system in Eq. 3.6, the muon detector momentum resolution can be parameterized as [43]:

$$\frac{\sigma_p}{p} = 0.18 + 0.005p \tag{3.8}$$

Compared with Eq. 3.6, the best determination of a muon's momentum is actually provided by the tracking system.

3.3.5 Forward Proton Detector (FPD)

The FPD is a series of momentum spectrometers that make use of accelerator magnets in conjunction with position detectors along the beam line in order to determine the kinematic variables t and ξ of the elastically or diffractively scattered $p\bar{p}$,

where $|t|$ is the four-momentum transfer of the scattered proton or anti-proton, and $\xi = 1 - x_p$, where x_p is the fractional longitudinal momentum of the scattered particle with respect to the incoming proton. The FPD is not used in this analysis.

3.3.6 Luminosity Detector (LM)

The LM is used mainly to measure accurately the luminosity of the Tevatron beams at the DØ interaction region. It consists of two arrays of twenty-four plastic scintillation counters with PMT readout as shown in Figure 3.18. The arrays, located in front of the end calorimeters at $|z| = 140$ cm, fill in the region between the beam pipe and the FPS. The counters are 15 cm long and cover $2.7 \leq |\eta| \leq 4.4$. The LM

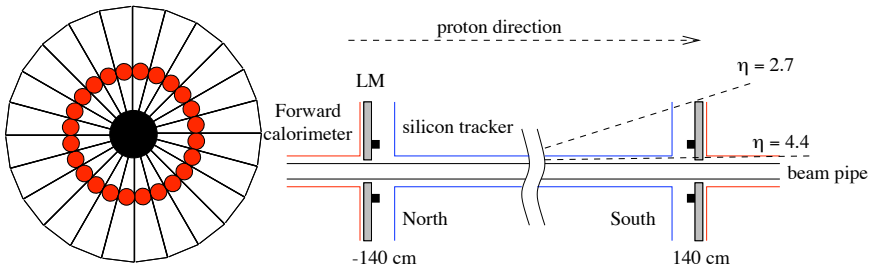

Figure 3.18: The scheme of LM. On the left is the $r - \phi$ view, the right is the $r - z$ view.

measured luminosity can be expressed as:

$$\mathcal{L} = \frac{R}{\epsilon A \sigma_{inel}} \tag{3.9}$$

where σ_{inel} is the $p\bar{p}$ inelastic cross section, R is the event rate, ϵ is the LM efficiency for the inelastic events and A is its geometric acceptance. Multiple $p\bar{p}$ collisions can occur in a single bunch crossing. The number of interactions per bunch crossing is described by a Poisson distribution. Collision products arrive at each set of scintillators roughly in coincidence, while beam halo products passing through the detector appear distinctly separated. Time-of-flight information from the two LM arrays and the $z-$vertex distribution can be utilized to separate these processes. A more detailed discussion on the luminosity calculation is in Chapter 4.

Chapter 4

Trigger and Data Acquisition Systems

The digitized detector signals (readout) from each of the detector systems need to be written to tape for future studies. At the Tevatron the $p\bar{p}$ bunch crossing rate is about 2.5 MHz, which results in an interaction rate of 1.7 MHz in RunIIa and about 7 MHz in RunIIb. For each interaction event, there are several hundred kilobytes information to be readout. For example, the SMT has 792,576 readout channels and the calorimeter has 55,296 readout channels. It is impossible to record all the information for every event in DØ due to the low tape event writing rate of about 50 Hz (storage and management of the tapes would also be impossible).

Fortunately we do not need to record all the events for majority part of the physics studies (to test the Standard Model) at the DØ. The colliding events contain about 20% elastic processes and 80% inelastic processes at the current Tevatron energy [47], and the only processes that are directly relevant to the testing of the Standard Model are the inelastic non-QCD-multijet events, such as the W/Z boson production and the Higgs boson production. The interesting processes have a typical cross section of several hundreds of pb compared to the inclusive $p\bar{p}$ cross section of about 60 mb, so we can manage to record the wanted physics data at a rate of about 50 Hz if only those interesting events are to be selectively recorded.

At DØ a 3-level trigger system controls the data acquisition system (DAQ) to select the interesting inelastic events. Up to 256 triggers at level one and 1024 triggers at level three are supported by the DØ trigger system. Different triggers are used for the studies of different processes. One complication caused by the trigger system is the precise calculation of the luminosity for a specific trigger because different triggers may have different dead time thus different exposure to data. Another problem is to determine the trigger efficiencies and the correlations. In this chapter a description of the 3-level trigger system, and its interaction with the DAQ and the detector front-end is given. Then the luminosity calculation with the trigger system added is

discussed. We will focus on the muon triggers and calculate their efficiencies, since muon triggers are used in this analysis to select the event data.

4.1 DØ Trigger and DAQ System

Data are pipelined from the detectors and the trigger system to the DAQ system through a series of finite length FIFO buffers as shown in Figure 4.1. These buffers leave enough time for the data transfer and trigger decision making at various DAQ stages. The trigger system controls the data pipeline as shown in Figure 4.2. On every tick detectors send data to the front-end buffers in the readout crates of the level 1 (L1) sub-detector trigger system. If the front-end buffer is full it sends the error message to the trigger frame work (TFW) and the TFW issues a front-end busy that stops the detector data into the front-end until the buffer regain room. The L1 trigger system makes their decisions during each tick interval for the currently pointed data in the buffer. These L1 decisions are sent to TFW in the form of And/Or Terms (AOT) for testing against the L1 triggers. When a L1 accept is issued by the TFW, the detector data plus the L1 trigger system data are sent to the buffer in the readout crates of the level 2 (L2) trigger system; if L1 reject is issued, the data is dumped and the buffer pointer moves to the next event data. If a buffer in the L2 crates is full, the TFW issues a L1 busy signal to prevent more L1 accepts from being issued until the buffer has free room. L2 trigger system sends their AOT decisions also to the TFW for testing against the L2 triggers via a L2 global computers. If the TFW also issued a L2 accept for the event, the detector data plus the L1 and L2 data are send to the buffer that will be read by the level 3 (L3) DAQ system.

The L3 DAQ transfers the data for an event from the readout crates to one of a series computers (L3 farm nodes). The collection of event data from all of the readout crates is assigned an event number by L3 DAQ. An event will be thrown away if it contains incomplete data (missing any crate readout). If the event satisfies a level 3 (L3) trigger, it is passed on to the online system which routes the data into different users. Events are organized exclusively by specific triggers criteria into different physical streams. A data taking run usually contains four physical streams, and each physical streams can be partitioned into many data files for easy storage and fetching. Completed files are recorded on tape. One copy of meta-data of the data files is sent to the luminosity DAQ ($\mathcal{L}$DAQ) for luminosity determination, the other one is sent to an Oracle database system (sequential data access system via meta-data, or SAM) for offline studies.

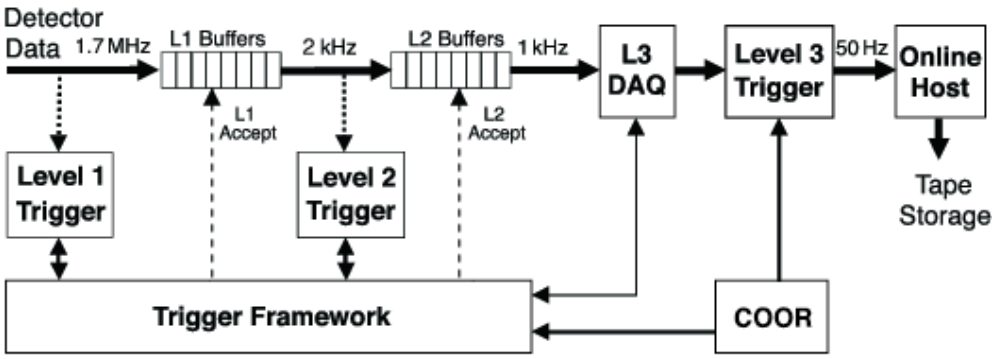

Figure 4.1: An overview of the DØ trigger system. The overall coordination and control of DØ trigger system is handled by a package – COOR – running on the online host. COOR interacts directly with the TFW (for L1 and L2 triggers) and the DAQ supervising systems (for the L3 triggers).

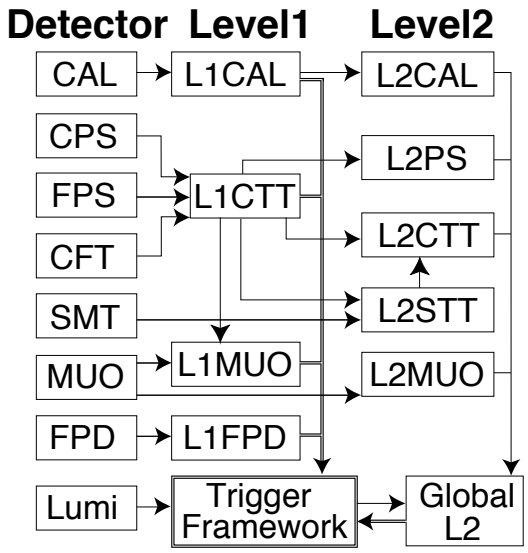

Figure 4.2: L1/L2 components and the TFW of the DØ trigger system that controls the data pipeline to the L3 DAQ and trigger system.

4.1.1 Level 1 Trigger System

The L1 trigger system is implemented in specialized hardware due to the stringent dead time requirement. The detector data are read out by the L1 trigger system with reduced precision in order to expedite data transfer rate. Due to the sheer volume of SMT data, the SMT is not read out for the L1 trigger. The list of L1 trigger term conditions (L1 script) are tested in each sub-detector trigger system separately.

The Level 1 calorimeter trigger (L1CAL) examines the E_T deposition pattern in the towers (see Section 3.3.3). The energy in each tower is determined with 4 coarse ranges: 3–5 GeV, 5–7 GeV, 7–10 GeV and $>$ 10 GeV. Trigger terms are formed by counting the number of towers with total energy exceeding one of a set of preprogrammed thresholds. For example, one could require three towers with total energy above 5 GeV or one tower with a total energy of 10 GeV. The energy in the electromagnetic layers are compared to a separate set of thresholds.

The central track trigger (L1CTT) searches the CFT for tracks exceeding predefined p_{T} thresholds by look up using a set of predefined CFT hit patterns (a.k.a. road) in $r-\phi$ plane. The track p_{T} is determined in 4 coarse p_{T} ranges: 1.5–3 GeV, 3–5 GeV, 5–10 GeV and $>$ 10 GeV. Isolated tracks are identified as well as tracks with matching CPS hits. The shower layer of the FPS is also searched for clusters with and without matching MIP layer hits. Trigger terms are formed by requiring u- and v- layer clusters in the same quadrant, but no attempts are made to match them with finer resolution.

The Level 1 muon trigger (L1Muon) functions similarly to the CTT by comparing hits in the detector to preloaded roads to build muon objects. The hit information in the wire chambers is used to form track stubs which are then used to confirm scintillator hits in each layer. Triggers are formed by matching confirmed scintillator hits between layers. In addition, tracks from the L1CTT are matched to hits in the muon scintillator system, thus provides a coarse muon p_{T} measurement. Backgrounds from cosmic rays and spurious hits due to the radioactive environment are rejected by requiring that the timing of the hits be consistent with muons originating from a beam crossing.

The L1 forward proton detector trigger (L1FPD) is used to select diffractively-produced events by triggering on protons or anti-protons scattered at very small angles.

4.1.2 Level 2 Trigger System

Due to the reduced input event rate from L1, the L2 trigger system has enough time to refines the output from Level 1 and forms simple physics objects (tracks, energy clusters, etc.) using some preprocessors for each detector sub-system. The preprocessor subsystems include tracking, preshower, calorimeter, and muon systems.

These preprocessors are also implemented in special hardware. The calorimeter preprocessor (L2CAL) collects information from all the L1 trigger towers and uses that to build simple jet and electron candidates with the help of clustering algorithms. The L2CTT sorts the list of L1CTT tracks according to transverse momentum. The L2 muon trigger improves muon identification by combining wire and scintillator hits to form muon objects with track quality and transverse momentum information. The preprocessors then pass the above information on to a L2 global processor (L2Global) for L2 trigger test.

L2Global is implemented with software programs running in a β computer. It only checks the L2 part of the triggers of which the L1 part have been fired. The software programs include physics object tool/worker and trigger filter. The tool and worker programs can combine and correlates physics objects from the different L2 preprocessors, for example a charged track in tracking preprocessor can be correlated with a EM object in calorimeter preprocessor, thus the better p_{T} measurement in the tracking system can be used to trigger on the EM object. The filter program tests the trigger terms in the L2 script. L2Global decision is then sent to the TFW to form the trigger decision.

The L2 Silicon Track Trigger (STT) is a new L2 trigger system [48]. It is designed to utilize the SMT hit information so that better triggers on charged particle tracks can be obtained at earlier trigger stage than L3. The STT matches the SMT hits to the L1CTT tracks and perform a track fit, as shown in Figure 4.3. Much higher precision on the charged particle track parameters can be achieve at L2, as shown in Figure 4.4. More importantly it provides the track impact parameter which can be used to trigger on the heavy flavor jets. This is very useful in selecting events for many DØ physics studies, such as the searches for the Higgs boson and new physics beyond the Standard Model .

4.1.3 Trigger Frame Work

The TFW controls trigger configuration, trigger system management and the L1/L2 trigger decision making. It receives the output trigger terms (bits) of the L1 and L2 trigger system and combines these terms using a series of logic and/or operation (and/or terms, AOT) that are predefined in a list of triggers. The logic computations are implemented using Field Programmable Gate Array (FPGA) codes that run in the TFW crate. The results of all the trigger AOT tests are OR-ed together to decide whether the event passes at least one of the trigger and should be send to L3. The TFW also has a number of scalars that are used to count the trigger rates for luminosity determination. The TFW supports up to 256 (L1) triggers.

The TFW itself is programmed and controlled by the Trigger Control Computer (TCC). TCC receives high-level programming requests from the COOR and implements the requests by programming the TFW hardware. The trigger configuration,

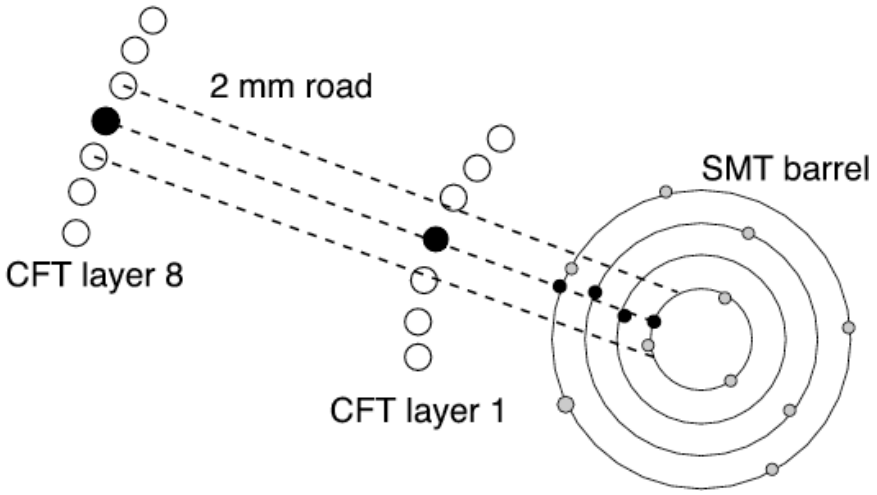

Figure 4.3: STT fitting algorithm. For each event accepted by L1, the L1CTT track informations and SMT readouts are sent to the STT. A 2 mm wide road is defined around each L1CTT track, and the SMT hits within that road are associated with the track. Only hits in the axial strips of the silicon ladders are used for this purpose. Hits in the innermost and outermost CFT layers are used along with hits in at least three of the four layers of the SMT (for Run II b, an additional layer of SMT is installed, called layer-0, the STT also uses layer-0 information and requires at least 4-layers of SMT hits for a track) to fit the track parameters. The track equation is $\phi(r) = b/r + \kappa r + \phi_0$, where b (impact parameter), κ (track curvature) and ϕ_0 are the fitted track parameters. The results of the track fit are combined with L2CTT.

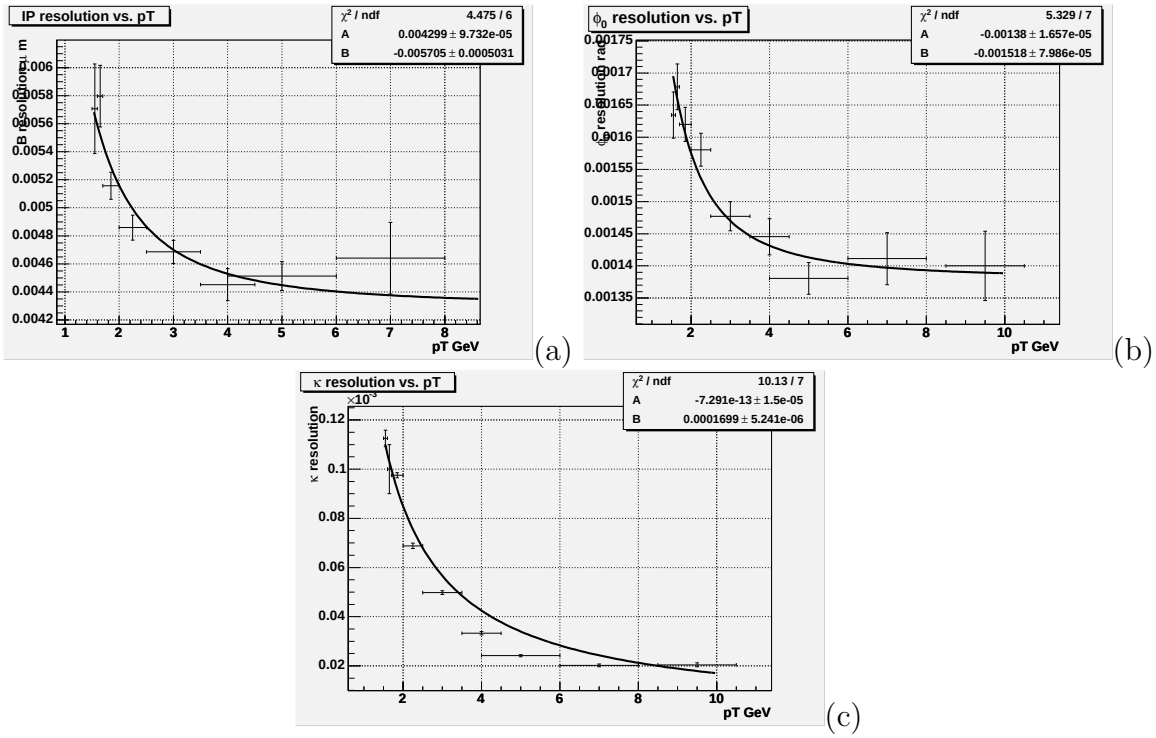

Figure 4.4: STT fitted track parameter resolutions as functions of track p_{T}. p_{T} is in GeV. The resolutions are fitted to function $\sigma^2 = A^2 + B^2/pT^2$. (a) IP b in μm; (b) ϕ_0 in rad; (c) κ in GeV^{-1}.[49]

such as disabled triggers, trigger prescales, can be changed by COOR at anytime. A sketch of the TFW and TCC is shown in Figure 4.5.

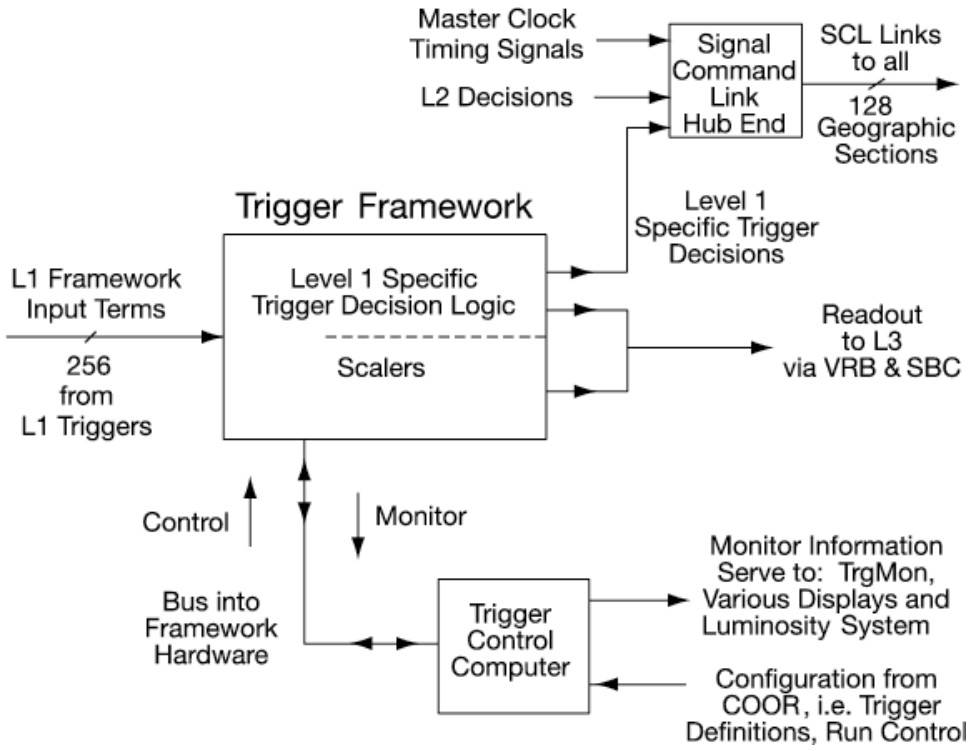

Figure 4.5: A sketch of the DØ trigger frame work. The TFW controls the L1 and L2 trigger decisions and data pipelines. It sends commands to and receive status messages from each component of the L1/L2 trigger systems via a two way serial command line (SCL).

4.1.4 Level 3 DAQ and Trigger System

Upon receipt of the L1 and L2 acceptance from the TFW, the detector data and trigger information from the L1/L2/TFW systems that are buffered in VME readout crates are read by a single board computer (SBC) in each crate. The data is sent to one or more farm nodes specified by routing instructions received from the routing master (RM). These farm nodes run two different programs: an event builder (EVB) and an event filter (the L3 Trigger, provided by COOR). The EVB selectively reconstructs the event based on which L1 and L2 trigger requirements have been satisfied. Complete events are kept in buffers for processing by the filtering processes. The event filter makes its decisions based on complete physics objects (including electron, jet, muon,

missing transverse energy, track, vertex, etc) as well as on the relationships between such objects (such as the separation ΔR in the $\eta - \phi$ plane between physics objects or the invariant mass of multiple objects). Like the L2Global, the L3 filters test the L3 script for the triggers which have fired L2 trigger terms. If an event passed an L3 filter, it is transmitted to an online host computer, which buffers the event on disk where it can be examined for the purposes of data quality monitoring. Finally, the event is saved on data storage tapes for later reconstruction. Figure 4.6 shows the above flow of information and data through the L3DAQ system.

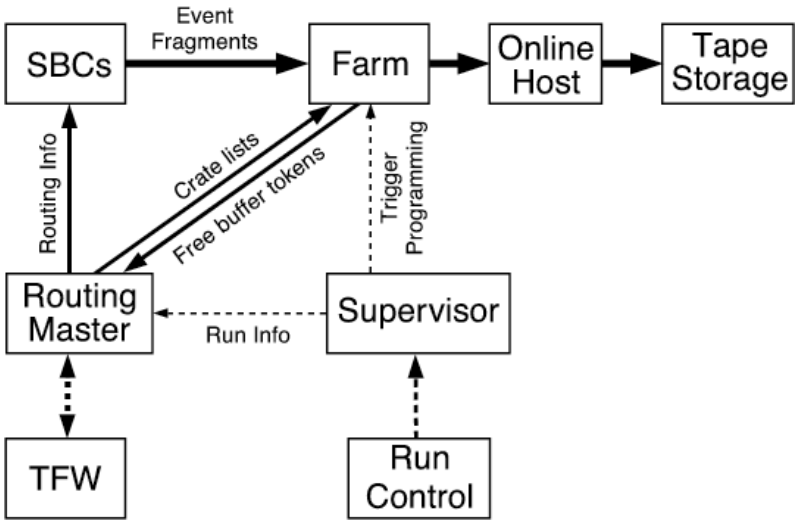

Figure 4.6: The DØ L3 DAQ and trigger system.

4.2 Luminosity

A precise luminosity measurement is important for physics analyses that involves absolute cross section determination, such as the one in this dissertation. Eq. 3.1 gives the Tevatron operating instantaneous luminosity, but it does not represent the luminosity delivered at DØ, because the crossing $p\bar{p}$ bunches vary at the different collision points, thus the bunch structure parameters. For example, at DØ the first bunch crossing is the colliding of the 1st p bunch with the 13th $\bar{p}$ bunch (the second bunch crossing is between the 2nd p with the 14th $\bar{p}$, and so on for the 36 bunch crossings in one resolution), while at CDF the first bunch crossing is between the 1st p bunch and the 25th $\bar{p}$ bunch. So it is not surprising that there may be some difference in the luminosity measurements between DØ and CDF. With the improved Tevatron $\bar{p}$ bunch uniformity, this difference is greatly reduced. At DØ , the luminosity detector (LM) is used to measure the delivered instantaneous luminosity directly.

4.2.1 Delivered Luminosity

The LM monitors a specific production process which has a known cross section, for example the inclusive inelastic process $p\bar{p} \rightarrow X$ where X stands for everything except for the $p\bar{p}$. When a $p\bar{p}$ bunch crossing results in such a event at the interaction region of the DØ, the products of the event will fire the scintillation counters at both ends within a few nanoseconds to produce a coincident signal. The LM does not discriminate single or multiple interactions, it just sends the coincident signals to a set of 159 scalers for each of the 159 tick intervals in a full bunch revolution. The number of the coincident signals are counted by these scalers.

Suppose the average number of interactions produced by each $p\bar{p}$ bunch crossing is μ. For example, we consider the first bunch crossing at DØ, then the number of interactions n per crossing follows a Poisson distribution, as shown in Figure 4.7. The probability of having n interactions is:

$$P(n) = \frac{\mu^n}{n!} e^{-\mu} \tag{4.1}$$

The probability of no interaction is $P(0) = e^{-\mu}$, thus the probability of getting LM coincident signals for the first bunch crossing in one full revolution is

$$P(n > 0) = 1 - P(0) = 1 - e^{-\mu} \tag{4.2}$$

Solving for μ from Eq. 4.2:

$$\mu = -\ln\left(1 - P(n > 0)\right) \tag{4.3}$$

μ times the revolution frequency $f = 47.7$ kHz is the event rate dN/dt of the monitored process produced by the first bunch crossing. dN/dt can also be written as the product of the instantaneous luminosity $\mathcal{L}$ times the process cross section σ, thus the $\mathcal{L}$ can be solved as:

$$\mathcal{L} = -\frac{f}{\sigma} \ln(1 - P(n > 0)) = -\frac{f}{\sigma} \ln(1 - \frac{\Delta^1_{LM}}{\Delta^1_{tick}}) \tag{4.4}$$

the second equation is because $P(n > 0)$ equals to the ratio of Δ^1_{LM}, the counted number of the LM coincident signals for the first bunch crossing in sampling time, to Δ^1_{tick}, the total number of the first bunch crossing. The sampling time is called a luminosity block. Each luminosity block is indexed by a 32 bit integer in DØ Run II. The luminosity block number (LBN) is monotonically incremented by one when the following happens:

- Upon request from TFW, COOR or Luminosity DAQ,

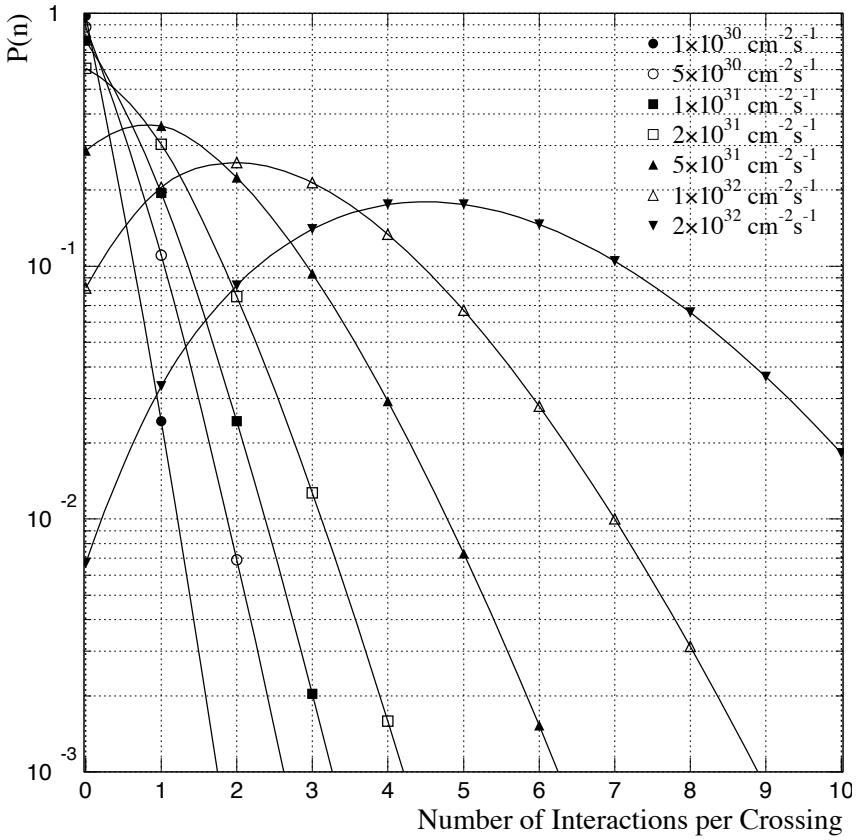

Figure 4.7: The Poisson distributions of the number of inclusive inelastic $p\bar{p} \rightarrow X$ event per crossing for different luminosities [34].

- TFW SCL initialization issued,
- Serial Command Link init issued,
- A store begin or end,
- A run transition (start, end, pause, resume)
- An internal timer counts to a 60-second interval.

These condition guarantees that the data within one luminosity block is subjected to the same run conditions. The time span of the luminosity block is short enough to ensure the instantaneous luminosity is effectively a constant within a block, while long enough to reduce the statistical uncertainty of $\Delta^i_{LM}/\Delta^i_{tick}$.

Eq. 4.4 gives the instantaneous luminosity for the first bunch crossing in the first tick interval. Average the $\mathcal{L}$ over all the 159 tick intervals, we can get the delivered luminosity of at DØ :

$$\mathcal{L} = -\frac{f/159}{\sigma}\sum_{i=1}^{159}\ln(1-\frac{\Delta^i_{LM}}{\Delta_{tick}/159}) \tag{4.5}$$

where Δ_{tick} is the total number of tick intervals within a luminosity block.

Taking into account the LM detector inefficiency and geometric acceptance, the σ in Eq. 4.5 should be replaced by the effective cross section σ_{eff}, which is also called the luminosity constant:

$$\sigma_{eff} = (\epsilon_{SD}f_{SD} + \epsilon_{DD}f_{DD} + \epsilon_{ND}f_{ND})\sigma \tag{4.6}$$

where ϵ is the LM efficiency, the f is the geometric acceptance, SD, DD and ND stand for single diffractive, double diffractive and non-diffractive inelastic scattering processes, respectively[1]. The efficiencies and acceptances are determined from Monte Carlo simulation. The overall efficiency including the acceptance is measured to be $\epsilon = 0.792 \pm 0.02$, the $p\bar{p}$ inelastic cross section at $\sqrt{s} = 1.96$ TeV is meausred to be $\sigma = 60.7 \pm 2.4$ mb [44, 45, 46], thus $\sigma_{eff} = 48.0 \pm 2.6$ mb [47].

Another source of the LM correction is that an inelastic event may not fire both ends of the LM detector, while multiple events may fire both end of the LM at the same time. So $P(0)$ in Eq. 4.2 should be corrected as:

$$P(0) = e^{-\sigma_{eff}\mathcal{L}}(2e^{-\sigma_{SS}\mathcal{L}/2} - e^{-\sigma_{eff}\mathcal{L}}) \tag{4.7}$$

[1]Another kind of inelastic process is call double Pomeron exchange. Its acceptance is negligible at DØ [50].

where $\sigma_{SS} = 9.4\text{m}b$ is the effective cross section for single-sided LM coincident event. This correction introduces a luminosity dependence of the delivered $\mathcal{L}$ calculated by Eq. 4.5. But this effect is rather small, to the leading order we can ignore it.

4.2.2 Triggered Luminosity

A trigger has a dead time. That is, it operates in a sequence of states: enable, disable and readout. It is only ready to be exposed to the detector data at L1 when it is in the enable state. Different triggers normally have quite different dead time, and the dead time is generally luminosity dependent. Additionally some triggers may be restricted to specific ticks at L1. For example the jet triggers may only be allowed to fire on the first bunch of a superbunch in order to eliminate the energy pileup effect. So if we use the trigger system to reject unwanted events, we need to determine the luminosities that different triggers are exposed to. This trigger dependent luminosity is called the triggered luminosity [51].

The triggered luminosity is defined in the same way as delivered luminosity except that the data exposure percentage for the trigger needs to be plugged in Eq. 4.5. The nth trigger's exposed luminosity is:

$$\mathcal{L}_T(n) = -\frac{f/159}{\sigma_{eff}} \sum_{i=1}^{159} \frac{\Delta_T(n,i)}{\Delta_{tick}/159} \ln(1 - \frac{\Delta^i_{LM}}{\Delta_{tick}/159}) \tag{4.8}$$

where $\Delta_T(n,i)$ is the nth trigger's exposure at the ith tick.

If Eq. 4.8 is to be used to calculate the triggered luminosity for each trigger, the number of needed scalers is $159 \times 256 = 40,704$. This is impractical. To reduce the number of scalars, several triggers are required to have the same dead time and be grouped to use the same set of scalars. Each of this group is called the exposure group (EG). In fact at DØ, all the supported 256 L1 triggers are grouped into one EG. Within the EG, different triggers may have different sources of enable and disable, and data from one detector could be partitioned so that a different part of the detector can be read out by different trigger, so aside from the 159×8 scalers needed (the TFW supports up to 8 EG's at the same time) for the common EG, another set of 128 scalers are needed for each of the 256 L1 trigger to decorrelate the EG counts for each of the trigger. Using this method, the triggered luminosity for a trigger can be written as:

$$\mathcal{L}_T(n) = -\frac{f/159}{\sigma_{eff}} \frac{\Delta_{decor}(n)}{\Delta_{tick}} \sum_{i=1}^{159} \frac{\Delta_T(i)}{\Delta_{tick}/159} \ln(1 - \frac{\Delta^i_{LM}}{\Delta_{tick}/159}) \tag{4.9}$$

where $\Delta_T(i)$ is EG L1 exposure count for each of the 159 ticks, $\Delta_{decor}(n)$ is the total L1 exposure count of the nth trigger within a luminosity block. If a trigger includes a

prescale, that is, only a fraction of events passed the trigger are accepted, the prescale factor also needs to be put into Eq. 4.9. In this analysis, we use triggers that have no prescales.

4.2.3 Recorded Luminosity

As we have seen in Section 4.1 events that pass the trigger can still be lost due to saturation of the event buffers at any stage from the detector to the tape recorder. The delivered and triggered luminosity do not take this kind of inefficiency into account. In order to get the luminosity that was recorded, we need to find the efficiency of the DAQ system. This is achieved with two special triggers: zero biased (ZB) trigger and minimum biased (MB) trigger. All sets of DØ trigger lists contains these two triggers. The zero biased trigger does not trigger on anything but the tick signals. The minimum biased trigger does not trigger on anything but the coincident signals of the inelastic events in the LM. These two triggers should exist in all stages of a perfectly efficient DAQ system. Thus by counting the loss of these two triggers the inefficiency of the data channel in the DAQ system can be obtained. The delivered luminosity corrected for the inefficiency is called the recorded luminosity [52]:

$$\mathcal{L}_R(n) = \frac{\#\text{ of ZB Recorded} + \#\text{ of MB Recorded}}{\#\text{ of ZB Exposed to L1} + \#\text{ of MB Exposed to L1}}\mathcal{L}_T(n) \qquad (4.10)$$

where the prescales of the two triggers are taken into account.

4.2.4 Integrated Luminosity

The luminosities discussed above are the instantaneous luminosities. The integrated luminosity for a given data set is in principle the sum of the instantaneous luminosity times the luminosity block sampling time over all the luminosity block in that data. There is a special software package called *lm_access* [53] that does the offline integrated luminosity calculation for a given trigger and data set.

Aside from the various inefficiencies that are introduced by the trigger and the DAQ system discussed above, there are some other sources of inefficiencies when calculating the integrated luminosity:

- a data taking run may have some kind of detector hardware malfunctions or software bugs that were not caught online,
- a luminosity block may be marked as bad due to corrupted data that caused reconstruction software crashes in the online L3DAQ farmnodes and/or offline event reconstruction software.

The bad runs and bad luminosity blocks are input into *lm_access* and the package skips them when doing the sum for the lumonosity calculation.

When multiple triggers are chosen in an analysis,the integrated luminosity calculation is more complicated due to the correlations between the triggers. A way to calculate the integrated luminosity in this case is as the following:

- First an series of luminosity block subsets that contains only one of the chosen triggers can be obtained for each of the trigger, the integrated luminosity for each of the luminosity block subset can be obtained from *lm_access* by assuming the luminosity blocks in the complement of the subset are all " bad". The sum of all these luminosities covers the uncorrelated part of the multiple triggers.

- Then the luminosity blocks that contain all combinations of two of the triggers can be selected. The luminosities for these subsets can be calculated in the same way as above.

- Repeat the above procedure until all combinations of the triggers have been covered. The total sum is the final integrated luminosity for the chosen multiple triggers.

4.3 Muon Trigger Efficiency

The data taking inefficiencies discussed in Section 4.2 only include the detector, trigger and DAQ systems hardware inefficiencies that are caused by the limited data collecting and processing power. They do not take into account the intrinsic trigger efficiencies of the trigger decisions that are made according to the requirements on the properties and correlation of physics objects. These intrinsic trigger efficiencies (without confusion, they are commonly referred to as just the trigger efficiencies) are important when comparing the detector data with the Monte Carlo (MC) simulated data. While the hardware inefficiencies can be accounted for by simply normalizing the MC data to the integrated data luminosity, the procedures for MC to include the trigger efficiency is much more complicated. Generally there are two ways to apply the trigger efficiency to the MC data: either by using the trigger simulation (*TrigSim*) to apply the trigger efficiency implicitly, or measuring the efficiencies (equivalently the probabilities) of a single physics objects to satisfy the trigger term conditions and folding these probabilities into the MC data. Due to various reasons, *TrigSim* usually shows discrepancy between simulation and data, thus a correction factor is generally needed. In this analysis, the second way is chosen. The detailed procedure for the single muon trigger efficiencies is discussed in this section. A more generalized discussion can be found at [54, 55] and the references therein.

4.3.1 Single Muon Triggers

Since the Z boson signal is very clean, this analysis starts by selecting events with $Z \rightarrow \mu^+\mu^-$ signals. To maximize the integrated luminosity while keeping the luminostiy and the trigger efficiency calculations as simple as possible, only one single muon trigger (instead of the di-muon triggers or the combinations of muon triggers) was used to select the event data. The single muon triggers used are **MUW_W_L2M3_TRK10** or **MUH1_TRK10** depending on the trigger versions of the data taking runs. The L1/L2/L3 scripts of these single muon triggers and their meanings are listed below:

- **MUW_W_L2M3_TRK10**
  - *L1:* mu1ptxwtxx_fz_ncu
    Description: A region = w (wide muon region, defined by the muon group) single muon trigger with tight scintillator and loose wire requirements. No calorimeter unsuppressed readout.
  - *L2:* MUON(0, 3., 2, 0, 0, MUON (0, 0, 5, 0))
    Description: pass events with at least one muon found with $p_{\mathrm{T}} > 3$ GeV meeting MEDIUM quality(=2) requirements (no region requirement).
  - *L3:* mp1000_L3FTrack (PhysGlobalTracker, 1, 10., 1., 8, 0)
    Description: The trigger bit set to true if one track is found by the GlobalTracker tool with $p_{\mathrm{T}} > 10$ GeV. Additionally, one event in 1000 is recorded and marked as 'unbiased' (M&P).
- **MUH1_TRK10**
  - *L1:* mu1pt4wtxx_TTK(1, 10.)_ncu.
    Description: A wide region single muon trigger based on tight scintillator. Requiring one track with $p_{\mathrm{T}} > 10$ GeV. No calorimeter unsuppressed readout.
  - *L2:* None.
  - *L3:* mp2500_Track(PhTrk10_8, 1, 10., 1., 8)
    Description: The trigger bit set to true if one track is found by the GlobalTracker tool with $p_{\mathrm{T}} > 10$ GeV. M&P: 1 in 2500.

The numbers of detector events before and after the trigger selection are listed in Table 4.1.

	Total	$Z + 2j$	$Z + 2j$ 1 b-tag	$Z + 2j$ 2 b-tag
Before	108451	676	85	11
After	89266	545	64	10

Table 4.1: The number of events before and after requiring the single muon trigger.

4.3.2 Trigger Term Efficiency

The first step in determining the trigger efficiencies is to measure the efficiencies of a single physics object satisfying each of the relevant L1/L2/L3 trigger terms. In our case, the only physics object we consider is the muon, since high p_{T} particles that can punch through the calorimeter are almost 100% muons. The trigger terms that are relevant to muons are mu1ptxwtxx, mu1pt4wtxx_TTK(1, 10.), L2M3 and the muon-track match at the L3.

A so called "Tag–Probe" method is used to measure these trigger term efficiencies. First $Z \to \mu^+\mu^-$ events are selected. One of the muons, the tag, or the control muon, is required to have very tight requirements. The other muon, the probe, or the test muon, is then tested against each of the trigger term conditions. The probability that the test muon passes the condition equals the trigger term efficiency. The efficiency is generally parameterized as a function of p_{T} and η, ϕ of the muon. This algorithm is implemented in the *muo_cert* package [56]. In order not to bias the measured efficiency, no muon trigger is applied to the control data sample. In this analysis, the 1MULoose data skim is used. The measured efficiencies of L1/L2/L3 muon trigger terms, L3 tracking times muon-track matching, the loose muon ID and SMT hit are given as functions of various variables as shown in Figures 4.8–4.14.

4.3.3 Event Averaged Trigger Efficiency

By combining the muon trigger term efficiencies mentioned above, the muon trigger efficiency for a MC data sample can be calculated. The procedure is the following: First, for each muon in an MC event in the sample, the muon trigger term efficiencies are calculated using the *muo_cert* results. The product of a specific set of L1, L2 and L3 terms is the probability of the muon passing one of the muon triggers. In order to account for the difference in the different versions of triggers used in the detector data, the integrated luminosity weighted average of the probabilities a muon passing all those different versions of muon triggers are calculated. This weighted average are calculated for all the muons in this MC event. Then the probability that at least one of the muons passes the single muon trigger is calculated according to the formula in Appendix A. The event average of this probability for all the events in the MC sample is the desired trigger efficiency that will be applied to the MC events as an scale factor.

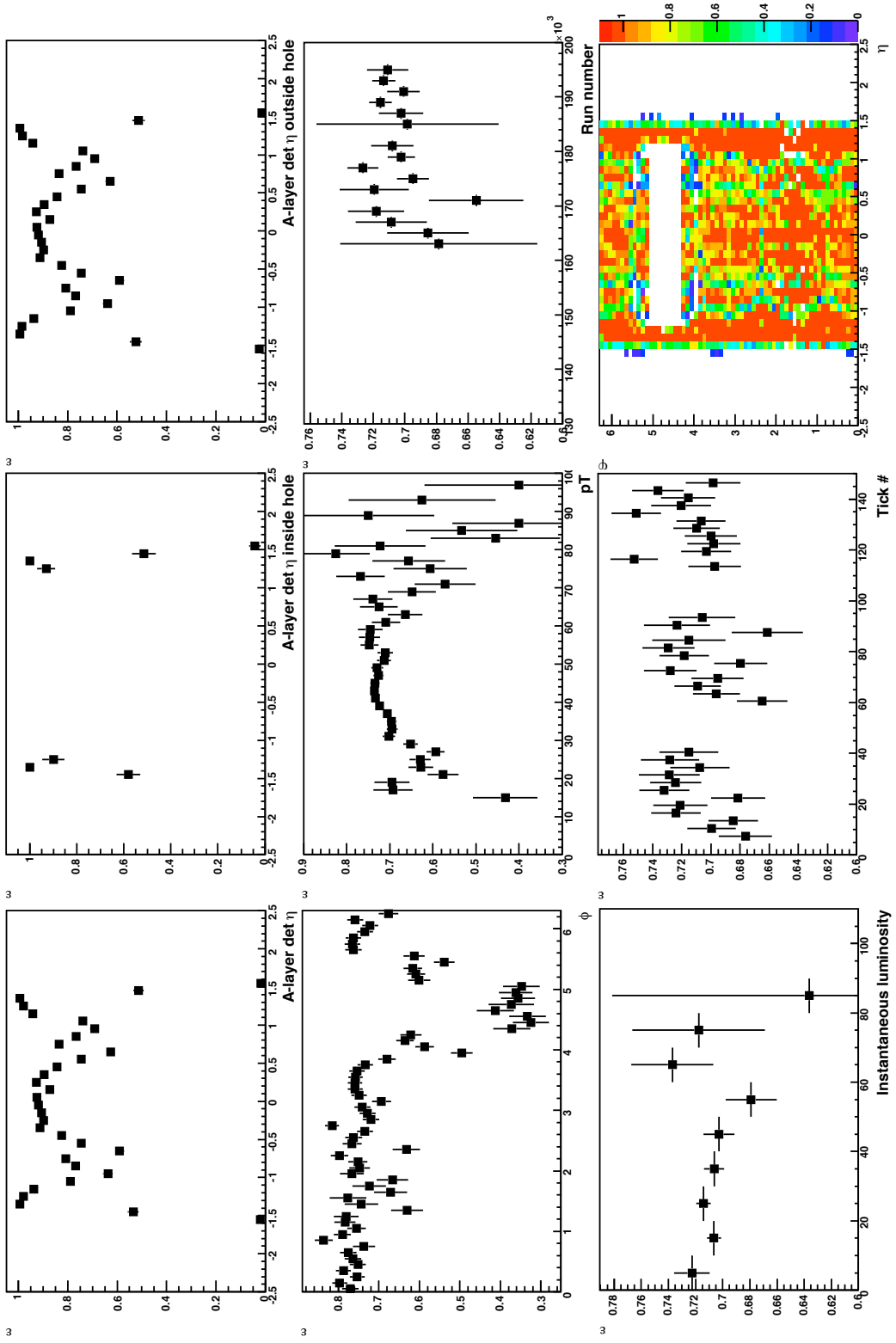

Figure 4.8: L1 muon trigger term mu1ptxwtxx efficiency as functions of muon kinematic variables and run configurations. 90

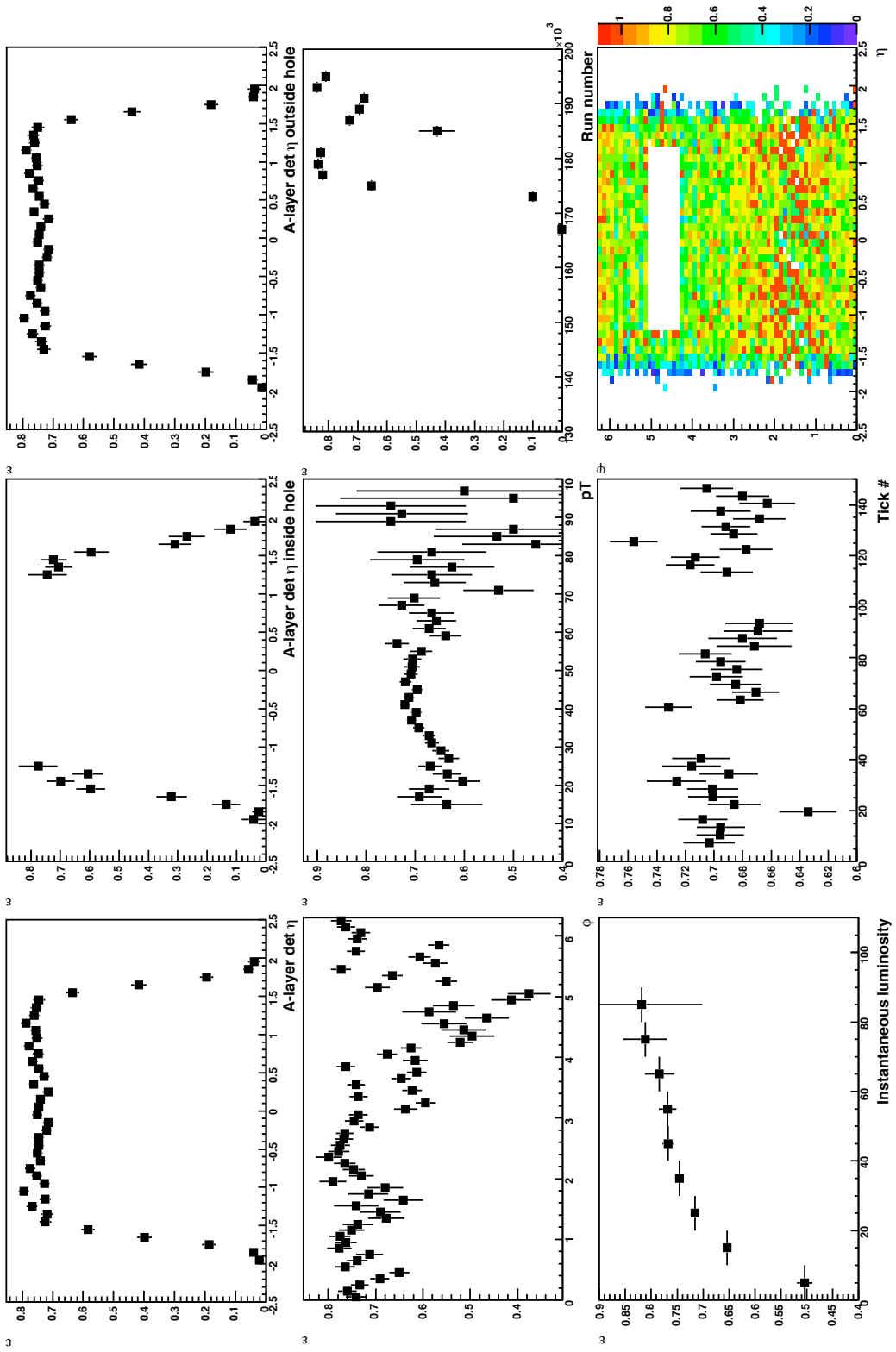

Figure 4.9: L1 muon trigger term mu1pt4wtxx_TTK(1, 10.) efficiencies as functions of muon kinematic variables and run configurations.

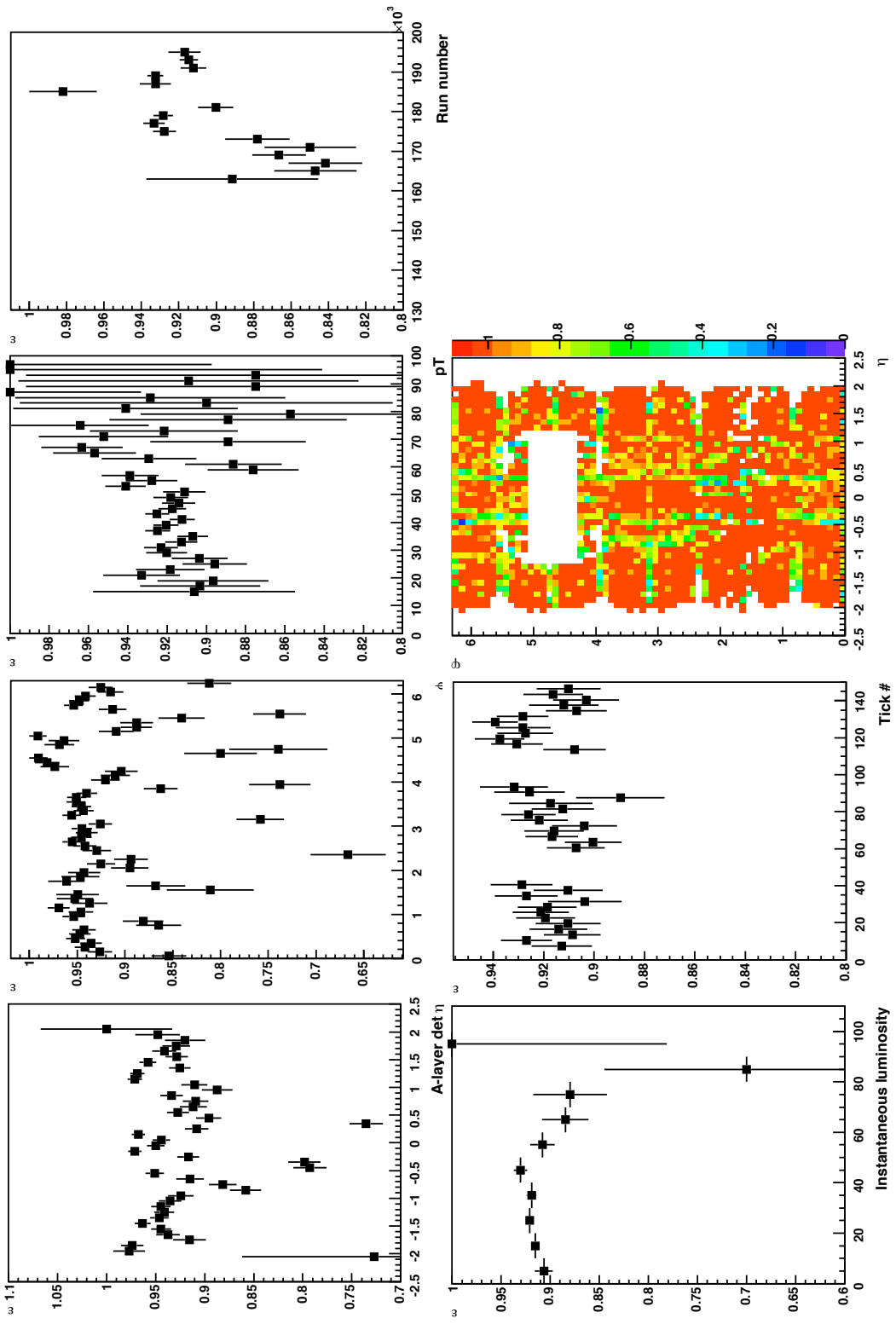

Figure 4.10: L2 muon trigger term L2M3 efficiencies as functions of muon kinematic variables and run configurations.

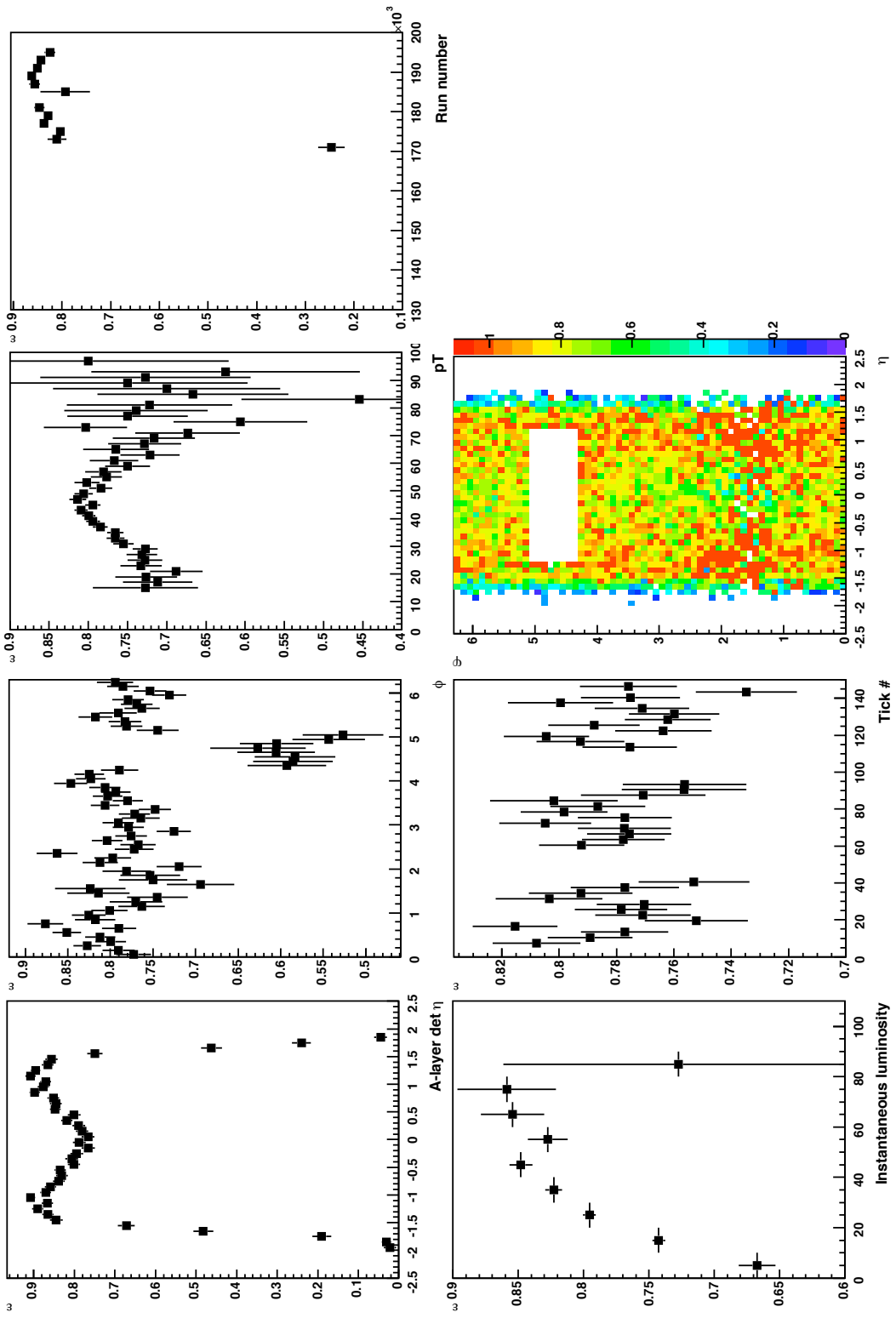

Figure 4.11: L3 muon trigger term L3TRK10 efficiencies as functions of muon kinematic variables and run configurations.

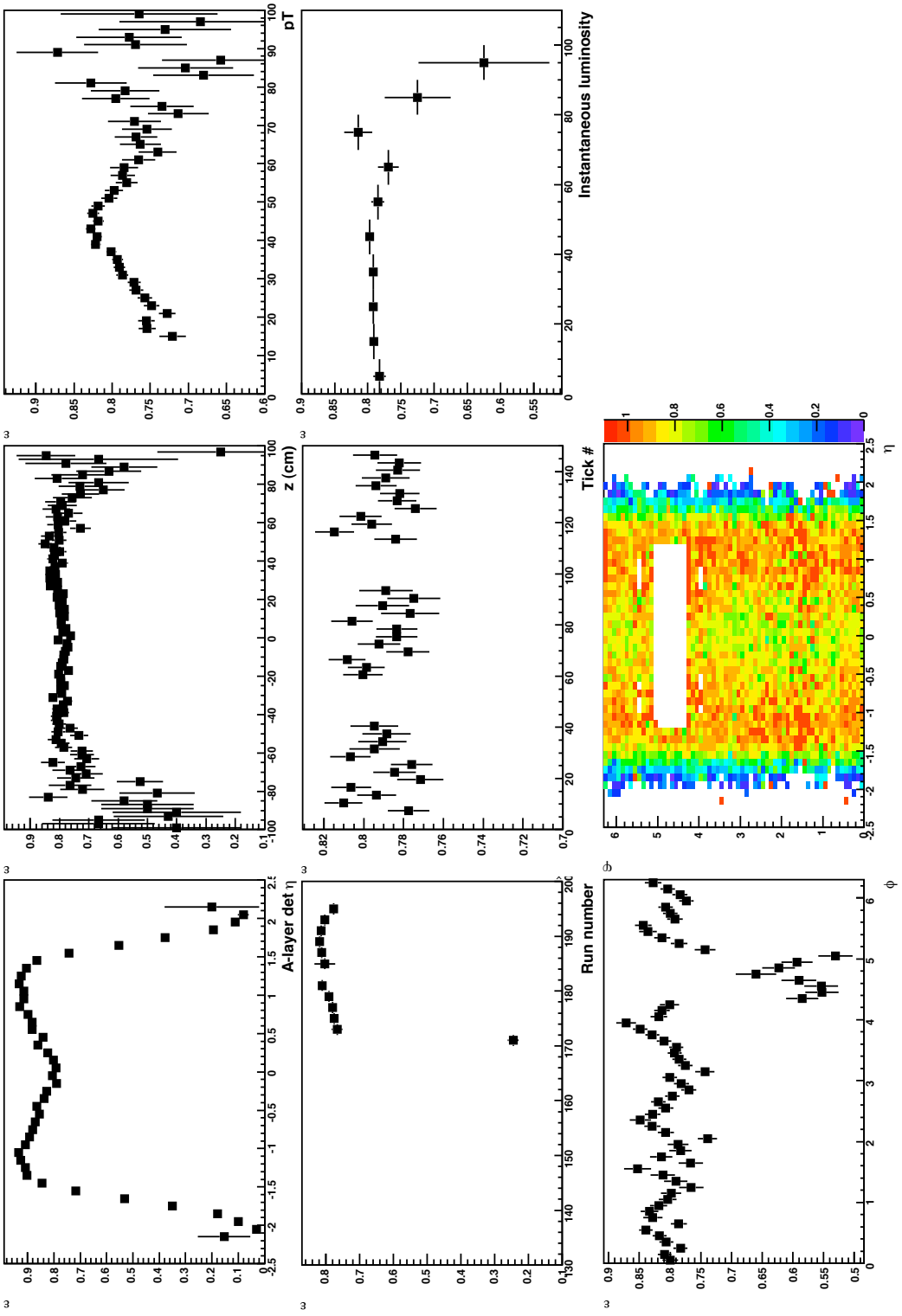

Figure 4.12: Muon L3 tracking and track matching efficiencies as functions of muon kinematic variables and run configurations.

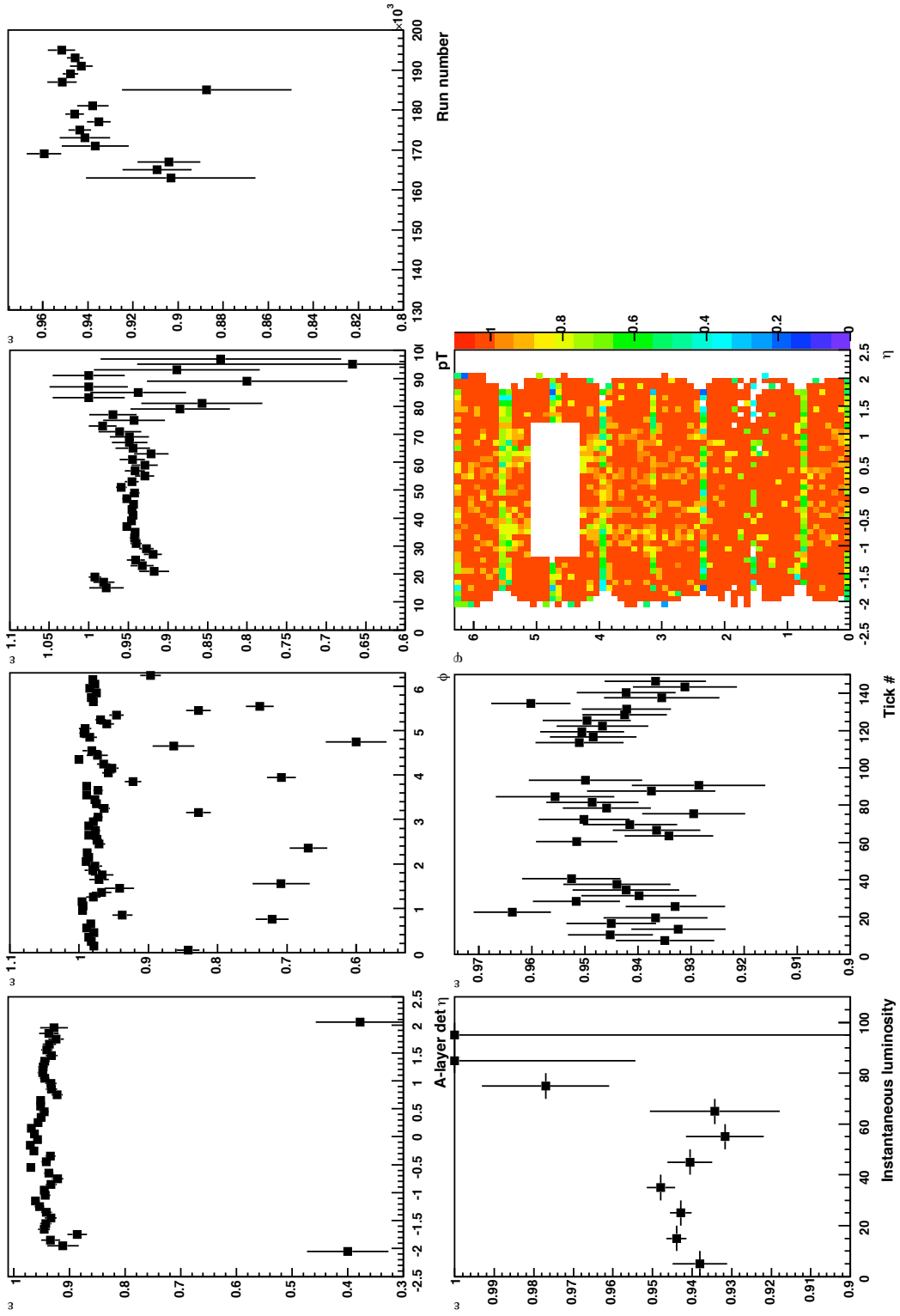

Figure 4.13: Muon RECO×ID efficiencies as functions of muon kinematic variables and run configurations.

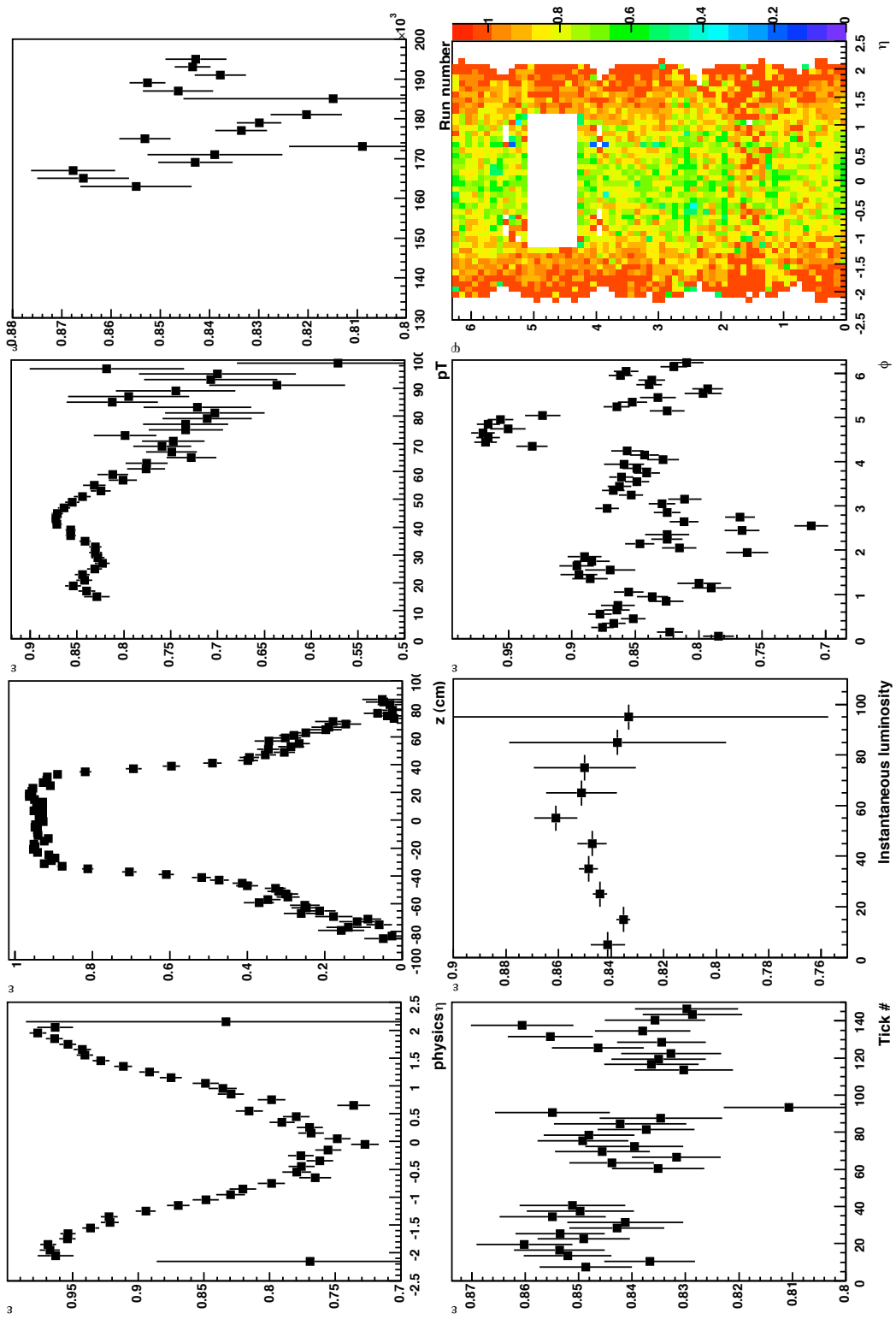

Figure 4.14: Muon SMT hit efficiencies as functions of muon kinematic variables and run configurations.

Chapter 5

Offline Event Reconstruction

The raw detector data collected by the DAQ systems (or created from the MC simulations) consist mainly of the digitized signals collected in each individual detector unit and the preliminary information of physics processes produced in the trigger systems. One can hardly make much physics meaning out of the raw data itself. To study fully these recorded physics processes, an offline reconstruction program, DØ RECO, is developed to process the raw data. It applies calibration information to each detector's read out data and applies thresholds to the signals. Within each detector system proto-physics quantities are calculated. For examples, tracks are found and EM energy clusters are built from calorimeter. It then correlates the information from different detectors to reconstruct the physics objects such as electrons, muons, jets and interaction points and forms an event that reflects what really happened in the detector. Finally, physics level correlations and calibrations are applied. DØ RECO runs on the offline production computer farm. The results are placed into the central data storage system (SAM) in the form of a custom-designed data structure, the event data model (EDM), for further analyses. The EDM stores the event information in blocks called chunks. The raw data, as the input to DØ RECO, is stored in the raw data chunk (RDC) which may be retained after DØ RECO for future studies. The output from DØ RECO fills many additional chunks associated with each type of reconstructed object, such as charged particle, muon, jet, *etc.*

DØ RECO reconstructs events in four steps. The first step is raw data unpacking. Detector unpackers decode the raw data of each detector electronics channel into meaningful signals in detector elements using physics coordinates. The second step is hit/cluster generation. Detector specific calibration constants are applied to the decoded detector signals in order to reduce the background noises. Adjacent signals above threshold in each detector element are then used to form clusters (in the calorimeter and preshower detectors) or hits (in the tracking detectors). In the third step, the most basic event geometric information, such as the global charged particle tracks and the vertices of the interaction, are reconstructed using the hits information

in the tracking systems (CFT and SMT). The final step involves the identification of various fundamental physics objects, such as electrons, photons, muons, jets and neutrinos. In this chapter, we will focus on the reconstruction of the global tracks, vertices, jets and muons. A description of EM object (electron and photon) and neutrino (corresponding to the $\not\!\!E_{\rm T}$) reconstruction can be found in [57, 58].

5.1 Global Track Reconstruction

A major component of the results of $p\bar{p}$ collisions is long lived charged particles, such as electrons, muons and pions. Thus the reconstruction of the charged particle tracks provides fundamental information from a collision. Charged particles leave signals in the central tracking system. Combining the signals in SMT and CFT, the global tracks are obtained.

Signal (Analog-to-Digital count, or ADC) in each SMT silicon strip is corrected for gain and offset. Consecutive strips with corrected ADC values higher than a certain threshold form a cluster. The centroid of each cluster is the ADC weighted average of the strip position. A cluster in CFT is generated in the same way as in SMT, except that the centroid of the CFT cluster is the geometric middle point of the CFT cluster. Two track finding algorithms, namely the Histogramming Track Finder (HTF) and the Alternative Algorithm (AA), use these clusters to find the initial candidates of the global tracks, then track quality requirements are applied to further reduce the fake tracks as described below.

5.1.1 HTF Algorithm

As discussed in Section 4.1.2, a track in the $x-y$ plane is characterized by three parameters: the radius of curvature ρ, the impact parameter b, and the azimuthal angle ϕ_0. For the tracks produced in the $p\bar{p}$ collisions, $b \approx 0$. As shown in Figure 5.1, to the first order approximation we can assume all the tracks originate from the beam spot (the interaction vertex of the event is not determined yet up to this stage). So for each hit in the SMT or CFT, we draw a family of tracks through the hit and the beam spot. One of these tracks best represents the real track. Each of these tracks can be denoted by a point in the $\rho - \phi_0$ track parameter plane, thus the track family around the hit corresponds to a trajectory line in the $\rho - \phi_0$ plane. For all the hits from the real track, their trajectories in the $\rho - \phi_0$ plane intersect at the same point, thus a maximum is produced when filling these trajectories into a 2-D histogram in $\rho - \phi_0$ plane. After doing this for all the hits in the tracking system, all the local maxima in the $\rho - \phi_0$ plane can be regarded as the parameters of the possible track candidates. By finding the hits corresponding to each of the maxima, the hits belonging to the same track can be found. Combining the track hits and the

track parameters (ρ, ϕ_0), the impact parameter b of a track can also be determined.

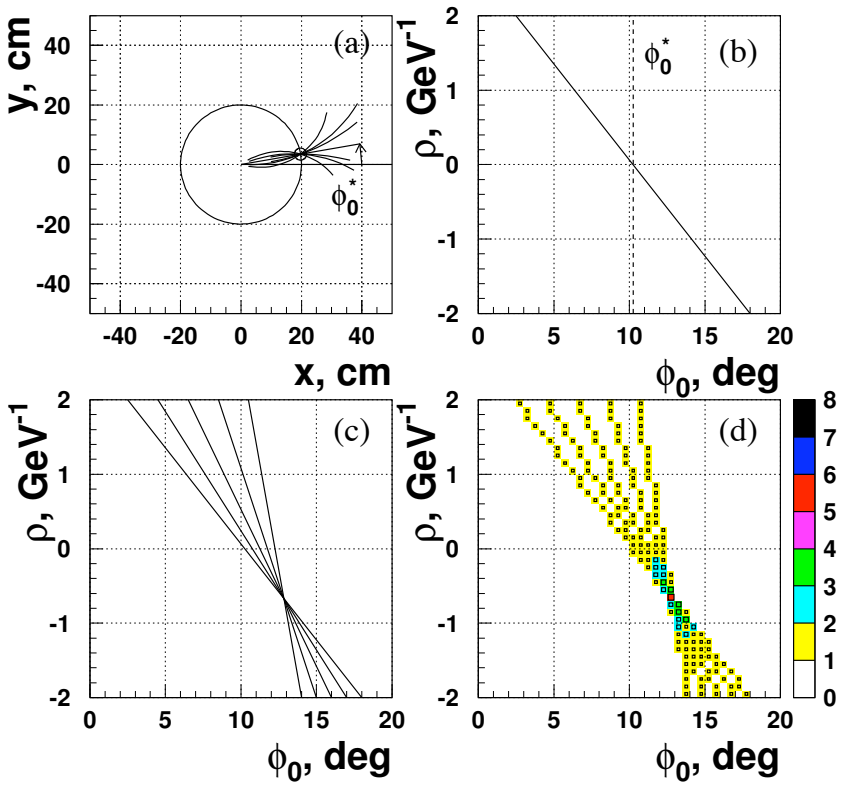

Figure 5.1: The Histrogramming Track Finder (HTF) Algorithm. (a) The family of the tracks through a hit. One of the tracks is the real track. (b) The parameter trajectory of the family of the tracks in the $\rho - \phi_0$ plane. (c) For each hit of the real track there is a family of the tracks. All of the parameter trajectories of these track families intersect at the same point in the $\rho - \phi_0$ plane. (d) The intersection is the maximum point in the 2-D histogram of the $\rho - \phi_0$ plane. Thus by finding the maximum the track parameters ρ and ϕ_0 of the true track are found, and consequently the impact parameter b can also be determined. [59]

The list of above 2-D track candidates is then passed to a 2-D Kalman filter [60] to filter on the track candidates. The 2-D Kalman filter uses the fitted track parameters of each track and an expectation propagator which takes into account the material effects (multiple scattering and energy loss) and the nonuniformity of the magnetic field. The remaining tracks pass through another histogramming algorithm which uses the hit (r, z) locations to form lines in (z_0, C) plane where z_0 is the starting location of the track along the z-axis and $C = dz/dr$. The maxima in the (z_0, C) plane generates a reduced list of track candidates. The list is processed through an η splitter which only allows hits moving away from the interaction point to be

associated with a track when the z component of the hits are increasing or decreasing for $\eta > 0$ or $\eta < 0$, respectively. A 3D Kalman filter is then used to further reduce the possible fake tracks.

5.1.2 AA Algorithm

The AA algorithm [61] builds track candidates starting from track segments that contain three SMT hits. The first hit of the segment may occur in any SMT barrel or F-disk. The second hit is selected by searching in a sector of $|\Delta\phi| < 0.08$ around the first hit in any SMT layer with greater radius. The third hit may be in any further SMT layer. The three track parameters of the segments containing these three hits are determined by a fit to a circle in the $x - y$ plane. The resulting track hypothesis is accepted if the radius of curvature $\rho \geq$ 30 cm (*ie.* $p_{\mathrm{T}} >$ 180 MeV) plus the fit $\chi^2 < 16$ and the beam spot DCA $<$ 2.5 cm.

The accepted track segment is used as a track seed to search for additional hits associated to it in the remaining SMT and CFT layers in order of increasing radius. A hit is considered to be associated with the track if the resulting track fit χ^2 is increased by less than 16 when the hit is included in the fitting. If multiple hits in the same layer are found to be associated with the same track candidate, the track hypothesis is split and each association is considered separately. The process stops for a given candidate once three contiguous missed hits occur (the dead and disabled channels are excluded) or all layers have been considered.

Due to the inefficiency and dead/disabled SMT channels, a track candidate may have less than three SMT hits to start with. Thus the tracking algorithm also considers tracks starting with CFT only clusters. In order to reduce the rate of fake track candidates, the track finding in this case begins after the reconstruction of the primary vertex of the event. The algorithm starts with clusters in the innermost layer of the CFT and continues to the outermost layer with the additional requirement that the impact parameter of the CFT track with respect to the reconstructed primary vertex is less than 1.5 cm. The CFT track candidate is then extrapolated into the SMT and any SMT clusters that can be associated with this track are kept.

5.1.3 Track Selection

The missing hit in a track is the primary tool to rule out the fake tracks and poorly reconstructed tracks from the track candidates of HTF and AA algorithms. Three types of misses are defined:

1. **Inside Misses.** Missed hits which that occur between the innermost and outermost hits on the track.

2. **Forward Misses.** Missed hits after the outermost hit on the track.

3. **Backward Misses.** Missed hits before the innermost hit on the track.

The forward and the backward misses are referred to as outside misses. A initial criteria to filter out the fake and/or bad tracks is:

- The track must have hits in at least four detector (SMT + CFT) layers, and each layer has hits in both the axial and stereo sub-layers.
- There may not be more than three inside misses.
- The total number of outside misses may not be greater than six.
- The track may have at most two inside misses in the SMT.
- The total number of hits must be at least five times the number of misses.
- For tracks with inside misses:
  - The total of the inside and forward misses must be less than five.
  - The total of the inside and backward misses must not be greater than three.

The remaining track candidates are sorted by the number of hits (in decreasing order), the number of misses (in increasing order) and the fit χ^2 (in increasing order).

The next tool to further filter out the fake tracks due to the combinatoric ambiguities is the shared hit. Two or more tracks are allowed to share the same clusters but the either one of the following two criteria has to be satisfied:

- $N_{shared} \leq \frac{2}{3} N_{total}$.
- $N_{shared} \leq \frac{1}{5} N_{total}$ and $N_{total} - N_{shared} > 3$

where N_{total} is the total number of axial hits on the track being examined, and N_{shared} is the number of such hits that are shared with track candidates preceding the track examined in the sorted track candidate list.

The remaining tracks are grouped together in the following way to form vertices: vertices are required to have at least five tracks with fit $\chi^2 < 36$, then the track candidates are filtered, refitted and sorted again, and for a track that is consistent with one of the vertices two artificial unshared hits are assigned to it. The procedures are repeated until the track candidate list is stable.

A typical track multiplicity distribution is shown in Figure 5.2, the data sample used in the plot is the 2MuHighPt data skim. Due to the large number of tracks in an event, the track reconstruction is the most time consuming process of the whole DØ RECO program.

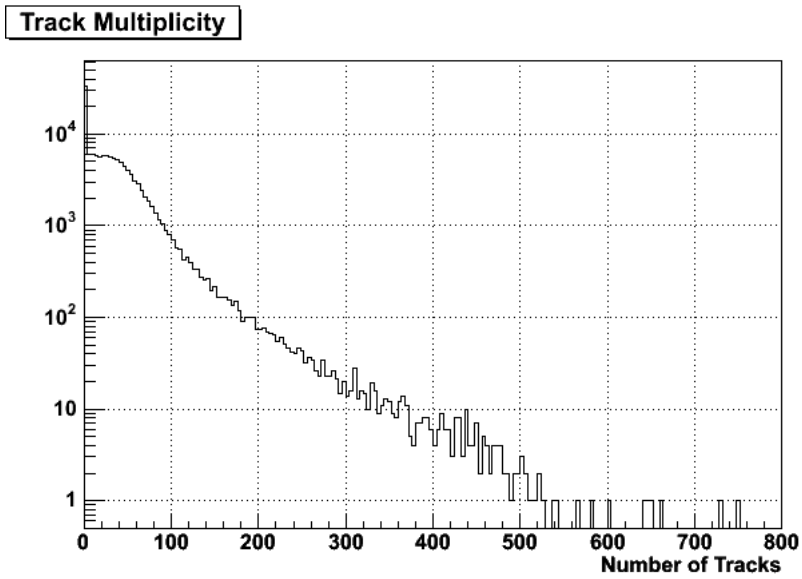

Figure 5.2: Reconstucted Track Multiplicity distribution for 2MuHighPt data skim.

5.1.4 Track p_{T} Resolution

The momentum resolution of the central tracking system has been improved through a re-alignment of the CFT and SMT. The track momentum resolution for data can be studied with the $Z \rightarrow \mu^+\mu^-$ or $J/\Psi \rightarrow \mu^+\mu^-$ events. The p_{T} of the two muons in the final state should be balanced. The distribution of the asymmetry

$$\mathcal{A} = \frac{p_{\mathrm{T}1} - p_{\mathrm{T}2}}{p_{\mathrm{T}1} + p_{\mathrm{T}2}} \tag{5.1}$$

thus can be fitted to a normal distribution. The RMS $\sigma_{\mathcal{A}}$ of this distribution is related to the relative muon (central track) momentum resolution (equal to the global track momentum resolution, see Section 5.4.1): $\sigma p_{\mathrm{T}}/p_{\mathrm{T}}$:

$$\frac{\sigma p_{\mathrm{T}}}{p_{\mathrm{T}}} = \sqrt{2}\sigma_{\mathcal{A}} \tag{5.2}$$

The resulting momentum resolution for Monte Carlo RECO-ed tracks is shown in Figure 5.3.

5.2 Vertex Reconstruction

The vertex is the $p\bar{p}$ collision point of an event. As discussed in Section 4.2.1, there could be several inelastic interactions in each $p\bar{p}$ bunch crossing, so there are usually

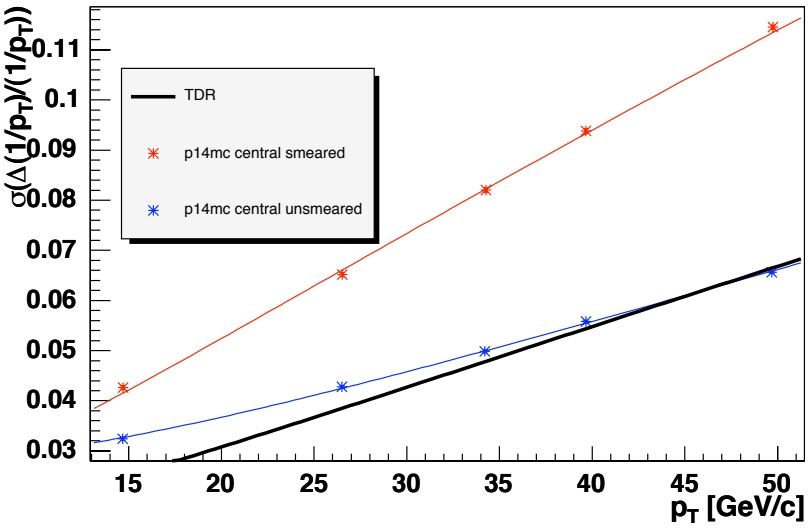

Figure 5.3: Global track p_{T}resolution obtained from the p14 MC muon samples. The plot shows the unsmeared muon with central track match, smeared muon with central track muon and the central track momentum resolution from the technical design report [81]. Refer to Section 6.2.2 for the detail of the muon smearing.

multiple vertices in an event, most of which are minimum bias (MinBias) interactions. Due to the (L1) trigger selection, most of the time only interactions with at least one hard scattering (inelastic colliding events that are characteristics of large transverse momentum transfer) are recorded. The vertex of the hard inelastic scattering is called the primary vertex (PV). The PV is the starting point in determining many physics quantities. The chance that more than one $p\bar{p}$ hard scattering occurs in an event is much smaller than the MinBias event probability, so the chance of multiple hard scattering occuring in an event is greatly reduced compared to that of multiple MinBias vertices. Besides the possible multiple PV from the $p\bar{p}$, decays of moderately long-lived ($\sim 10^{-12}$ s, usually corresponding to weak interactions) particles produced at the hard scattering PV can also generate a series of vertices displaced from the PV. These vertices are called the secondary vertices. A distribution of the number of primary vertices in an event is shown in Figure 5.4, the data sample used in the plot is the 2MuHighPt data skim.

The vertex reconstruction algorithm determines the vertex candidates in two passes based on the reconstructed global tracks. In the first pass, vertex candidates are built from tracks that satisfy loose selection requirements:

- $p_{\mathrm{T}} \geq 0.5$ GeV,

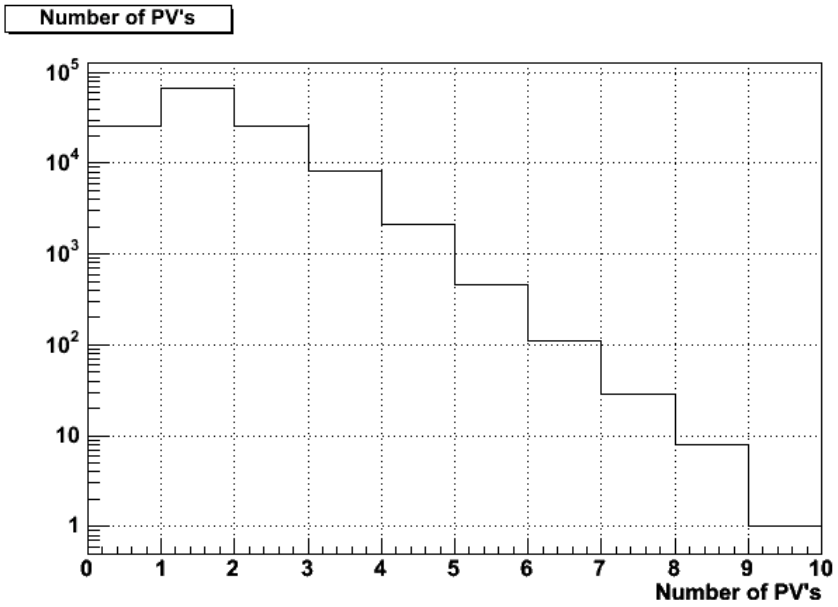

Figure 5.4: Reconstructed number of primary vertices in an event for 2MuHighPt data skim. The distribution follows a power law, as one would expect with a naive perturbation argument. The first bin represents the events without a PV, this is due to the various inefficiencies in the detector and the global track RECO.

- number of SMT hits ≥ 2,[1]
- DCA significance $DCA/\sigma_{DCA} \leq 100$,

where the track DCA and its uncertainty σ_{DCA} are measured with respect to the detector origin. The selected tracks are fit to a common vertex position with the Kalman filter algorithm. If the resulting χ^2 is greater than 10, then the track with the largest contribution is removed. This process is repeated until the fit χ^2 is less than 10. The algorithm then iterates over the excluded tracks to identify additional vertices. In this way, a preliminary list of vertex candidates is generated. In the second pass, the preliminary vertex positions are used to determine the location of the beam spot. The first stage algorithm is applied again, except that the input tracks are required to have $DCA/\sigma_{DCA} < 3$, now measured with respect to the beam spot position [2].

The PV is selected from the set of all found vertices based on the fact that tracks from the MinBias interactions have smaller transverse momenta p_{T} than tracks from the hard scatter interactions. The probability $P(p_{\mathrm{T}})$ of a track to come from a minimum bias vertex is defined as:

$$P(p_{\mathrm{T}}) = \frac{\int_{\log_{10} p_{\mathrm{T}}}^{\infty} F(x)dx}{\int_{\log_{10} 0.5}^{\infty} F(x)dx} \tag{5.3}$$

where F(x) is the $\log_{10} p_{\mathrm{T}}$ distribution of tracks from simulated MinBias events shown in Figure 5.5(a).

For each vertex, the product Π of the single track probabilities $P(p_{\mathrm{T}})$ of all its associated tracks are used to construct a probability that is independent of the number of tracks N [62]:

$$\mathcal{P} = \Pi \sum_{k=0}^{N} \frac{(-\ln \Pi)^k}{k!} \tag{5.4}$$

$\mathcal{P}$ is the probability for a vertex to originate from a minimum bias interaction. The vertex with the lowest minimum bias probability is chosen as the hard scatter PV as shown in Figure 5.5(b).

A distribution of the track multiplicity of a vertex is shown in Figure 5.6. The data sample used in the plot is the 2MuHighPt data skim.

The efficiency of the vertex reconstruction is about 100% in the central $|z|$ region and drops quickly outside the SMT fiducial volume ($|z| < 36$ cm for the barrel) due to the requirement of two SMT hits per track in forming the vertices. In the

[1] This requirement is not applied when using MC samples.

[2] The tracks that have $DCA/\sigma_{DCA} > 3$ are used to form the secondary vertices since large DCA significance implies decays of the long lived particles from the PV.

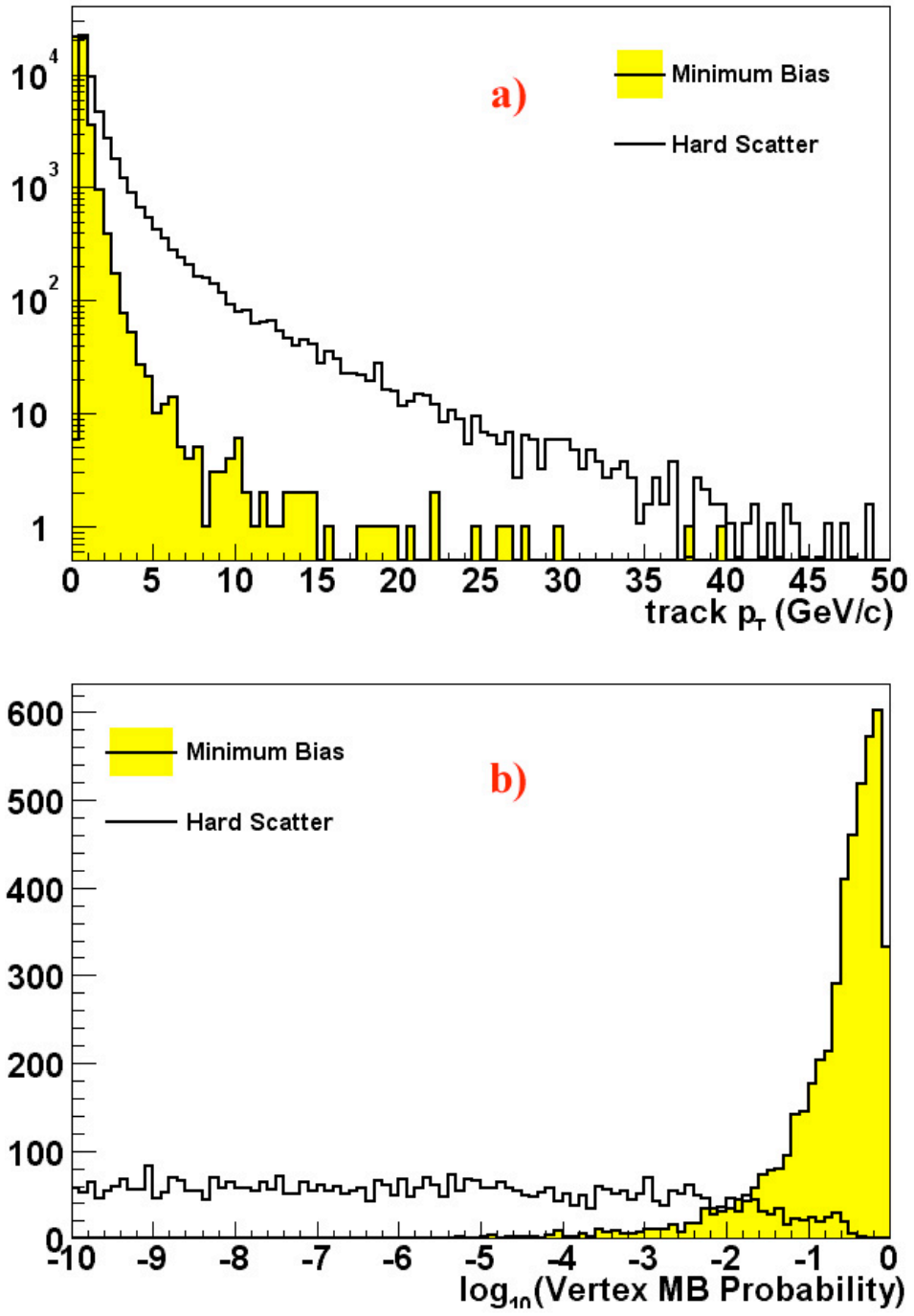

Figure 5.5: (a)p_{T}distributions of tracks that come from the hard-scatter vertex (dots) and the minimum bias interaction generated by MC (line). (b)The distribution above is used to create a probability $\mathcal{P}$ that describes the probability of a vertex to be a minimum bias vertex. The flat distribution is for the MinBias events, the yellow one is for the hard-scattering vertices [62, 63].

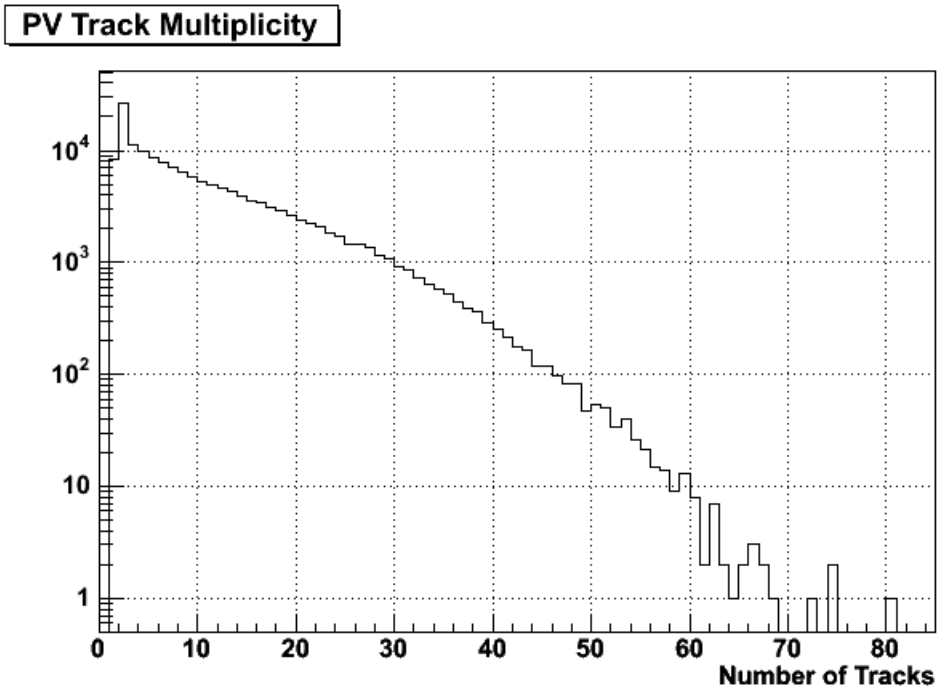

Figure 5.6: Reconstructed vertex track multiplicity distribution for 2MuHighPt data skim.

transverse plane, the vertex resolution is dominated by the beam spot size and is about 36 μm [63]. [3]

5.3 Jet Reconstruction and ID

Due to color confinement, the quarks and gluons in the final state of the hard scattering (and its underlying events) hadronize into sprays of hadrons (π, K ...) before they reach the detector. These hadrons produce tracks in the central track system and showers in the calorimeter system. Showers of the hadronic particles that originate from the same partons appear as a cone of energy deposition in the calorimeter. The cone is called a jet, which is the manifestation of the final state parton. The object of jet reconstruction is to cluster the calorimeter energy cones to reflect the original final state partons and to measure the energy of these partons precisely.[4]

5.3.1 Calorimeter Noise

The calorimeter noise, generally defined as energy deposition not related to the hard interaction, needs to be treated before the reconstruction of jets. The noise can be classified as:

- **Hot noise.** Hot cells are related to detector problems (hardware failure, abnormal electronic noise), or to physics processes like backscattering of particles interacting in the beam pipe outside of the vertex interaction region into the calorimeter. Their energy is typically large ($>$ 1 GeV).

- **Warm noise.** Warm cells are due to pedestal subtraction problems or hardware deficiencies. The cell energy levels are typically lower, on the order of hundred of MeV. However, they might appear in great numbers in a definite region of the detector, creating so-called warm zones.

- **Normal noise.** Normal noise cells appear due to Gaussian electronic noises that survive the zero suppression (correction for the asymmetry of the pedestal distributions). They are at lower energies, typically below 4-5 σ_{ped}. σ_{ped} is RMS of the pedestal distribution which represents the CAL energy readout in the absence of beam, for EM layers $\sigma_{ped} \approx 25$ MeV, for the FH layers, $\sigma_{ped} \approx 40$ MeV. A typical number of cells containing such noise is between 1000 and 3000 per event.

[3] Due to the wider ($\sim$ 50 cm) vertice distribution along the z-axis, the $z-$resolution is not measured.

[4] EM object also produce jets in the calorimeter, the reconstruction of EM jet and their energy scale can be found in [57], in this dissertation we will focus on the hadronic jets.

An algorithm, T42, is introduced to reduce the normal noise [64, 65]. It is applied before reconstructing the calorimeter objects. For the T42 algorithm, an isolated cell is considered a noise cell and thus discarded if it is not signal-like. A cell is considered to be signal-like if its energy is positive (negative energy cells can originate from electronics noise and from pile-up which is baseline subtracted) and above a high threshold of $+4\sigma_{ped}$, or if its energy is above $+2.5\sigma_{ped}$ and the energy of a neighboring cell is above $+4\sigma_{ped}$. The acronym T42 stands for threshold $4\sigma_{ped}$ and $2\sigma_{ped}$.[5] The first electromagnetic layer (layer 1), and the layers 8, 9 and 10 of the intercryostat region are not considered by the algorithm; so all cells in those layers with positive energy are kept in the event, and are not used as neighbors. A detailed description of the current implementation of the T42 algorithm can be found in [66].

The ratio of rejected cells by T42 over the number of cells in the event ranges from 30% to 60%. In the central region of the calorimeter ($|\eta| < 3.2$), the fraction of cells rejected by T42 corresponds to the number of cells expected from noise between $2.5\sigma_{ped}$ and $4\sigma_{ped}$, assuming a Gaussian distribution[65]. This is a good indication that T42 is indeed reducing mainly noise cells. In the forward region, more cells than expected are rejected since cells from pile-up effects accumulate close to the beam-pipe; however, this has no influence on high p_{T} physics, which is the subject of the analysis presented here.

Some types of the hot and warm noise are "coherent noise", "missing crate", "noon noise" and "ring of fire". These noise are identified using dedicated algorithms, the events that contain any of these noises are rejected by *cal_daq_quality* package after the jet reconstruction [67].

5.3.2 Jet Reconstruction Algorithm

The first step of the jet reconstruction algorithm is to cluster the CAL energy deposits. The energy deposits are segmented into calorimeter towers with a size of 0.1×0.1 in $\eta - \phi$ plane. Cells in the coarse hadronic calorimeter, the end cap massless gap, or the end cap hadronic layer 16 or 17 are not considered due to the enhanced noise level in those regions. Cells with $E_{\mathrm{T}} < E_{cut}^{cell}$ are ignored to reduce the contamination from noisy cells according to the new anomalous deposit algorithm (NADA) [68]. Then, using the tower with the highest transverse energy E_{T} as a seed, CAL towers are formed into clusters of cones with the size of $R_{cluster} = 0.3$ in $\eta - \phi$ plane around the seeds. Only clusters with $E_{\mathrm{T}} > E_{cut}^{cube}$ are kept. The value of E_{cut}^{cell} and E_{cut}^{cube} depends on the cell energy [69], typical values of $E_{cut}^{cell} = 0.5$ GeV and $E_{cut}^{cube} = 1.0$ GeV.

[5] The current implementation corresponds to threshold $4\sigma_{ped}$ and $2.5\sigma_{ped}$.

The η, ϕ and E_{T} of a cluster is defined as:

$$\eta = \frac{\sum_i E_{\mathrm{T}}^i \eta^i}{\sum_i E_{\mathrm{T}}^i} \tag{5.5}$$

$$\phi = \frac{\sum_i E_{\mathrm{T}}^i \phi^i}{\sum_i E_{\mathrm{T}}^i} \tag{5.6}$$

$$E_{\mathrm{T}} = \sum_i E_{\mathrm{T}}^i = \sum_i E_{\mathrm{T}}^i \sin(\theta_i) \tag{5.7}$$

where i runs over all the towers in a cluster, and η, ϕ are measured with respect to the PV. These energy clusters are sorted by E_{T}.

The next step is to produce the initial jet candidates. As in the first step, starting from the CAL energy clusters with the highest E_{T} as jet candidate seeds, cones of size $R_{cone} = 0.5$ are formed [6]. The jet direction and E_{T} are estimated with Equations 5.5–5.7, where i in this case runs over the clusters. Around this jet direction, all energy deposits within a cone of size R_{cone} are accumulated, and a new direction of the jet is re-calculated, this step is iterated until the direction is stable.

Up to this stage the reconstructed jets are not stable with respect to the effects of infrared radiation, jet collinearity and seed ordering as shown in Figures 5.7–5.9, respectively. These problems arise from the use of threshold and seeds to define the initial jet candidates (proto-jets). Seedless algorithms exist that avoid these difficulties; however, they are too computationally intensive for practical use in hadron collider environments.

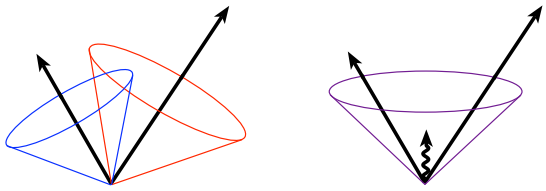

Figure 5.7: Example of infrared sensitivity to soft gluon radiation. On the left, two partons are reconstructed into two jets. On the right, an additional low energy gluon becomes a seed for the reconstruction algorithm that clusters both high energy partons into a single jet.

A good approximation to the seedless algorithm can be achieved by the following method [70]. In the case that two stable reconstructed jets are separated by more than R_{cone} but by less than $2R_{cone}$, a new jet axis is defined at the E_{T} weighted midpoint of the two stable jets. This new axis is then used as a cluster to to try the

[6] This is called JCCB algorithm. Different algorithms, such as JCCA, JCCC, *etc* have different cone size.

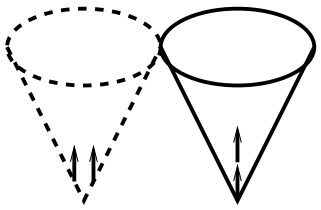

Figure 5.8: Illustration of collinear sensitivity. On the left, no jet is reconstructed because the energy is distributed between two collinear partons (or adjacent detector elements), both below the seed threshold. On the right, the energy is more narrowly distributed and the reconstruction succeeds.

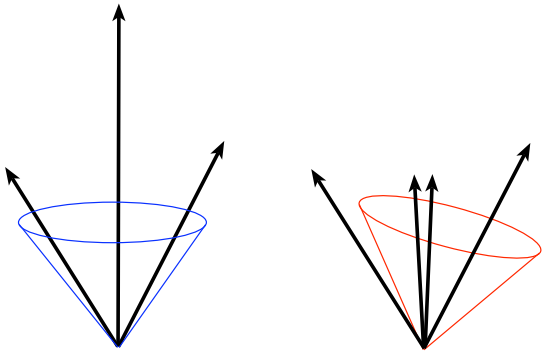

Figure 5.9: Example of the seed order problem. The reconstruction processes particles in order of E_{T}, removing them from the list of seeds as they are added to jets. On the right, the energy of the central parton from the left is split. Therefore, the initial seed changes, resulting in a decrease of the total energy clustered into the jet.

possibly of an additional reconstructed jet. If two jets share energy in clusters, they are merged if the shared energy is higher than half of the energy of the lowest energy jet. If the shared energy is lower, each of the shared clusters is assigned to the closest jet. And finally jets with $E_{\mathrm{T}} < 8$ GeV are rejected.

Once jet candidates are formed following the cone algorithm, further quality selection requirements are applied to each jet. The following criteria are aimed at removing jets which are not reconstructed from hadronic particles from the hard interaction:

- To remove jets from EM objects, a requirement on the energy fraction deposited in the electromagnetic section of the calorimeter (EMF) is applied at $0.05 <$ EMF < 0.95.

- To remove jets which predominantly deposit their energy in the coarse hadronic section of the calorimeter, a requirement on the fraction of the jet energy deposited therein (CHF) is applied at CHF < 0.4. The noise level is higher in the coarse hadronic section; this requirement is essentially aimed at removing those jets which clustered around noise in the coarse hadronic section.

- To remove jets clustered from hot cells, a requirement on the ratio of the highest to the next-to-highest transverse energy cell in the jet (HotF) is applied at HotF < 10.

- To remove those jets clustered from a single hot tower, the number of towers containing 90% of the jet energy (n90) is required to be greater than 1.

- To remove the fake jets originating from the noise in the CAL readout crates, the ratio of the total energy in Level 1 trigger towers associated with the jet cone of size $R = 0.5$ to the reconstructed energy excluding the energy in the coarse hadronic layers (L1 confirmation) must be at least 0.4 (or 0.2 in the inter-cryostat region).

5.3.3 Jet Energy Scale (JES)

At DØ, three main factors caused discrepancies between the reconstructed jet energy E_{reco} in Eq. 5.7 and the energy E_{parton} of the jet's original final state particle (at parton level): the collider environment, the inherent nature of a sampling calorimeter and the jet cone size. The correction to these effects are the energy offset $O(E_{reco},\ \eta)$, the calorimeter response $R(E_{reco}, \eta_{det})$ and shower correction $S(E_{reco},\ \eta)$, respectively

[7]:

$$E_{parton} = \frac{E_{reco} - O(E_{reco},\ \eta)}{R(E_{reco},\ \eta_{det})S(E_{reco},\ \eta)} \tag{5.8}$$

Energy Offset Correction

The $O(E_{reco},\ \eta)$ consists of the contributions which are not directly related to the physics process of interest. This correction is assumed to be independent of the physics process being analyzed, hence independent of the E_{reco}. This term arises from various contributions:

- the underlying event,
- multiple $p\bar{p}$ interactions per bunch crossing,
- calorimeter energy pile-up due to residual signals from the previous bunch crossing since the calorimeter electronics have a longer shaping time than the spacing of the bunches,
- noise due to radioactive decay of the uranium absorber.

In the central region of interest here, the $O(E_{reco},\ \eta)$ can be approximated by the calorimeter energy density in the MinBias events times the jet cone volume.

Calorimeter Response Correction

The DØ calorimeter is a sampling calorimeter. As discussed in Section 3.2.3 the response correction factor $R(E_{reco},\ \eta_{det})$ is needed due to the imperfect compensation of ^{238}U. It is generally less than one due to dead material in the calorimeter and uninstrumented regions. The cell-to-cell difference determines its dependence on the detector η instead of the physics η. Because of the different response to various species of particles inside a jet (dominantly $e,\ \gamma, \pi,\ n$ and K), $R(E_{reco},\ \eta_{det})$ is generally a function of the E_{reco} and the jet flavor (namely EM, gluon/light quark, c quark and b quark). Especially for b jets, the $R(E_{reco},\ \eta_{det})$ may be different from the other flavors of jet since b quark may decay to a muon and a ν_μ which leave little or no energy in the calorimeter.

[7]These corrections can be broken down to a cell-by-cell level, where the pedestal, the zero suppression, the energy responses and its non-linearity can be obtained for each individual cell, thus results in a correction factor depends on η, ϕ, layer, *etc*, and it is essential for the precise measurements, *e.g.* the W/Z physics. Here for simplicity the physics object level is assume, these correction terms to be symmetric in ϕ. They are in general also functions of instantaneous luminosity, but not currently modeled yet. This luminosity dependence is usually included in the systematic uncertainties.

Currently there is no official jet flavor dependent CAL response available for data (there are flavor dependent jet energy scales for MC samples). Possible jet flavor difference is either included in the systematic uncertainties, or corrected by muon-in-jet correction when a muon is determined to be in the jet ($\Delta R(\mu, \text{jet}) < 0.5$):

$$E'_{parton} = E_{parton} - E_{\mu}^{CAL} + E_{\mu} + E_{\nu} \tag{5.9}$$

where E_{parton} and E'_{parton} are the (b) jet energy before and after the muon-in-jet correction, E_{μ}^{CAL} is the muon energy deposition in the calorimeter, E_{μ} and E_{ν} are the muon and neutrino energies, respectively. The muon-in-jet correction is done with the DØ software package *d0correct* v01.01.02 [71].

The $R(E_{reco},\ \eta_{det})$ is measured in back-to-back γ+jet events [72]. The calorimeter response to electrons and photons is determined from mass resonances, such as the Z and the J/Ψ. Since γ + jet events rarely contain high energy neutrinos, after applying the EM object calibration, any momentum imbalance is dominated by mismeasurement of the jet energy, thus $R(E_{reco},\ \eta_{det})$ can be measured. The uncertainty of this correction factor is the main contributor to the JES uncertainty.

Shower Correction

The jet cone will not always encompass all of the constituent particles arising from the parent parton. Furthermore, some particles that are initially contained within the cone may bend out of it because of the magnetic field in the tracker, or induce showers in the calorimeter outside of the cone (this is not yet corrected by DØRECO). The fraction of energy included in the cone, $S(E_{raw},\ \eta)$, parameterizes these out-of-cone corrections, and is measured by studying the energy fraction profile as a function of jet cone size [73].

These correction factors will differ between the data and MC samples because of imperfect detector modeling. Rewriting Eq. 5.8 as:

$$E_{parton} = C(E_{reco}, \eta) E_{reco} \tag{5.10}$$

$C(E_{reco}, \eta)$ is called the effective jet energy scale correction factors (JES). This analysis used JES provided by *JetCorr* v5.3 package for data and MC samples. Two sets of JES's and their uncertainties as functions of jet E and η are shown in Figures 5.10 and 5.11, respectively[74].

5.3.4 Jet Energy Resolution

Using the same technique as in Section 5.1.4, the jet energy resolution for data can be measured by the jet E_{T} asymmetry distribution of the back-to-back di-jet or

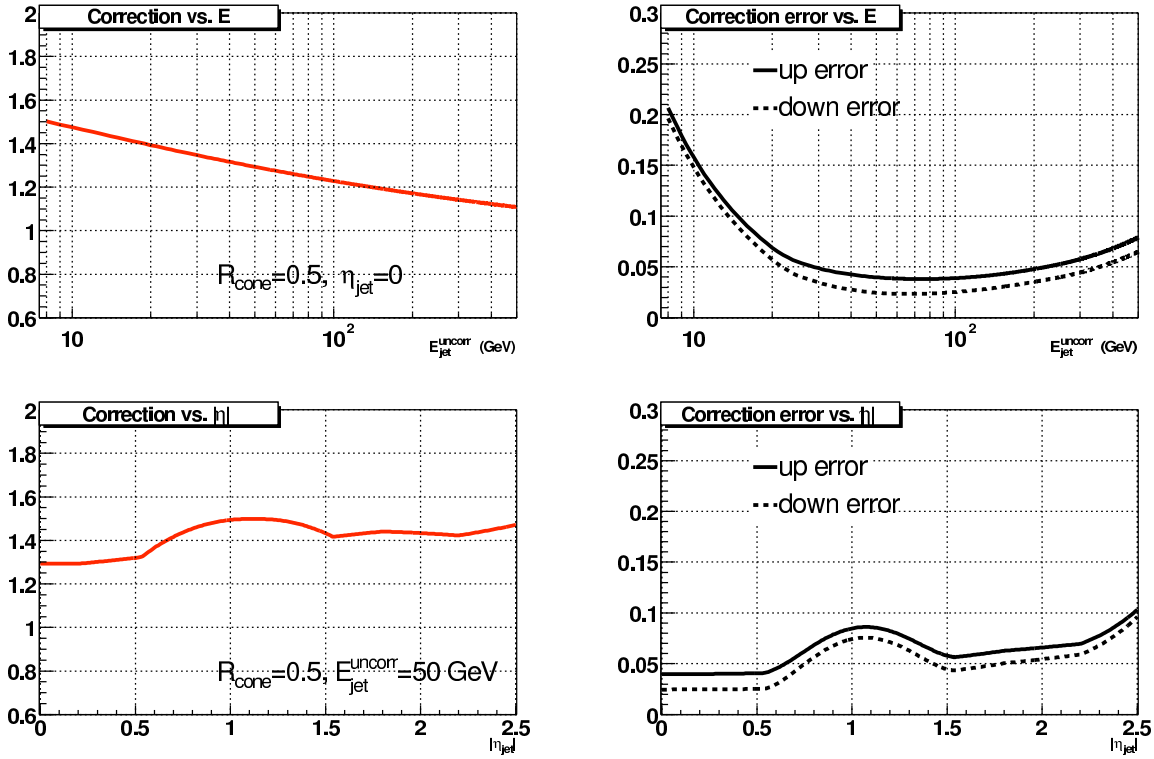

Figure 5.10: JES measurement in data. Left: JES correction as a function of uncorrected jet energy (top) and as a function of jet η (bottom). The respective statistical and total uncertainties are shown on the right.

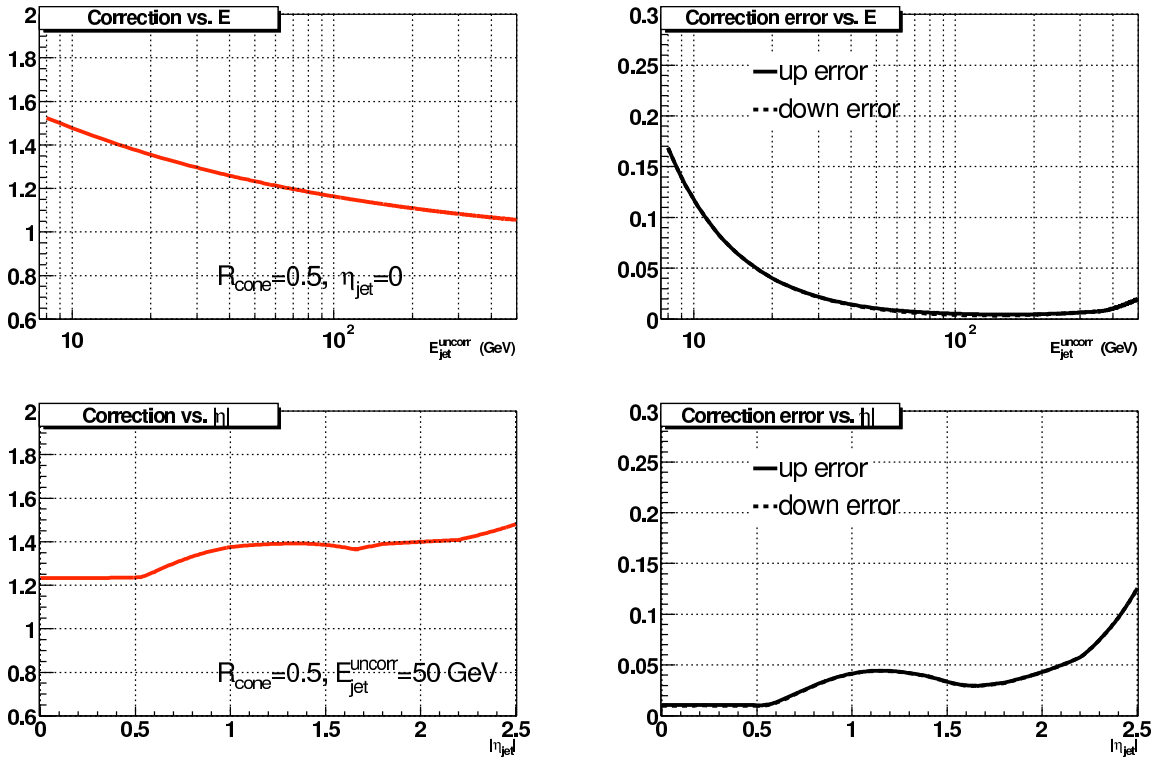

Figure 5.11: JES measurement in MC. Left: JES correction as a function of uncorrected jet energy (top) and as a function of jet η (bottom). The respective statistical and total uncertainties are shown on the right.

γ+jet events. The result can be written as:

$$\frac{\sigma_{E_{\mathrm{T}}}}{E_{\mathrm{T}}} = \sqrt{\frac{N^2}{E_{\mathrm{T}}^2} + \frac{S^2}{E_{\mathrm{T}}} + C^2} \tag{5.11}$$

where N, S and C represent the contributions from electronics noise, statistical fluctuations in the jet shower evolution, and calibration errors, respectively. The parameterizations for different η_{det} regions are listed in Table 5.3.4.

$\lvert\eta_{det}\rvert$ range	Monte Carlo			Data		
	N	S	C	N	S	C
0.0 - 0.5	4.26	0.658	0.0436	5.05	0.753	0.0893
0.5 - 1.0	4.61	0.621	0.0578	0.0	1.20	0.0870
1.0 - 1.5	3.08	0.816	0.0729	2.24	0.924	0.135
1.5 - 2.0	4.83	0.0	0.0735	6.42	0.0	0.00974

Table 5.1: Parameterization of the jet momentum resolution for Monte Carlo and data [75].

5.3.5 Jet Reconstruction×Identification Efficiency

The jet Reconstruction×Identification (RECO*ID) efficiency in detector data can be measured using the tag-probe method. Depending on the data sample used to measure the efficiency, the tag can be a variety of well defined non-jet physics objects, for example, if we choose γ+j samples (the dominant process is q+$g \rightarrow \gamma$+q), the high p_{T} isolated photon will be the tag. The probability of finding a jet found back-to-back with the photon is the jet RECO*ID efficiency. In this analysis, the data sample used is Z+j events. The Z acts as the tag, the probability of a recoil jet found back-to-back with the Z boson is the jet RECO*ID efficiency [76]. The efficiency is measured with both detector data and MC samples, and are parameterized as functions of jet p_{T} and η. The ratio of the efficiencies for the detector data and MC data is the jet RECO*ID Data/MC scale factor (SF). This SF will be folded into the jets in the MC samples to account for the different between the data and MC samples (See Section 8.3.2). Due to the limited event statistics in the detector data, the SF and its uncertainty (systematic plus statistics) are parameterized only as the function of the jet p_{T} as shown in Figure 5.12:

$$\begin{aligned}
\mathrm{SF} &= 1.00 \times \mathrm{Erf}(0.0285p'_{\mathrm{T}} + 0.262) && (5.12)\\
+\mathrm{Err} &= 0.0199 + 0.0750 \times \exp(1.97 - 0.0826p'_{\mathrm{T}}) && (5.13)\\
-\mathrm{Err} &= 0.0172 + 0.217 \times \exp(-0.0503p'_{\mathrm{T}}) && (5.14)
\end{aligned}$$

where Erf is the error function, the p'_{T} is the un-smeared Z boson p_{T} in the MC samples, which is related to the jet p_{T} in the calorimeter by the following equation:

$$p'_{\mathrm{T}} = 0.719 + 0.953 \times p_{\mathrm{T}} \tag{5.15}$$

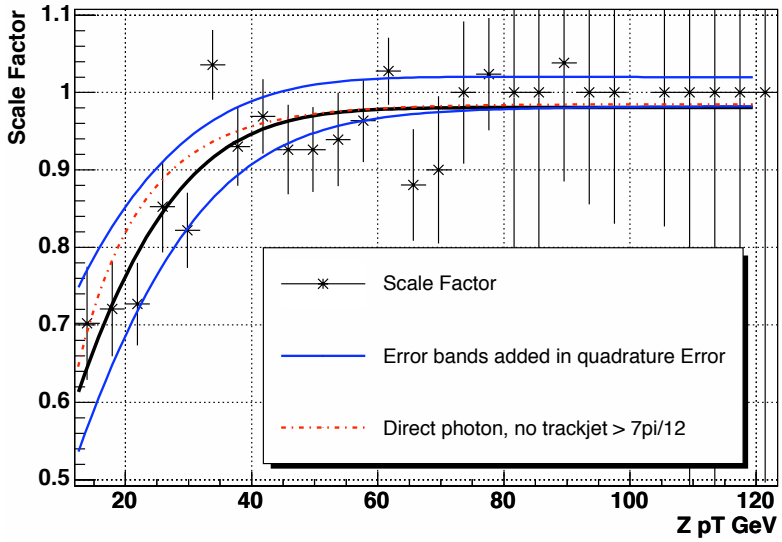

Figure 5.12: Jet RECO*ID Data/MC correction scale factor as a function of the un-smeared Z boson pt [76].

5.4 Muon Reconstruction and Identification

Local muons (muons detected in the muon detector) are reconstructed from the straight line segments that are independently obtained by fitting the hits in each of the three muon detector layers. The event display in Figure 5.13 shows the geometry of the muon detector and the reconstructed segments. These local muons are then combined with the global tracks to form global muons. A final set of muon ID requirements is imposed to supress fake and background muons.

5.4.1 Muon Reconstruction

The muon reconstruction consists of the following steps:

- Segment Pattern Recognition
- Scintillator Match

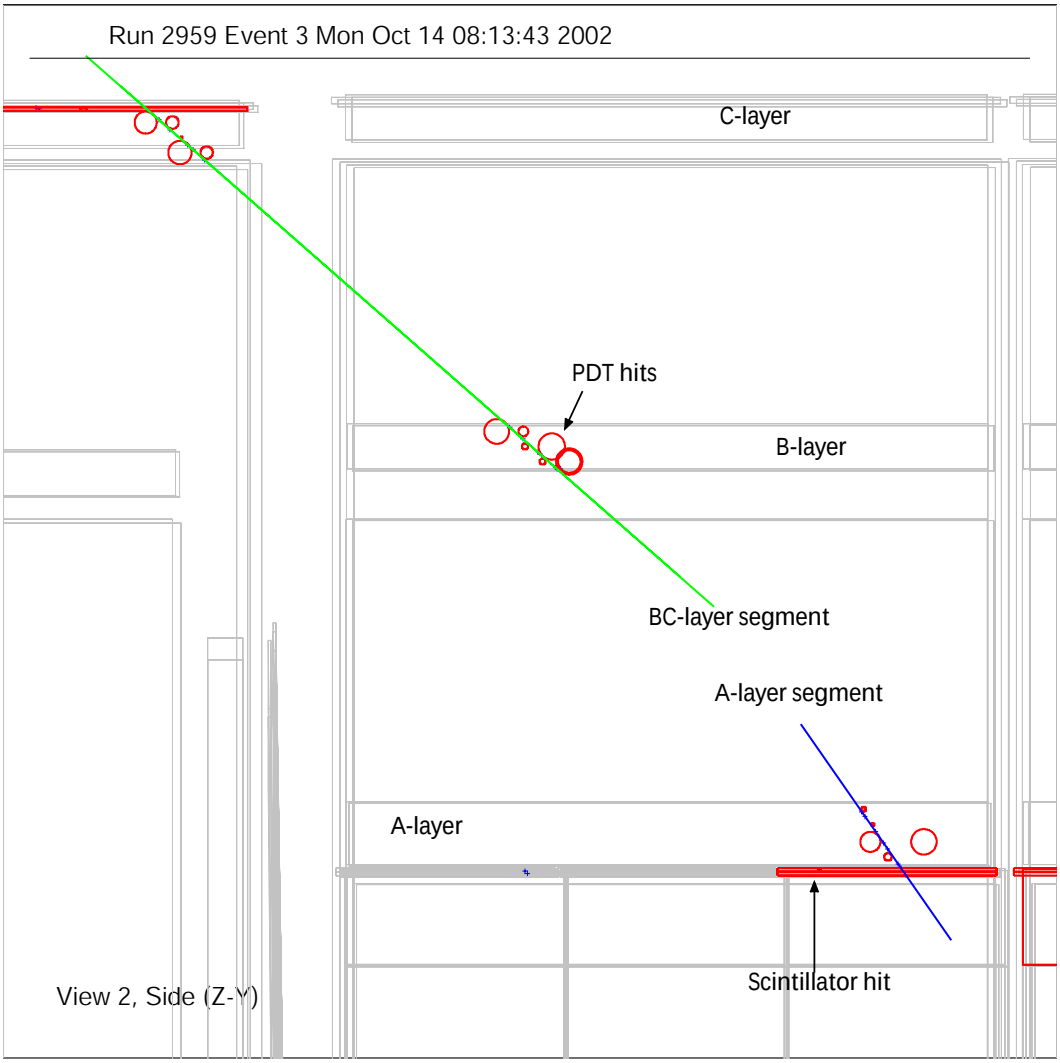

Figure 5.13: Local muon track reconstruction from the segments in the A and B+C muon detector layers. The scintillator hits are also displayed [77].

- B/C Layer Segment Match
- Central Track Match

These steps are decribed in detail below.

Segment Pattern Recognition

As discussed in Section 3.3.4, the wire hit time of the PDT can provide both the radial drift time and the axial time (corresponding to the ϕ information); for the MDT, the axial time is calculated from the matching scintillator hit if it is available, otherwise it is is assumed to be at the center of the wire. Then the radial drift time is calculated from the MDT wire time minus the axial time. Given the radial drift time and the ϕ position from the axial time, the muon track pattern can be built, as shown in Figure 5.14.

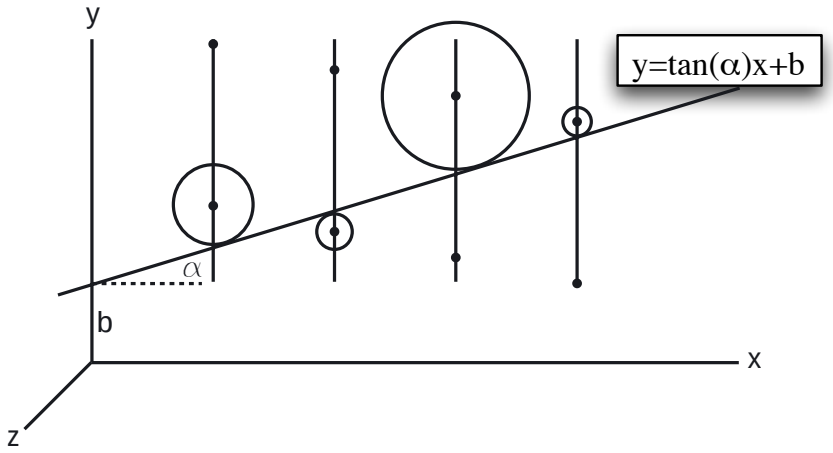

Figure 5.14: Muon segment pattern reconstruction in A layer muon detector. A local coordinate system is used, in which the wires (shown as the dots) are along the z-direction, the wire tubes are stacked along the y-direction and the normal of detector sublayer is along the x-direction. The four $y-$direction lines represents the four sublayers in A layer. The radii of the drift circles (the large circles) for the hits is proportional to the radial drift time. The reconstructed segment in the $x-y$ plane is the diagonal line. The z information of the segment pattern can be determined from the axial time in each wire.

First, straight line segments (the link) that are tangent to the drift circles of all the possible combinations of the wire hit pairs are formed. The pair of wire hits are required to have a separation along the $y-$axis (see Figure 5.14) of at most 20 cm in one drift chamber to ensure that uncorrelated hits are not matched; also they are

required not to be on the same sublayer unless the link between them crosses the sublayer of the wire hit pair (*eg.* consistent with a track passing between adajcent wires in the sublayer). This prevents fake links at the early reconstruction stage while allowing those instances in which a muon track passes through two neighbering tubes in one sublayer. The direction of the link in the $x-y$ plane is defined as:

$$\tan(\alpha) = \frac{y_2 - y_1}{x_2 - x_1} \tag{5.16}$$

where $x_i,\ y_i,\ (i = 1, 2)$ are the coordinates of the link points on the drift circle, which are related to the wire hit coordinates $x_i^w,\ y_i^w$, the radius of the drift circle r_i and the direction α of the link:

$$x_i = x_i^w - n \cdot r_i \sin(\alpha) \tag{5.17}$$
$$y_i = y_i^w + n \cdot r_i \cos(\alpha) \tag{5.18}$$

where $n = \pm 1$ depending on whether the link point on the circle is above (+) or below (-) the wire hit. α is determined by iterating Eqs. 5.16-5.18 with the initial α estimated by a straight line from the PV to the position of the wire hit.

Second, the links found in this initial step are matched in a recursive manner, in which the differences in angle and position of the links are compared to determine whether they belong to a straight line segment. Whenever two links are found to be compatible with a straight line segment, they are merged into one larger link that contains all the hits of the two original links. This procedure is repeated until all links have been tested for link merging. Then for each of the merged links, a straight line is fitted to all the hits in the link.to form the segment. The segments are sorted, first by the number of wire hits then by the fit χ^2; only the first four segments are used. For segments with only two wire hits (most likely in B/C layers where only three sublayers exist), the segment that points best to the PV is selected.

Scintillator Match

After the direction and position of the segment have been calculated using the wire hits. Scintillator hits are matched to the segment by extrapolating the segment to the scintillator in the drift plane of the wire hits. If a match with a scintillator hit is found, the segment is refitted taking into account the scintillator hit position information. Thus the $z-$axis information can be obtained. The resolution is about 7 cm. For the WAMUS, the axial position from the PDT wire hit time is also used for the $z-$axis fitting, for the FAMUS, if no scintillator match is available, the center of the wire is assumed to be the $z-$coordinate of the hit, thus results in a much larger $z-$coordinate uncertainty of about 60-90 cm.

B/C Layer Segment Match

Segments are initially reconstructed in the individual layers of the muon system separately. Due to the absence of a magnetic field between the B- and C-layers, segments in the B- and C-layer are expected to be part of the same straight line segment. So each pair of reconstructed B- and C-layer segments found in the same octant and region is merged, and a new fit is performed using all hits on both segments. The old B- and C-layer segments are kept available for the selection of the best segment in the next step.

Central Track Match

The toroidal magnet provides a local p_{T} measurement for muons with segments in both the A and B (or C) layers by a track fit. If the fit does not converge, then an estimate of the muon pT is obtained by using the bending angle between segments. The resolution of the transverse momentum measurement is limited at low energies ($\approx$ 6 GeV) by multiple scattering in the iron of the magnet, and at high energies ($\approx$ 10 GeV) by the spatial resolution of the drift chambers and scintillators and the strength of the toroidal field.

Central tracks with $p_{\mathrm{T}}>$ 1 GeV, and angular separations from a local muon with $\Delta\phi\ < 1$ and $\Delta\theta\ < 1$ are considered for track match to the muon. If the local muon track fit converges, the resulting measurements of the local muon momentum and the A layer position are propagated back to the point of the closest approach (PCA) with respect to the PV. The central track with the best fit to is selected as the match [78]. If the local muon track fit does not converge, local muon segments are propagated to the A layer and the closest (up to $\Delta\eta, \Delta\phi < 1$) global track in $\theta - \phi$ plane is chosen. Since the central tracking system provides much better momentum resolution, the muon kinematic variables in this dissertation are those of the matching central track.

For muons that match to a CFT only global track, a special muon momentum correction factor is applied since the momentum determination of the global track can be improved by assuming the PV as an additional track point and refitting the central track [79]. This correction is rare for the central region muon since most of them are in the good SMT coverage.

The momentum resolution of the muon depends on the number of the associated hits in the tracking system. Thus it is separately studied in two η_{det} region: $|\eta_{det}| < 1.62$ with full SMT+CFT coverage, and $|\eta_{det}| \geq 1.62$, the parameterization of the momentum resolution is:

$$\sigma\left(\frac{1}{p_{\mathrm{T}}}\right) = a \oplus \frac{b}{p_{\mathrm{T}}} \tag{5.19}$$

where a and b are listed in Table 5.2:

η_{det} range	a (GeV^{-1})	b
$\lvert\eta_{det}\rvert < 1.62$	0.00152	0.0279
$\lvert\eta_{det}\rvert \geq 1.62$	0.00226	0.0479

Table 5.2: Muon momentum resolution in the Monte Carlo for the two different η_{det} regions [43].

5.4.2 Muon ID

Reconstructed muon candidates are classified using two quantities: muon type and muon quality. The muon type is given by a parameter *nseg* as defined in Table 5.3. The muon quality can be either tight, medium or loose based on the muon *nseg* and the number of hits in the muon system [81]. The muon quality criteria are listed below:

nseg	Segment	Central Track Match	MTC Match Criterion
3	A+BC	Muon to central or central to muon	$\Delta\eta$, $\Delta\phi$ between MTC and central track extrapolated to CAL.
2	BC only	central to muon	as above
1	A only	central to muon	as above
0	Muon hit or MTC	central to muon/CAL	as above
-1	A only	no match	$\Delta\eta$, $\Delta\phi$ between MTC and A layer segment.
-2	BC only	no match	$\Delta\eta$, $\Delta\phi$ between MTC and BC layer segment.
-3	A+BC	no match	$\Delta\eta$, $\Delta\phi$ between MTC and local muon track at A layer if fit converged otherwise A segment position.

Table 5.3: Definition of the reconstructed muon categories. Categories are defined exclusively. MTC stands for muon track in the calorimeter. At the time the analysis was done the MTC was still under development so it was not used. "muon to central" means a converged local muon track matches to the central track, "central to muon" is the match between the muon segment and the central track when the muon local track fit did not converge.

- **Tight Muon**
  Only |nseg| = 3 muons can be tight. A muon is tight if it has:

- at least two A layer wire hits
- at least one A layer scintillator hit
- at least three BC layer wire hits
- at least one BC scintillator hit
- a converged local fit

- **Medium/Loose Muon, |nseg| = 3**
  When an |nseg| = 3 muon candidate fails the tight criteria, it may still be a medium muon if:

  - at least two A layer wire hits
  - at least one A layer scintillator hit
  - at least two BC layer wire hits
  - at least one BC layer scintillator hit (except for central muons with less than four BC wire hits)

  An |nseg| = 3 loose muon is defined as an |nseg| = 3 medium muon but allow one of the above tests to fail.

- **Medium/Loose Muon, nseg = 2**
  An |nseg| < 3 muon candidate can only be medium or loose muon if it matches to a central track. An nseg = 2 loose muon satisfies:

  - at least two BC layer wire hits
  - at least one BC layer scintillator hit

  An nseg = 2 medium muon passes the above two tests and is located in the bottom part of the detector (octant 5 and 6 with $|\eta_{det}| < 1.6$).

- **Medium/Loose Muon nseg = 1**
  An nseg = 1 muon candidate is loose if it has:

  - at least two A layer wire hits
  - at least one scintillator hit

  An nseg = 1 medium muon passes the above two tests and is located in the bottom part of the detector (octant 5 and 6 with $|\eta_{det}|| < 1.6$). Low momentum nseg = 1 muons are also defined as medium. An nseg = 1 muon is qualified as low momentum muon is its probability to reach the BC layer is less than 0.7 [81].

5.4.3 Muon Reconstruction×Identification Efficiency

The muon reconstruction×identification (RECO*ID) efficiency is measured using the same tag-probe method implemented in the *muo_cert* package as mentioned in Section 4.3.2. As usual, the $Z \rightarrow \mu^+\mu^-$ events are searched for in the data sample. A set of very stringent muon selection criteria is applied to the tag muon, the probe is a good quality charged track that can be combined with the tag muon to reconstruct a good quality Z event. Then probability of finding a given quality muon matches to the probe charged track is the single muon RECO*ID efficiency [56].

In order not to bias the efficiency measurement, the data sample should be selected with a single muon requirement. Thus for the efficiency measurement in detector data, the 1MULoose skim in which only one ID-ed muon is required to present is used. The efficiency for the MC data sample is measured using $Z \rightarrow \mu^+\mu^-$ sample. The ratio of the efficiencies in detector data and MC samples is the scale factor that accounts for the difference between detector data and MC simulation, this scale factor will be folded into the MC events (see Section 8.3.1).

Chapter 6

Monte Carlo Simulation

Monte Carlo simulation (MC) is indispensable for search experiments, for example the Higgs boson search in this dissertation. It is used to design and optimize the event selection criteria and to compare the theoretical prediction to the data. In DØ , the generation of Monte Carlo event data involves several stages and executables[82]:

- first, event generator programs simulate $p\bar{p}$ collisions to produce a particular final state;
- the results of the event generator is then run through *d0gstar*, a C++ wrapper program for the *GEANT* particle-material-interaction simulation program, to trace the particles through the DØ detector, determine where their paths intersect active areas, and simulate their energy deposition and secondary interactions This is the most time-consuming process in the full MC chain;
- the output of *d0gstar* is then processed by *d0sim* which does electronics simulation and pile-up of minimum bias events. The output at this stage has the same format the the raw detector data plus additional MC information which makes it possible to correlate detector data with the original generator output;
- optionally, the output of the *d0sim* can be input into *d0trigsim*[83] which simulates the DØ trigger selections. *d0trigsim* contains simulation code only for the L1 triggers. For the L2 and L3 triggers the same software packages that run in the L2 hardware and L3 farm nodes are used;
- at last, the DØ RECO processes the raw MC data for further studies just as for real collider data.

Imperfect MC modeling causes the simulated data to have resolutions and efficiencies that are frequently superior to those observed in the real detector. Therefore, corrections are applied to the reconstructed physics objects in the MC samples. In

this chapter, we will focus on the event generator, and the corrections on the MC jets and muons.

6.1 MC Event Generation

There are many kind of MC event generators that are suitable to different situations and physics processes [82]. Among these event generators, a general purpose MC generator, *PYTHIA* [84], is widely used. It combines the calculations of the perturbative leading order (LO) parton-parton hard-scatter processes with non-perturbative processes at the initial and final states as discussed in Section 2.4.2:

- In order to describe the composite nature of the initial state particles (p and $\bar{p}$), an interface to parton distribution functions (PDF) is used. In this dissertation, the CTEQ5M PDF is used [85].
- Incoming and outgoing partons radiate gluons which form initial-state and final-state radiation. The parton radiation is described by the evolution using the Dokshitzer-Gribov-Lipatov-Altarelli-Parisi (DGLAP) equations [86] which give the probability for a parton to radiate.
- Initial and final-state color coherence effects are incorporated via the Angular Ordering approximation.
- The two incoming partons participate in the hard $2 \rightarrow 2$ process to produce two outgoing partons which may contain short lived resonances such as W and Z bosons.
- The remaining partons in the two incoming hadrons which did not participate in the hard process form the beam remnants that populate the forward region.
- Outgoing quarks and gluons fragment to color neutral hadrons following the string fragmentation model. The decays of the produced unstable hadrons are also incorporated.

PYTHIA allows events which contains high jet multiplicities in the final states due to the initial and final state radiation. But these soft and collinear jets do not model well those high jet multiplicity events which contains $2 \rightarrow n$ ($n > 2$) hard-scattering processes. *ALPGEN* [87], on the contrary, is a next-to-leading order (NLO, though still at tree-level) event generator which calculates the matrix elements for a larger set of parton-level processes. Therefore, it improves on the description of the these multiple final state partons events compared with PYTHIA. *ALPGEN* utilizes the *PYTHIA* hadronization libraries and the CTEQ5L PDF. In this analysis, most MC samples are produced by the combined results of *ALPGEN* and *PYTHIA*.

The boundaries between the perturbative radiation of hard gluons modeled by ALPGEN and the softer partons emitted in the hadronization described by PYTHIA is somewhat ambiguous. Therefore, care must be taken to avoid double counting multi-jet events: a low jet multiplicity PYTHIA sample will contain a few events that have many jets and are thus also described by a high multiplicity ALPGEN sample. The MLM matching scheme is used to avoid this danger [88].

The cross sections for MC samples which contain final states of $Z/\gamma^* + 2$ partons are calculated using the *MCFM* program [90] up to the NLO. The cross sections for the other MC samples are based on various theoretical calculations [89, 93].

6.2 Data vs. MC Correction

Limitation of theoretical models and computational techniques in MC event generators is one source of the data vs. MC discrepancy and are usually accounted for in the systematic uncertainties. Yet even if the event generator provides a good simulation of the underlying physics, the complexity of the particle-material interaction, the detector electronics characteristics and the collider background all make it almost impossible to accurately reproduce the data in the MC. MC samples usually have better kinematic/spatial resolution and better detector response. While trying to fine-tune the MC programs for better simulations is done, it is easier to develop empirically parameterized corrections to the MC outputs based on data control samples. These parameterized corrections are applied at the analysis stage and can be roughly divided into two categories: corrections to the momentum/energy resolutions in MC, or smearing; corrections to the physics object RECO*ID efficiency and selection criteria efficiency, called Data/MC scale factor (SF).

6.2.1 Jet Smearing

For a given MC RECO-ed jet, the data and MC jet energy resolutions can be calculated with the parameterization of Eq. 5.11 and the constants in Table 5.3.4. A random variable that follows a normal distribution $N(1, \sigma)$ is applied to the MC RECO-ed jet E_{T}, where $\sigma^2 = \sigma^2_{E_{\mathrm{T}}}(data) - \sigma^2_{E_{\mathrm{T}}}(MC)$. The MC RECO-ed jet ($\eta$, ϕ) coordinate resolutions agree with the data well, so there is no need to smear them.

6.2.2 Muon Smearing

The muon momentum smearing is determined with $Z \to \mu^+\mu^-$ data and MC events. The momentum of the MC RECO-ed muon is smeared according to:

$$\frac{1}{p_{\mathrm{T}}{}'} = \frac{1}{\alpha \cdot p_{\mathrm{T}}} + \beta \tag{6.1}$$

where α is a scale factor and β is a normally distributed random variable with width σ. The Z peak from the smeared di-muon is compared to that from the data. The optimum values of α and σ are obtained by making the MC and data Z peak match using the Kolmogorov-Smirnov test. The fit is performed in two η_{det} region: $|\eta_{det}| < 1.62$ with full SMT+CFT coverage, and $|\eta_{det}| \geq 1.62$. The values are listed in Table 6.1.

η_{det} range	α	σ (GeV^{-1})
$\|\eta_{det}\| < 1.62$	0.991	0.00231
$\|\eta_{det}\| \geq 1.62$	0.999	0.471

Table 6.1: MC muon p_{T} smearing factors for the two η_{det} regions [80].

6.2.3 Data/MC Scale Factors

The determination of the jet and muon RECO*ID efficiency data/MC SFs are discussed in Section 5.3.5 and 5.4.3. There are two ways to fold these scale factors into the MC events (taking muons as an example):

- **Random Removal.**
  In this method, for each muon in a MC event, a random number ρ between 0 to 1 is generated, if ρ is larger than the SF (assumed to be smaller than one) corresponding to the kinematic variables of the muon, the muon is removed from from further analysis; otherwise the muon is retained.

- **SF Convolution.**
  In this method, for each muon in an MC event, the SF (in fact a SF, a relative likelihood that a MC muon also present in the data, can be greater than one) is obtained according to the kinematic variables of the muon, then the likelihood of this event is calculated according to the formula in Appendix A. A convoluted scale factor $\mathcal{S}$ is obtained by dividing the sum L of the likelihoods over all the events in a MC sample with the total number of MC events N (at the current event selection stage). $\mathcal{S}$ can then be used to as a normalization factor for the MC samples.

The second method is used throughout this analysis in order to reduce the statistical uncertainty and account for the cases in which the data/MC SFs are greater than one.

Chapter 7

Special Object Identification

In Chapter 5, the reconstruction and ID of the general "stable" physics objects in the final states, *eg.* muons and jets are discussed. For the study of a specific interaction channel, more can be done. For example, for the Higgs search in this analysis, the final state consists of a pair of muons and a pair of jets. As discussed in Section 2.4.3, there are processes other than $p\bar{p} \to Z + H \to \mu^+\mu^- + b\bar{b}$ that could produce such final state. If only the general RECO and ID information on the muons and jets is used, the dominant multi-jet QCD events will overwhelm the selected events. Thus we need to use more ID information about the final state particles, such as whether the muons in the final state come from the Z boson decays, whether the two jets are from the b-quark. Furthermore, after we are able to find the events with a pair of muons from Z boson decay and a pair of b-jets, we need to tell whether they are from $Z + H$ or some other processes. In this chapter, we will focus on the special ID of the Z muons and the flavor tag of the b-jets and the optimizations of the special ID selection criteria for the $Z + H$ events. The search for the $Z + H$ signal will be discussed in Chapter 8.

7.1 Isolation of Z Muons

The main background for Z muons comes from semi-leptonic decays in jets [1]. Compared to muons originating from the leptonic decay of a Z boson, those muons tend to be close to a jet and have a lower transverse momentum. The isolation of a muon from all the jets in an event is the most powerful tool to ID the Z muons. There are many different definitions of muon isolation criteria:

- **Muon-jet Separation.**
  From the geometric configurations of muon and jet kinematics, we can define a

[1] Other contributions include the Drell-Yan process, the $t\bar{t}$ production, W+jets. They will be discussed in Chapter 8

requirement on the separation of a muon and a jet in the $\eta - \phi$ plane as:

$$\Delta R \;=\; \sqrt{(\eta_\mu - \eta_{jet})^2 + (\phi_\mu - \phi_{jet})^2} \;>\; 0.5 \tag{7.1}$$

The commonly used value of 0.5 is adapted from the average jet transverse size and can be adjusted for tighter or looser isolation requirement.

- **Halo and TrkCone.**
  Halo(0.1, 0.4) is the sum of the $E_{\rm T}$ of calorimeter clusters in a hollow cone between $R = 0.1$ and $R = 0.4$ around the muon. In forming this sum, cells in the electromagnetic and fine hadronic calorimeters are considered. Due to an enhanced noise level, the coarse hadronic calorimeter is excluded from the sum. TrkCone(0.5) is the sum of the $p_{\rm T}$ of all tracks within a cone of radius $R = 0.5$ surrounding the muon. The track matched to the muon is excluded from this sum. An isolated muon should have smaller jet energy deposition in the halo and fewer high $p_{\rm T}$ tracks nearby compared to a muon from a jet. The following muon isolation requirement has been found by the muon ID group:

$$\text{Halo}(0.1,\, 0.4) \;<\; 2.5 \text{ GeV and TrkCone}(0.5) \;<\; 2.5 \text{ GeV}. \tag{7.2}$$

- **Muon $p_{\rm T}$ Scaled Halo and TrkCone.**
  A variation of the above isolation requirement is to use the muon $p_{\rm T}$ to scale the Halo and TrkCone:

$$\frac{\text{Halo}(0.1,\, 0.4)}{p_{\rm T}} \;<\; 0.08 \text{ and } \frac{\text{TrkCone}(0.5)}{p_{\rm T}} \;<\; 0.06. \tag{7.3}$$

  this scaled requirement accounts for radiation from the very energetic muons as discussed in Section 3.2.1.

- **Relative Transverse Momentum $p_{\rm T}^{rel}$**
  Since a muon from a jet is likely to be collinear with the jet and the momentum transfer of the hadron's semi-leptonic decay is less than that of the colliding process, we can place a requirement on the $p_{\rm T}^{rel}$ for the muon isolation as:

$$p_{\rm T}^{rel} \equiv \frac{|\vec{p}_\mu \times (\vec{p}_\mu + \vec{p}_{jet})|}{|\vec{p}_\mu + \vec{p}_{jet}|} \;>\; 10 \text{ GeV}. \tag{7.4}$$

  This quantity takes into consideration both the small muon-jet momentum separation of and the low momentum of the muon if the muon is from a jet.

These isolation requirements and their combinations have comparable performance. Generally the scaled Halo and TrkCone provides the best signal efficiency for the

same background rate as shown in Figure 7.1.

7.1.1 Muon Isolation Probability

Although the isolation requirements discussed above provide good performance, they do not have a clear physics meaning in their requirement values. Thus we will define yet another isolation discriminant that has a more intuitive meaning. We will define the isolation discriminant f_{iso}, as the muon $|\vec{p}|$ scaled (Halo+T), since it has the best performance as shown in Figure 7.1 (b):

$$f_{iso} = \frac{\text{TrkCone + Halo}}{|\vec{p}_{\mu}|} \tag{7.5}$$

Similar to the definition of the hard-scattering vertex probability in Eq. 5.3 and Eq. 5.4, we will define the probability that a muon is non-isolated by using the f_{iso} distribution $\mathcal{F}_{iso}^{QCD}$ of a sample which contains mostly non-isolated muons, for example the QCD multi-jet events which contain muons:

$$P_{iso}(f) = \frac{\int_0^f \mathcal{F}_{iso}^{QCD}(x)dx}{\int_0^{\infty} \mathcal{F}_{iso}^{QCD}(x)dx} \tag{7.6}$$

where f is the isolation discriminant of the muon.

The discriminant distribution for the QCD multi-jet events is shown in Figure 7.2 (2 "good" jets are required to be present in data, see Section 8.2). The same distribution with 1 and 2 b-tag requirements are shown in Figures 7.3 and 7.4. Since b-jets are required to be present in these two plots, the increased number of non-isolated muons decaying from the b-jets shift these distributions compared to Figure 7.2. The detector data set used is the skimmed 6 million JetTrigger events mentioned in Section 8.1.1).

By defining the probability as in Eq. 7.6, the non-isolation probabilities (without confusion, we will refer to it as isolation probability in the future) P_{iso} of muons from the QCD multi-jet background are evenly distributed between 0 and 1. The f_{iso} distribution for Z muons is more populated toward 0 compared with the background muons as shown in Figure 7.2, so the isolation probabilities P_{iso} for Z muons are more concentrated near 0. By making a requirement on the probability, the isolated Z muons can be easily identified as shown in Figure 7.5.

7.1.2 Di-muon Isolation

From the muon isolation discriminant definition Eq. 7.5 we can see that for a very energetic isolated muon, the f_{iso} can be very close to zero (for a isolated muon

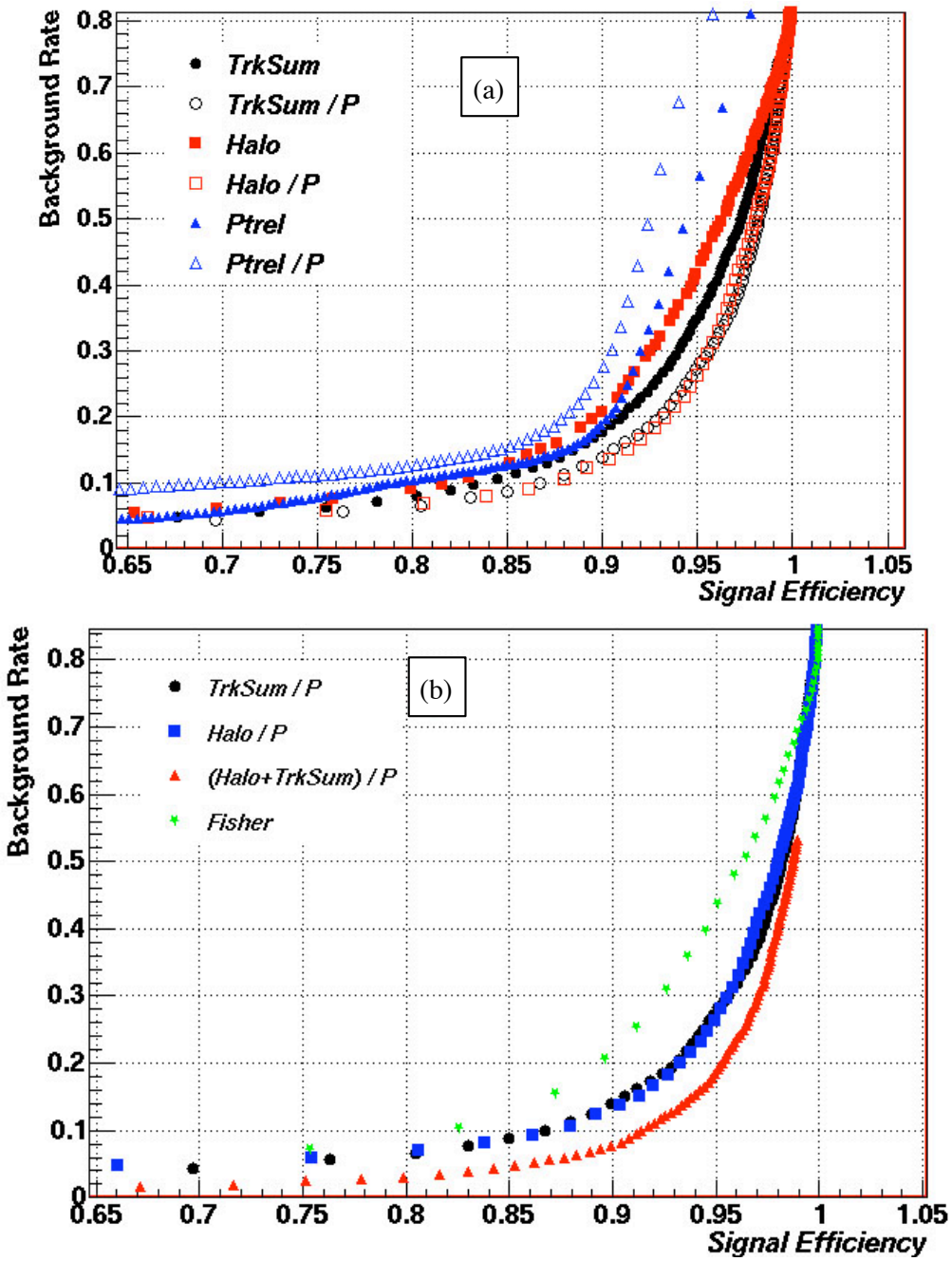

Figure 7.1: Comparison of the background rate vs. the signal efficiency for all the single muon isolation discriminants. (a)the muon momentum scaled versions of these discriminants generally have better performance than the un-scaled discriminants, the scaled Halo and TrkCone have the equal best performance; (b) the sum of the scaled Halo and TrkCone have even better performance than each individual. Fisher is another isolation discriminant. [2]

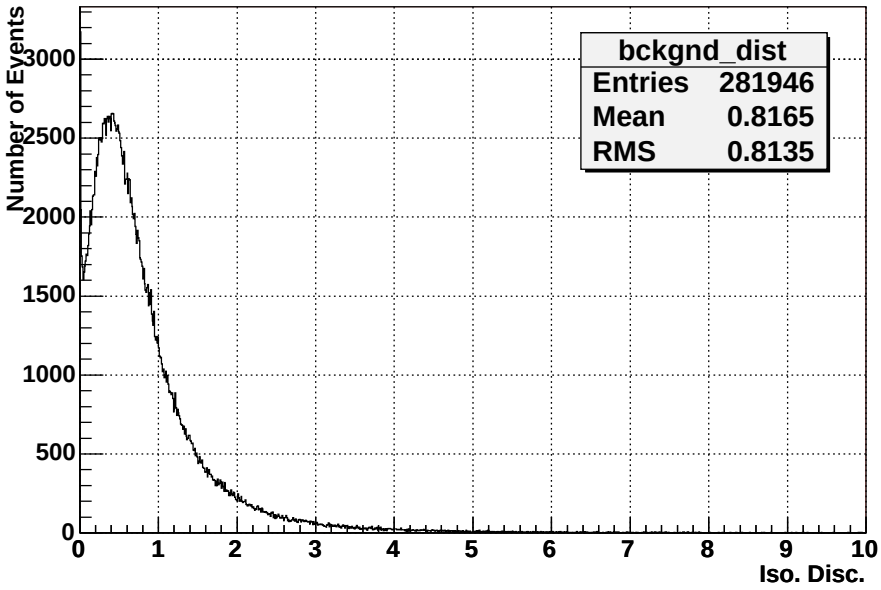

Figure 7.2: Muon isolation discriminant distribution for QCD multi-jet events from JetTrigger skimmed data with additional requirement of 1 muon and 2 or more jets. The muon and the jets passed the same kinematic requirements as used in the event selection. This discriminant describes the muon behavior of the $Z \rightarrow \mu\mu$ process's QCD background. It is used to construct the muon isolation probability.

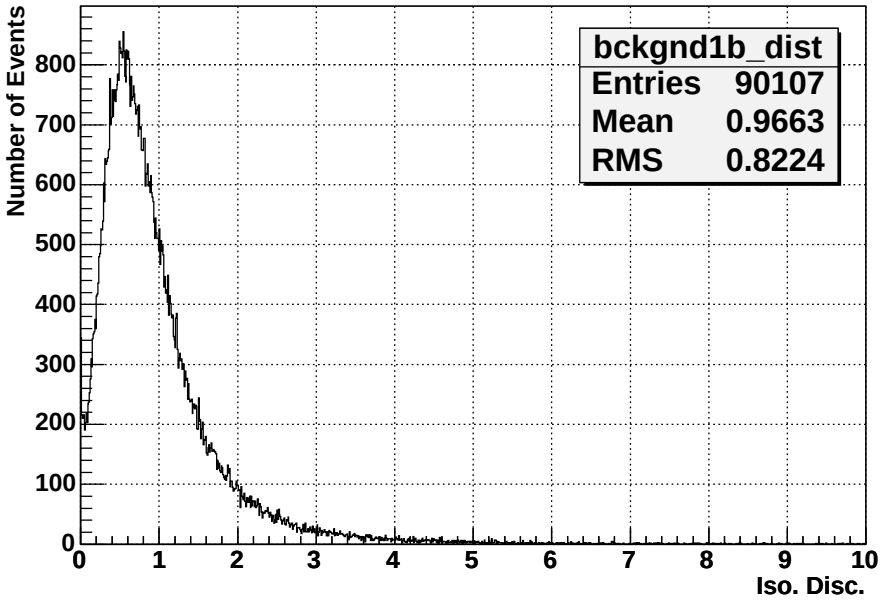

Figure 7.3: The same distribution as in Figure 7.2 except 1 b-tag jet is required.

the sum of the Halo and TrkCone is usually less than 5 GeV as can be seen from Eq. 7.2), consequently its isolation probability can be approximately zero. On the other hand, when a isolated muon is not so energetic ($\sim$ 15 GeV, for example), the sum of the Halo and TrkCone is still in the same range of a few GeV due to the background, so its isolation probability can be close to one. Due to the invariant mass constraint on the Z muon pair, if one of the muons from the Z decay is very energetic, the other one is likely to be less energetic. Thus we can predict for the Z muon pair, their isolation probabilities are correlated: if the isolation probability of one of the muon is very close to 0, the isolation probability of the other muon could be well away from 0, although it is may still be isolated according to the other isolation criteria (for example, the ΔR in Eq. 7.2); if both of the muons are moderately relativistic, their probabilities are likely to be close to zero. For the QCD multi-jet background, we can predict the isolation probabilities of the two muons from the jets are not correlated. If we draw the 2-D isolation probability distribution for the muon pairs in an event sample, the QCD multi-jet background events will be distributed evenly in an unit square, while for the events containing Z bosons, the distribution is close to the axis, as shown in Figures 7.6 and 7.7. The distinct behaviors of the 2-D isolation probability distributions provide a very efficient way to select the Z signals and to requirement on the QCD multi-jet background events: we can make a requirement

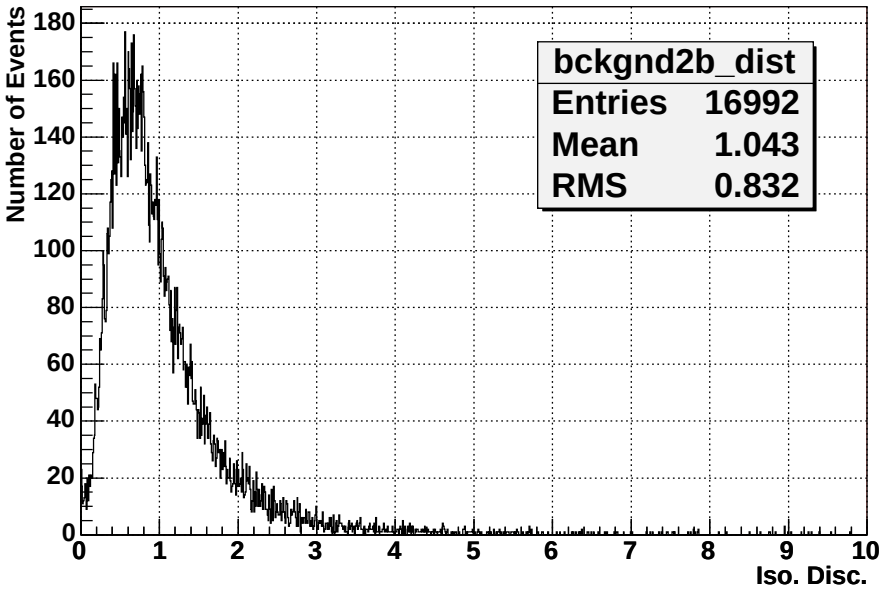

Figure 7.4: The same distribution as in Figure 7.2 except 2 b-tag jet is required.

on the product $P_{iso1} \times P_{iso2}$ of the isolation probabilities of the muon pair [2].

7.1.3 Di-muon Isolation Efficiency

The isolation requirement efficiency ϵ_{iso} is defined as the ratio of the event yield after and before the di-muon isolation requirement. In the following 3 sections, ϵ_{iso} is calculated for both $Z/\gamma^* \rightarrow \mu^+\mu^-$, $t\bar{t}$ and the QCD background w.r.t the events which contain $\mu^+\mu^-$+2 or more jets (see Figure 8.1).

Di-muon isolation requirement efficiency for $Z/\gamma^* \rightarrow \mu\bar{\mu}$

There are three direct ways to measure the Z and/or Drell-Yan process di-muon isolation requirement efficency:

1. Use the Z+2j events from the data sample. Fit the Z peak and the background–which contains both the QCD and Drell-Yan processes–within the mass window. The efficiency for a given isolation requirement is obtained by taking the ratio of the number of the fitted Z signals at that isolation requirement to the number of fitted Z signals when there is no isolation requirement.

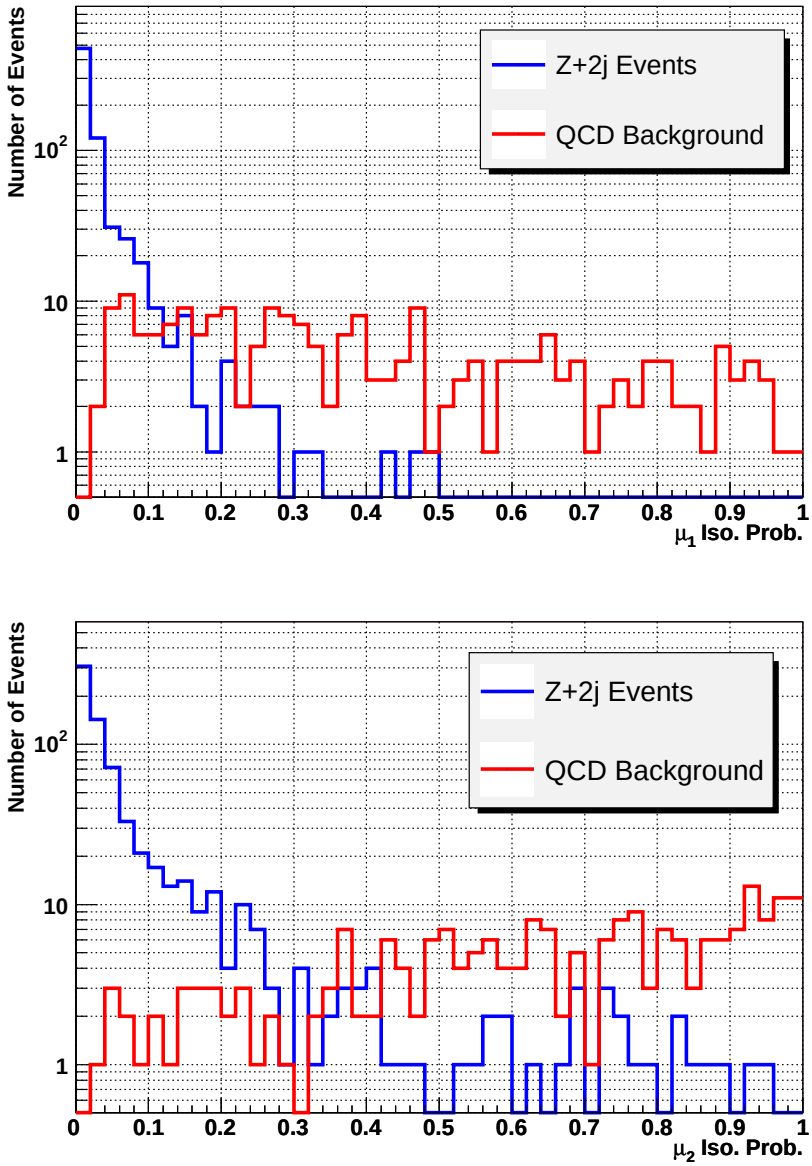

Figure 7.5: Isolation probability distributions for the first(upper panel) and the second(lower panel) Z muon candidates (blue lines) from $Z + 2$ jets events in data compared with the isolation probabilities of the first and second muons from the multi-jet plus 2 muon events(red lines)–these events satisfy the same event selection requirement as $Z + 2$ jet events except for that they fail the di-muon isolation probability requirement. Referring to Figures 7.8 and 7.9 these anti-isolated($p_1 \times p_2 \geq 0.02$) $Z + 2$ jet events are mostly the QCD background of the $Z + 2$ jet events. Z muon isolation probability distribution is distinctly different from the muons from multi-jet events.

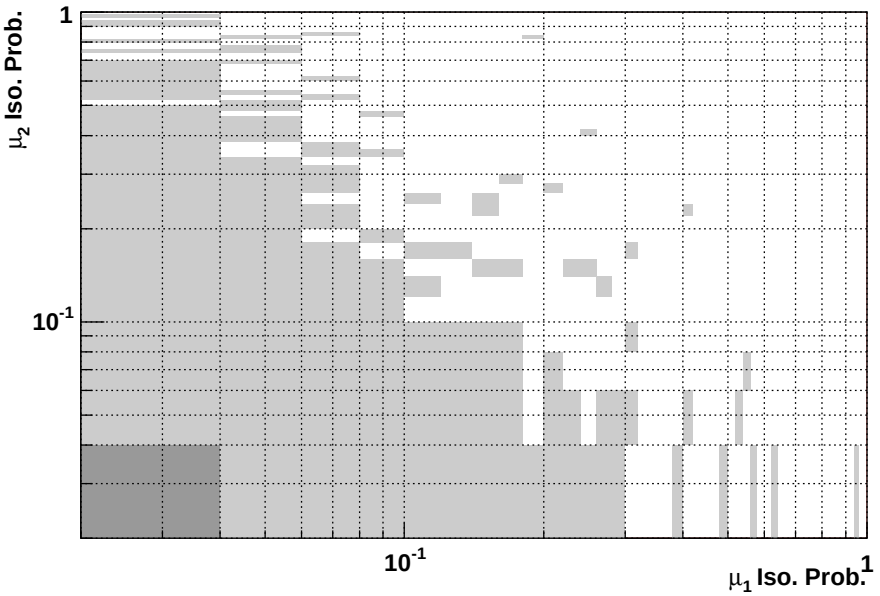

Figure 7.6: 2-D di-muon isolation probability distribution for the MC $Z \rightarrow \mu\mu$ events. The requirement on the product of 2 muons' isolation probability yields higher signal efficiency than a requirement on each muon when keeping the background rate at about the same level.

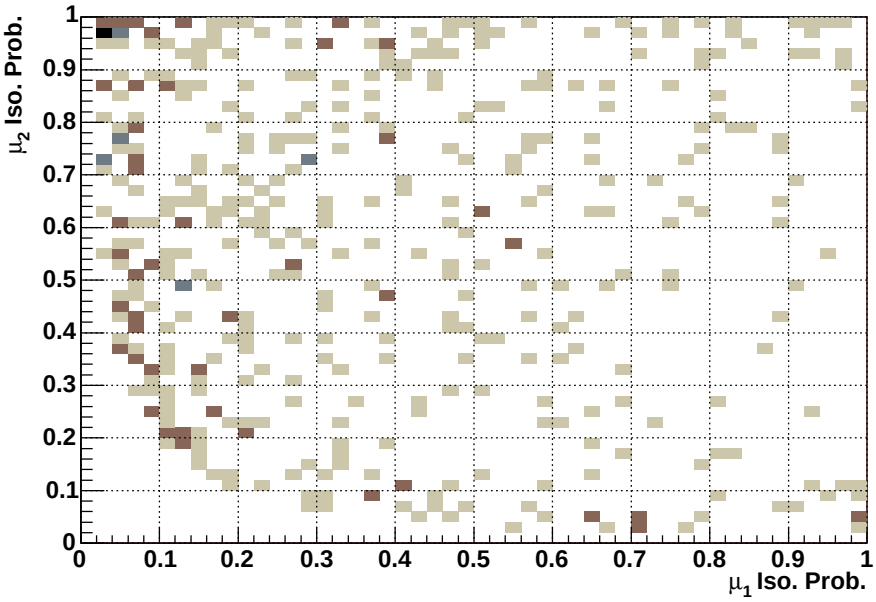

Figure 7.7: 2-D di-muon isolation probability distributions for the QCD background of 2 $Z + 2$ jets. The di-muon isolation probability from the QCD background are evenly distribution within the unit square. A requirement of the product of the di-muon isolation prbabilities > 0.02 is applied.

2. Use the MC Z+nj sample. Still fit the Z peak and the background–in this case only Drell-Yan process is involved in the background–and the isolation requirement efficiencies of both Z and Drell-Yan processes can be calculated by using the same techniques above.

3. Use the MC Z+nj sample. Don't fit the Z peak and the Drell-Yan background, instead assume Z and Drell-Yan processes have the same isolation requirement efficiencies due to the similarity of the kinematics. Count the total number of events within the mass window, the efficiency is given by the ratio of the number of events with and without the isolation requirement.

For data we can only use the first method, while for MC samples the second and the third methods are suitable. Figures 7.8–7.13 show the fit results for data with and without the isolation requirement for 0,1 and 2 b-tagged jets. The MC fits resemble that of data with the isolation requirement.

The second way and the third way give similar efficiencies for the MC samples. The third way is used in order to avoid the need for fitting to the background, thus achieving smaller statistical uncertainties. The measured Z and Drell-Yan isolation requirement efficiencies for different Z MC samples are shown in Figure 7.14, along with the data isolation requirement efficiency measured using the first method. It is obvious the MC Z processes and data have the same isolation requirement efficiencies at the isolation requirement region we are interested in(~ 0.02). Also the plot shows that the isolation requirement is independent of the jet and b-jet multiplicity. The averaged isolation requirement efficiencies are listed in Table 7.1.

Iso. Requirement	0.1	0.07	0.05	0.03	0.02	0.01	0.007	0.005	0.003	0.001
ϵ^{Z}_{iso}	0.996	0.995	0.992	0.987	0.981	0.960	0.940	0.918	0.875	0.743

Table 7.1: Di-muon isolation requirement efficiencies for Z/Drell-Yan for different isolation requirement points. This efficiency is an average for all the MC samples which contain the Z boson. The relative uncertainty is around 2%.

Di-muon isolation requirement efficiency for $t\bar{t}$.

The $t\bar{t}$ decay process does not contain a Z boson, but two muons can come from independent decay of the two W's produced in top pair decay and thus fake the Z signal. The third method is used to measure the isolation requirement efficiency and the results are listed in Table 7.2. As one would expect for the di-leptonic decay channel the efficiency is similiar but slightly lower than the process which contains Z. For the single lepton decay mode the efficiency is much lower due to the un-isolated muon from b decay..

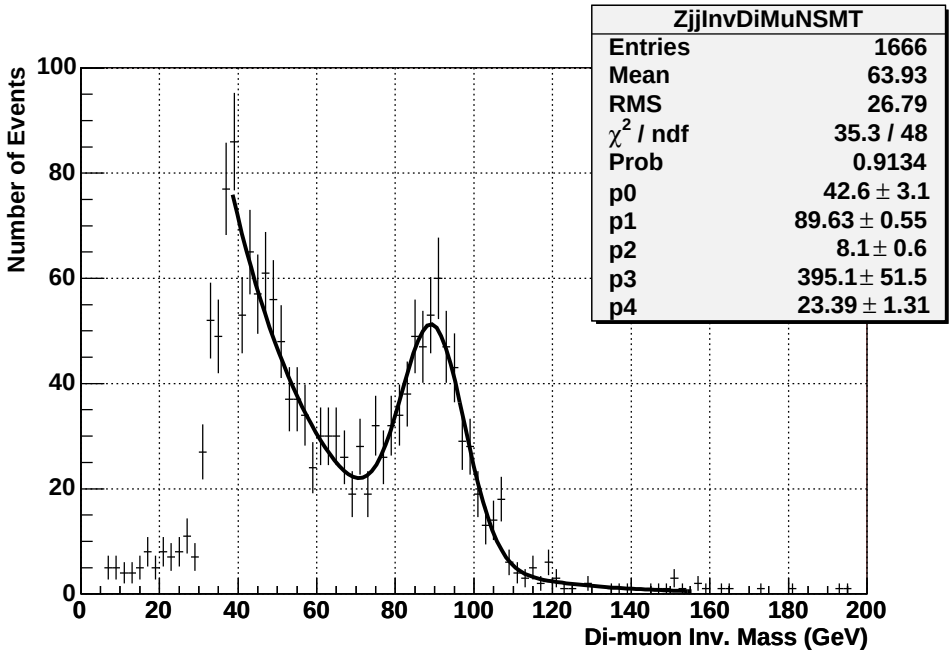

Figure 7.8: Di-muon invariant mass distribution for $Z + 2$ jet with 0 btag events. No isolation requirement is applied. Z peak is modelled by Gauss function $p0 \cdot e^{\frac{(x-p1)^2}{2p2^2}}$ for simplicity. It has almost the same fit result as the convoluted function of Gauss function and Breit-Wigner function. The QCD and Drell-Yan is modelled by $p3 \cdot e^{-p4 \cdot x}$. The total number of QCD + Drell-Yan events is the integration of the fit function within the Z mass window. The Z signal is the total number of events within the Z mass window subtracted by the total number of QCD and Drell-Yan process with the constraint of the measured γ_1 and γ_2 (defined in Eq. 8.6 and 8.7 in section 8.4.1.)

	0 btag	1 btag	2 btag
$t\bar{t} \to \mu\mu + 2j$	0.952 ± 0.01	0.944 ± 0.01	0.949 ± 0.01
$t\bar{t} \to \mu + 2b + 2j$	0.713 ± 0.02	0.702 ± 0.02	0.668 ± 0.03

Table 7.2: The di-muon isolation requirement efficiencies for $t\bar{t}$ processes with 0, 1, 2 btagged jets at isolation requirement = 0.02. The efficiency is as expected to be lower than the MC Z samples, and it is weakly dependent on the number of b-tagged jets.

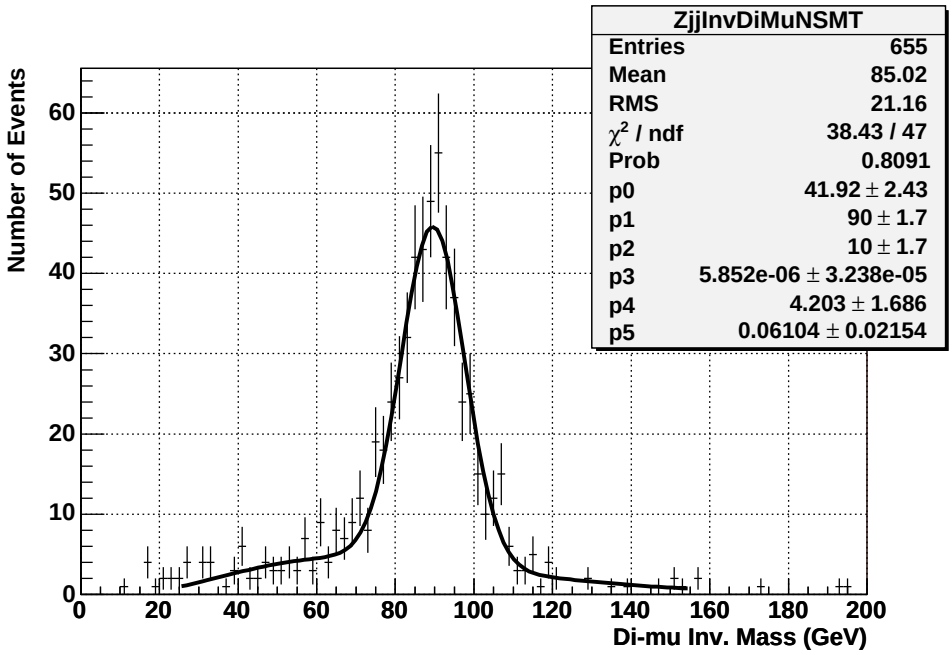

Figure 7.9: Di-muon invariant mass distribution for $Z + 2$ jet with 0 btag events. Isolation requirement 0.02 is applied. Z peak is modelled by Gauss function $p0 \cdot e^{\frac{(x-p1)^2}{2p2^2}}$. The QCD and Drell-Yan is modelled by $p3 \cdot x^{p4} \cdot e^{-p5 \cdot x}$.

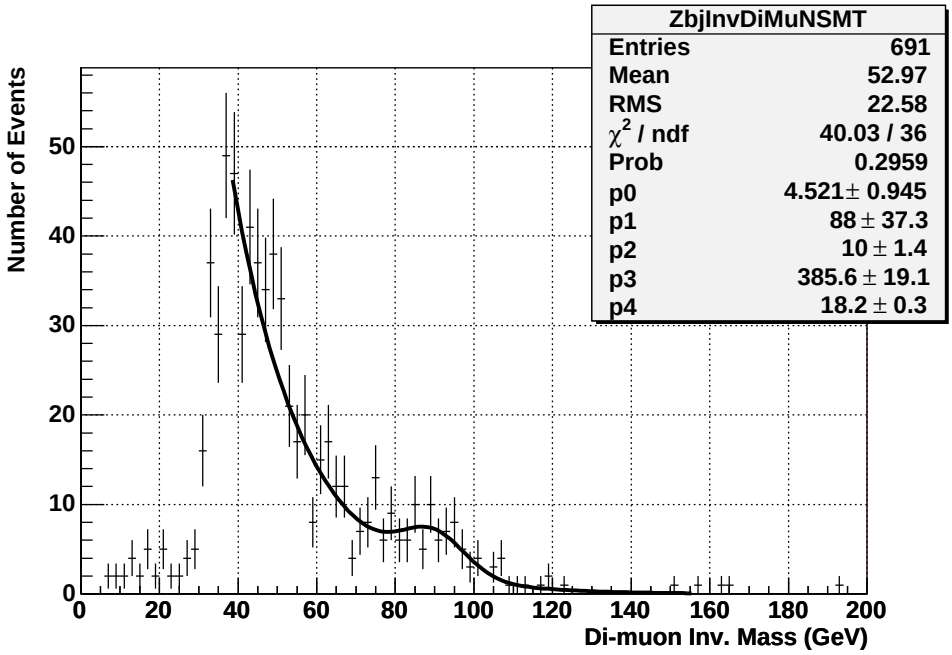

Figure 7.10: Di-muon invariant mass distribution for $Z + 2$ jet with 1 btag events. No isolation requirement is applied. Z and Drell-Yan+QCD are modelled using the same functions as in 0 btag case with p1 and p2 forced to be the same values as the fit results of the 0 btagged events. The numbers of QCD + Drell-Yan and Z are calculated using the same method as in 0 btag too.

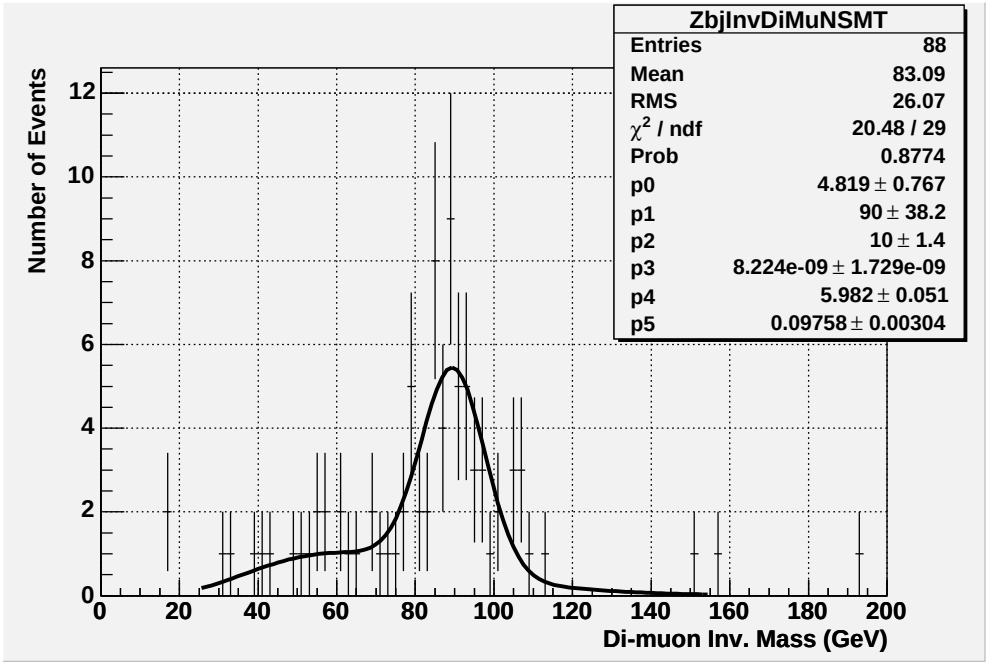

Figure 7.11: Di-muon invariant mass distribution for $Z + 2$ jet with 1 btag events. Isolation requirement 0.02 is applied. Z and Drell-Yan+QCD are modeled using the same functions as in 0 btag case with p1 and p2 forced to be the same values as the fit results of the 0 btagged events.

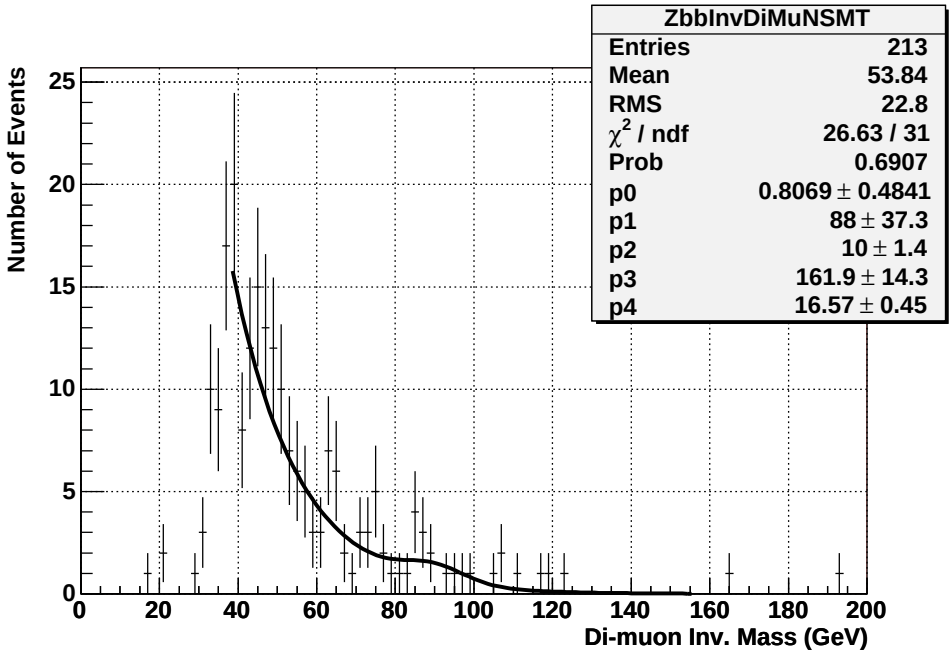

Figure 7.12: Di-muon invariant mass distribution for $Z + 2$ jet with 2 btag events. No isolation requirement is applied. Z and Drell-Yan+QCD are modeled using the same functions as in 1 btag case. The number of Z is calculated by integrating the fit function, the number of QCD+Drell-Yan is the total number of events within the Z mass window subtracted by the number of Z.

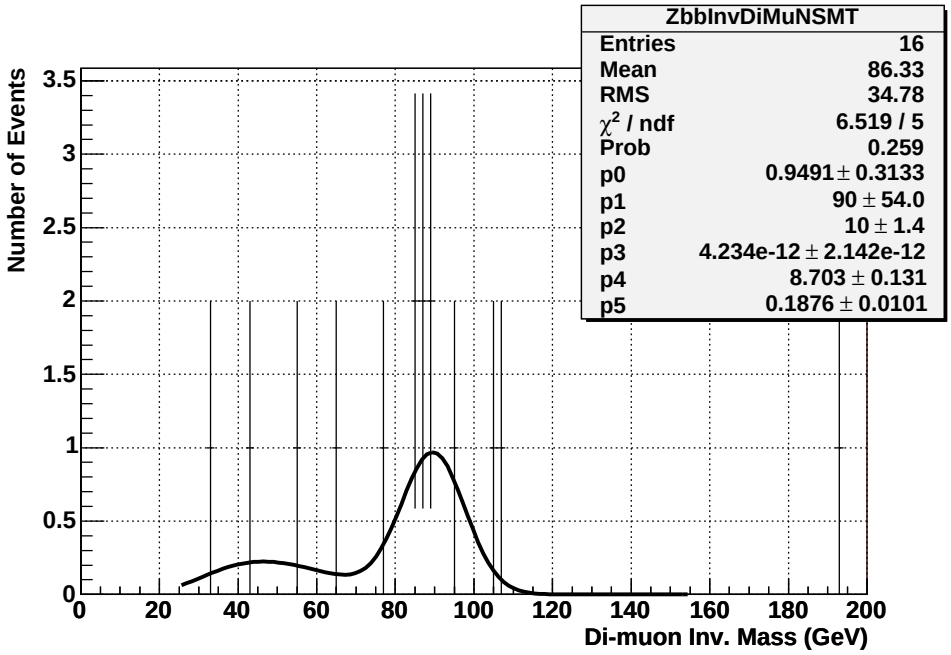

Figure 7.13: Di-muon invariant mass distribution for $Z + 2$ jet with 2 btag events. Isolation requirement 0.02 is applied. Z and Drell-Yan+QCD are modeled using the same functions as in 1 btag case.

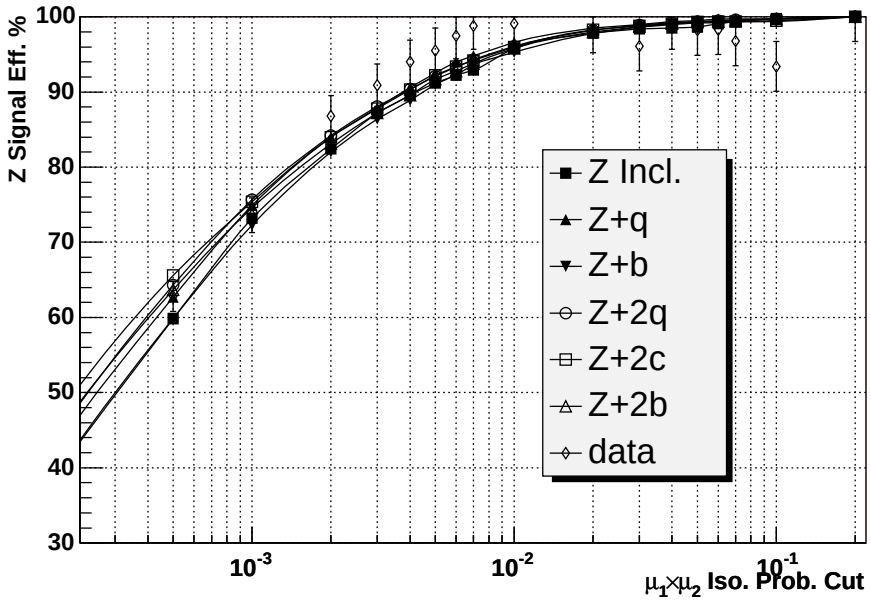

Figure 7.14: Di-muon isolation probability requirement efficiencies for $Z + 2j$ events selected from MC $Z + nj$ and $Z + nb$ samples and data. For the MC samples, the third method is used; for the data sample, the first method is used. As one can see within uncertainties the efficiency from data agrees with those from MC calculations. The average of the MC efficiencies are used in this analysis.

Di-muon isolation requirement efficiency for QCD background

Contrary to the Z/Drell-Yan which has the isolation requirement efficiency independent of the number jets/b-jets, the QCD isolation requirement efficiency is expected to be dependent on the b-jet requirement. We will show in detail in section 8.4 how we use the matrix equation method to subtract the QCD background from the Z/Drell-Yan signal and calculate the QCD efficiency for different number of final b-jets.

The di-muon isolation requirement efficiency for QCD background without b-tagged jets is the simplest to calculate. As discussed before, the single muon isolation probability in this case is a evenly distributed number from 0 to 1. Assuming there is no correlation between the 2 muons in the QCD background, one can model the di-muon QCD isolation probability distribution by using the product of 2 random numbers. This method has been tested using the anti-isolated samples [94]. The isolation requirement efficiency for QCD with 2 muon and 2 jets without b-tag is summarized in Table 7.3.

Iso. Requirement	0.1	0.07	0.05	0.03	0.02	0.01	0.007	0.005	0.003	0.001
ϵ_{iso}^{QCD}	0.330	0.256	0.200	0.134	0.098	0.056	0.042	0.032	0.021	0.008

Table 7.3: Di-muon isolation requirement efficiencies for 2μ+2 jets QCD background without b-tagged jet requirement. The relative statistical uncertainties are less than 1% for all selection points and can be ignored. The systematic uncertainties are discussed in Section 8.4.

The optimized isolation requirement is determined by maximizing the the signal significance $Z/\sqrt{Z+QCD}$ as a function of isolation requirement. It is detailed in section 8.4. The result requirement is set to $f_{iso} = 0.02$.

7.2 b-jet Tagger

The identification of b-jets is essential for many interesting physics processes. Hadrons containing heavy quarks have lifetimes of roughly one picosecond; those with a b-quark live somewhat longer than those with a c-quark, due to a suppression factor from the quark mixing matrix. Monte Carlo simulations show that the distance in the transverse plane between the PV and the point where B-meson decays, L_{xy}, has a mean value of $\approx$ 3 mm, furthermore, 70% of events with $L_{xy} > 1$ mm have at least 2 tracks with $DCA/\sigma_{DCA} > 3.0$. These tracks are excluded from the PV finding algorithm and can form secondary vertices.

There are mainly three kinds of b-jet taggers: the Counting of Signed Impact Parameter (CSIP) [95], the Secondary Vertex Tagger (SVT) [96] and the Jet Lifetime Impact Paramter (JLIP) [97]. CSIP relies on counting the tracks with large impact parameters (IP) in the b-jets; SVT find the existence of the secondary vertex to tag the b-jets; JLIP exploits the fact that a large number of tracks inconsistent with PV interaction implies the existence of the b-jets. In this dissertation the JLIP tagger is used.

7.2.1 Track Jet and Taggability

The JLIP b-jet tagger algorithms rely on the tracks associated with the jet to be tagged; therefore a calorimeter jet is required to be taggable before being tagged with the JLIP b-tagger. A taggable calorimeter jet is defined as a calorimeter jet that matches to a track jet with $\Delta R < 0.5$ in the $\eta - \phi$ plane. The track jet is reconstructed using the same jet cone algorithm discussed in Section 5.3.2 except that calorimeter energy disposition clusters are replaced with the global tracks that satisfy:

- at least one SMT hit
- $p_{\mathrm{T}} > 0.5$ GeV
- $DCA_{xy} < 0.2$ cm and $DCA_z < 0.4$ cm
- at least two tracks are required, one of which has $p_{\mathrm{T}} > 1$ GeV.

The taggability requirement improves the jet quality by reducing contaminations from fake jets originating from noisy cells in the calorimeter, or a high p_{T} photon reconstructed as a jet since in these cases there are normally not enough tracks pointing to them to form a matching track jet. The taggability is generally data sample dependent due to the track requirement. The average taggability measured in several different data samples are shown in Figure 7.15. The measurement of the taggability efficiency and the data-MC scale factor for the data sample used in this dissertation will be discussed in Chapter 8.

7.2.2 V^0 Particle Removal

Besides the B mesons, light-flavored long-lived hadrons such as K_S^0 meson (K_L^0 is not likely to decay within the DØ detector since $c\tau \sim 16$ m where c is speed of light and τ is the rest life time) and Λ baryon can also be sources of tracks with high IP significance. The contamination from these hadrons is $\sim 6-8\%$ in the un-tagged jets and $\sim 20-25\%$ in the heavy-flavor-like jets. To remove this kind of background, the

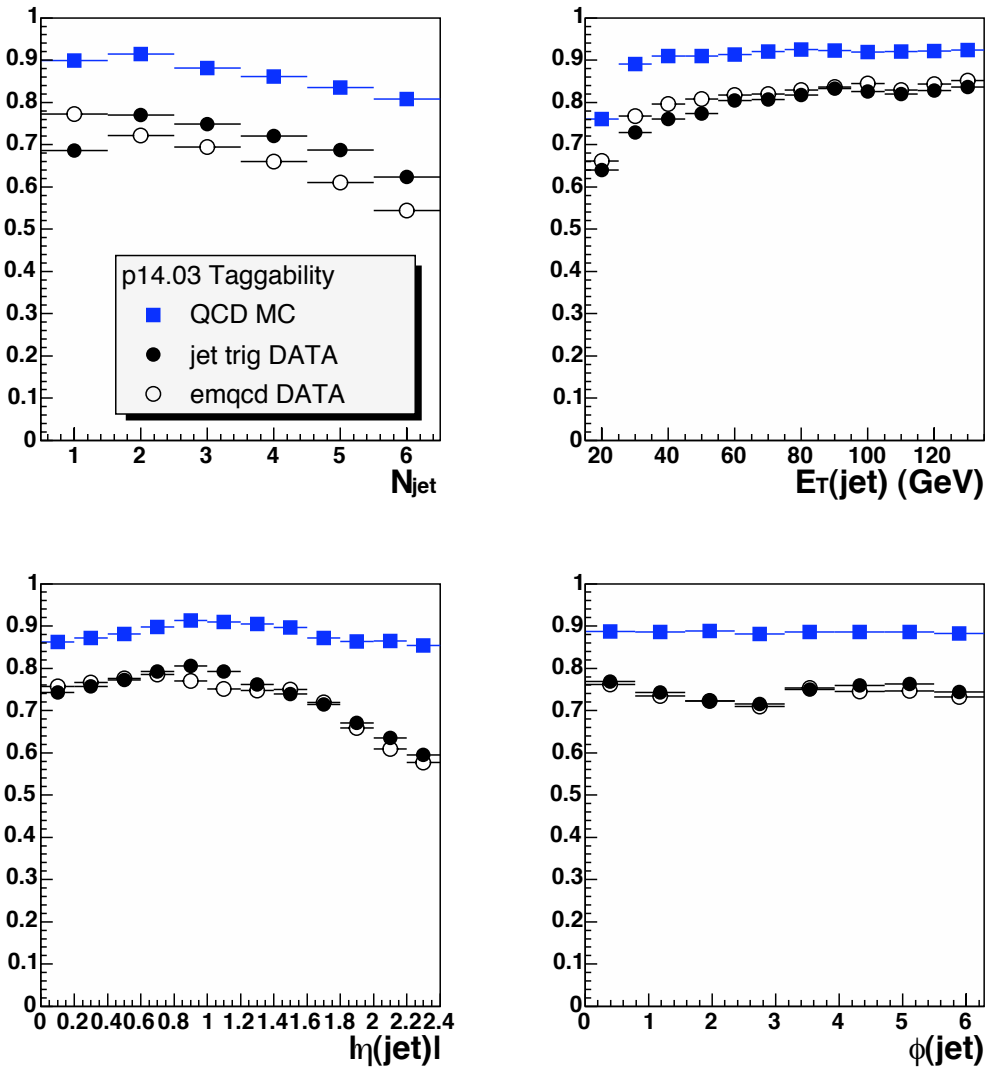

Figure 7.15: The jet taggability is usually data sample dependent since different requirements on the samples affect the track distributions. The plots show the taggability as a function of jet multiplicity, E_{T}, η and ϕ measured for a few different data samples.

invariant masses of all the track pair combinations in the track jet are calculated. If the invariant mass of two tracks with opposite sign is within a mass window of 22 MeV centered about the nominal K_s^0 mass (0.497 GeV) or of 7 MeV around the Λ mass (1.112 GeV), both tracks are removed from the track jet.

Another source of background is from e^+e^- pair production from energetic photons. The two electrons will be reconstructed as two tracks with high DCA. Thus a pair of tracks will be removed if they satisfy the following conditions:

- pull of the angle between tracks in the $(r-z)$ plane less than 3;
- distance between trajectories in $(r-\phi)$ plane less than 30 cm;
- invariant mass less than 25 MeV.

7.2.3 JLIP b-tagging Probability

The JLIP b-tagger uses the IP of the tracks in a jet to do the b-tagging only when the track satisfies the following conditions:

- track and jet separation in the $\eta-\phi$ plane $\Delta R < 0.5$
- track $p_{\mathrm{T}} > 1$ GeV
- $DCA_{xy} < 0.2$ cm and $DCA_z < 0.4$ cm
- at least 1 SMT hit

A jet lifetime probability is constructed from the signed impact parameter (IP) of individual tracks [98].The determination of the sign of the IP is shown in Figure 7.16, if the DCA points to the same direction as the momentum direction of the jet, the IP is taken to be positive; otherwise, it is defined to be negative.

Tracks from the decay of a b- or c-flavored meson will tend to have a large positive IP since the 3-momentum vector of the SVT should always have the same direction as the vector from the PV to the DCA; while in the case of the tracks in a light flavored jet originated from the PV, the IP is mainly due to the mis-measurement of the limited SMT resolution, therefore these two vectors have randomly distributed directions and generate symmetrically distributed positive and negative signed IP. Thus the background (light flavor jets) IP distribution (including resolution of the smeared RECO PV) may be obtained from the negative signed IP distribution for QCD multi-jet events.

The IP significance $\mathcal{S}_{IP}$ is a better variable to define the displacement of a track from the PV:

$$\mathcal{S}_{IP} = \frac{\mathrm{IP}}{\sigma_{\mathrm{IP}}} \tag{7.7}$$

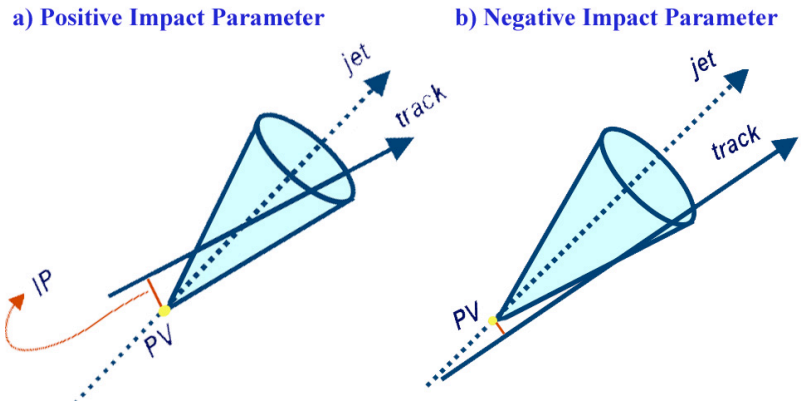

Figure 7.16: Determination of the sign of the track IP. The track gets a positive impact parameter with respect to the jet if the track crosses the jet axis in front of the PV (towards the jet) and gets a negative impact parameter if it crosses behind the PV.

where $\sigma_{\rm IP}$ is the IP resolution after the correction for multiple scatterings. In order to parameterize $\sigma_{\rm IP}$, the tracks are classified into 5 categories according to their CFT and SMT coverage [97].

We will denote the negative part of the signed IP significance distribution as the IP resolution function $\mathcal{R}(\mathcal{S}_{IP})$. In order to parameterize $\mathcal{R}(\mathcal{S}_{IP})$, the five track categories mentioned above are further classified into 29 categories by the track χ^2, η and $p_{\rm T}$. The IP resolution functions are shown in Figure 7.17 for tracks of various qualities. As in Section 7.1.1, we can define a track probability $\mathcal{P}_{trk}$ which indicates the level at which a track in a jet with IP significance $\mathcal{S}_{IP}$ is consistent with the hypothesis of the jet being a light flavor jet (equivalently being originating from the primary vertex):

$$\mathcal{P}_{trk}(\mathcal{S}_{IP}) = \frac{\int_{-50}^{-|\mathcal{S}_{IP}|} \mathcal{R}_{IP}(s)ds}{\int_{-50}^{0} \mathcal{R}_{IP}(s)ds} \tag{7.8}$$

Distributions of $\mathcal{P}_{trk}$ for jet trigger data (mostly QCD multijet events) and MC samples are shown in Figure 7.18. Note that tracks from heavy quark jets have a peak near zero. The peak is also present, but much smaller, for light quark jets. The (positive) JLIP probability $\mathcal{P}^{+}_{jet}$ of a jet is calculated by all tracks in the jet with positive IPs, and it gives the probability that the jet is originated from the primary vertex:

$$\mathcal{P}^{+}_{jet} = \Pi^{+} \sum_{k=0}^{N^{+}_{trk}-1} \frac{(-\ln \Pi^{+})^{k}}{k!} \tag{7.9}$$

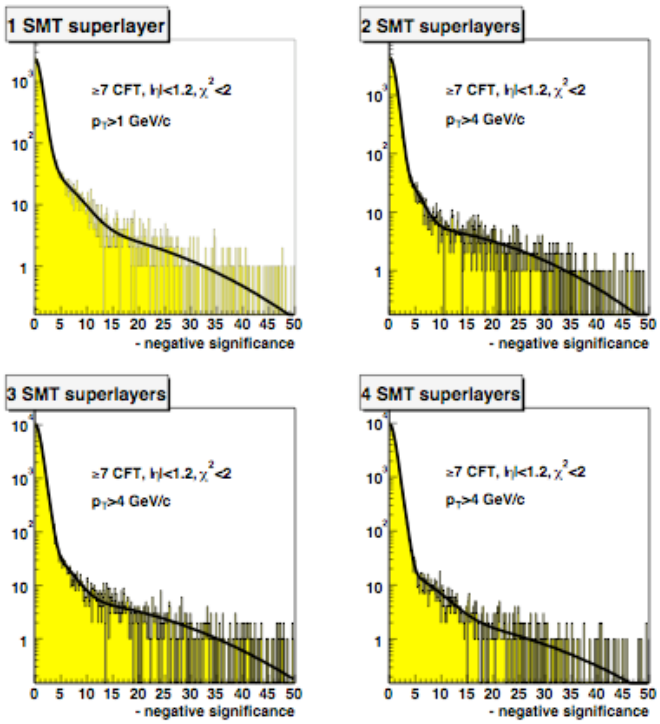

Figure 7.17: IP resolution function for four out of the 29 kinds of tracks with different numbers of SMT and CFT hits, track χ^2, p_{T} and η. The distributions are parameterized with the sum of four Gaussian distributions [97].

where $\Pi^+ = \prod_{i=1}^{N^+_{trk}} \mathcal{P}_{trk}$, and N^+_{trk} is the number of positive IP tracks. A similar quantity, the negative JLIP probability $\mathcal{P}^-_{jet}$, is determined from tracks with negative IPs. The positive and negative JLIP probabilities $\mathcal{P}^+_{jet}$ and $\mathcal{P}^-_{jet}$ are shown in Figure 7.19. Clearly a requirement on the JLIP probability $\mathcal{P}^-_{jet}$ of a jet can be used to tag whether the jet is a b-jet or a light flavor jet. The JLIP MC b-tag efficiencies for $b-$ and $c-$jets as a function of the light flavor jet mis-tag rate are shown in Figure 7.20. A series of JLIP $b-$tag requirement points exist to tag b-jets: ExtraTight, Tight, Medium, Loose and ExtraLoose. A jet is considered b-tagged if its $\mathcal{P}^+_{jet} < \sim 0.1\%$, $\sim 0.4\%$, $\sim 0.7\%$, $\sim 1.4\%$, $\sim 2.0\%$ $\sim 4.0\%$, respectively. Notice that for the light flavor jets, the JLIP probability distribution is almost flat between 0 and 1 (see Figure 7.19), so the corresponding light flavor jet mis-tag rates for these requirement points are about the same as the requirement value, *eg.* $\sim 0.1\%$, $\sim 0.3\%$, $\sim 0.5\%$, $\sim 1.0\%$, $\sim 2.0\%$ $\sim 4.0\%$, respectively.

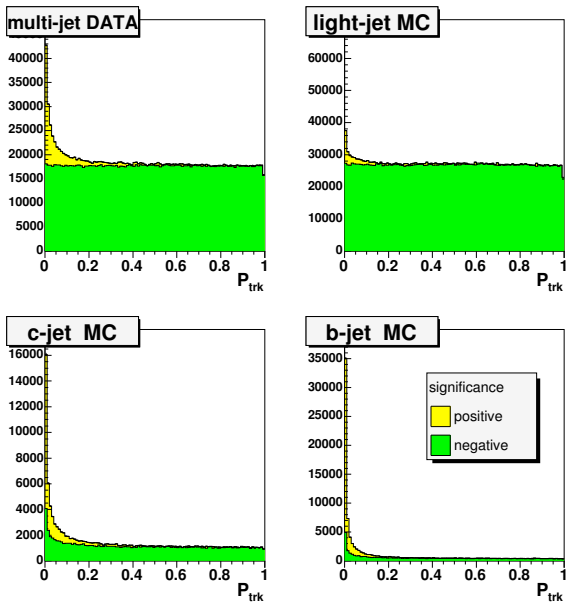

Figure 7.18: The track probability distribution for jet trigger data, light jet MC, c-jet MC and b-jet MC samples [97].

7.2.4 JLIP Tag Rate Functions

As seen from the above discussion, the JLIP probability calculation involves detailed track-in-jet and vertex analyses. The detailed modeling of tracks in jets is a difficult task, giving rise to large systematic uncertainties. For MC samples where the jet flavor is well deducible from the parent parton of the jet (determined by searching

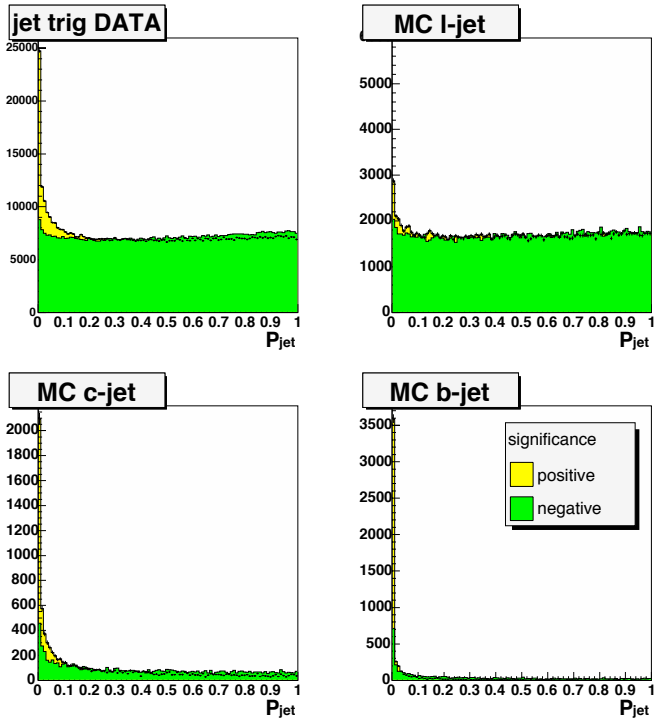

Figure 7.19: The positive and negative JLIP probabilities $\mathcal{P}^{+}_{jet}$ and $\mathcal{P}^{-}_{jet}$ distributions for jet trigger data, light jet MC, c-jet MC and b-jet MC samples. When the jet energy gets higher, the multiplicity of long lived particles and their average decay lengths increase, giving larger IP to their decay products. The charged particles get closer to the jet axis, leading also to a larger number of wrongly signed IP. These effects contribute to explain why the negative and positive tag rates increase with E_{T} for light flavor jets as shown in the upper two plots.

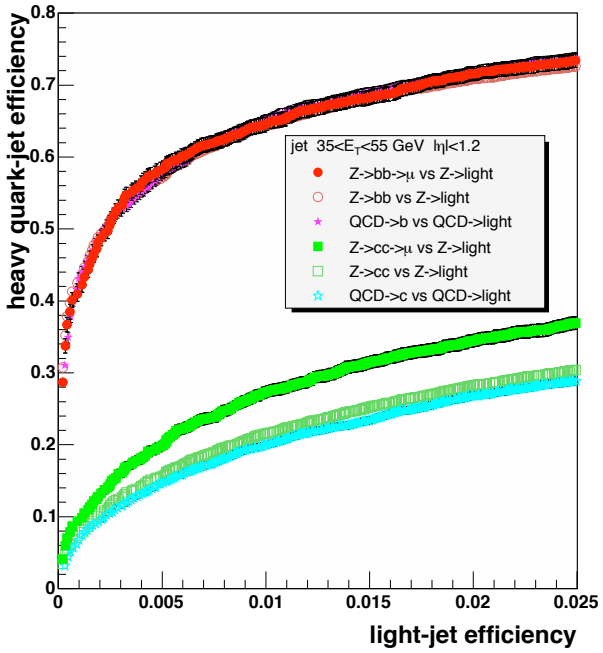

(a)

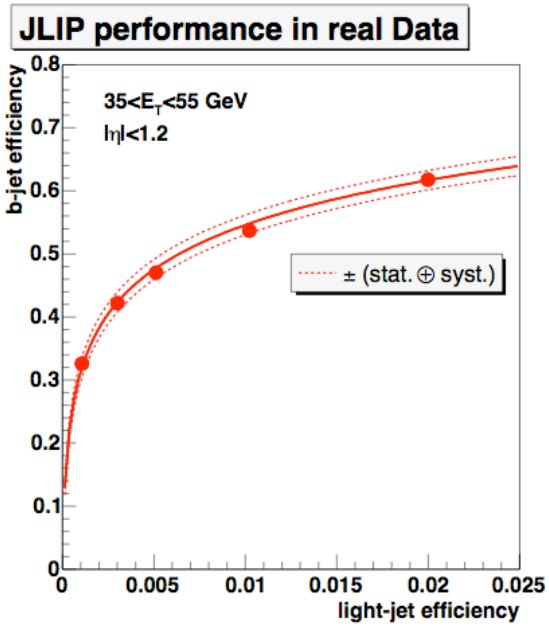

(b)

Figure 7.20: (a). The JLIP b-tagger efficiencies for $b-$ and $c-$ flavor jets *vs.* the mis-tag rate of the light flavor jets for various p14 MC data samples [97]. Note the presence of a muon in jet improves the tag efficiency for $c-$jets due to the muon track. The presence of the muon has almost no effect for the b-jet tagging. (b). the JLIP b-tagger efficiencies in real detector data [97].

the record of generated partons for b- or c-quarks within the jet cone), these complexities can be reduced — the only thing one needs to know is the rate (efficiency) of a given flavor jet passing the JLIP b-tagger requirement. The rates for each flavor of jet are provided by the JLIP b-tagger in a set of functions called the tag rate functions (TRF). The tagging probability can be used to calculate a weight for the contribution of each event to the total expected yield.

The TRF is expected to increase with the jet E_{T} since with higher E_{T} the track multiplicity in the jet is increased and the IP resolution is improved. It should decrease for jets in the forward region due to the reduced SMT coverage. Thus the TRFs are parameterized by jet E_{T} and η. [2]

The tracks in jets with negative impact parameter in jet trigger data samples can be used to determine the light flavor jet TRF. The effects of the $b-$ and $c-$ flavor jet contaminations in data are corrected using the MC QCD samples. The $b-$ and $c-$jets TRFs are measured in pure MC samples. $b-$ and $c-$ jet TRF data/MC scale factors SF_b and SF_c are derived by comparing the b-tagging efficiency to collider data, these scale factors will be folded into the b-tagged MC events to account for the difference between the detector data and the MC samples (see Section 8.3.3). The TRFs for light flavor, $c-$ and $b-$ jets are shown in Figures 7.21 – 7.23, respectively.

7.2.5 Double JLIP b-tag

In this analysis, two b-tagged jets are searched for in the data sample. Similar to the muon pair from the Z boson decay discussed in Section 7.1.2, the two b-jets are expected to be from the Higgs boson decay, and their JLIP probabilities are expected to be correlated. Thus we would like to make a requirement on the product of the JLIP probabilities of the two b-jets in an event instead of the fixed point requirement on both of the jets. The difficulty is that the TRFs are only officially available for the five selection requirement points mentioned in Section 7.2.3. In order to make a requirement on the product of the JLIP probabilities, much more looser selection requirement points than the currently loosest 4% are needed, but they are not available. So we will use the same fixed requirements for both of the jets, but optimize the JLIP b-tagger requirement point. By maximizing the signal significance $S/\sqrt{B}$ where S and B stand for the number of expected ZH signals and the backgrounds after double b-tagging, the optimized b-tag requirement point for double b-tag is determined to be $2 \sim 4\%$, contrary to the nominal standard selection requirement 1% [99]. In this analysis we will choose 4% as the JLIP b-tag requirement.

[2] The TRF should also be the function of luminosity, vertex, *etc*, for simplicity we are not considering their effects.

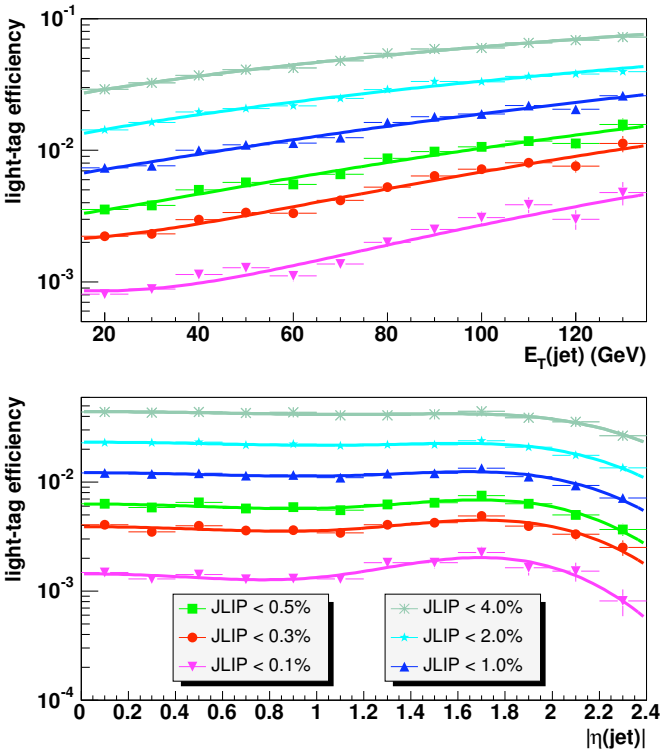

Figure 7.21: Mistag rate for light flavor jet as a function of jet E_{T} and η [97].

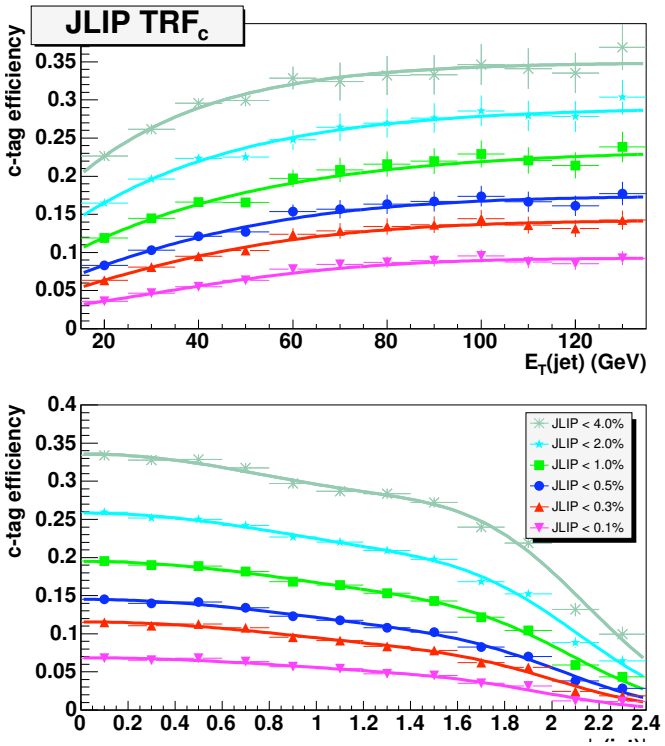

Figure 7.22: TRFs for c-jets as a function of jet E_{T} and η [97].

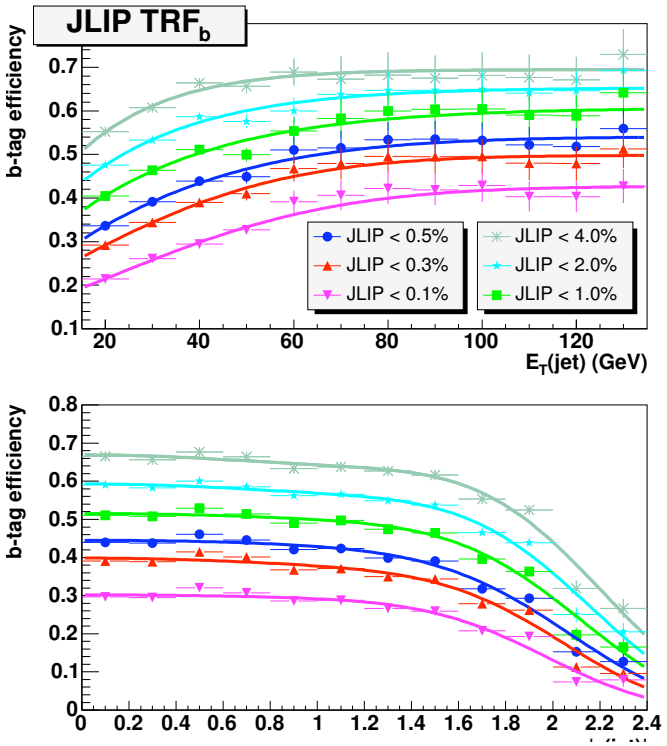

Figure 7.23: TRFs for $b-$jets as a function of jet E_{T} and η [97].

Chapter 8

ZH Analysis

Having finished the preparation, we now describe the search for the ZH signal. First, the detector data set and the MC samples are selected and prepared. The single muon trigger is used in filtering the detector data set so that the luminosity and the trigger efficiency can be calculated. The cross sections for various MC samples are calculated using the MCFM and other theoretical models. Then for the detector data the events that contain a reasonable quality pair of muons and jets are selected. The di-muon isolation probability requirement is applied so that the Z event signals can be selected and the QCD multi-jets events can be suppressed. The remaining QCD background in the selected detector data is estimated. The taggability and JLIP b-tag is then applied on the two jets. Only those events with two b-tagged jets are retained. For the MC samples, the same set of event selection criteria are applied so that the background to the ZH signals can be obtained. The MC samples are normalized by the luminosity in the detector data, the trigger efficiency and various data/MC scale factors for each of the event selection requirements. Then the invariant mass distributions of double b-jet for both the detector data and the MC backgrounds are plotted together. ZH signals are searched for as a deviation in these distributions between the detector data and the expected background from the MC samples. The upper limit on Higgs associated production cross sections can be then set. The procedure is shown in Figure 8.1

8.1 Data Set

8.1.1 Detector Data

The data used in this analysis was collected at the DØ experiment between April 2002 and June 2004. For our study the common sample group (CSG) 2MUhighPt skim [100] is used which simply requires the presence of 2 loose muons with $p_{\mathrm{T}} > 15.0$

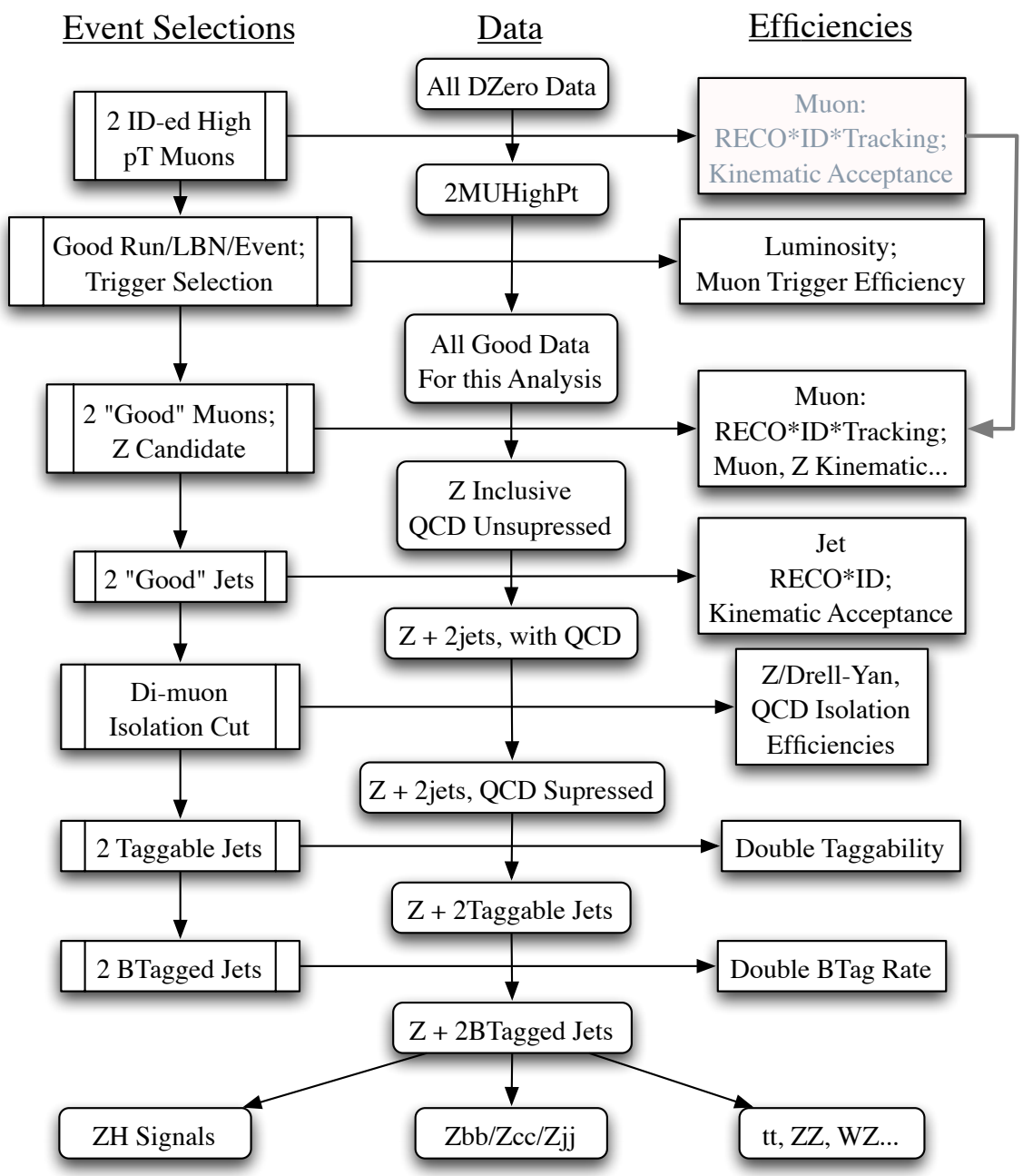

Figure 8.1: The requirement flow of the event selection. All the efficiencies are measured with respect to the data before the corresponding requirement, for example, the isolation efficiency is measured w.r.t $Z + 2j$ events, *eg.* the number of $Z + 2$ jets events after the isolation requirement divided by the number of $Z + 2$ jets events before the isolation requirement. There are two muon selection efficiencies, the first one is gray. Since the second one is tighter than the past one, the efficiency will be measured at the second stage.

GeV. The events are reconstructed with different minor versions of p14 DØ RECO. All events have been fixed for different reconstruction deficiencies with the pass2 TMB fixing. Object level corrections are done with d0correct v8. The analyze package is based on the top group Ipanema *top_analyze* package and top_trees [101]. The data is post-processed by this version of *top_analyze*, too.

The runs flagged as "bad" by SMT, CFT or MUON detectors are rejected from the analysis. We also reject events flagged as "bad" by the Calorimeter Data Quality Group [102].

We require events to have fired triggers listed in Table 8.1. The events within the luminosity blocks flagged as "bad" by lm_tools utility getLuminosity using these triggers are also removed from the analysis [103]. The remaining number of events is 128,874.

Run Range	Trigger Name	$\int \mathcal{L}$ (pb^{-1})
173522-175517	MUW_W_L2M3_TRK10	17.9
175518-194566	MUW_W_L2M3_TRK10	312.6
194567-196584	MUH1_TRK10	39.4

Table 8.1: Triggers used for the analysis. The data set is divided into 3 ranges. The first 2 ranges contain data taken with the trigger version less than 12. The last one contains data from trigger version that is greater than or equal to 12. The division of the first 2 ranges is due to the L2CFT and L3 tracking improvement described in [56].

Finally the events flagged as "coherent noise", "missing crate", "noon noise" or "ring of fire" are rejected by the *cal_daq_quality* package. There are 20,423 events contains these noises.

After the above requirements, a total number of 108451 events are left, corresponding to the integrated luminosity of 370 pb^{-1}. The integrated luminosity is lower than the other p14 Higgs searches because of the simplified muon trigger selection.

We introduced the muon isolation discriminant and muon isolation probability in this analysis in order to optimize the di-muon isolation requirement. To construct the muon isolation discriminant the JetTrigger skimmed events (at least one JCCB jets with $p_{\mathrm{T}} > 10$ GeV as described in Section 5.3, also at least one of all the muon triggers must have been fired.) were used. About 6 million events were selected after requiring two or more jets and only one reconstructed muon (with the same kinematic requirements as applied to event selection, see section 8.2).

8.1.2 MC Samples

Table 8.2 lists the Higgs signal samples, Table 8.3 lists the the background samples. The cross sections for the Higgs channel are based on the NLO calculations in [89]. The cross sections for the background samples are based on the NLO MCFM calculations [90, 91, 92, 93]. The PDF used was CTEQ5M. The PDG'04 [104] branching ratios are used in the calculations. These MC samples were run thought the same DØ RECO and top analyze packages as the data but not through the trigger simulation.

M_H (GeV)	$\sigma\times$Br (pb)	SAM req. ID	# of events
105	0.0040	11667	5000
115	0.0028	11668	5000
125	0.0018	11669	5000
135	0.0011	11670	5000
145	0.0005	11671	5000

Table 8.2: PYTHIA v6.203 generated MC Higgs events for the channel $ZH \to \mu^+\mu^- + b\bar{b}$.

Process	$\sigma\times$Br (pb)	SAM req. ID	Generator	# of events
$Zbb \to \mu\bar{\mu}b\bar{b}$	0.533	11409, 11410	Alpgen+Pythia	96500
$Zcc \to \mu\bar{\mu}b\bar{b}$	1.15	15553-15560	Alpgen+Pythia	46250
$Zjj \to \mu\bar{\mu}bb$	29.4	10721-10724	Alpgen+Pythia	188000
ZZ inclusive	1.56	15528	Pythia	53500
WZ inclusive	3.68	15527	Pythia	34250
$t\bar{t} \to \ell\nu b\ell\nu\bar{b}$, $M_t = 175$ GeV	0.671	15385	Alpgen+Pythia	36000
$t\bar{t} \to \ell bbjj$, $M_t = 175$ GeV	2.676	15326, 15343, 15344	Alpgen+Pythia	1353000
$Z \to \mu\mu$	266.7	12014, 12016	Pythia	202000

Table 8.3: PYTHIA v6.203 (+Alpgen v1.3x) generated MC events for the backgrounds of the channel $ZH \to \mu^+\mu^- b\bar{b}$. $Zcc \to \mu^+\mu^- b\bar{b}$ sample is a special parameterization from $W + c\bar{c}$ [2].

8.2 Event Selection

The final state of the signal processes studied contains 2 high p_{T} muons from Z boson decay and 2 b jets from Higgs boson decay. The event selection criteria on the

jets, muons and the Z candidate are listed below:

- 2 or more good jets, where a good jet is defined as [105]
  - T42 and L1 confirmation
  - $0.05 < EMF < 0.95$
  - $CHF < 0.4$
  - $n90 > 1$
  - Jet energy scale corrections
  - $E_T > 20.0$ GeV
  - $|\eta| < 2.5$
- Jet taggability selection: require each jet match to a track-jet within $\Delta R \equiv \sqrt{\Delta\eta^2 + \Delta\phi^2} < 0.5$
- Jet B-tagging selection [97], using the JLIP b-tagger at the ExtraLoose (0.04 mis-tag rate) operating point.
- Muon selection
  - 2 or more muons with loose muon quality requirement [81]
  - Each muon has a central track match
  - Number of SMT hits > 0
  - $p_{\mathrm{T}} > 15$ GeV
  - $|\eta| < 2.0$
  - Track $r - \phi$ DCA < 0.25 cm w.r.t the primary vertex.
  - The muons are required to be isolated
- Z candidate selection
  - The 2 candidate muons have opposite charge
  - The di-muon's opening angle in the transverse plane $\Delta\phi > 0.4$
  - Di-muon invariant mass satisfies 65 GeV $\leq M_{\mu_1,\mu_2} \leq 115$ GeV

At each requirement stage an inefficiency on the signal and background is introduced. Figure 8.1 shows the requirement flow chart and all the efficiencies that need to be measured and what events they are measured with respect to.

There can be more than two muons and two b-taggable jets in an event. In such case, all the combinations of muon pairs are tested with the Z muon selection

requirements, the pair of muons which has the invariant mass closest to the Z boson mass is retained; all the combinations of b-jet pairs are also tried, the one which has the invariant mass closest to the expected Higgs mass is retained.[1]

8.3 Efficiencies and Scale Factors

As shown in Figure 8.1, at each stage of the event selection requirement, an inefficiency is introduced. The requirement flow and the inefficiencies at all the stages in the detector data are listed in Table 8.4. The same set of the requirements are also applied to the MC background samples. In order to match the combined MC backgrounds to the detector data, the ineffiicency and the corresponding data/MC correction scale factor for each MC sample at each requirement stage needs to be calculated using the convolution method discussed in previous chapters. These efficiencies and scale factors are:

- single muon trigger efficiency
- muon RECO*ID data/MC SF
- jet RECO*ID data/MC SF
- jet taggability SF
- JLIP b-tagger data/MC SF
- muon isolation requirement efficiency
- the acceptances of all the remaining kinematic requirements

The determination of these efficiencies are discussed in the following sections. The uncertainties of these efficiencies and scale factors are discussed in Section 8.7.

8.3.1 Event Averaged Muon Efficiencies

As discussed in Sections 4.3 and 5.4.3, muon trigger, ID, tracking and SMT hit efficiencies for a single muon are measured using muo_cert package[106]. The data sample used to measure the efficiencies is the 1MULoose skim [107].

These efficiencies need to be applied to all the MC samples for the data and MC comparisons since the MC events are not run through the trigger simulation. In doing that we need to calculate the average event efficiency by convoluting the single

[1]For all the 545 events in the detector data that contain Z signals plus two good jets, only two events have three good muons.

Event Selection Requirement	# of Events	Relative Eff.	Absolute Eff.
None	108451	100%	100%
Single Muon Trigger	89266	82.3%	82.3%
2+ RECO-ed Muons	68825	77.1%	63.5%
2+ Loose Muons	68808	100%	63.4%
Muon-Track Match	68802	100%	63.4%
# of Muon SMT Hit	41419	60.2%	38.2%
Muon p_{T}	40852	98.6%	37.7%
Muon η	40508	99.2%	37.4%
Muon $r-\phi$ DCA	31057	76.7%	28.6%
Muon Open Angle	28308	91.1%	26.1%
Muon Charge	27359	96.6%	25.2%
Di-Muon Iso. and Z Mass Window	20838	76.2%	19.2%
2+ Standard Jets	1705	8.2%	1.57%
Jet E_{T}	590	34.6%	0.05%
Jet η	545	92.4%	0.05%
2+ Taggable Jets	353	64.9%	0.03%
Jet JLIP B-tag	10	2.8%	0.01%

Table 8.4: Detector data event selection requirement flow and the efficiency at each requirement stage.

muon efficiencies measured above. As discussed in the appendix, the convolution is done using Eq. A.1 where ζ is replaced with the following for trigger efficiency, (ID×Tracking) and SMT hit efficiency respectively:

$$\zeta_{trig} = L1_{mu}(\eta,\phi)\cdot L2_{mu}(\eta,\phi)\cdot L3_{mu}(\eta,\phi) \quad (8.1)$$

$$\zeta_{ID\ \cdot Trk} = ID_{mu}(\eta,\phi)\cdot Trk_{mu}(\eta,\phi) \quad (8.2)$$

$$\zeta_{SMTHit} = SMT(\eta,\phi) \quad (8.3)$$

where $L1, L2, L3$ are the single muon L1/L2/L3 trigger efficiencies respectively, ID, Trk are the ID and tracking efficiencies, and SMT is the efficiency of a muon producing a SMT hit. The convolution should be done over all the good events without any muon or jet selection applied (see Figure 8.1).[2] Yet in order to get the efficiency values in Eq. 8.1 and 8.2, the muons must have been RECO-ed and this will introduce the muon RECO efficiency. So in order not to double count the RECO efficiency the convolution is done over all the good events that have two or more RECO-ed muons, and the efficiencies are measured with respect to the number of events in which two or more muons are found instead of the number of all good events.[3] Due to the statistical limitations the various single muon efficiencies are expressed just as functions of muon η and ϕ.

The convoluted efficiencies are the (expected) data efficiency for each of the MC samples. For the trigger efficiency Eq. A.4 is used since we required single muon triggers; for the (ID×tracking) and SMT hit efficiencies Eq. A.5 is used since we required two or more loose muons that have central track matching and each muon has at least one SMT hit in a event. We did not try to fit the efficiencies. Instead the bin values in the efficiency plots are used. The results for all MC samples are listed in Table 8.5.

The MC muon (ID×Tracking) and SMT hit efficiencies for each of the MC samples are calculated by the ratio of the number of events that have at least two loose muons with central track match or that have at least two muons with at least a SMT hit and the total number of events respectively, as shown in Figure 8.1.

The muon p_{T}, η and ϕ distributions of the selected $Z \to \mu^+\mu^-$ events from the MC samples in Table 8.2, 8.3 are compared with those from the data sample as shown in Figure 8.2. It is clear the MC describes the kinematic variables of muons from $Z \to \mu^+\mu^-$ events acceptably, so the efficiencies convoluted over the MC sample are

[2]For MC samples, the good event selection also need to be applied as shown in Figure 8.1, namely there is a small potion of events that are labeled as having the 4 kind of CAL noises, so the total number of effective MC events are slightly smaller than those listed in Tables 8.2 and 8.3.

[3]An alternative and better way is to use the muon ID×Tracking efficiency data/MC scale factor, the difficulty is that there is no priori knowledge of the $Zjj, Zcc, Zbb, t\bar{t}$... composition of data, and the muon ID×Tracking efficiencies are notably different as shown in Table 8.5, so we cannot determine the data/MC scale factor directly.

reliable descriptions of efficiencies for real data.

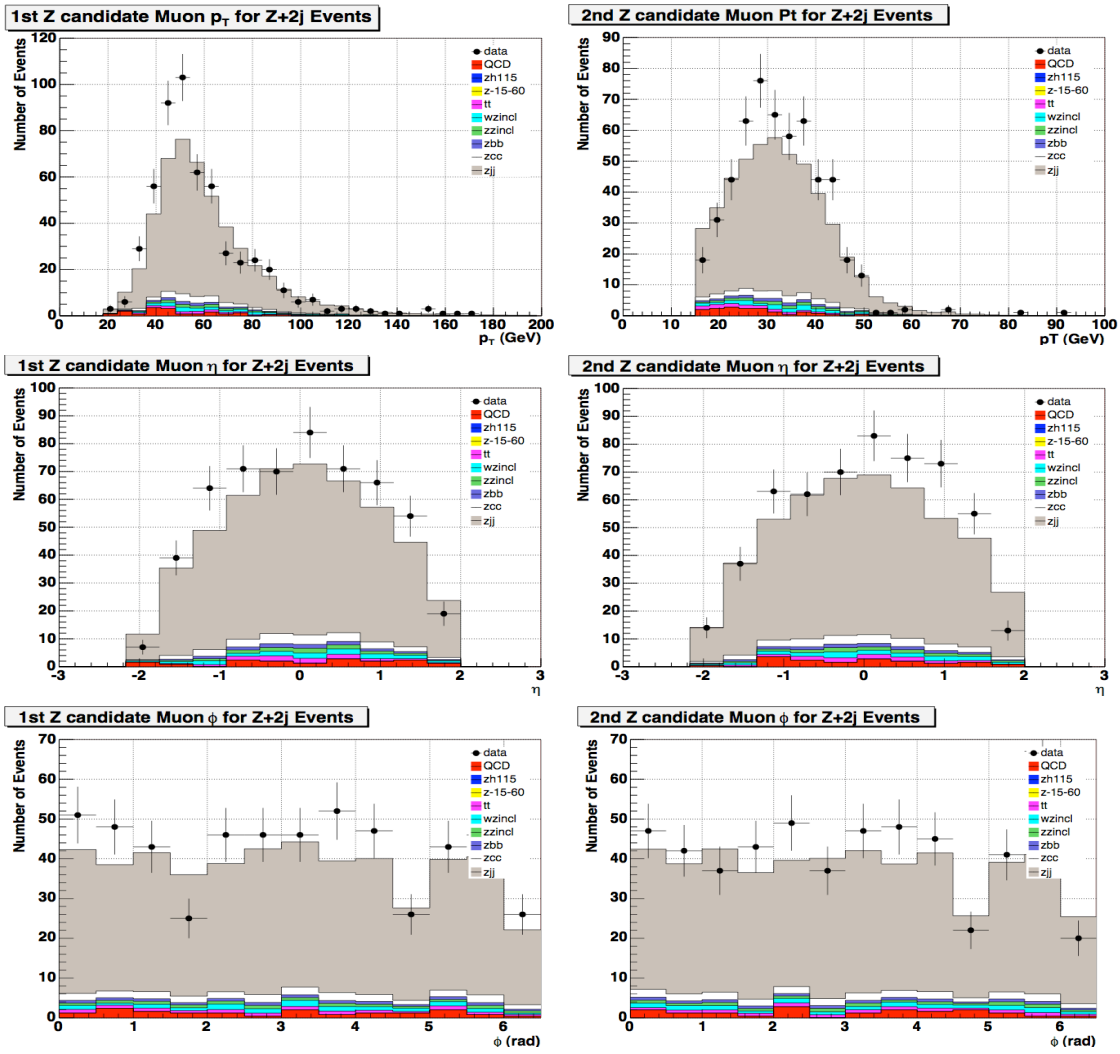

Figure 8.2: p_{T}, η, ϕ distributions of the first and second Z candidate muon for $Z + 2$ jet 0 btag events.

8.3.2 Event Averaged Jet Efficiencies

The event average of the MC jet RECO×ID efficiency is calculated by the ratio of the number of events that have $Z + 2$ or more jets(no good jet requirement applied) to the number of the events that have passed the Z selection.

Process	Zbb	Zcc	Zjj	$ttdl$	$ttsl$	ZZ	WZ	Z
Trigger	0.831	0.839	0.806	0.873	0.908	0.828	0.802	0.782
(ID×Trk)$_{data}$	0.606	0.645	0.557	0.502	0.487	0.478	0.465	0.513
(ID×Trk)$_{MC}$	0.673	0.636	0.573	0.405	0.34	0.562	0.406	0.504
(ID×Trk) SF	0.901	1.01	0.972	1.24	1.43	0.85	1.15	1.02
(SMT Hit)$_{data}$	0.679	0.727	0.642	0.747	0.822	0.717	0.701	0.613
(SMT Hit)$_{MC}$	0.823	0.842	0.805	0.85	0.873	0.836	0.827	0.784
(SMT Hit) SF	0.824	0.863	0.798	0.879	0.942	0.858	0.847	0.782

Process	$ZH(105)$	$ZH(115)$	$ZH(125)$	$ZH(135)$	$ZH(145)$
Trigger	0.875	0.876	0.876	0.878	0.882
(ID×Trk)$_{data}$	0.686	0.704	0.695	0.7	0.711
(ID×Trk)$_{MC}$	0.775	0.778	0.783	0.791	0.797
(ID×Trk) SF	0.886	0.905	0.888	0.885	0.892
(SMT Hit)$_{data}$	0.734	0.74	0.735	0.736	0.743
(SMT Hit)$_{MC}$	0.84	0.831	0.848	0.846	0.842
(SMT Hit) SF	0.874	0.89	0.866	0.87	0.883

Table 8.5: Event average of muon (trigger × ID × tracking × SMT Hit) efficiency and muon ID×Tracking, SMT hit data/MC scale factor(SF) for the di-muon events for each MC sample. The branching ratio is also included automatically in these efficiencies for WZ, ZZ and $t\bar{t}$ processes. $ttsl$ and $ttdl$ stand for $t\bar{t}$ single leptonic and di-leptonic decay channel respectively. The systematic and statistical uncertainties in this and the following tables that are not explicitly listed here but in Section 8.7.

For each MC sample the jet RECO×ID data/MC scale factor of a single jet is convoluted with the selected Z events as shown in Figure 8.1 to get the event average. Since two or more jets are required for each event, Eq. A.5 is used to calculate the event average, where ζ is replaced with jet RECO×ID SF.

The event average of the MC jet (RECO×ID) efficiencies, the data/MC scale factor and the data efficiencies for ZH signal and backgrounds are listed in Table 8.6.

Process	Zbb	Zcc	Zjj	$ttdl$	$ttsl$	ZZ	WZ	Z
MC Eff.	0.361	0.375	0.363	0.812	0.989	0.528	0.516	0.0509
Data Eff.	0.281	0.29	0.28	0.761	0.987	0.458	0.422	0.0341
Data/MC SF	0.777	0.774	0.77	0.938	0.997	0.868	0.818	0.669

Process	$ZH(105)$	$ZH(115)$	$ZH(125)$	$ZH(135)$	$ZH(145)$
MC Eff.	0.809	0.827	0.84	0.87	0.877
Data Eff.	0.716	0.751	0.769	0.814	0.819
Data/MC SF.	0.885	0.908	0.915	0.935	0.934

Table 8.6: Event averages of jet RECO×ID efficiencies for the selected Z candidates with two or more jets for ZH signals and the backgrounds. The branching ratio for the double jet production is also included in these efficiencies.

To ensure the MC samples model the jet well, jet multiplicity, p_{T}, η and ϕ distributions are compared with those of jets in data. All of them require the presence of a $Z \to \mu^+\mu^-$ signal. The plots are shown in Figures 8.3-8.6. The simulation agrees with the data acceptably.

8.3.3 Jet Taggability and B-tag Efficiency

The JLIP b-tagger provides the b-tag rate data/MC scale factor for a single b-jet and c-jet. The event average of the b-tag TRF (data/MC) scale factor can be calculated using the convolution method. The light jet tag rate is determined directly from data so no scale factor is needed.

The single jet taggability as a function of a given jet kinematic variable is derived by dividing the kinematic variable distribution of the taggable jets with that of all the good jets. This was done for events containing the $Z + 2$ jets events in both the detector data and each of the MC samples. The results are shown in Figures 8.7-8.16.

Before determining taggability data/MC scale factor, there are some behaviors of the jet taggability worth mentioning:

- The taggability in the multi-jet sample may be biased because the found muon(s) often occur within a jet, so at least one track is already provided by the muon.

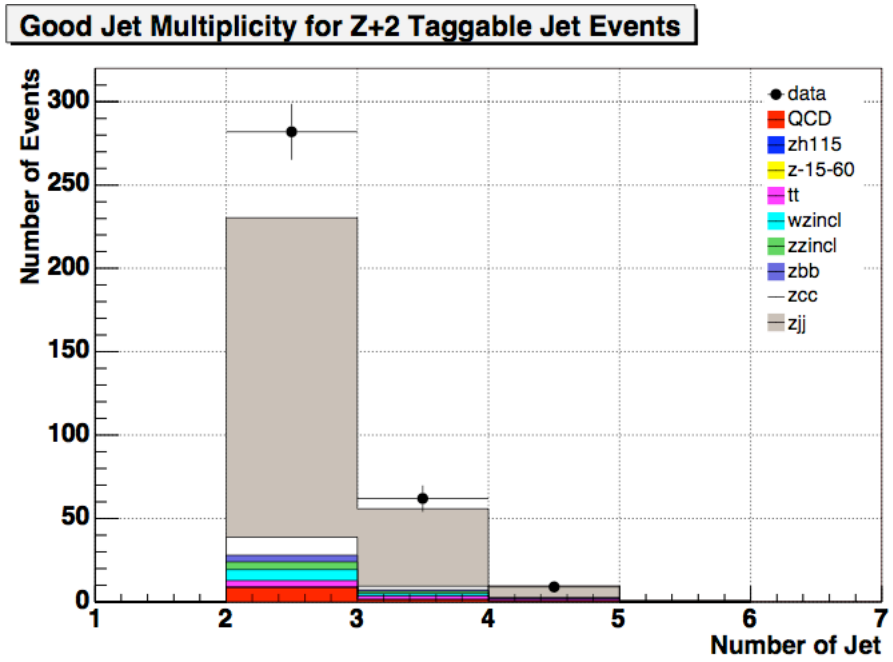

Figure 8.3: Exclusive jet multiplicity distribution for the $Z+ \geq 2$ jet events with 0 btag.

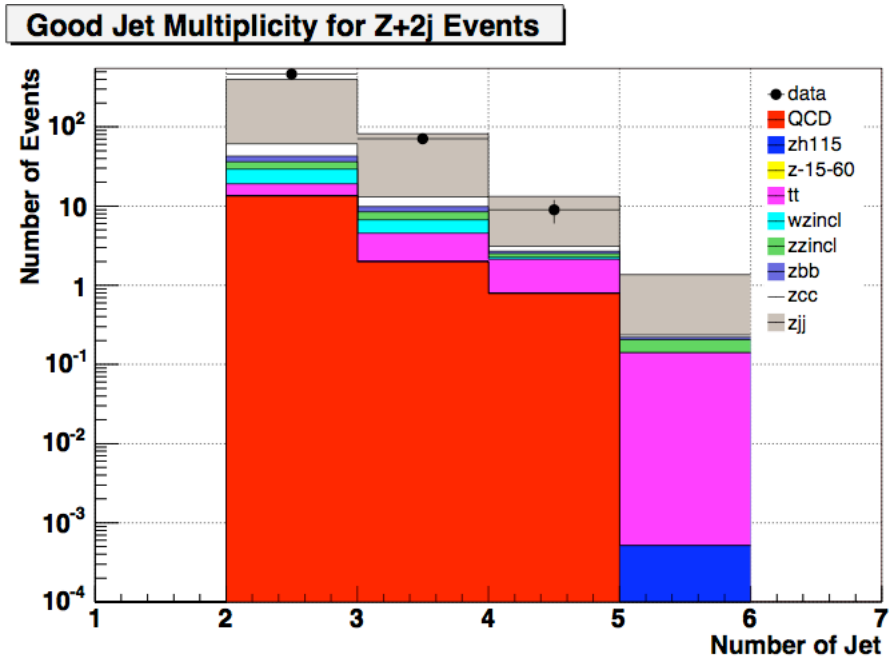

Figure 8.4: Exclusive jet multiplicity distribution for the $Z+ \geq 2$ jet events with 0 btag in log scale.

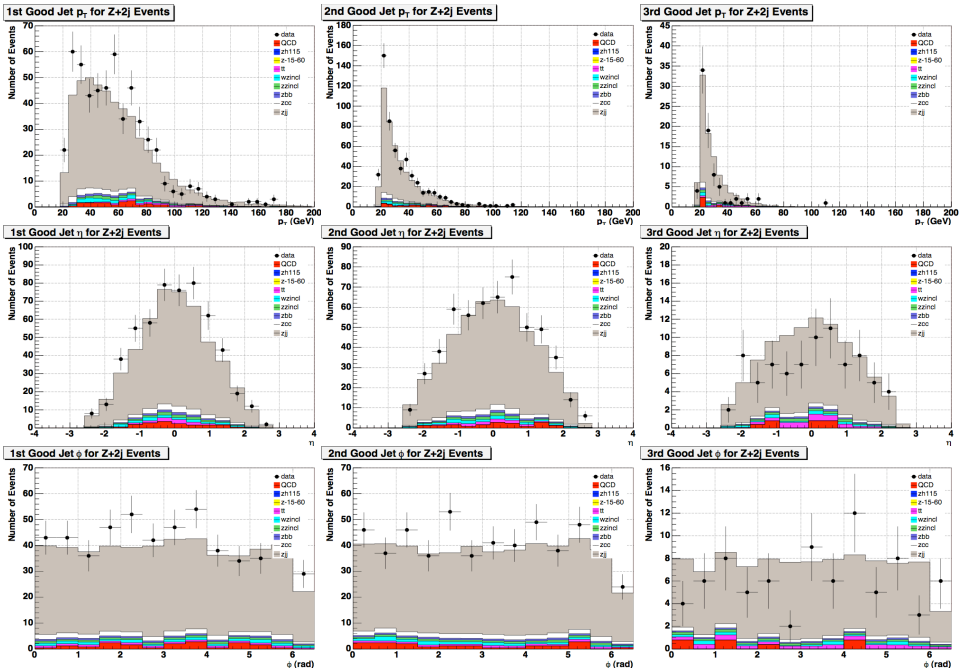

Figure 8.5: The first, second and third good jet p_{T}, η, ϕ distribution for the $Z+ \geq 2$ jet events.

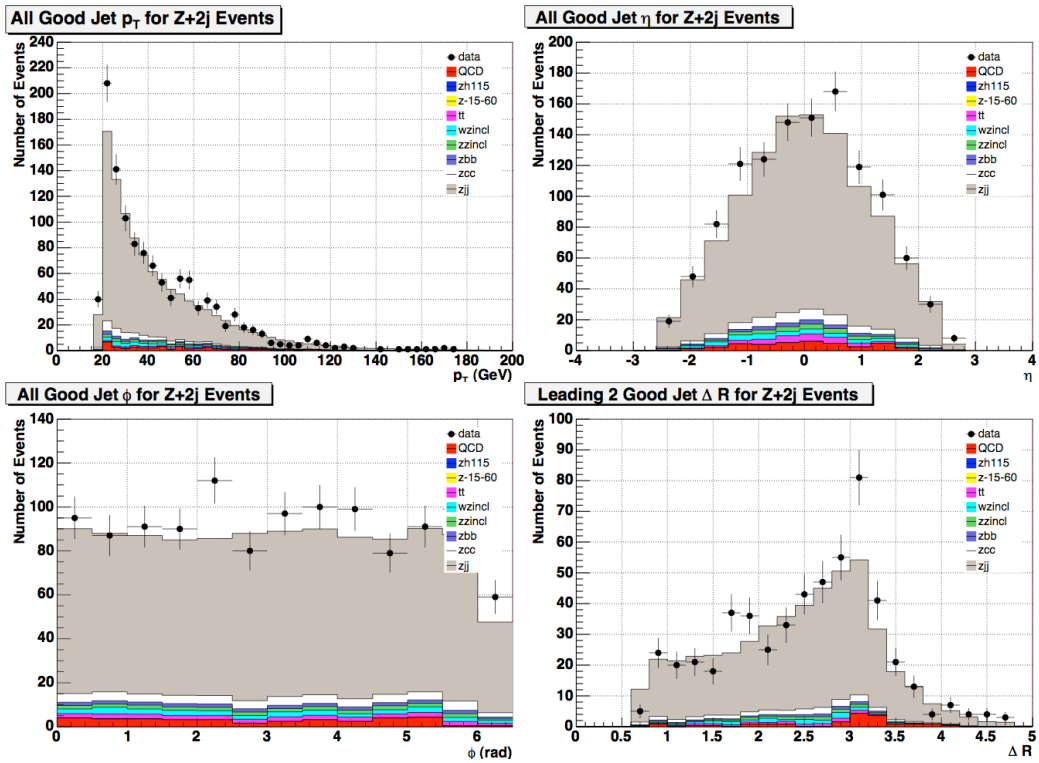

Figure 8.6: All good jet p_{T}, η, ϕ and the leading two good jets' dR distribution for the $Z+ \geq 2$ jet events.

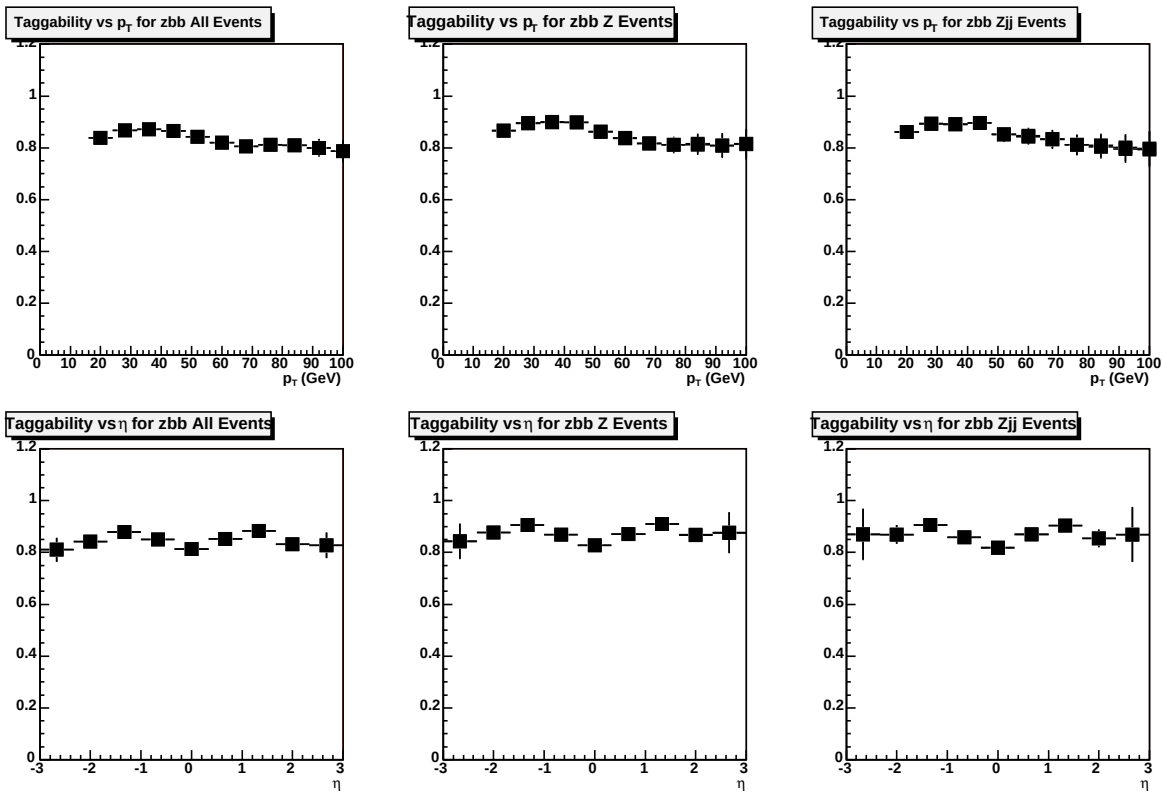

Figure 8.7: Jet taggability calculated for Zbb MC sample. In this plot, as in Figures 8.8-8.16, the upper and lower rows are taggablity as a function of jet $p_{\mathrm{T}}$and η respectively; the first, second and third columns are the taggability measured w.r.t all good jets in events without Z event selection, all good jets in events with a Z candidate and all good jets in events with $Z + 2$ or more jets. For the second and third columns each plot contains taggabilities of both Z event with and without the di-muon isolation requirement, since they have very small difference we will not differentiate them explicitly. The 3 types of events have slightly different taggability as shown in this and the following taggabilities for MC samples. The third column is used in the analysis (see Figure 8.1).

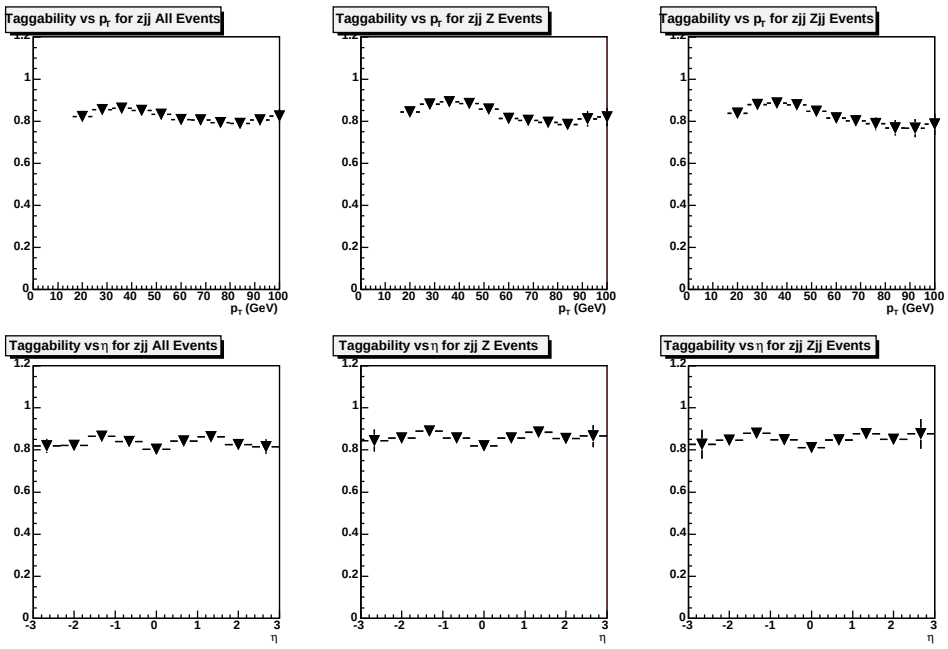

Figure 8.8: Jet taggability for Zjj MC sample. There is no difference compared to Figures 8.7 and 8.9, so we conclude that the jet taggability is jet flavor independent.

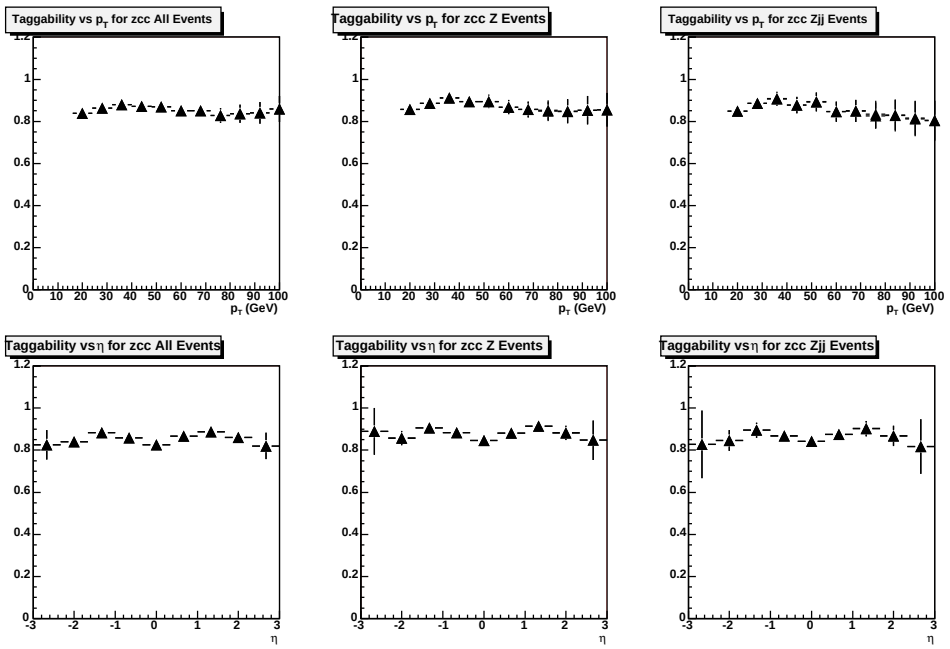

Figure 8.9: Jet taggability for Zcc MC sample.

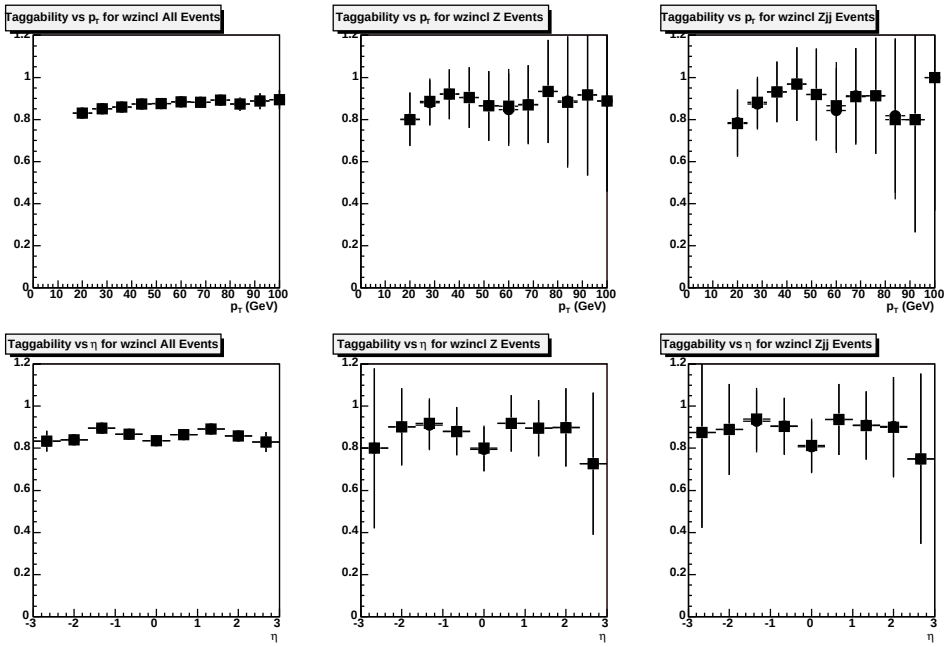

Figure 8.10: Jet taggability for WZ MC sample.

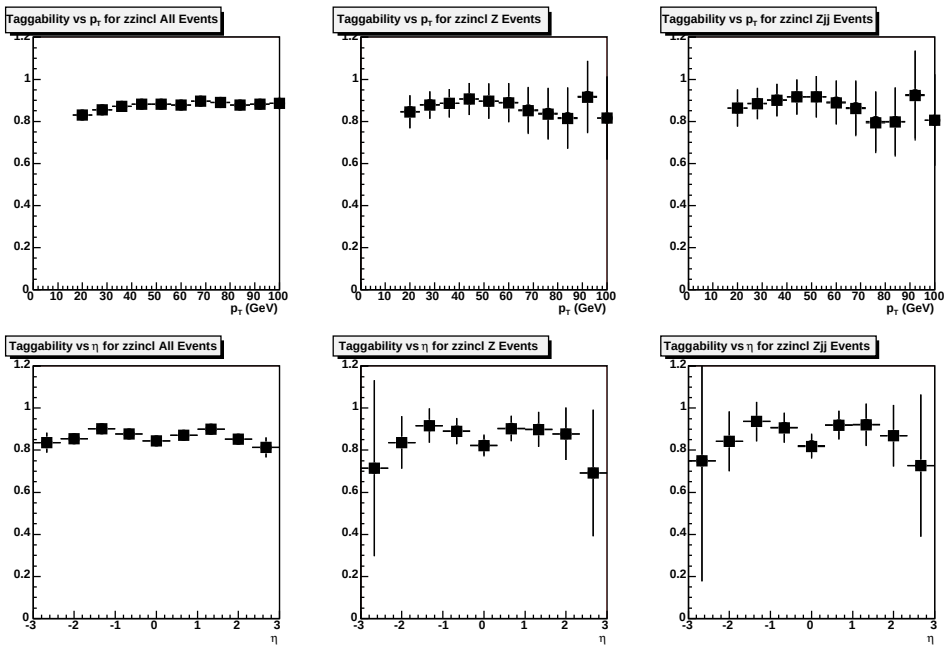

Figure 8.11: Jet taggability for ZZ MC sample.

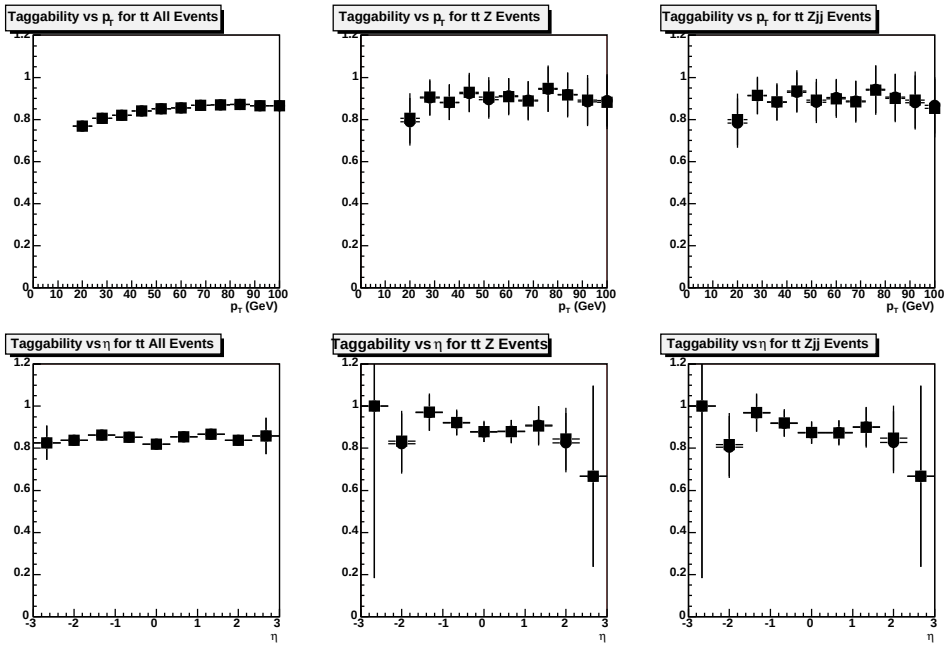

Figure 8.12: Jet taggability for $t\bar{t}$ di-leptonic decay channel MC sample.

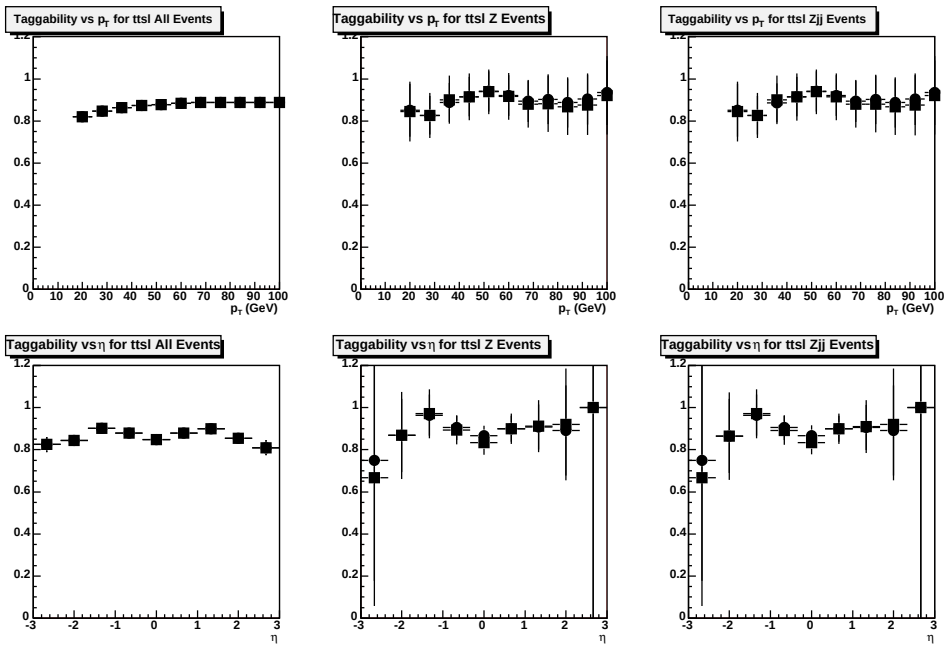

Figure 8.13: Jet taggability for $t\bar{t}$ single leptonic decay channel MC sample.

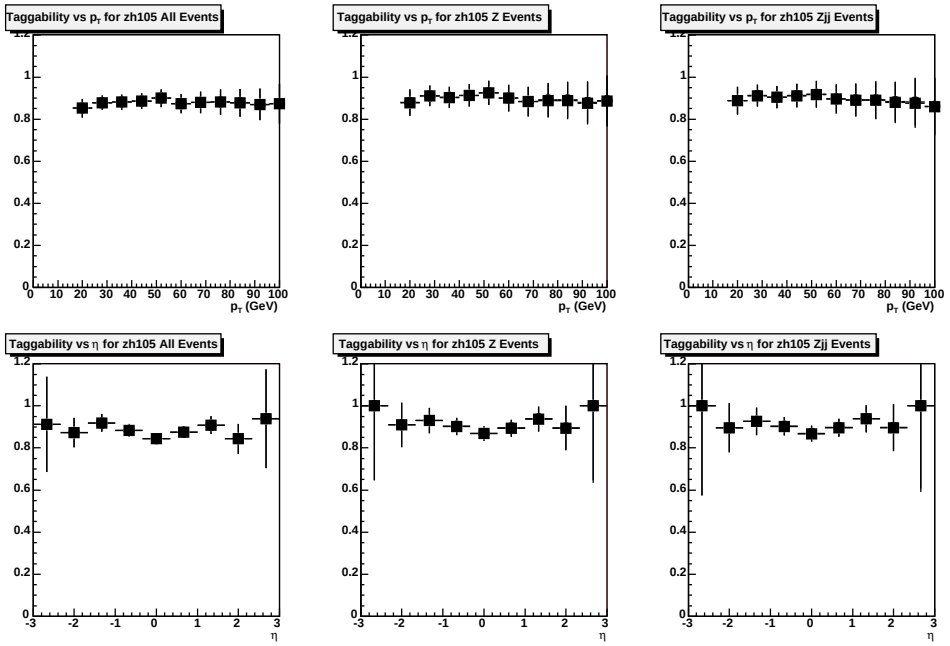

Figure 8.14: Jet taggability for $ZH(105)$ MC sample.

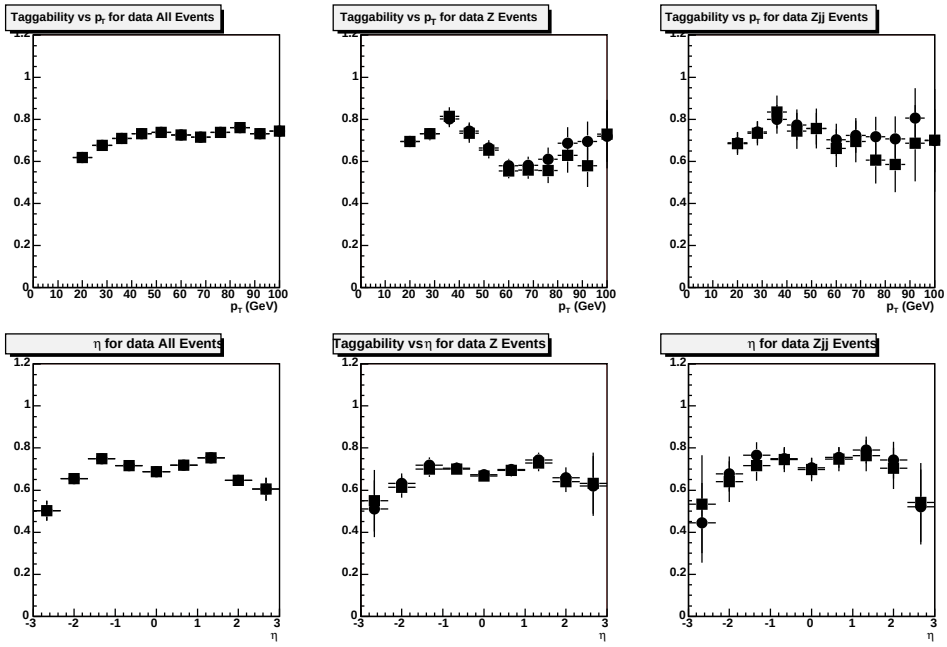

Figure 8.15: Jet taggability for detector data without the muon trigger requirement. There is clearly a data/MC difference, especially in the second column. The reason for the taggability drop at high jet $p_{\mathrm{T}}$is due to fact that the muon isolation requirement used in this analysis does not explicitly exclude the jet that is close to a muon. The same drop can be seen in Figures 8.7–8.9 in a less severe degree. This is due to the Data/MC difference.

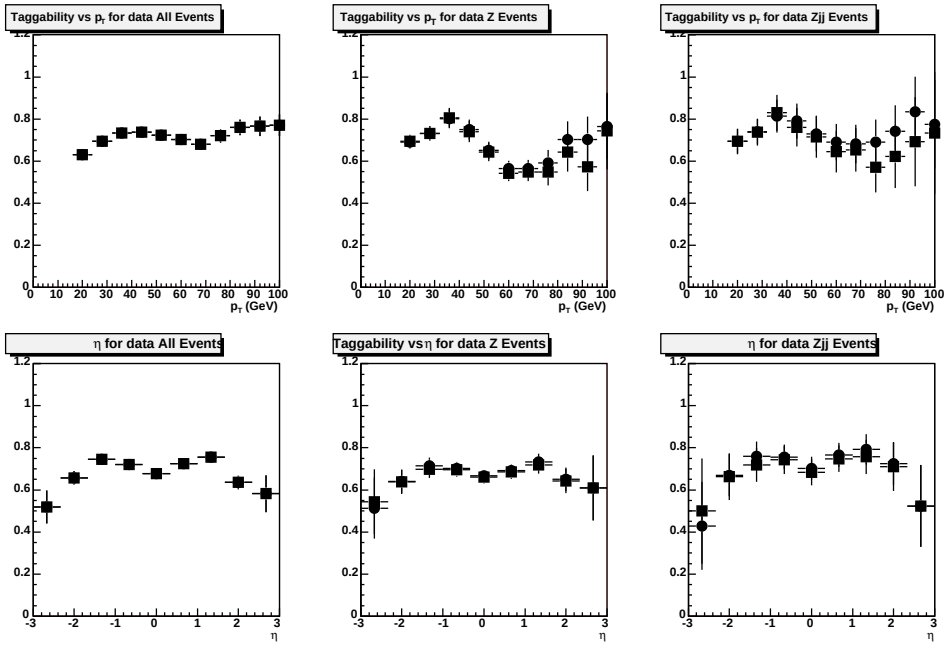

Figure 8.16: Jet taggability for detector data with the muon trigger requirement.

The taggability computation must exclude jets with muons when those muons are ID-ed as the Z muon instead of a muon in jet. With the standard muon isolation requirement which normally requirement on the ΔR between the muon and jet, this bias is excluded automatically. For this analysis the muon isolation requirement does not explicitly requirement on the muon and jet distance, so the taggability can actually be quite different from the taggability calculated using the standard muon isolation requirement.

- The taggability could be slightly process dependent due the non-standard muon isolation requirement which could introduce process dependent bias.
- Jet taggability is not sensitive to the jet flavor, for example Zbb, Zcc and Zjj have the similar taggability as shown in Figures 8.7–8.9.
- The data taggability is independent of the di-muon isolation requirement.
- The difference in taggability between data without and with the trigger selection is shown in Figure 8.17. The two tagabilities are identical within uncertainty.

To calculate the data jet taggability, we need to use the $Z + 2$ jets events with trigger selection and muon isolation requirement (see Figure 8.1). However, with

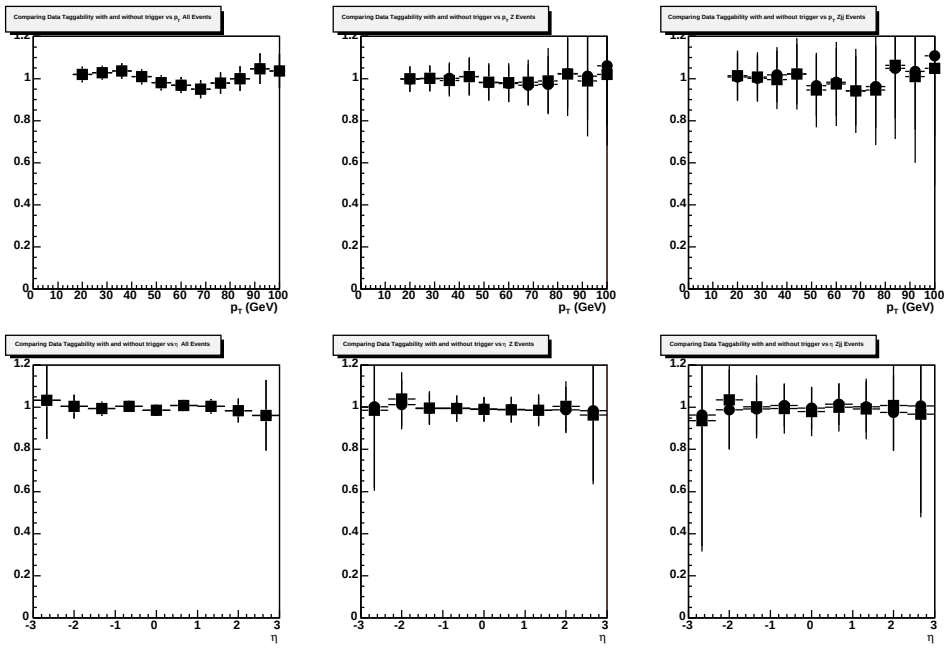

Figure 8.17: Jet taggability difference between data with and without the muon trigger requirement. Clearly there is no difference within error. So we use the data without trigger requirement to measure the taggability in order to reduce the statistical uncertainty.

the above mentioned points in mind, one can improve the statistics by loosening the selection of Z inclusive events by removing the di-muon isolation requirement or the trigger selection.

Since the Zbb, Zcc and Zqq events compose most of the selected $Z+2$ jets events in data(with or without b-tag requirement), and they have almost identical taggability, we can calculate the taggability data/MC scale factor by taking the ratio of data taggability in Figure 8.15 and the MC $Zbb/Zcc/Zqq$ tagabilities in Figure 8.7 and 8.8. The combined average is shown in Figure 8.18.

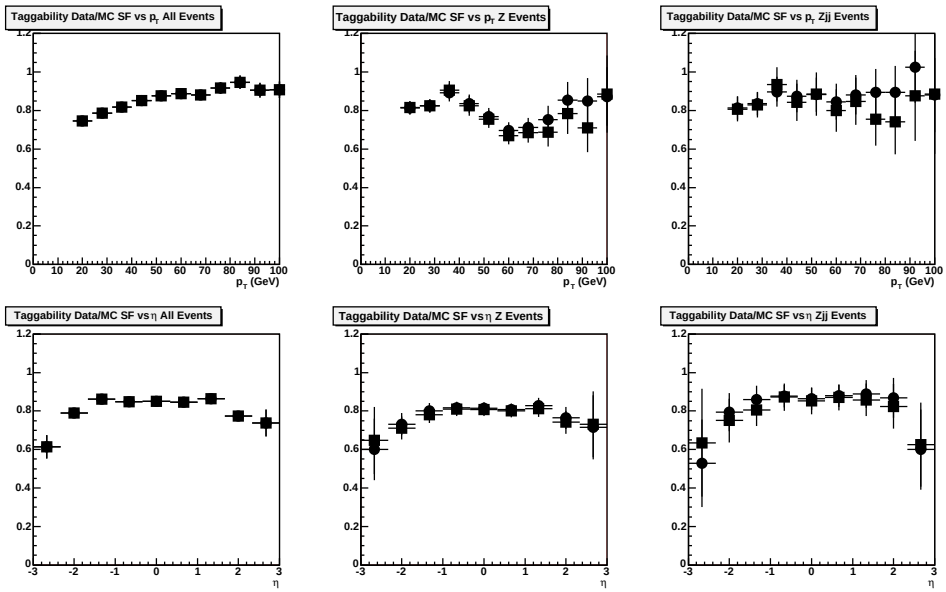

Figure 8.18: Jet taggability data/MC scale factor. It's combined from data/Zjj, data/Zbb and data/Zcc since these three kinds of events comprise most of the selected events in data, and they have the similar scale factor.

Now that both the taggability and b-tag rate data/MC scale factors are available, we simply convolute them[4] over the $Z+2$ jets events to get the event average for the single and double (Taggability×B-tag) efficiencies. The results are listed in Tables 8.7-8.8 for all the MC samples.

[4]Due to the limited statistics, the (p_{T}, η) 2-D taggability is modeled by the product of the tagabilities as 2 functions of $p_{\mathrm{T}}$and η, the function of η is properly normalized so that the overall taggability is not double counted.

Process	Zbb	Zcc	Zjj	$ttdl$	$ttsl$	ZZ	WZ	Z
Data Tag Eff.	0.971	0.971	0.965	0.989	0.997	0.985	0.982	0.95
MC Tag Eff.	0.99	0.993	0.985	0.997	0.995	0.982	0.995	0.977
Data/MC Tag SF.	0.947	0.946	0.941	0.981	0.994	0.968	0.963	0.908
Data B-tag Eff.	0.614	0.323	0.0866	0.8	0.809	0.238	0.165	0.0774
MC B-tag Eff.	0.785	0.413	0.109	0.924	0.884	0.289	0.172	0.095
Data/MC B-tag SF.	0.795	0.757	0.798	0.878	0.892	0.819	0.764	0.747

Process	$ZH(105)$	$ZH(115)$	$ZH(125)$	$ZH(135)$	$ZH(145)$
Data Tag Eff.	0.989	0.989	0.993	0.991	0.989
MC Tag Eff.	0.992	0.998	0.996	0.995	0.993
Data/MC Tag SF.	0.977	0.978	0.98	0.981	0.983
Data B-tag Eff.	0.752	0.768	0.783	0.785	0.77
MC B-tag Eff.	0.883	0.894	0.889	0.885	0.886
Data/MC B-tag SF.	0.854	0.859	0.868	0.875	0.876

Table 8.7: Event averages of the inclusive single jet taggability and ExtraLoose JLIP b-tag efficiencies for $Z + 2$ jets events for all the MC samples with di-muon isolation requirement $f_{iso} = 0.02$. Btag efficiencies include the taggability. The MC efficiencies are simply the ratio of events after/before tag. The data efficiencies and the scale factors are calculated using the convolution method.

Process	Zbb	Zcc	Zjj	$ttdl$	$ttsl$	ZZ	WZ	Z
Data Tag Eff.	0.714	0.71	0.685	0.819	0.949	0.783	0.765	0.618
MC Tag Eff.	0.874	0.883	0.841	0.952	0.984	0.92	0.879	0.767
Data/MC Tag SF.	0.696	0.688	0.687	0.792	0.931	0.752	0.741	0.626
Data B-tag Eff.	0.146	0.0325	0.00357	0.304	0.333	0.0435	0.00474	0.00325
MC B-tag Eff.	0.294	0.0617	0.00771	0.516	0.466	0.0801	0.00505	0.00413
Data/MC B-tag SF.	0.538	0.558	0.582	0.628	0.674	0.553	0.541	0.642

Process	$ZH(105)$	$ZH(115)$	$ZH(125)$	$ZH(135)$	$ZH(145)$
Data Tag Eff.	0.817	0.828	0.858	0.845	0.828
MC Tag Eff.	0.95	0.962	0.968	0.964	0.959
Data/MC Tag SF.	0.765	0.775	0.785	0.795	0.808
Data B-tag Eff.	0.255	0.27	0.292	0.291	0.282
MC B-tag Eff.	0.446	0.463	0.48	0.49	0.477
Data/MC B-tag SF.	0.581	0.586	0.604	0.604	0.621

Table 8.8: Event average of the inclusive double jet taggability and ExtraLoose JLIP b-tag efficiency for $Z + 2$ jets events for all the MC samples with di-muon isolation requirement $f_{iso} = 0.02$.

8.3.4 Kinematic Acceptance

All the remaining event selection requirements are classified as the kinematic requirements. Their purpose is to confine the jets and the muons in the DØ detector fiducial range, to further reduce the QCD background and to reduce the cosmic muons. The acceptances of the kinematic requirements are calculated by taking the ratio of the number of events after and before a requirement. MC samples are used for these calculations, and no data/MC scale factor is used since the MC describes the kinematic variables well. All the kinematic acceptances are measured with respect to events with two muons and two jets present, no di-muon isolation or b-tag on jets is required. Table 8.9 lists the acceptances for different MC samples.

Due to the better momentum resolution in MC which is largely corrected by the smearing of the muon $\frac{q}{p_{\mathrm{T}}}$, the opposite charge requirement has higher efficiency in MC than in the data. The difference is accounted for by a scale factor. The opposite charge requirement efficiencies of data, MC and the Data/MC scale factor are listed in Table 8.10

Process	Zbb	Zcc	Zjj	$ttdl$	$ttsl$	ZZ	WZ	Z
$\mathcal{A}_{kine}$	0.386	0.393	0.392	0.0805	0.00984	0.235	0.156	0.285

Process	$ZH(105)$	$ZH(115)$	$ZH(125)$	$ZH(135)$	$ZH(145)$
$\mathcal{A}_{kine}$	0.511	0.521	0.53	0.538	0.529

Table 8.9: Kinematic acceptances $\mathcal{A}_{kine}$ for all MC samples. Measured with respect to the events in which 2 loose muon with central track match and 2 jet presents.

Data	MC	Data/MC SF
0.96 ± 0.01	0.99 ± 0.01	0.97 ± 0.01

Table 8.10: Di-muon opposite charge data, MC efficiencies and the data/MC scale factor. The MC efficiency is the average of Zjj, Zcc, Zbb MC samples.

8.4 QCD Subtraction

This section deals with the QCD multi-jet background subtraction from the selected $Z + 2$ jet events in the detector data. The QCD di-muon isolation efficiency will also be calculated for the events with b-tagged jets. The calculation is based on the so called matrix method described below.

The matrix equation is established by counting the total number of Z candidates with and without the isolation requirement:

$$\text{QCD} + \text{DY} + \text{Z} = N_{non-iso} \quad (8.4)$$

$$\epsilon_{QCD} \cdot \text{QCD} + \epsilon_{DY} \cdot \text{DY} + \epsilon_{Z} \cdot \text{Z} = N_{iso} \quad (8.5)$$

where Z refers to the Z peak in the distribution which includes all of the processes in Table 8.2, 8.3 except for the $t\bar{t}$ processes where no Z peak is present. The "flat" distribution under the Z peak consists of the QCD background (QCD) and non-QCD process (DY): Drell-Yan process and $t\bar{t}$[5]; $\epsilon_{QCD}, \epsilon_{DY}, \epsilon_{Z}$ are the isolation requirement efficiencies of QCD, Drell-Yan and Z signals, $N_{non-iso}$ and N_{iso} are the total number of events within the mass window without and with isolation respectively. According to Table 7.1, 7.2, the $t\bar{t}$ has a similar di-muon isolation efficiency as the processes which contain a Z boson, so we also include it into Z. The slight difference in the isolation requirement efficiency will be accounted for as systematic error.

The equations hold for 0, 1, 2 b-tag cases[6], but due to various reasons discussed

[5]For simplicity we will refer to both of them as Drell-Yan process.

[6]From now on we will study only the inclusive b-tagged event, thus the inclusive single or double btag are referred to as 1, 2 b-tag.

in the following section, the equation will be solved differently for each of these cases.

8.4.1 $Z + 2$ jets, 0 b-tag

Due to the kinematic similarity between the Drell-Yan and the Z process, $\epsilon_{DY} = \epsilon_Z$, and it has been calculated using MC and detector data samples as described in section 7.1.3.

For the $Z + 2$ jet event without b-tag requirement, we have also calculated the di-muon isolation requirement efficiency for QCD using 2 evenly distributed random numbers in section 7.1.3. So we can solve the equations for QCD and (DY+Z).

We can also get the Drell-Yan and Z signal ratio. In doing so we need to extract Z by fitting the Z peak in Figures 7.8, 7.10, 7.12. The Z peak is modeled by a Gaussian convoluted with a Breit-Wigner function. The QCD background plus Drell-Yan is fitted with an exponential function [7]. The fits are shown in Figure 7.8, 7.10, 7.12 for $Z + 2j$ with 0, 1, 2 b-tag without the di-muon isolation requirement. The results are listed in Table 8.11.

Process	Z	Drell-Yan + QCD
$Z + 2j$ 0 b-tag	450.87 ± 19.96	253.13 ± 15.43
$Z + 2j$ 1^+ b-tag	53.70 ± 11.03	92.29 ± 8.06
$Z + 2j$ 2^+ b-tag	8.17 ± 4.94	30.83 ± 5.32

Table 8.11: Fitting results of the Z peak and QCD+Drell-Yan background for $Z+2j$, $Z + 2j$ with 1^+ b-tag and $Z + 2j$ with 2^+ b-tag. No di-muon isolation requirement applied.

As shown in Figures 7.10, 7.12, the Z peaks for 1, 2 btagged events are not so pronounced as in Figure 7.8. We need to find other ways to confirm the fit results are reliable.

We introduce 2 variables:

$$\gamma_1 = \frac{N_{zbj}}{N_{zjj}} \tag{8.6}$$

$$\gamma_2 = \frac{N_{zbb}}{N_{zjj}} \tag{8.7}$$

where $N_{zjj}, N_{zbj}, N_{zbb}$ are the total number of events within the Z mass window of selected Zjj with 0, 1, 2 b-tag respectively.

[7] Although the fits look good with and without the di-muon isolation requirement, we only use the fit which isolation requirement is not applied since in this case the QCD + Drell-Yan process has much larger statistics and thus is much better modeled.

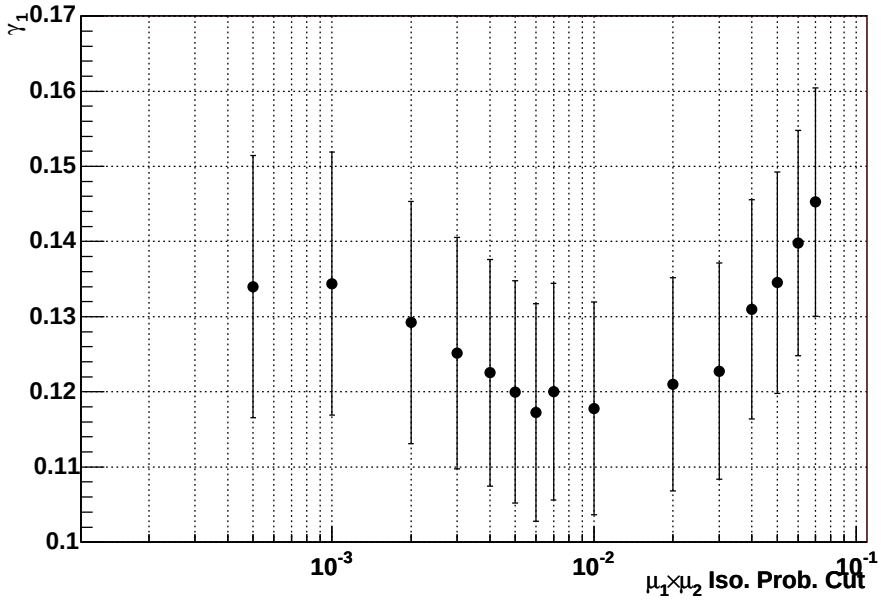

Figure 8.19: γ_1 as a function of di-muon isolation requirement for detector data. With tighter (smaller) isolation requirement, γ_1 decreases until reaching to a plateau. The plateau is the Z + Drell-Yan processes' single btag (including taggability) rate. In practice when the isolation requirement is too small (< 0.01), the assumption that $Z + 2j, Z + 2c, Z + 2b, t\bar{t}, WZ, ZZ$ has the same isolation requirement efficiencies begins not to hold any more, see Figure 7.14, so the btag rate is only obtained around isolation requirement equals 0.01 where the QCD contribution is small enough to be ignored. The plateau is $\gamma_1 = 0.121 \pm 0.014$.

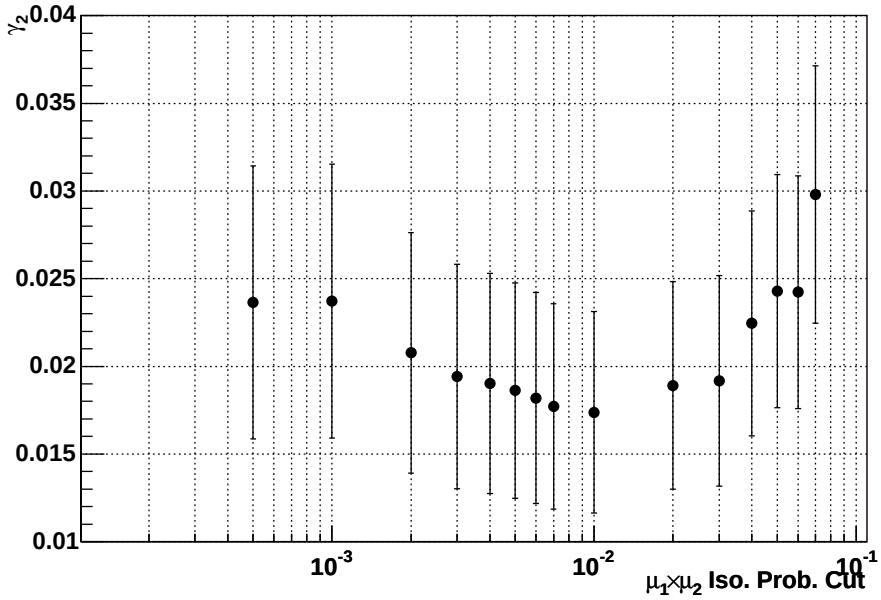

Figure 8.20: γ_2 as a function of di-muon isolation requirement for detector data. Using the same arguments as for γ_1, the plateau is $\gamma_2 = 0.019 \pm 0.006$.

Figures 8.19 and 8.20 show the γ_1 and γ_2 as a function of isolation requirement. Clearly γ_1 and γ_2 decrease when the isolation requirement is tighter (smaller), and when the isolation requirement is about 0.02, γ_1 and γ_2 reach to a plateau. It can be proven that the plateau where isolation requirement is very tight is an approximation of the direct measurement of detector data single b-tag and double b-tag rate for Z+Drell-Yan process:

$$\begin{aligned}
\lim_{IsoCut\to 0}\gamma_1 &= \lim_{IsoCut\to 0}\frac{N_{zbj}}{N_{zjj}} \\
&= \lim_{IsoCut\to 0}\frac{\epsilon_Z\cdot(Z+DY)_{zbj}+\epsilon_{QCD}\cdot QCD_{zbj}}{\epsilon_Z\cdot(Z+DY)_{zjj}+\epsilon_{QCD}\cdot QCD_{zjj}} \\
&= \lim_{IsoCut\to 0}\frac{\epsilon_Z\cdot(Z+DY)_{zbj}}{\epsilon_Z\cdot(Z+DY)_{zjj}} \\
&= \frac{(Z+DY)_{zbj}}{(Z+DY)_{zjj}}=\frac{(Z)_{zbj}}{(Z)_{zjj}} \qquad (8.8)\\
\lim_{IsoCut\to 0}\gamma_2 &= \frac{(Z+DY)_{zbb}}{(Z+DY)_{zjj}}=\frac{(Z)_{zbb}}{(Z)_{zjj}} \qquad (8.9)
\end{aligned}$$

At the working isolation requirement point 0.02, $\gamma_1 = 0.121 \pm 0.014$ and $\gamma_2 = 0.019 \pm 0.006$. They are in good agreement with the ratio of fitted Z peaks in Table 8.11. So the fit results are reliable.

The ratio of Z, Drell-Yan and QCD results for $Z + 2j$ without b-tag requirement are listed in Table 8.12 (Z mass window is included). The combined D-Y/Z ratio g is determined from Figure 8.21:

$$g = 0.1964 \pm 0.0418 \qquad (8.10)$$

In [56] the same ratio calculated by PYTHIA is 0.21 when no Z mass window requirement is applied. This agrees with this result as expected because we have the Z mass window requirement in place.

Isolation Requirement	# of Z + Drell-Yan	Drell-Yan/Z ratio	QCD
0.1	536.98 ± 20.28	0.1970 ± 0.0412	42.02 ± 1.66
0.02	528.87 ± 19.96	0.1946 ± 0.0418	16.13 ± 0.66

Table 8.12: QCD subtraction results for $Z + 2j$ detector data for different dimuon isolation requirement.

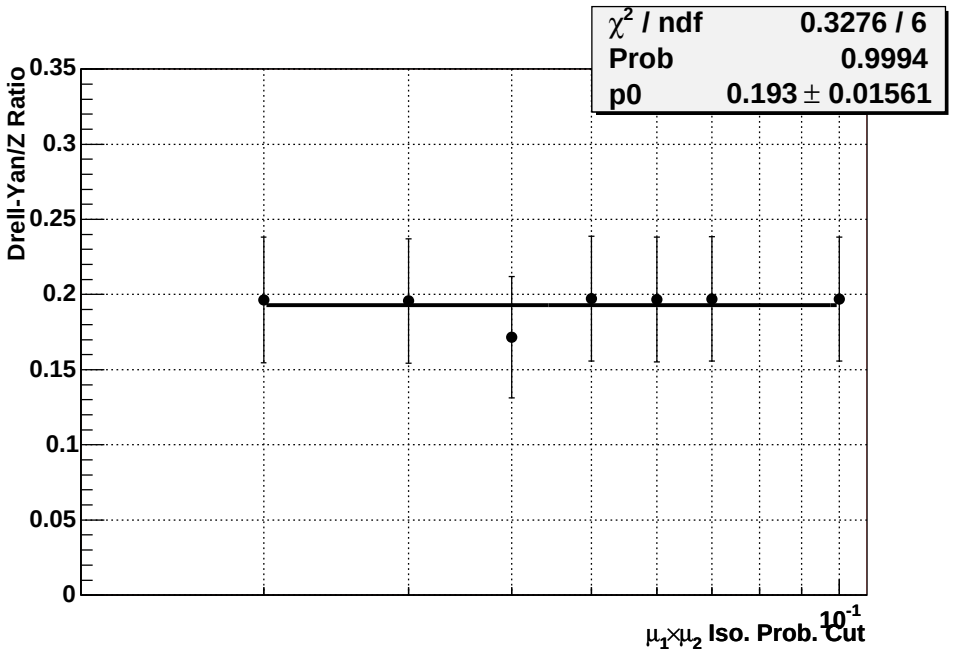

Figure 8.21: Drell-Yan/Z ratio calculated using the matrix method for the $Z + 2$ jet events without b-tag requirement at different isolation requirements. The Z mass window requirement is applied. Clearly the ratio is independent of the isolation requirement, which confirmed the assumption that Drell-Yan and Z have the same dimuon isolation requirement efficiency. The ratio obtained in this analysis is consistent with ratio obtained in the $Z \rightarrow \mu\mu$ cross section measurement analysis[56]. This value is slightly lower than the $Z \rightarrow \mu\mu$ result because of the Z mass window requirement in this analysis.

8.4.2 $Z + 2$jets, 1, 2b-tag

For $Z+2$jet events with b-tag requirements, the method to solve the matrix equation Eq. 8.4 is different. Because with b-tag requirements, the QCD content in the selected sample will have more muons from the b jets and these muons are not isolated, the QCD isolation efficiency will be lower than that without b-tag requirement. There is not a simple way to calculate the isolation requirement efficiency for QCD in this case.

The method to solve the equations in this case is to solve for QCD and ϵ_{QCD}. Since we have shown the ϵ_Z is independent of b-tag, we can still use the ϵ_Z in Table 7.1 in this case. Also, the Drell-Yan and Z ratio should not change with different b-tag, since the di-muon and double b-jet are kinematically uncorrelated with each other. Plugging in the ϵ_Z values from Table 7.1, Z and Drell-Yan/Z ratio in Table 8.12, the results of the matrix equations are listed in Table 8.13, 8.14.

Isolation Requirement	# of Z + Drell-Yan	# of QCD	ϵ_{QCD}
0.1	63.94 ± 7.93	14.06 ± 3.25	0.17 ± 0.09
0.02	63.04 ± 7.89	0.96 ± 3.25	0.01 ± 0.08

Table 8.13: Summary of QCD subtraction results for $Z + 2j$ with 1 b-tag detector data for different dimuon isolation requirement.

Isolation Requirement	# of Z + Drell-Yan	# of QCD	ϵ_{QCD}
0.1	9.73 ± 3.23	6.27 ± 1.11	0.21 ± 0.10
0.02	9.59 ± 3.19	0.41 ± 1.11	0.01 ± 0.11

Table 8.14: Summary of QCD subtraction results for $Z+2b$ detector data for different dimuon isolation requirement.

8.5 Data and MC Comparisons

In this section detector data is compared with the combined MC backgrounds. The MC samples are normalized to the luminosity, and the normalization factor for each of the MC samples is calculated using:

$$s = \frac{\sigma \times \mathrm{BR} \times \mathrm{L}}{N} \times \mathrm{SF} \tag{8.11}$$

where $\sigma \times$ BR is the cross section times branching ratio of the process, L is the integrated luminosity, N is the total number of MC events after the good data selection and before any event selection requirements, and SF is the combined Data/MC correction factor of all the event selection requirements, which includes the Muon trigger efficiency, the Data/MC scale factor of Jet RECO×ID efficiency, Muon RECO×ID×Tracking×SMT, jet taggability and JLIP b-tagger for events with b-tag requirements. For the other kinematic requirements the Data/MC scale factor is very close to 1 so they are not included in the calculation except for the di-muon opposite charge scale factor. The normalization factors for $Z + 2$ jet events with 0,1,2 b-tag requirements are listed in Table 8.15.

Process	Zbb	Zcc	Zjj	$ttdl$	$ttsl$	ZZ	WZ	Z
0 btag	0.48	0.568	0.482	0.892	1.22	0.524	0.637	0.417
1+ btag	0.382	0.429	0.384	0.784	1.09	0.429	0.487	0.312
2+ btag	0.258	0.317	0.28	0.56	0.823	0.29	0.345	0.268

Process	$ZH(105)$	$ZH(115)$	$ZH(125)$	$ZH(135)$	$ZH(145)$
0 btag	0.599	0.641	0.617	0.632	0.649
1+ btag	0.512	0.55	0.536	0.553	0.569
2+ btag	0.348	0.375	0.373	0.382	0.403

Table 8.15: Combined scale factor SF in Eq. 8.11 for MC $Z + 2$ jet events with 0, 1, 2 b-tag requirements. The uncertainties are determined in Section 8.7.

Although the *top_analyze* package processed MC samples have smeared the muon momenta according to the official smearing factors listed in Table 6.1, and the MC Z signals match the detector data Z signals without jet requirements well, we found the smearing is not good enough for the $Z+2$ jet events. Thus the muon momenta in the $Z+2$ jet events for all the MC samples were re-smeared by the following equation [108],

$$\frac{1}{p_T} = \frac{\alpha}{p_T^{MC}} + \text{Gauss}(0, \sigma) \tag{8.12}$$

where $\alpha = 1.01375, \sigma = 0.00123125$, the parameters are determined by finding the (α, σ) grid point in a reasonable range that yields the best Z peak match between detector data and MC samples for $Z + 2j$ events. The di-muon invariant mass distributions before and after the re-smearing process are shown in Figure 8.22.

Kinematic variable distributions from data are compared to the sum of contributions of MC samples in Figures 8.23 - 8.28. The shape of the QCD background in these distributions is determined from the "semi-anti-isolated" $Z + 2j$ events in data, *eg.* we subtract the distribution with the di-muon isolation requirement at 0.05 by the same distribution with the di-muon isolation requirement at 0.01. From Tables

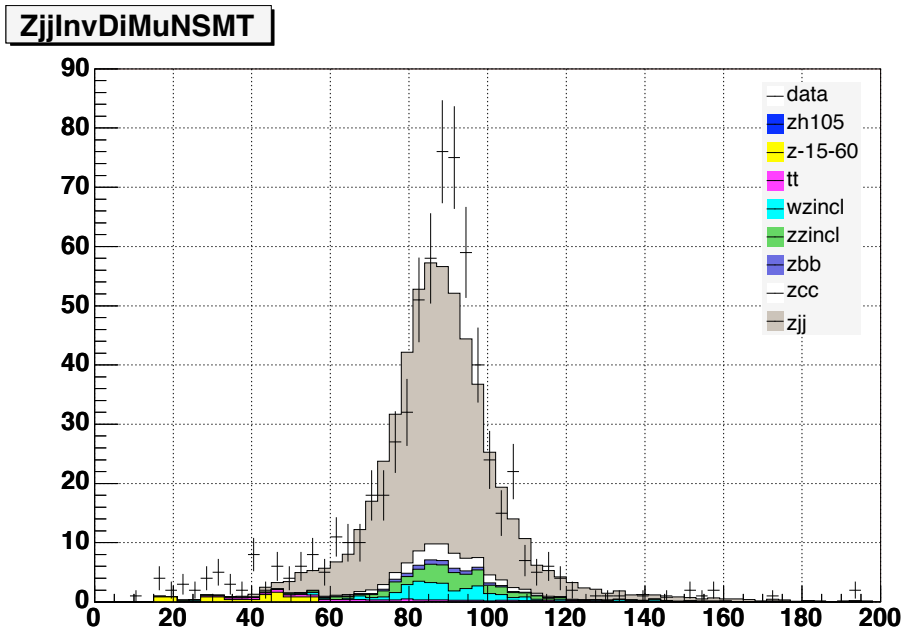

(a)

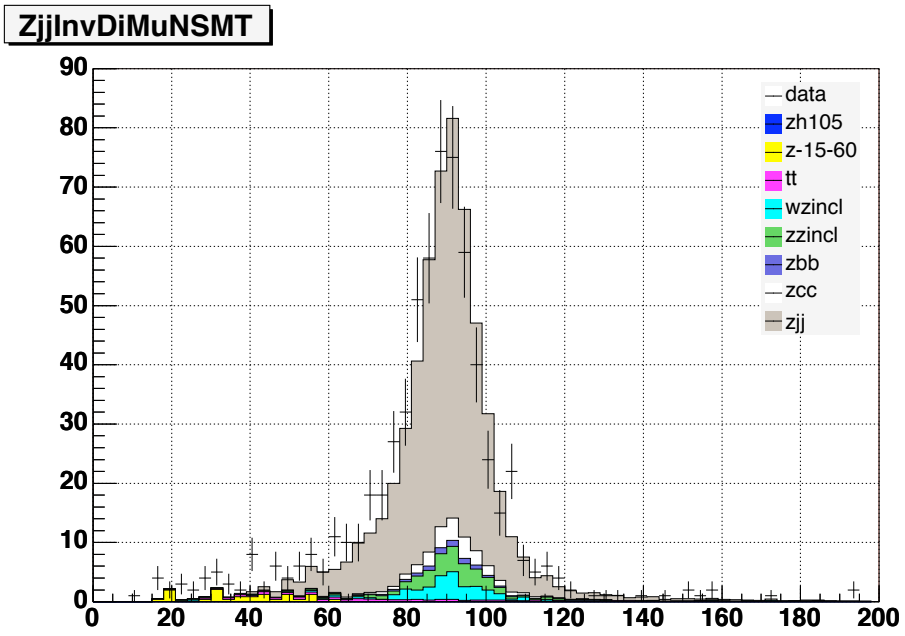

(b)

Figure 8.22: Di-muon invariant mass distribution of the $Z + 2$ jet with 0 btag events before (a) and after (b) the muon re-smearing. As can be seen from (a), the muon transverse momenta are over-smeared and due to the presence of the two recoil jets, the muon p_{T} is not well modeled, too. By re-smearing the muon momenta, these problems are solved as shown in (b).

7.3, 7.1 and 8.12 we can determine the composition of this semi-isolated sample is a mixture of $\sim$ 70% qcd background and $\sim$ 30% signal. We do not use the anti-isolated (*eg.* di-muon isolation > 0.02) events to determine the shape because the QCD shape is highly di-muon isolation requirement dependent. The remnant is then normalized to the number of QCD events in Tables 8.12-8.14. The effect of the signal contamination on the QCD background shape is small and is covered by the large QCD background uncertainty.

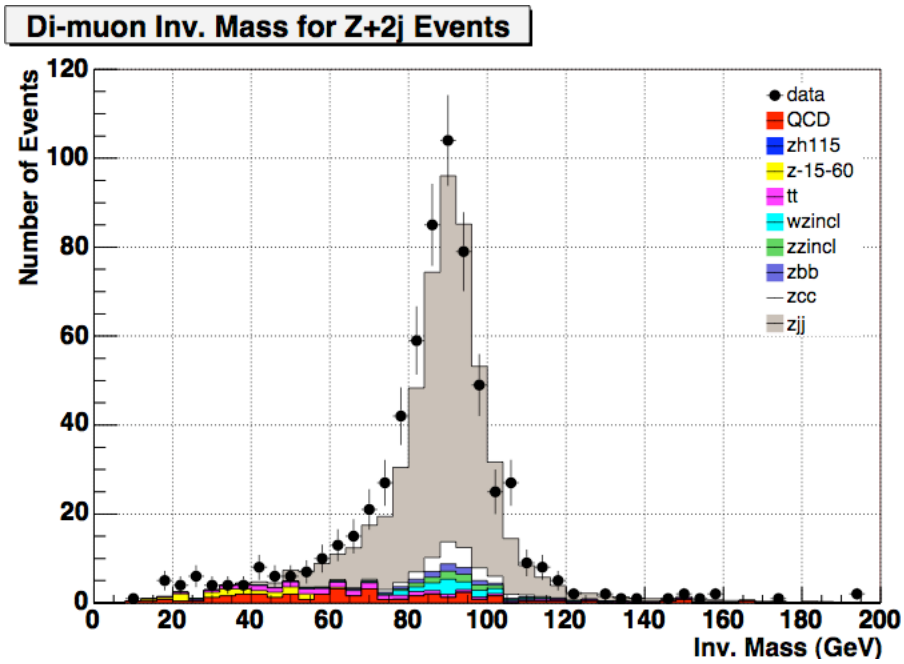

Figure 8.23: Di-muon invariant mass distribution of the $Z+2$ jet with 0 btag events.

The breakdown of the predicted backgrounds from the MC samples, the number of QCD multi-jet background and the number of events in data for $Z+2$ jet events with 0, 1, 2 btags are shown in Table 8.16. It is clear MC agrees with data well.

8.6 Higgs Search

Since for the expected ZH signal the double $b-$jets are from the Higgs boson decay while for the background the double $b-$jets are from the QCD processes or from uncorrelated semi-leptonic decays of top quarks, the invariant mass distribution of the double $b-$jet should be most straightforward place to search for the Higgs signal. We search for the ZH signal based on the Standard Model at 6 Higgs mass points from

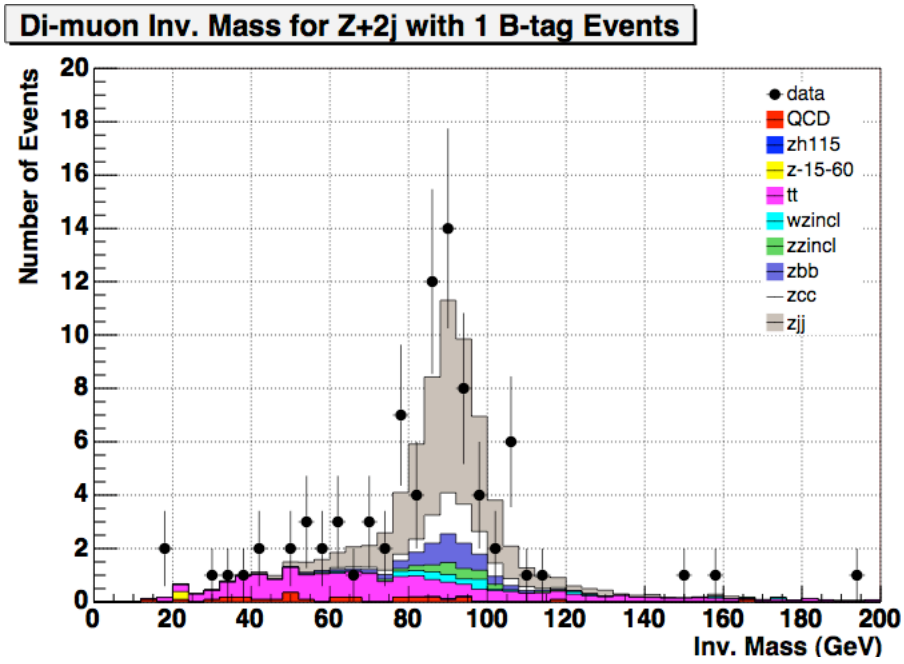

Figure 8.24: Di-muon invariant mass distribution of the $Z + 2$ jet with 1 btag events.

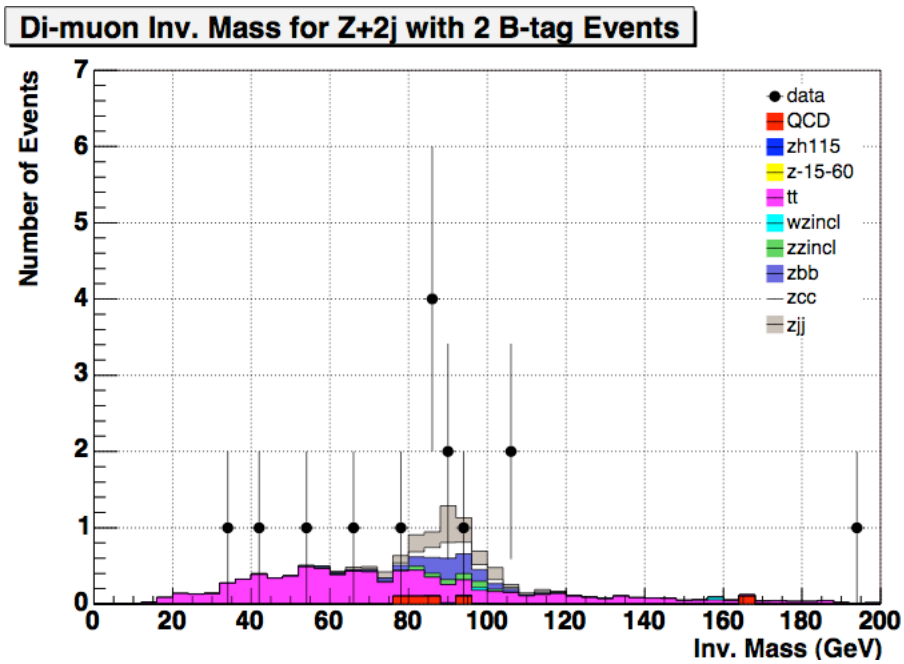

Figure 8.25: Di-muon invariant mass distribution of the $Z + 2$ jet with 2 btag events.

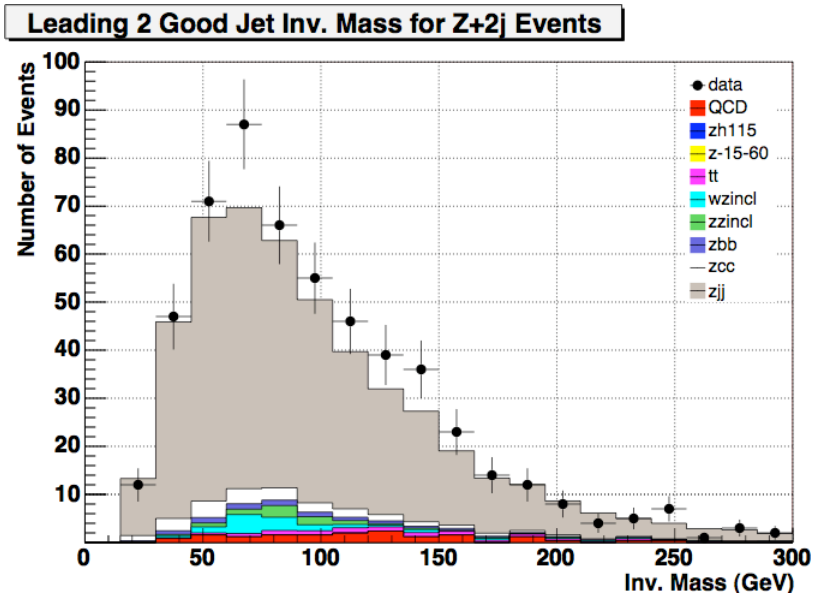

Figure 8.26: The leading 2 jets' invariant mass distribution for the $Z + 2$ jet events without b-tag requirement. Z mass window requirement is applied.

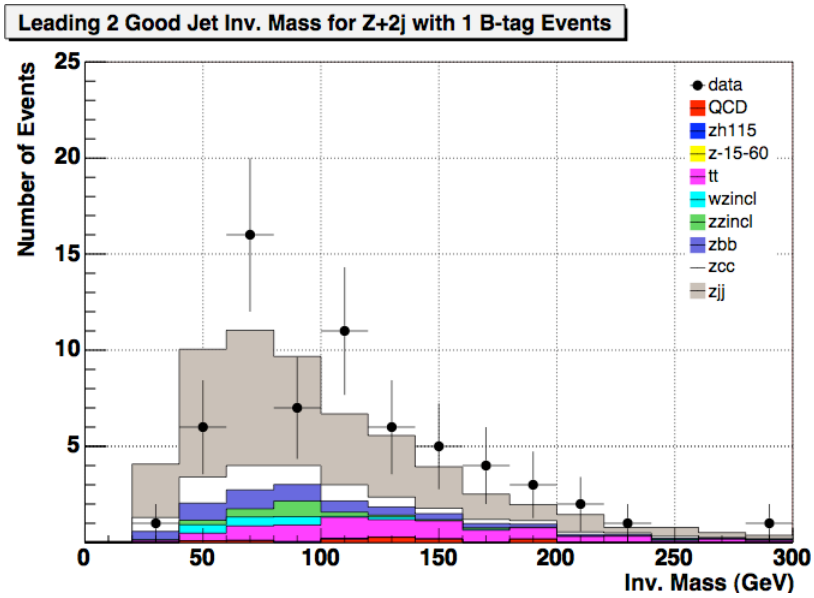

Figure 8.27: The leading 2 jets' invariant mass distribution for the $Z + 2$ jet events with 1 b-tag requirement. Z mass window requirement is applied.

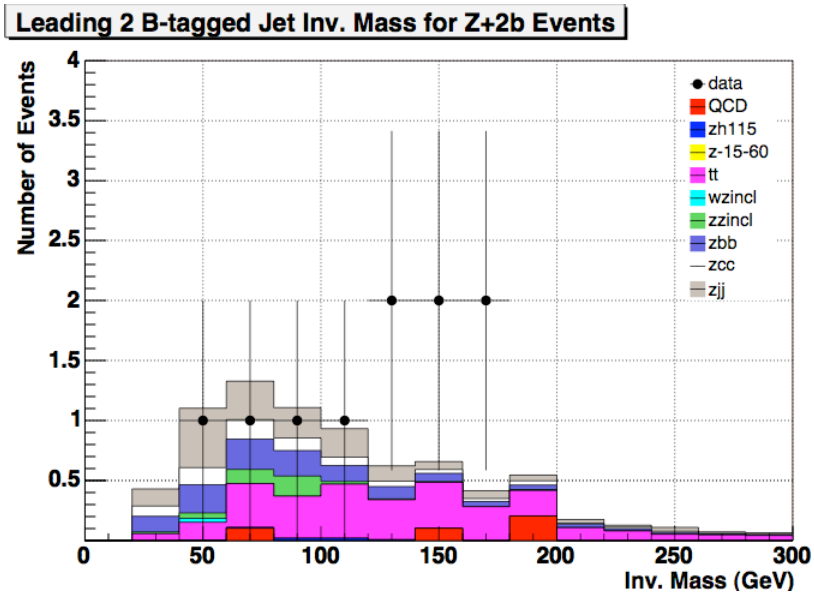

Figure 8.28: The 2 b jets' invariant mass distribution for the $Z + 2$ jet events double b-tag requirement. Z mass window requirement is applied.

MC sample	0 btag	1 btag	2btag
Zjj	$415 \times 1.04 = 431$	$36.2 * 1.24 = 44.8$	$1.86 * 1.45 = 2.70$
Zcc	22.1	6.90	0.76
Zbb	8.32	5.19	1.32
ZZ	8.90	2.11	0.39
WZ	12.5	1.63	0.03
$t\bar{t}$	9.57	7.69	3.06
ZH	0.22	0.17	0.06
QCD	16.13	0.96	0.41
MC Total	$493 + 17 = 510$	$60.9 + 8.7 = 69.6$	$7.91 + 2.69 = 10.6$
Data	545	64	10

Table 8.16: The breakdown of MC samples in $Z + 2$ jet events with 0, 1, 2 b-tag requirements. Z mass window requirement is applied. $m_H = 115$ GeV. $t\bar{t}$ includes both the single and di-leptonic decay channels. The difference between the MC and data are well within the systematic and statistical uncertainties as will be discussed in Section 8.7.

105 GeV to 155 GeV. The double $b-$jet invariant mass distributions of the $Z + 2$ $b-$jet events shown in Figures 8.29 are each fit to a Gauss function. For each mass point we apply a mass window requirement as 1.5σ of the Higgs mass peak resolution determined from the fit. These Higgs search windows are listed in Table 8.17.

Higgs mass(GeV)	mean(GeV)	width(GeV)	resolution(%)	search window(GeV)
105	91.3	17.7	19.3	65 - 118
115	99.5	19.1	19.2	70 - 128
125	107.9	19.7	18.3	78 - 137
135	115.8	21.1	18.2	84 - 147
145	125.7	22.6	18.0	92 - 160

Table 8.17: Higgs search window for 6 Standard Model Higgs masses of 105 GeV to 145 GeV. The resolution is defined as width/mean.

8.7 Systematic Uncertainties

The sources of systematic uncertainties are listed in Table 8.18 for ZH signals, Table 8.19 for QCD background and in Table 8.20 for each of the non-QCD backgrounds. The contribution of each systematic uncertainty source in ZH and each non-QCD background process is calculated by varying its central value by $\pm\sigma$ and calculating the change of the expected number of $Z + 2b$ jet events within the Higgs search window. The uncertainties of Zjj, Zcc, Zbb are treated as fully correlated. All the other backgrounds are assumed to be uncorrelated. All sources of the uncertainties are also treated as uncorrelated so they are added quadratically to get the overall signal and background uncertainties. The uncertainty of QCD is estimated by assuming the the QCD background within the Higgs search window has the same relative uncertainty as the whole QCD background within the Z mass window, so the absolute uncertainty is the whole QCD background uncertainty in Table 8.14 times the percentage of the QCD that is within the Higgs search window.

8.8 Cross Section Limit

Using the double b-tagged events, the Bayesian 95% limit[109] on the ZH $\sigma\times$BR are listed in Table 8.21.

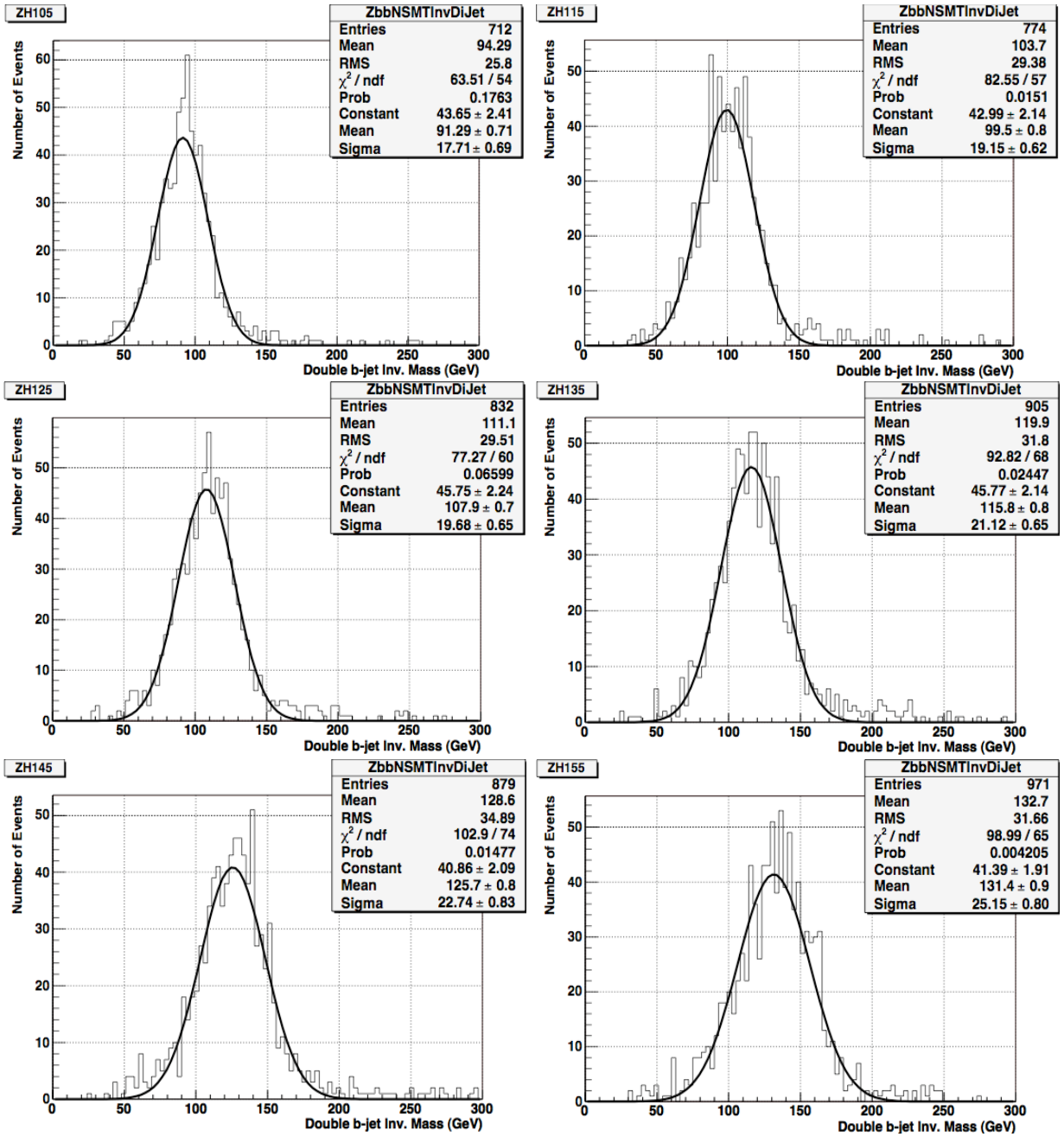

Figure 8.29: Double b jet invariant mass distribution of Standard Model ZH signals at Higgs mass from 105 GeVto 155 GeV, Z mass window requirement has been applied. The distributions are fitted to Gauss function. The $\pm 1.5\sigma$ mass window around the peak is set as the Higgs search windows for different Higgs masses.

Error Source	ZH(105)	ZH(115)	ZH(125)	ZH(135)	ZH(145)
MuSMTHit	0.022	0.021	0.022	0.022	0.021
MuTrack	0.102	0.097	0.099	0.097	0.095
MuID	0.065	0.060	0.061	0.061	0.059
L3MuTrig	0.053	0.051	0.052	0.051	0.049
L2MuTrig	0.027	0.026	0.026	0.026	0.027
L1TrkTrig	0.005	0.005	0.005	0.005	0.005
L1MuTrig	0.027	0.027	0.026	0.027	0.027
JetRECOID	0.064	0.060	0.055	0.049	0.045
JES	0.033	0.031	0.025	0.020	0.016
Btag TRF	0.086	0.089	0.088	0.091	0.091
Taggability	0.137	0.137	0.136	0.135	0.133
SFErrTotal	0.225	0.221	0.219	0.217	0.212
Cross Section	0.07	0.07	0.07	0.07	0.07
Luminosity	0.065	0.065	0.065	0.065	0.065
Total Syst. Err.	0.244	0.230	0.229	0.226	0.222
Stat. Err.	0.039	0.037	0.035	0.034	0.035
Acceptance Err.	0.0046	0.0047	0.0049	0.0050	0.0054

Table 8.18: Relative systematic and statistical uncertainties for ZH signals.

Higgs Mass (GeV)	105	115	125	135	145
Percentage in Higgs window(%)	10.3	10.3	6.90	6.90	10.3
Absolute Uncertainty	0.115	0.115	0.077	0.077	0.115

Table 8.19: Absolute QCD systematic uncertainties for different Higgs mass.

Error Source	tt	zz	zbb	zcc	zjj
MuSMTHit	0.022	0.024	0.026	0.022	0.029
MuTrack	0.090	0.109	0.122	0.111	0.137
MuID	0.055	0.064	0.073	0.066	0.080
L3MuTrig	0.050	0.059	0.062	0.059	0.067
L2MuTrig	0.027	0.031	0.033	0.031	0.035
L1TrkTrig	0.005	0.006	0.007	0.006	0.007
L1MuTrig	0.027	0.032	0.034	0.033	0.038
JetRECOID	0.047	0.072	0.107	0.112	0.111
JES	0.013	0.045	0.047	0.025	0.046
Btag TRF	0.091	0.085	0.086	0.083	0.047
Taggability	0.132	0.135	0.136	0.133	0.136
SFErrTotal	0.209	0.234	0.258	0.245	0.261
Cross Section	0.08	0.06	0.19	0.19	0.12
Luminosity	0.065	0.065	0.065	0.065	0.065
Total Syst. Err.	0.233	0.250	0.327	0.317	0.295
Stat. Err.	0.084	0.182	0.032	0.111	0.165

Table 8.20: Relative systematic and statistical uncertainties for backgrounds. Contributions from WZ and $Z \to \mu^+\mu^-$+anything where the di-muon invariant mass is between 15 GeV and 60 GeV are negligible.

m_H (GeV)	105	115	125	135	145
Expected ZH	0.0588	0.0473	0.0327	0.0221	0.0103
Acceptance	0.0014	0.0016	0.0017	0.0019	0.0019
$t\bar{t}$	1.08	1.17	1.13	1.26	1.30
ZZ	0.292	0.278	0.219	0.175	0.088
Zbb	0.545	0.526	0.478	0.436	0.398
Zcc	0.290	0.278	0.232	0.201	0.194
Zjj	0.765	0.685	0.590	0.637	0.590
QCD	0.17	0.16	0.17	0.17	0.20
Total BKGD	3.11	3.09	2.82	2.89	2.77
Total BKGD Syst. Err.	0.57	0.55	0.49	0.50	0.49
Total BKGD Stat. Err.	0.17	0.16	0.14	0.15	0.15
Total BKGD Err.	0.59	0.57	0.51	0.52	0.51
Events in Data	3	3	4	5	6
95% Obs. Limit (pb)	10.5	9.2	10.6	11.1	13.1
95% Exp. Limit (pb)	10.5	9.2	7.3	6.5	6.5
SM prediction (pb)	0.119	0.083	0.054	0.031	0.015

Table 8.21: Standard Model $\sigma(p\bar{p} \to ZH) \times Br(H \to b\bar{b})$ limit using Bayesian limit calculator [110]. The acceptances include the $Z \to \mu\bar{\mu}$ branching ratio 3.366%.

Chapter 9

Conclusion

A search for ZH associated production in $\mu^+\mu^- b\bar{b}$ channel is performed using 370 pb^{-1} data. The expected upper limits of the cross section at 95% C.L. are set to be between 9.2 to 13.1 pb. With the optimized di-muon isolation requirement, about two times more $Z \to \mu\mu$ signals were obtained compared to the standard $\Delta R > 0.5$ muon isolation requirement as shown in Table 9.1. At the same time the rate of the background events is still at an acceptable level as shown in Figures 9.1-9.3.

	Zjj 0 b-tag	Zjj 1 b-tag	Zjj 2 b-tag
$\Delta R > 0.5$	275	38	7
Di-muon Isolation	545	64	10

Table 9.1: The number of event signals using the standard $\Delta R > 0.5$ requirement and the di-muon isolation probability requirement.

The Standard Model Higgs boson production is also searched for in many other different channels at DØ and CDF [111]. The results of DØ searches (including this analysis) and CDF searches by 2006 are shown in Figure 9.4. With searches for direct Higgs production in the channel $H \to W^+W^-$, the fourth generation model has been ruled out for Higgs mass between 150 and 185 GeV. The DØ and CDF combined results are shown in Figure 9.5. At Higgs masses of 115 GeV and 160 GeV, the combined expected cross section limit is 7.6 and 5.0 times larger than the Standard Model prediction. With the increased Tevatron performance, the luminosity is being accumulated at a much better rate than before. The integrated luminosities by 2009 at DØ and CDF are expected to be ~ 8 fb^{-1}. Combined with refined analysis methods, such as the neural network b-tagger, better jet energy scale and the inclusion of the τ channels, the Higgs observation is not a mission impossible before the Tevatron shutdown.

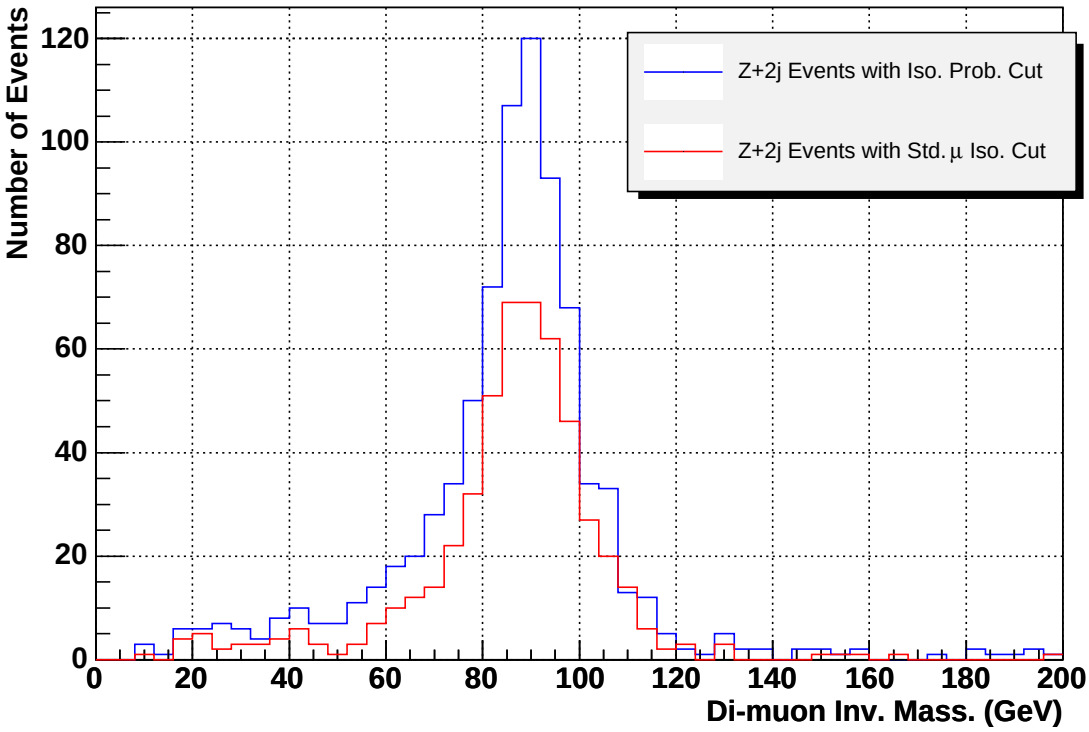

Figure 9.1: For $Z + 2$ jets events the di-muon invariant mass distribution using optimized di-muon isolation requirement (blue line) is compared with that of using the standard muon isolation requirement (red line). Clearly by using the di-muon isolation probability requirement we get 2 times more signals than using the standard requirement, while keep the background at about the same level.

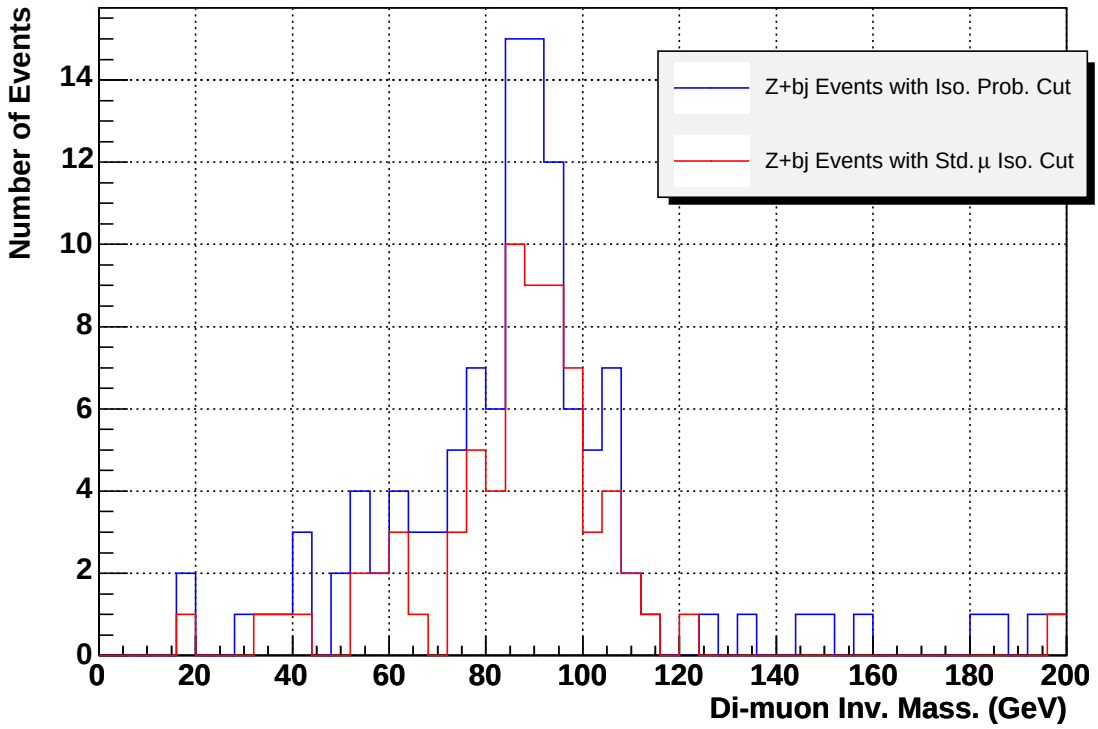

Figure 9.2: For $Z + 2$ jets with 1 or more b-tag events the di-muon invariant mass distribution using optimized di-muon isolation requirement (blue line) is compared with that of using the standard muon isolation requirement (red line).

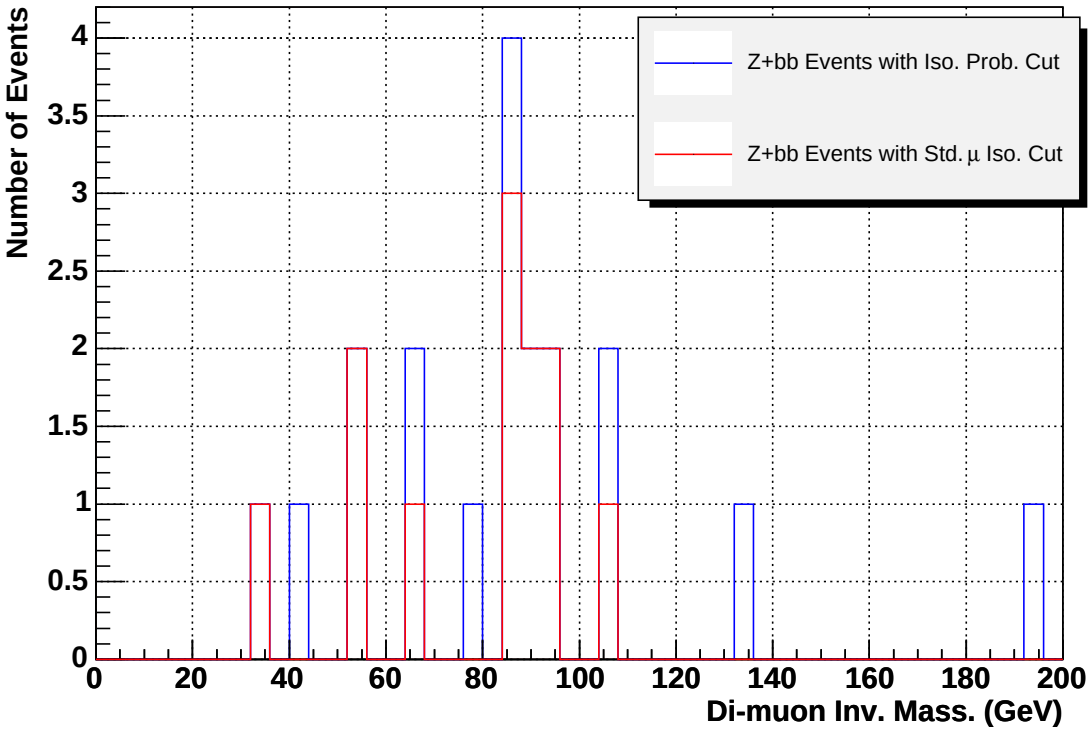

Figure 9.3: For $Z + 2$ jets with 2 or more b-tag events the di-muon invariant mass distribution using optimized di-muon isolation requirement (blue line) is compared with that of using the standard muon isolation requirement (red line).

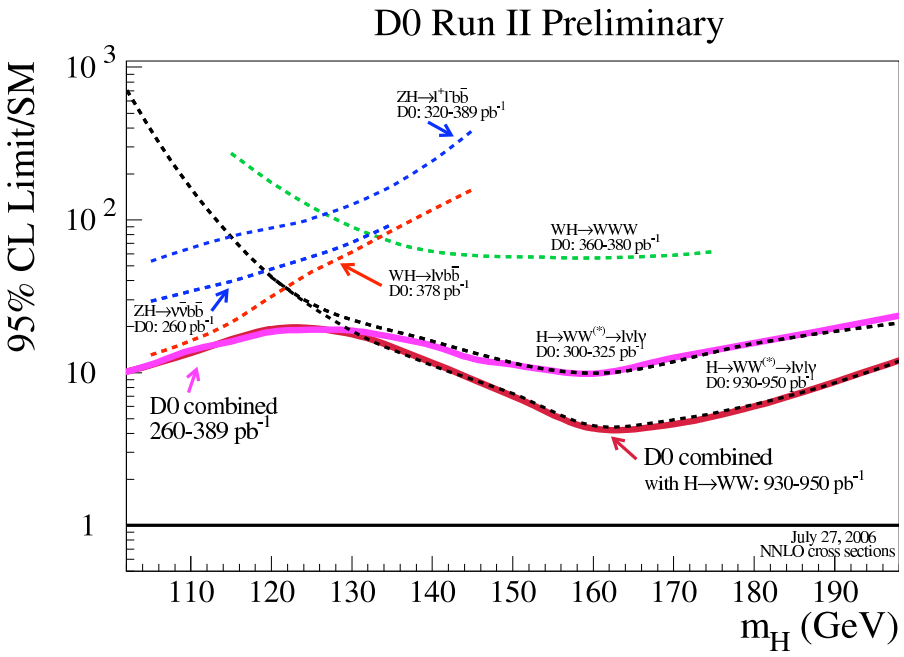

(a)

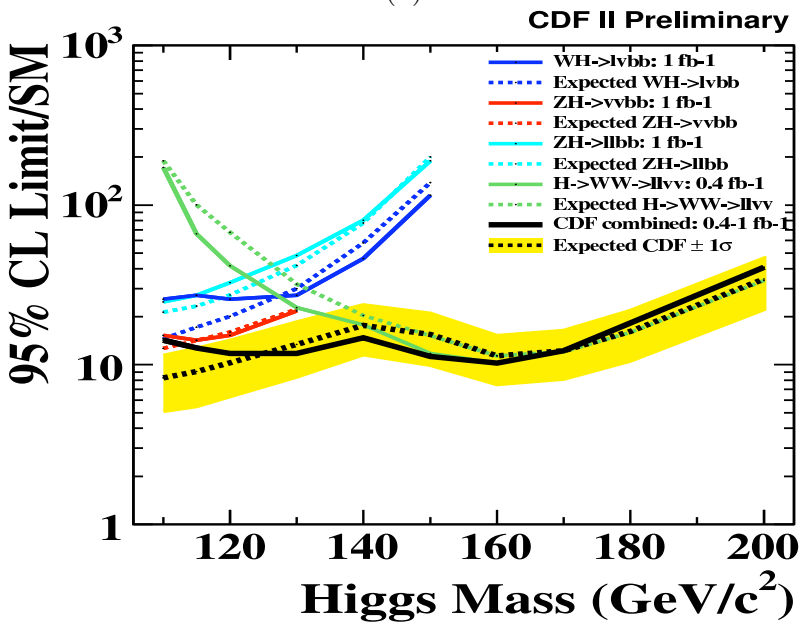

(b)

Figure 9.4: Results of the DØ and CDF Standard Model Higgs searches in different channels, (a) DØ results; (b) CDF results.

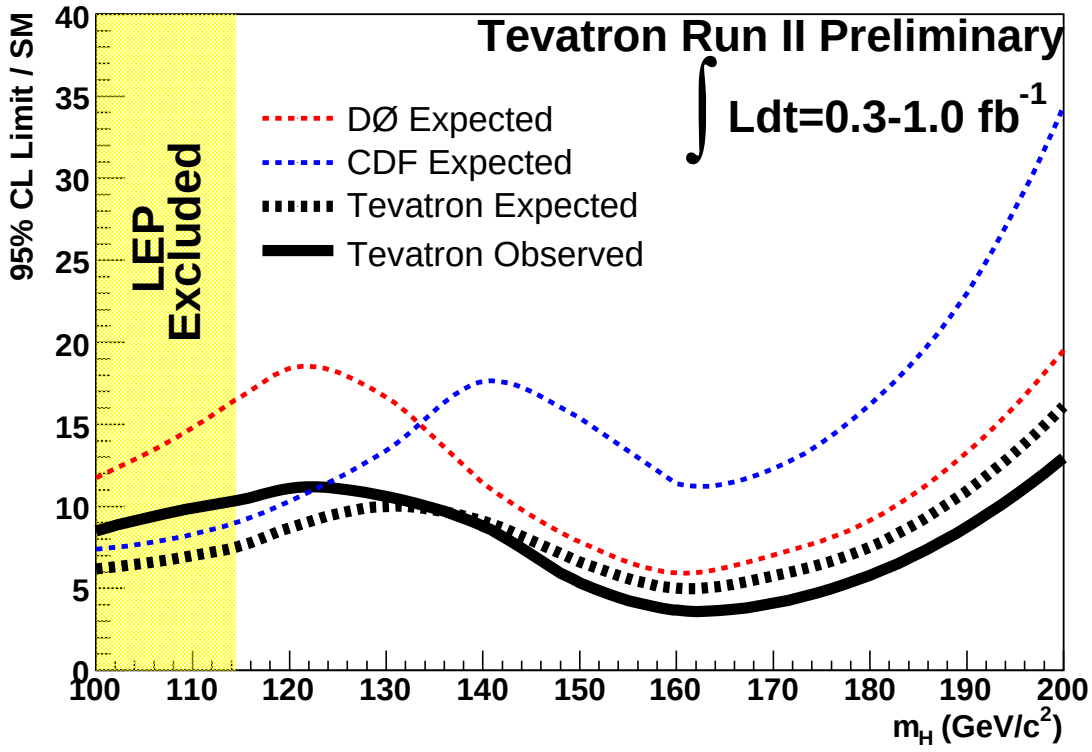

Figure 9.5: Combined results of the DØ and CDF Standard Model Higgs searches at 95% CL. The difference in the shapes of the DØ and CDF results are due to the different size of data set used by the two groups. The combined results is effectively a set of 1.3 pb^{-1} data in all channels.

Appendix A

Event average convolution formula

Given the probability ζ that a single object passes some kind of selection criteria, this section will show how to calculate the event average of the probability when there are n object in the event. The probability that there is 0, 1, 2 such object that pass the selection in this event is show in Eq. A.1:

$$P_0(\zeta) = \prod_{i=1}^{n}(1-\zeta_i) \tag{A.1}$$

$$P_1(\zeta) = \sum_{i=1}^{n}\zeta_i \prod_{j\neq i}^{n}(1-\zeta_j) \tag{A.2}$$

$$P_2(\zeta) = \sum_{i\neq j}^{n}\zeta_i\zeta_j \prod_{k\neq i,j}^{n}(1-\zeta_k) \tag{A.3}$$

where the sum is over all the objects in the event before the criteria selection.

The probability that there are $\geq 1, \geq 2$ such objects that pass the selection in this event is show below:

$$P_{1^+} = 1 - P_0 \tag{A.4}$$

$$P_{2^+} = 1 - P_0 - P_1 \tag{A.5}$$

To calculate the event average, just sum up the probability P over all the events in a given sample and divide the summed probability by the total number of events.

Appendix B

Event Display

The visualization and the event characteristics of the $Z + 2$ b-tagged jets events from data are shown in this section. The detailed event information are shown below. Listed are all muons' p_{T}, η, ϕ, isolation probability, 2-D DCA, A/BC layer time, whether they pass the loose muon ID, all jets' p_{T}, η, ϕ, JLIP probability and whether they are taggable, $E_{\mathrm{T}}^{\mathrm{miss}}$ and its x/y components and direction. The units in this and the following plots are in GeV, cm, μs and rad.

- **Run 189182 Event 21885837**
  Di-muon Inv. Mass=77.7, Double b-jet Inv. Mass=152.3;
  Muon1: p_{T}=29.0,η=-0.23,ϕ=0.10, iso.prob.=0.052, DCA=0.006,$t_a = -0.730, t_{bc} =$ 0, Y;
  Muon2: p_{T}=28.4,η=1.41,ϕ=3.40, iso.prob.=0.202, DCA=0.016,$t_a = 0.625, t_{bc} =$ -0.874, Y;
  Jet1: p_{T}=62.4,η=1.32,ϕ=3.29, JLIP prob.=1.8e-4, taggable;
  Jet2: p_{T}=52.0,η=-0.23,ϕ=0.27, JLIP prob.=6.4e-3, taggable;
  $E_{\mathrm{T}}^{\mathrm{miss}}$=11.3,$E_{\mathrm{T}}^{\mathrm{miss}}X$=1.78,$E_{\mathrm{T}}^{\mathrm{miss}}Y$=11.1,$E_{\mathrm{T}}^{\mathrm{miss}}$ ϕ=1.41.

- **Run 178870 Event 47281409**
  Di-muon Inv. Mass=90.0, Double b-jet Inv. Mass=113.8;
  Muon1: p_{T}=88.2,η=-1.04,ϕ=3.00, iso.prob.=0.004, DCA=3.2e-4,$t_a = 0.745, t_{bc} =$ N/A, Y;
  Muon2:p_{T}=19.4,η=-0.13,ϕ=5.73,iso.prob.=0.034,DCA=-0.008,$t_a = -2.29, t_{bc} =$ -2.69, Y;
  Muon3: p_{T}=8.81,η= 0.14,ϕ=2.69, iso.prob.=0.933, DCA=-0.011,$t_a = 2.70, t_{bc} =$ 0.920, Y;
  Muon4: p_{T}=5.49,η= 0.80,ϕ=5.93, iso.prob.=1.000, DCA=-0.081,$t_a = 1.37, t_{bc} =$ -5.28, Y;
  Muon5: p_{T}=1.20,η= 0.70,ϕ=6.07, iso.prob.=1.000, DCA=-0.093,$t_a = 11.7, t_{bc} =$ N/A, Y;

Jet1: $p_{\rm T}$=63.1,η=0.77,ϕ=5.99, JLIP prob.=4.5e-7, taggable;
Jet2: $p_{\rm T}$=43.4,η=0.01,ϕ=2.62, JLIP prob.=0.03, taggable;
$E_{\rm T}^{\rm miss}$=23.8,$E_{\rm T}^{\rm miss}X$=23.3,$E_{\rm T}^{\rm miss}Y$=-4.76,$E_{\rm T}^{\rm miss}$ ϕ=6.08.

- **Run 194319 Event 9978507**
Di-muon Inv. Mass=106.9, Double b-jet Inv. Mass=76.6;
Muon1:$p_{\rm T}$=35.7,η=-1.70,ϕ=4.04,iso.prob.=0.021,DCA=-2.2e-4,$t_a = -2.62, t_{bc} = -2.75$, Y;
Muon2: $p_{\rm T}$=29.9,η=0.45,ϕ=0.70, iso.prob.=0.025, DCA=-0.002,$t_a = -4.67, t_{bc} = -7.37$, Y;
Muon3: $p_{\rm T}$=15.7,η=1.58,ϕ=1.26, iso.prob.=0.114, DCA=0.008,$t_a = N/A, t_{bc} = N/A$, N;
Jet1: $p_{\rm T}$=34.1,η=1.61,ϕ=1.21, JLIP prob.=0.023, taggable;
Jet2: $p_{\rm T}$=20.7,η=-0.18,ϕ=4.63, JLIP prob.=0.014, taggable;
Jet3: $p_{\rm T}$=12.0,η=-0.18,ϕ=1.95, JLIP prob.=99, un-taggable;
$E_{\rm T}^{\rm miss}$=11.8,$E_{\rm T}^{\rm miss}X$=-0.02,$E_{\rm T}^{\rm miss}Y$=-11.8,$E_{\rm T}^{\rm miss}$ ϕ=4.71.

- **Run 194024 Event 25222547**
Di-muon Inv. Mass=84.3, Double b-jet Inv. Mass=166.8;
Muon1: $p_{\rm T}$=37.3,η=-0.23,ϕ=4.99, iso.prob.=0.075, DCA=-6.7e-4,$t_a = N/A, t_{bc} = -4.33$, Y;
Muon2: $p_{\rm T}$=24.5,η=1.69,ϕ=2.98, iso.prob.=0.0, DCA=-1.8e-4,$t_a = -0.376, t_{bc} = 0.376$, Y;
Muon3: $p_{\rm T}$=11.4,η=-0.05,ϕ=2.09, iso.prob.=0.918, DCA=0.096,$t_a = N/A, t_{bc} = N/A$, N;
Muon4: $p_{\rm T}$=8.20,η=-0.57,ϕ=1.95, iso.prob.=0.765, DCA=0.066,$t_a = -2.58, t_{bc} = 0$, Y;
Muon5: $p_{\rm T}$=4.53,η=0.20,ϕ=5.58, iso.prob.=1.0, DCA=-4.5e-4,$t_a = -0.435, t_{bc} = N/A$, Y;
Jet1: $p_{\rm T}$=91.5,η=0.20,ϕ=5.53, JLIP prob.=0.003, taggable;
Jet2: $p_{\rm T}$=74.9,η=0.04,ϕ=2.05, JLIP prob.=9.3e-6, taggable;
Jet3: $p_{\rm T}$=13.1,η=0.67,ϕ=2.68, JLIP prob.=0.34, taggable;
$E_{\rm T}^{\rm miss}$=22.6,$E_{\rm T}^{\rm miss}X$=5.94,$E_{\rm T}^{\rm miss}Y$=-21.8,$E_{\rm T}^{\rm miss}$ ϕ=4.98.

- **Run 187834 Event 99936835**
Di-muon Inv. Mass=88.6, Double b-jet Inv. Mass=142.8;
Muon1: $p_{\rm T}$=95.0,η=-1.07,ϕ=1.42, iso.prob.=0.0, DCA=-3.0e-4,$t_a = 3.87, t_{bc} = -0.376$, Y;
Muon2: $p_{\rm T}$=83.7,η=-0.59,ϕ=2.32, iso.prob.=0.0, DCA=8.6e-4,$t_a = -1.65, t_{bc} = -1.93$, Y;
Muon3: $p_{\rm T}$=59.9,η=-0.45,ϕ=4.84, iso.prob.=0.323, DCA=-0.007,$t_a = N/A, t_{bc} = N/A$, N;

Muon4: p_{T}=4.53,η=1.58,ϕ=1.85, iso.prob.=0.643, DCA=-0.004,$t_a = N/A, t_{bc} = N/A$, N;
Muon5: p_{T}=0.95,η=1.41,ϕ=2.58, iso.prob.=0.798, DCA=0.023,$t_a = N/A, t_{bc} = N/A$, N;
Jet1: p_{T}=160.7,η=-0.46,ϕ=4.84, JLIP prob.=7.3e-4, taggable;
Jet2: p_{T}=31.2,η=1.50,ϕ=1.94, JLIP prob.=0.19, taggable;
Jet3: p_{T}=31.7,η=1.00,ϕ=6.08, JLIP prob.=0.007, taggable;
$E_{\mathrm{T}}^{\mathrm{miss}}$=25.9,$E_{\mathrm{T}}^{\mathrm{miss}}X$=18.2,$E_{\mathrm{T}}^{\mathrm{miss}}Y$=-18.5,$E_{\mathrm{T}}^{\mathrm{miss}}$ ϕ=5.49.

- **Run 190059 Event 47955473**
Di-muon Inv. Mass=105.3, Double b-jet Inv. Mass=135.0;
Muon1: p_{T}=76.0,η=0.48,ϕ=3.63, iso.prob.=0.011, DCA=-7.0e-4,$t_a = 5.40, t_{bc} = -1.44$, Y;
Muon2: p_{T}=38.7,η=0.35,ϕ=0.99, iso.prob.=0.070, DCA=-2.2e-4,$t_a = N/A, t_{bc} = 3.63$, Y;
Muon3: p_{T}=12.1,η=-0.27,ϕ=6.13, iso.prob.=0.893, DCA=-2.7e-4,$t_a = N/A, t_{bc} = N/A$, N;
Muon4: p_{T}=5.15,η=1.41,ϕ=2.03, iso.prob.=0.405, DCA=-0.008,$t_a = N/A, t_{bc} = N/A$, N;
Muon5: p_{T}=2.17,η=1.22,ϕ=2.34, iso.prob.=0.966, DCA=0.057,$t_a = N/A, t_{bc} = N/A$, N;
Jet1: p_{T}=96.7,η=-0.27,ϕ=6.11, JLIP prob.=0.008, taggable;
Jet2: p_{T}=28.3,η=1.35,ϕ=2.07, JLIP prob.=0.029, taggable;
Jet3: p_{T}=16.2,η=-0.19,ϕ=0.77, JLIP prob.=0.390, un-taggable;
$E_{\mathrm{T}}^{\mathrm{miss}}$=34.0,$E_{\mathrm{T}}^{\mathrm{miss}}X$=-26.1,$E_{\mathrm{T}}^{\mathrm{miss}}Y$=21.8,$E_{\mathrm{T}}^{\mathrm{miss}}$ ϕ=2.44.

- **Run 1887735 Event 61321639**
Di-muon Inv. Mass=94.1, Double b-jet Inv. Mass=44.3;
Muon1: p_{T}=85.2,η=0.77,ϕ=6.13, iso.prob.=0.0, DCA=-3.9e-4,$t_a = -3.60, t_{bc} = -5.10$, Y;
Muon2:p_{T}=50.3,η=0.30,ϕ=1.34,iso.prob.=0.006,DCA=-1.2e-4,$t_a = -3.97, t_{bc} = -7.58$, Y;
Muon3: p_{T}=3.99,η=1.92,ϕ=3.60, iso.prob.=0.946, DCA=-0.046,$t_a = N/A, t_{bc} = N/A$, N;
Jet1: p_{T}=72.4,η=1.53,ϕ=3.14, JLIP prob.=2.75e-7, taggable;
Jet2: p_{T}=45.0,η=1.97,ϕ=3.70, JLIP prob.=3.37e-4, taggable;
$E_{\mathrm{T}}^{\mathrm{miss}}$=14.5,$E_{\mathrm{T}}^{\mathrm{miss}}X$=10.3,$E_{\mathrm{T}}^{\mathrm{miss}}Y$=-10.2,$E_{\mathrm{T}}^{\mathrm{miss}}$ ϕ=5.51.

- **Run 194723 Event 41758582**
Di-muon Inv. Mass=85.9, Double b-jet Inv. Mass=169.8;
Muon1: p_{T}=53.2,η=-0.92,ϕ=3.54, iso.prob.=0.020, DCA=-0.001,$t_a = -3.06, t_{bc} = 1.79$, Y;

Muon2: $p_{\rm T}$=34.0,η=-1.19,ϕ=0.46, iso.prob.=0.009, DCA=-0.001,$t_a = 1.88, t_{bc} = -0.50$, Y;
Muon3: $p_{\rm T}$=9.42,η=0.75,ϕ=6.14, iso.prob.=0.998, DCA=5.3e-5,$t_a = N/A, t_{bc} = N/A$, N;
Muon4: $p_{\rm T}$=3.61,η=-0.03,ϕ=2.72, iso.prob.=0.865, DCA=-0.049,$t_a = N/A, t_{bc} = N/A$, N;
Muon5: $p_{\rm T}$=2.17,η=0.93,ϕ=0.01, iso.prob.=1.0, DCA=-0.003,$t_a = N/A, t_{bc} = N/A$, Y;
Muon6: $p_{\rm T}$=0.99,η=0.43,ϕ=3.03, iso.prob.=0.860, DCA=0.022,$t_a = N/A, t_{bc} = N/A$, N;
Jet1: $p_{\rm T}$=107.0,η=0.82,ϕ=6.27, JLIP prob.=1.12e-6, taggable;
Jet2: $p_{\rm T}$=65.2,η=1.05,ϕ=3.27, JLIP prob.=0.003, taggable;
$E_{\rm T}^{\rm miss}$=21.5,$E_{\rm T}^{\rm miss}X$=-20.2,$E_{\rm T}^{\rm miss}Y$=7.24,$E_{\rm T}^{\rm miss}$ ϕ=2.80.

- **Run 194729 Event 52983409**
Di-muon Inv. Mass=86.5, Double b-jet Inv. Mass=133.7;
Muon1: $p_{\rm T}$=60.4,η=0.76,ϕ=3.42, iso.prob.=0.023, DCA=-0.003,$t_a = -1.33, t_{bc} = -1.52$, Y;
Muon2: $p_{\rm T}$=35.2,η=0.53,ϕ=1.03, iso.prob.=0.017, DCA=-0.011,$t_a = -1.79, t_{bc} = N/A$, Y;
Muon3: $p_{\rm T}$=11.1,η=-0.18,ϕ=5.44, iso.prob.=0.967, DCA=0.122,$t_a = -1.69, t_{bc} = 2.36$, Y;
Jet1: $p_{\rm T}$=55.3,η=-0.23,ϕ=5.32, JLIP prob.=0.022, taggable;
Jet2: $p_{\rm T}$=32.1,η=1.97,ϕ=3.40, JLIP prob.=0.023, taggable;
$E_{\rm T}^{\rm miss}$=85.8,$E_{\rm T}^{\rm miss}X$=61.9,$E_{\rm T}^{\rm miss}Y$=59.3,$E_{\rm T}^{\rm miss}$ ϕ=0.76.

- **Run 195168 Event 22923518**
Di-muon Inv. Mass=87.1, Double b-jet Inv. Mass=96.0;
Muon1: $p_{\rm T}$=51.9,η=-0.82,ϕ=5.88, iso.prob.=0.008, DCA=-4.8e-4,$t_a = 1.67, t_{bc} = 1.01$, Y;
Muon2:$p_{\rm T}$=49.4,η=-0.04,ϕ=1.33,iso.prob.=0.005,DCA=-0.002,$t_a = -1.65, t_{bc} = -1.72$, Y;
Muon3: $p_{\rm T}$=6.84,η=0.49,ϕ=3.15, iso.prob.=0.985, DCA=-0.025,$t_a = N/A, t_{bc} = N/A$, N;
Muon4: $p_{\rm T}$=1.04,η=-0.22,ϕ=3.11, iso.prob.=0.997, DCA=0.828,$t_a = N/A, t_{bc} = N/A$, N;
Jet1: $p_{\rm T}$=51.9,η=0.40,ϕ=3.19, JLIP prob.=0.038, taggable;
Jet2: $p_{\rm T}$=38.7,η=-0.96,ϕ=4.89, JLIP prob.=2.7e-4, taggable;
$E_{\rm T}^{\rm miss}$=19.3,$E_{\rm T}^{\rm miss}X$=-17.0,$E_{\rm T}^{\rm miss}Y$=9.24,$E_{\rm T}^{\rm miss}$ ϕ=2.64.

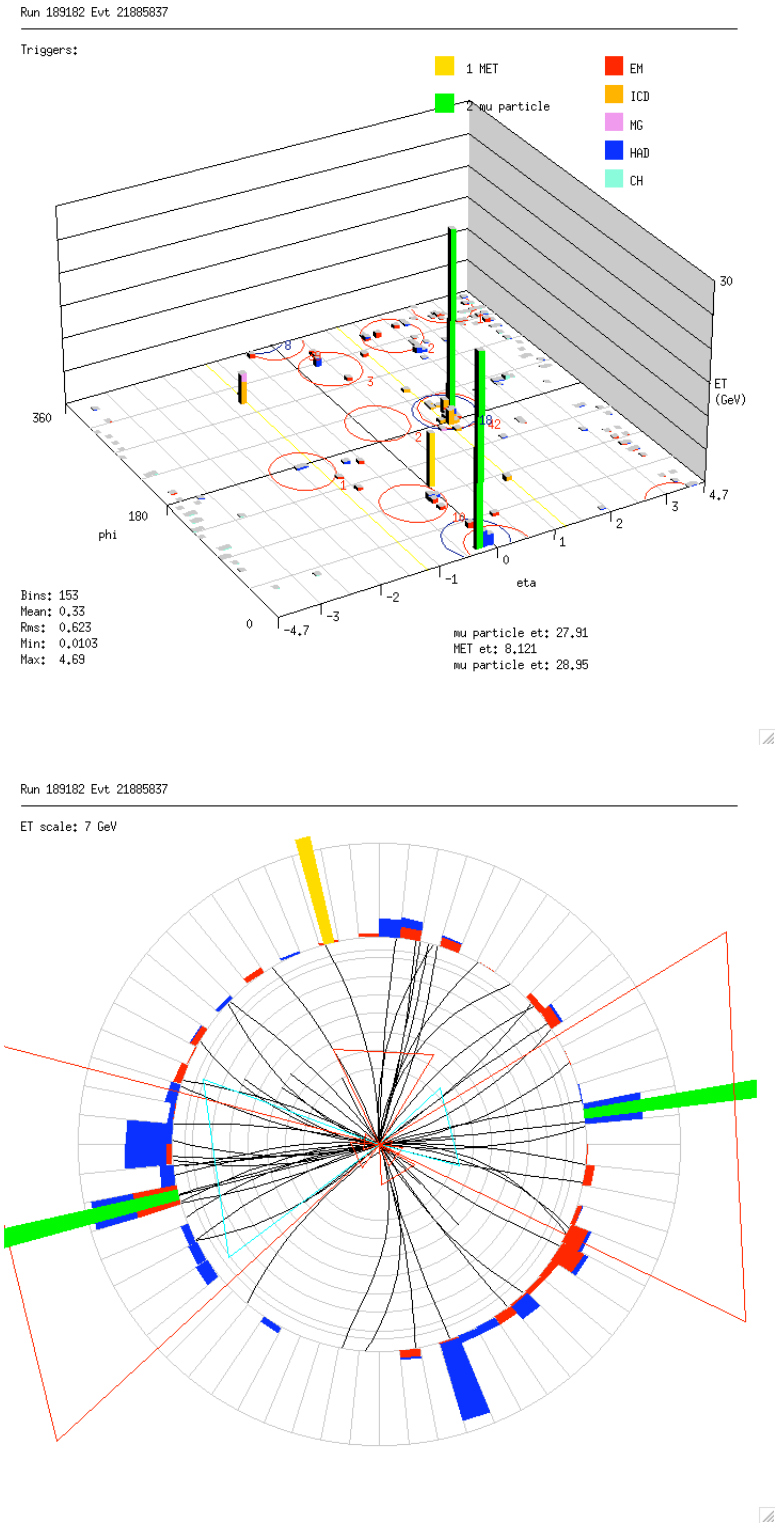

Figure B.1: Event display for run 189182 event 21885837.

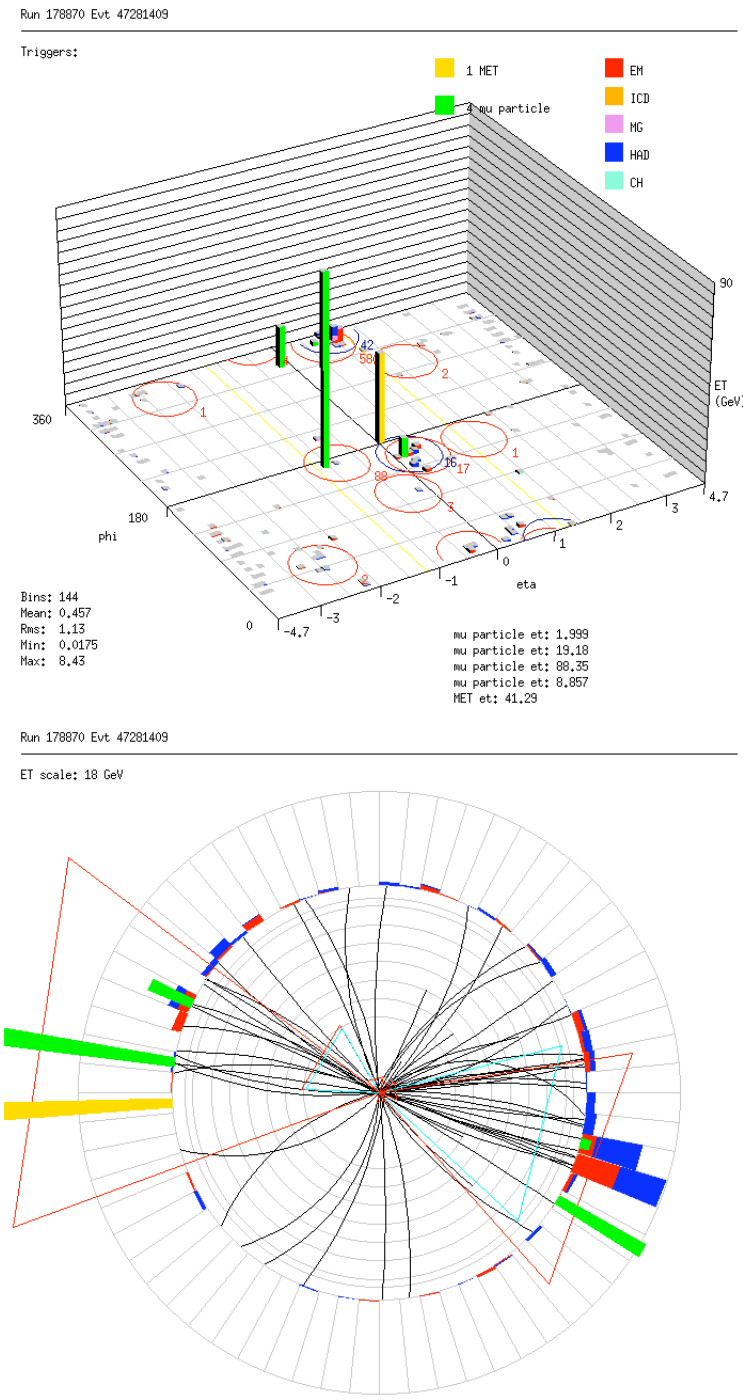

Figure B.2: Event display for run 178870 event 47281409.

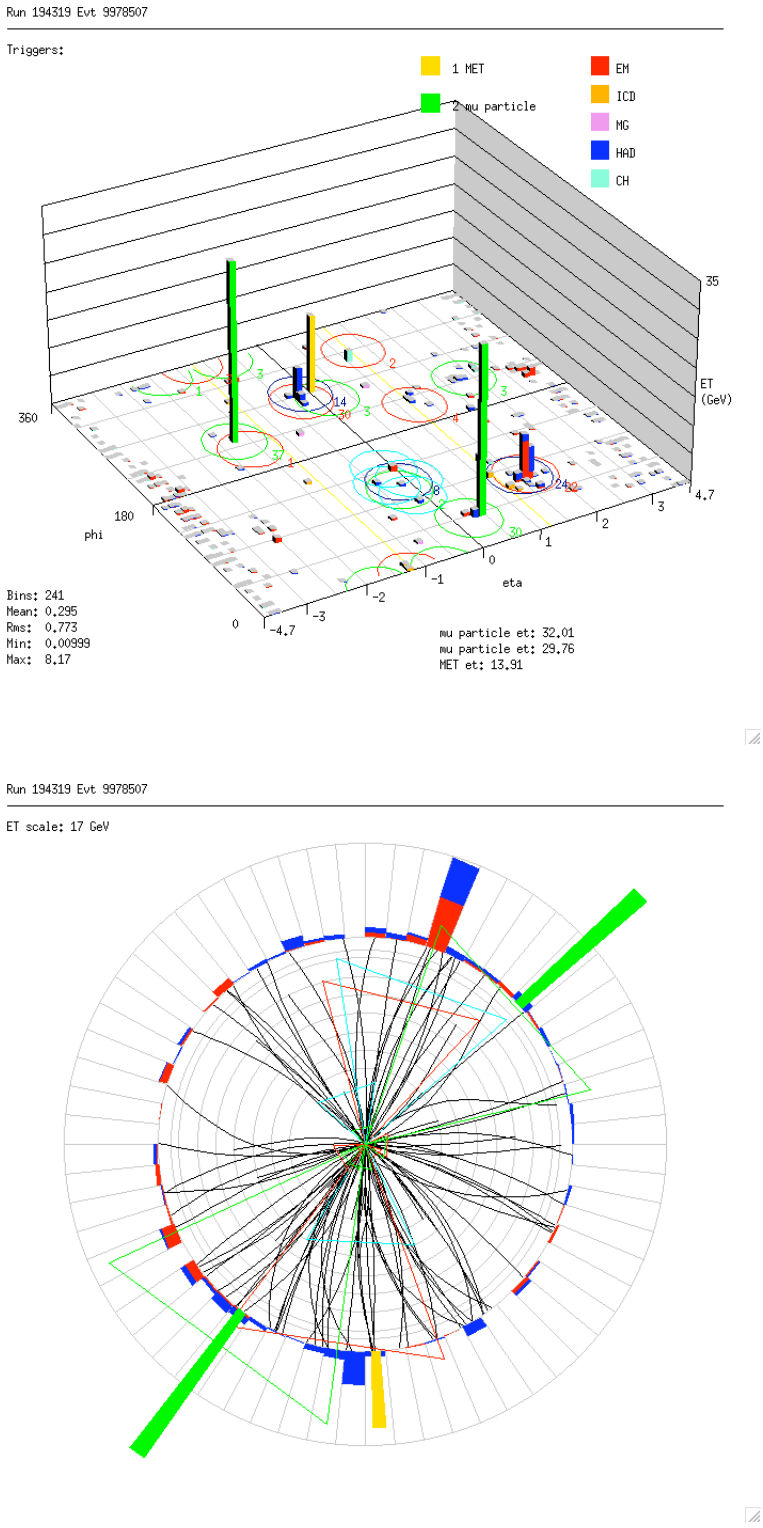

Figure B.3: Event display for run 194319 event 9978507.

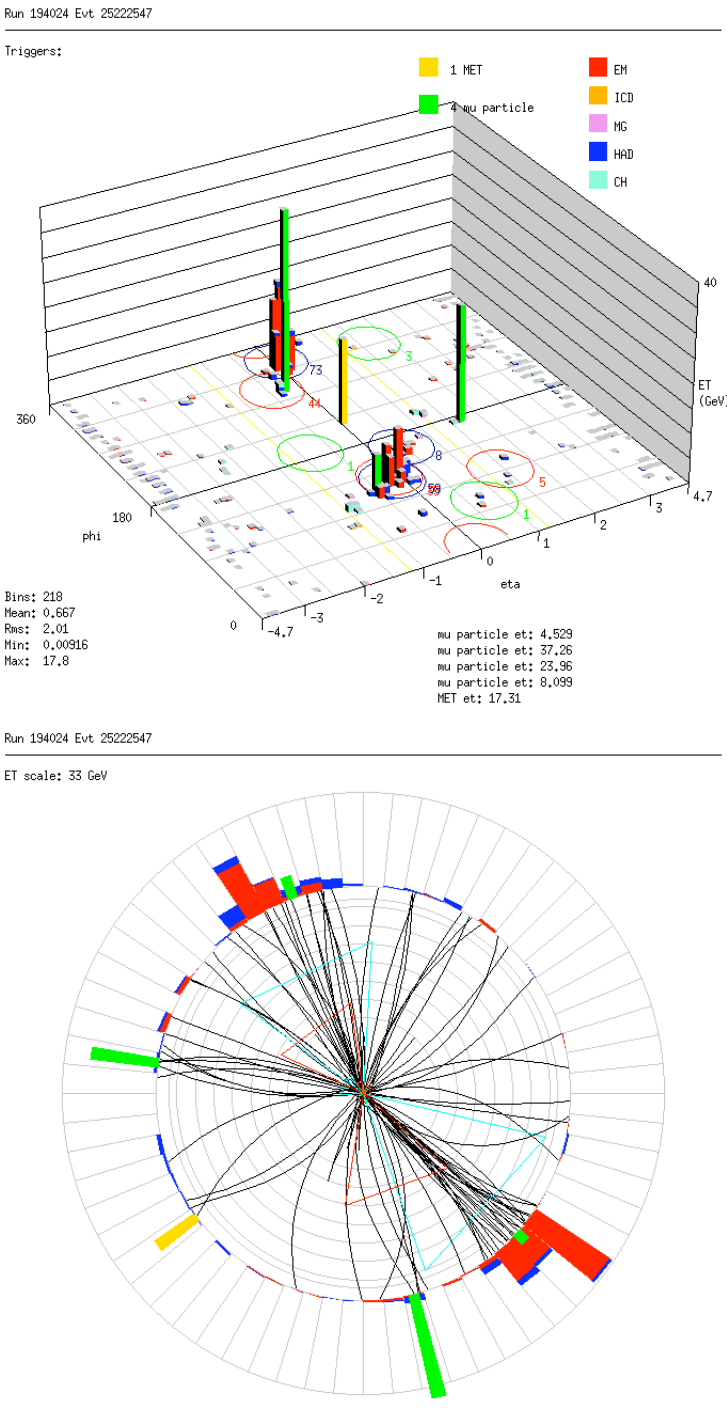

Figure B.4: Event display for run 194024 event 25222547.

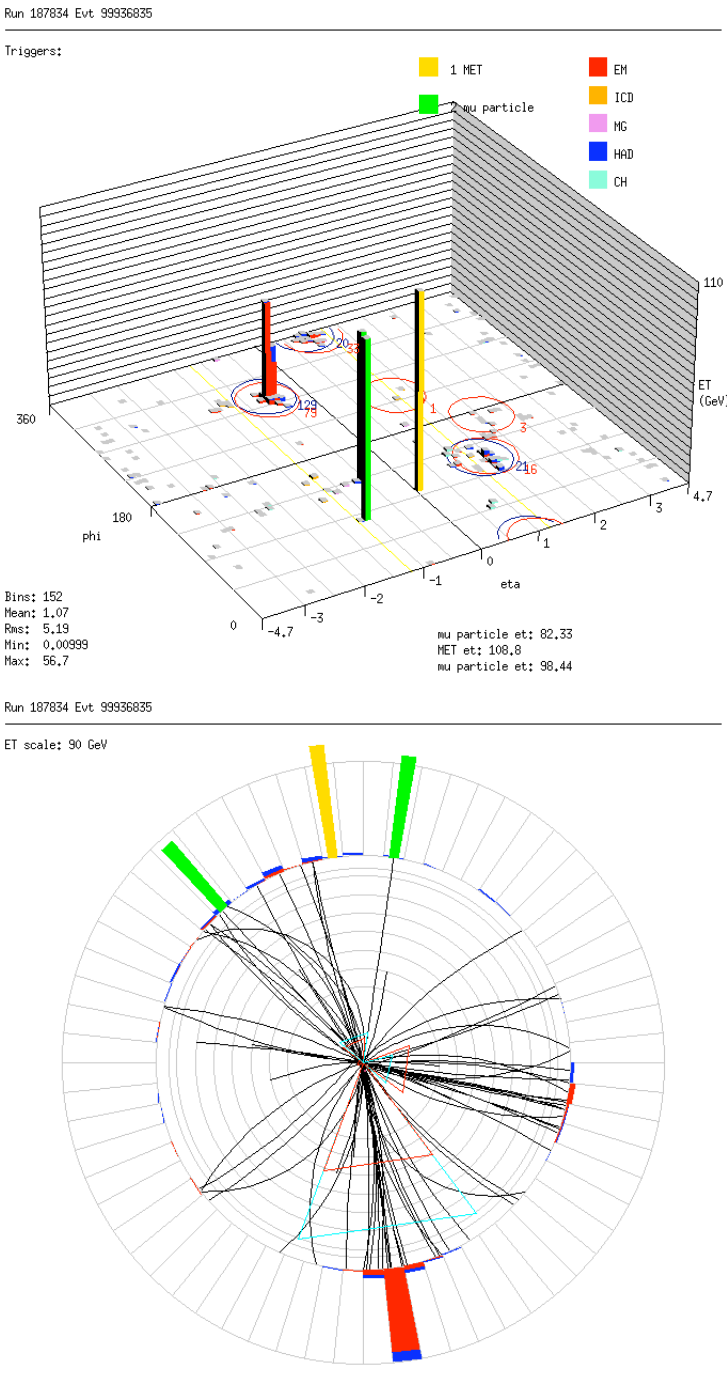

Figure B.5: Event display for run 187834 event 99936835.

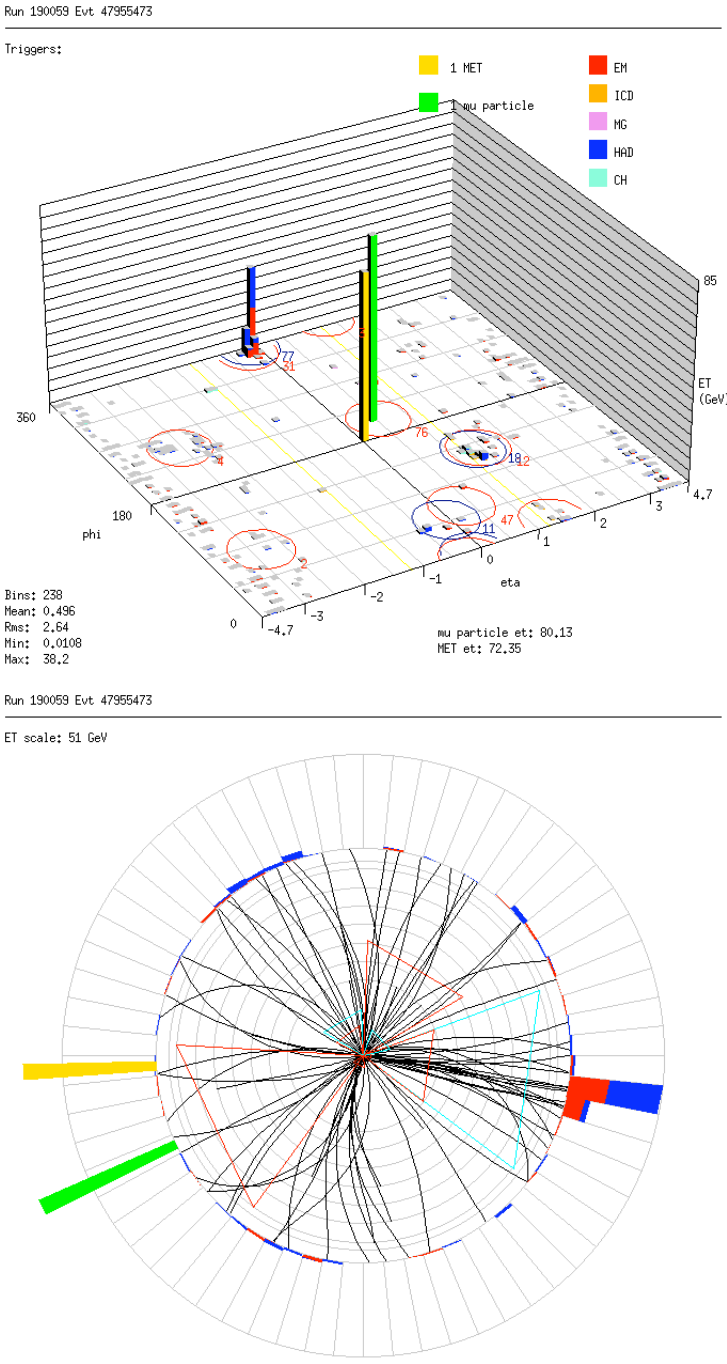

Figure B.6: Event display for run 190059 event 47955473.

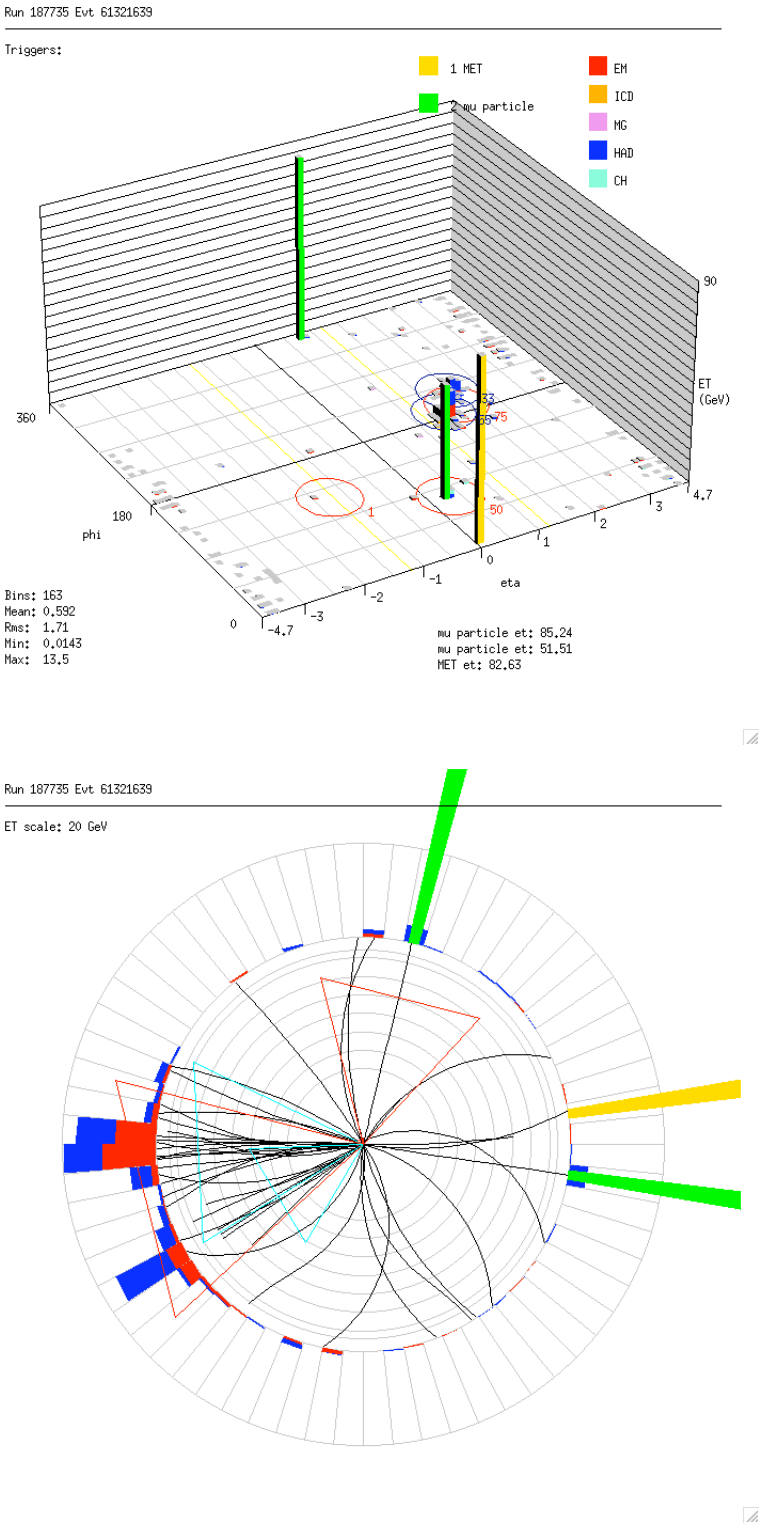

Figure B.7: Event display for run 1887735 event 61321639.

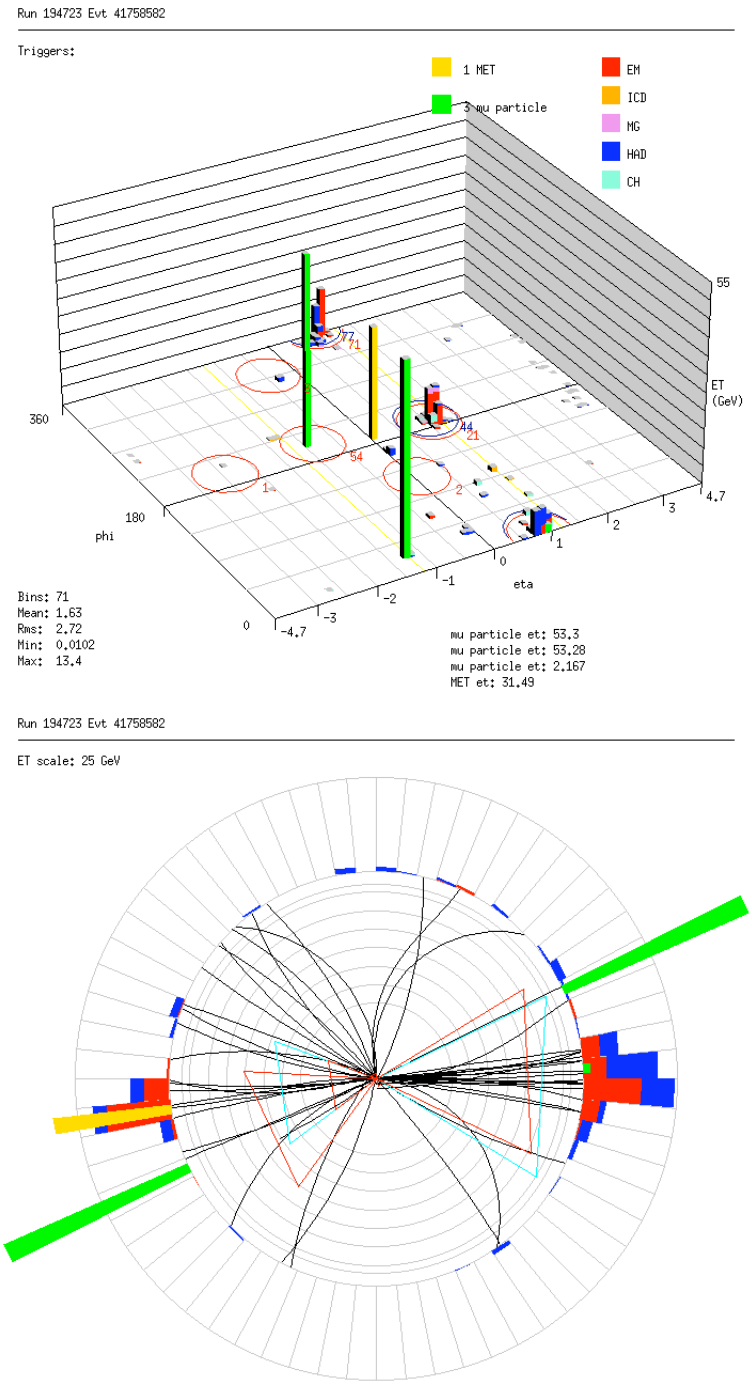

Figure B.8: Event display for run 194723 event 41758582.

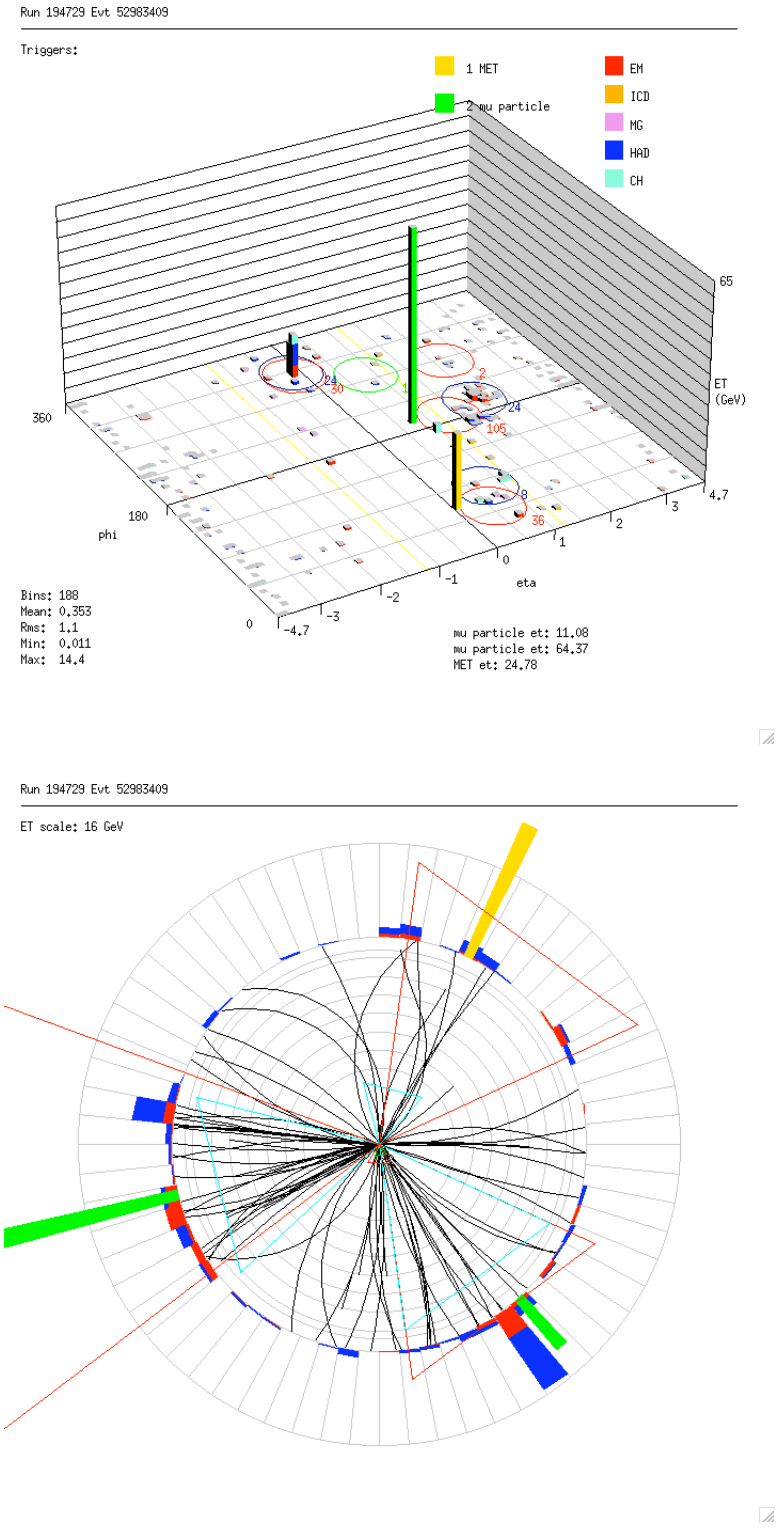

Figure B.9: Event display for run 194729 event 52983409.

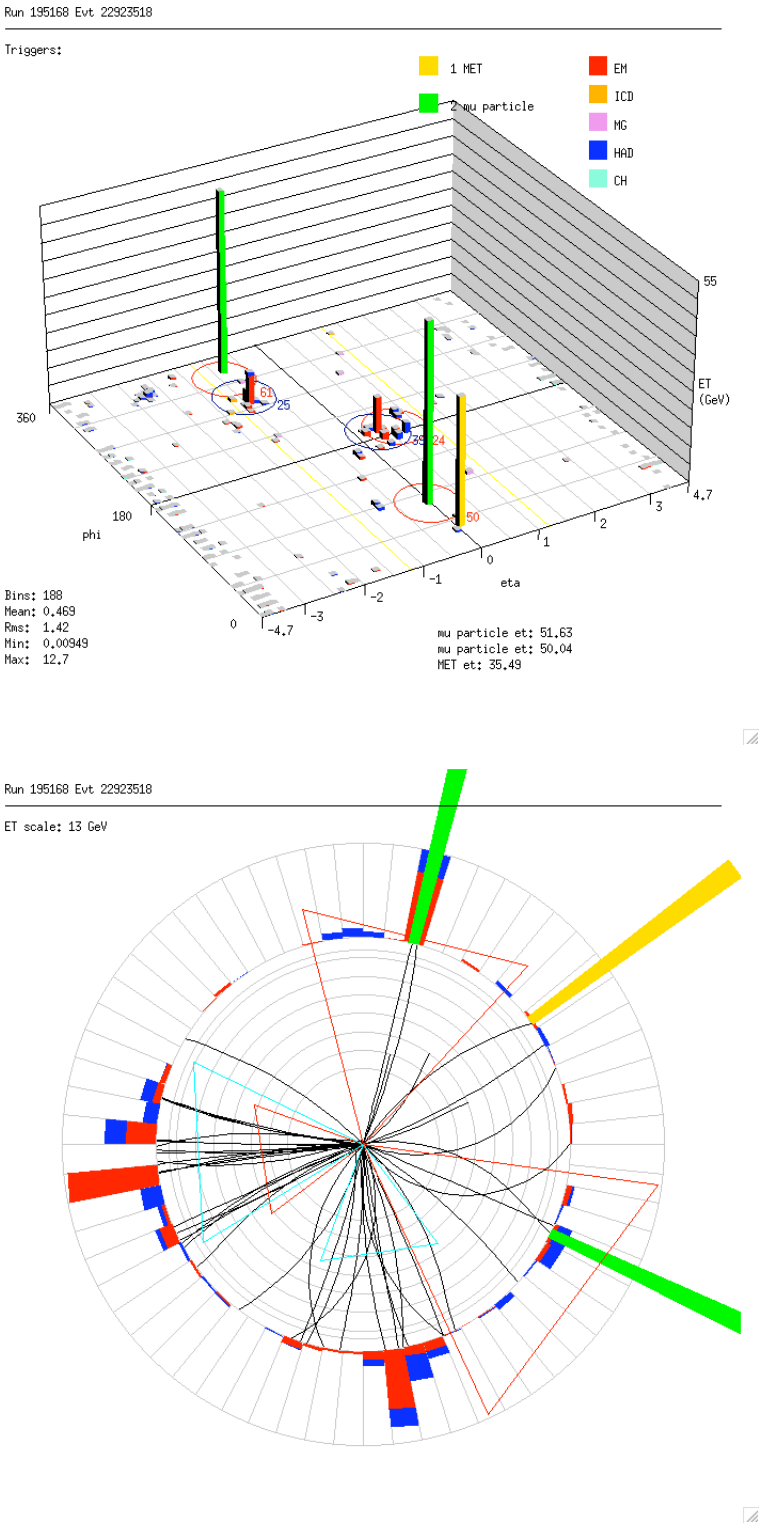

Figure B.10: Event display for run 195168 event 22923518.

Bibliography

[1] M. Carena, *et al. Report of the Tevatron Higgs Working Group*, hep-ph/0010338

[2] Y.D. Mutaf, *Topological Analysis Method and High Efficiency Event Selection for* $Z(\mu\bar{\mu} + b\bar{b})$, DØ note 4587

[3] There are tons of books, papers and web pages. For example, Steven Weinberg, *The Quantum Theory of Fields*, **vol. 1**, Chapter 1, and the references therein; the wikipedia.org listed many useful references under "particle physics".

[4] Steven Weinberg, *The Quantum Theory of Fields*, **vol. 1**, pg. 78-81

[5] T.P. Cheng and L.F. Li, *Gauge Theory of Elementary Particle Physics* **pg.349**

[6] L. Scodellaro, *Perspectives for Higgs Boson Search in Full Hadronic Final States at CDF II*, Ph.D thesis, Universita' degli Studi di Padova, 2001

[7] K. Riesselmann, *Limitations of a Standard Model Higgs Boson*, hep-ph/9711456

[8] Abbiendi, G. *et al* Phys. Lett. B., 565 61, 2003.

[9] The LEP Electroweak Working Group. 2006. http://lepewwg.web.cern.ch/LEPEWWG/

[10] D. Rainwater, *Searching for the Higgs Boson*, help-ph/0702124, Mar. 16 2007

[11] T. Hahn, S. Heinemeyer, F. Maltoni, G. Weiglein and S. Willenbrock, arXiv:hep-ph/0607308; see http://maltoni.web.cern.ch/maltoni/TeV4LHC/SM.html for references to all the specific latest calculations.

[12] U. Aglietti et al., arXiv:hep-ph/0612172

[13] A. Djouadi, J. Kalinowski and M. Spira, Comput. Phys. Commun. 108, 56 (1998).

[14] G. Altarelli, *The Standard Electroweak Theory and Beyond*, hep-ph/0011078, Nov. 6, 2000.

[15] Chris Quigg, Lectures on the Standard Model .

[16] Davison E. Soper, hep-lat/9609018, hep-ph/9702203

[17] T.P. Cheng and L.F. Li, *Gauge Theory of Elementary Particle Physics*

[18] George Sterman, *An Introduction to Quantum Field Theory.*

[19] H. L. Lai *et al.* (CTEQ Collaboration), *Global QCD Analysis of Parton Structure of the Nucleon: CTEQ5 Parton Distributions*, Eur. Phys. J. C 12 375 (2000).

[20] W.-M. Yao *et al.* (Particle Data Group), J. Phys. G 33, 1 (2006) (URL: http://pdg.lbl.gov)

[21] Onne Peters, *Measurement of the b−jet Cross Section at* $\sqrt{s} = 1.96$ *TeV*, Ph.D dissertation (2003).

[22] John Campbell and R. K. Ellis, *Radiative Corrections to Zbb Production*, hep-ph/0006304,

[23] J. M. Campbell, R. K. Ellis, F. Maltoni and S. Willenbrock, Phys. Rev. D 69, 074021 (2004).

[24] Cosmic ray/Gamma ray/Neutrino and similar experiments around the world, http://www.mpi-hd.mpg.de/hfm/CosmicRay/CosmicRaySites.html#cosmic-ray+gamma-ray

[25] Accelerators around the world, http://www-elsa.physik.uni-bonn.de/accelerator_list.html

[26] Matthew Early Wright, *Riding the Plasma Wave of the Future*, Symmetry: Dimensions of Particle Physics (Fermilab/SLAC), April 2005, p. 12.

[27] Richard C. Fernow, *Introduction to experimental particle physics*, Cambridge University Press 1986. Chap. 4, 5 and references therein.

[28] P. J. Bryant, *A Brief History and Review of Accelerators*, CERN 1994, and references therein.

[29] T. Cole *et al.*, *Introduction to Colliding Beams at Fermilab*, Fermilab TM-1909 (1994); Run II Handbook, http://www-bd.fnal.gov/runII/

[30] A. M. Abazov *et al.*, *The Upgraded DØ Detector*, arXiv:physics/0507191, 2005

[31] D. McGinnis, *The Tevatron Run II Handbook*, http://www-bd.fnal.gov/runII/index.html

[32] Tevatron Status Jagons. http://www.fnal.gov/pub/news02/definitions/ Accelerator_States/

[33] Fermilab beam division, Tevatron Run II b data, http://www-bdnew.fnal.gov/tevatron/data.html; Valeri Lebedev, *Update on Run II Luminosity Progress and Projection*, DØ ADM talk, Jan 26, 2007.

[34] Sung Hwan Ahn *et. al*, *DØ Luminosity in Run 2: Delivered*, DØ note 3970, 04/08/02

[35] Donald H. Perkins, *Introduction to High Energy Physics*, 3rd Edition, Addison-Wesley (1987)

[36] K. Hagiwara *et. al*, Phys. Rev. D 66, 010001 (2002).

[37] *DØ Fiber Tracker Technical Design Report*, 1997, http:/d0server1.fnal.gov/users/stefan/www/CFT_TDR/CFT_TDR.ps

[38] *The DØ upgrade, the Detector and its Physics*, Fermilab Pub-96/357-E

[39] P. Baringer *et. al*, *Cosmic ray data analysis for the DØ preshower detector*, D0 note 3765, July 2000.

[40] Fast Monte Carlo (PMCS) configuration files, http://www-d0.fnal.gov/D0Code/source/pmcs_jet/rcp/

[41] Private talk with Dr. Junjie Zhu.

[42] Mikko Voutilainen, *Update on jet resolutions*, DØ Jet Energy Scale Meeting, Nov. 21, 2006.

[43] T. Diehl *et. al*, *Technical Design of the Central Muon System*, DØ note 3365, March 1998.

[44] Gustavo J. Otero Y Garzon, *Measurement of the Top Quark Pair Production Cross Section in $p\bar{p}$ Collisions at sqrts = 1.96 TeV* DØ thesis 2006, pg. 51–55 and the reference therein

[45] S. Klimenko, J. Konigsberg, T. M. Liss, FERMILAB-FN-0741, 2003.

[46] T. Edwards et al.: FERMILAB-TM-2278-EB, 2004.

[47] Brendan Casey, *et. al*, *Determination of the Effective Inelastic p pbar Cross-Section for the DØ Luminosity Measurement Using Upgraded Readout Electronics*, DØ note 4958, 11/15/05

[48] T. Adams, *et. al*, *The D0 Run II Impact Parameter Trigger*, hep-physics/0701195

[49] H. Dong, J. Hobbs and W. Taylor, *Performance of the DØ STT Track Fitting Algorithm*, DØ note 5208.

[50] Tamsin Edwards, Ph.D dissertation, *Diffractively produced Z bosons in the muon decay channel in $p\bar{p}$ collisions at $\sqrt{s}$ = 1.96 TeV, and the measurement of the efficiency of the DØ Run II Luminosity Monitor*

[51] Sung Hwan Ahn *et. al*, *DØ Luminosity in Run 2: Triggered*, DØ note 3971, 04/08/02

[52] Sung Hwan Ahn *et. al*, *DØ Luminosity in Run 2: Recorded*, DØ note 3972, 04/08/02

[53] lm_access package, DØ note 3969.

[54] M.Angelou *et. al*, *TopTrigger Efficiency Measurements and the top_trigger package*, DØ note 4512, 07/19/04.

[55] Sabine Lammer, *Trigger OR-ing for the Masses*, April 27, 2007, http://www-d0.hef.kun.nl//askArchive.php?base=agenda&categ=a07678&id=a07678s1t0/ transparencies

[56] Emily Nurse, Paul Telford, *Measurement of cross section times branching ratio for $Z \to \mu^+\mu^-$ in $p\bar{p}$ collisions at 1.96 TeV.*, DØ note 4284, 10/27/03

[57] DØ EM object ID certification page, http://www-d0.fnal.gov/phys_id/emid/d0_private/emid.html

[58] DØ Jet and Missing E_{T} certification page, http://www-d0.fnal.gov/∼d0upgrad/d0_private/software/jetid/jetid.html

[59] A. Khanov, *HTF: Histogramming Method for Finding Tracks*, DØ Note 3778, 2000.

[60] H. Greenlee, *The DØ Kalman Track Fit*, DØ Note 4303, 2004.

[61] G. Borisov *Technical Details of AA Tracking*, 2004, http://www-d0.fnal.gov/global_tracking/talks/20030228/talk-adm-030228.ps

[62] A. Schwartzman and M. Narain, *Probabilistic Vertex Selection*, DØ note 4042 (November 2002)

[63] A. Garcia-Bellido *et al.*, *Primary Vertex Reconstruction in p14*, DØ Note 4320 (7 Jan. 2004).

[64] U. Bassler and G. Bernardi, *Towards a Coherent Treatment of Calorimetric Energies: Missing Transverse Energy, Jets, E.M. Objects and the T42 Algorithm*, DØ Note 4124 (24 Mar. 2003).

[65] G. Bernardi, E Bustato and J.R. Vlimant, *Improvements from the T42 Algorithm on Calorimeter Objects Reconstruction*, DØ Note 4335 (26 Jan. 2004).

[66] J-R. Vlimant, U. Bassler, G. Bernardi and S. Trincaz-Duvoid, *Technical description of the T42 algorithm for the calorimeter noise suppression*, DØ Note 4146 (May 2003).

[67] Laurent Duflot, Viatcheslav Shary, Robert Zitoun and Ingo Torchiani, cal_event_quality package, DØ note 4614 (Oct. 4, 2004)

[68] NADA: B. Olivier *et al*, *A New Event by Event Hot Cell Killer*, DØ Note 3687 (28 Jul. 2000).

[69] Refer to the CalNada.rcp file in the p14.06.01 version of the DØ cal_nada CVS package.

[70] G. Blazey *et al*, *Run II Jet Physics* (10 May 2000), hep-ex/0005012.

[71] *d0correct* package manual.

[72] N. Gollub and L. Shabalina, *Measurement of the ttbar Production Cross Section at $\sqrt{s}$ = 1.96 TeV in the muon-plus-jets Final State using a Topological Method on 363 pb^{-1} of PASS2 data*, DØ Note 4954(December 2005).

[73] F. Canelli, *et al.*, *Jet Energy Scale at DØ in Run II* DØ Note 4011.

[74] DØ Jet Energy Scale study group, *Jet Energy Scale at DØ RunII*, DØ Note 4720 (February 2005).

[75] T. Golling, *Measurement of the $t\bar{t}$ Production Cross-Section at $\sqrt{s}$ = 1.96 TeV in the Muon+Jets Final State using a Topological Method*, DØ Note 4667 (16 Dec. 2004)

[76] James Heinmiller and Nikos Varelas, *Jet Reconstruction Efficiency*, Sept. 16, 2005

[77] Onne Peters, DØ Ph.D dissertation, *Measurement of the b-jet cross section at $\sqrt{s} = 1.96$ TeV*, 2003

[78] L. Chevalier *et al. Track Parameter Error Matrix Propagation in Matter and Magnetic Field, Error Matrices Combination*, http://www-clued0.fnal.gov/∼tuchming/myprop.ps, (24 Oct. 2001).

[79] Gavin Hesketh, *A Measurement of the Z^0 Boson Production Cross Section Times Muon Branching Fraction in $p\bar{p}$ Collisions at 1.96 TeV*, Ph.D thesis, p194.

[80] M. Agelou *et al.*, *DØ Top analyses and data sample for the winter conference 2004*, DØ Note 4419.

[81] C. Clement *et al.*, *MuonID Certification for p14*, DØ Note 4350 (Mar. 4, 2004)

[82] DØ Monte Carlo Simulation Homepage, http://www-d0.fnal.gov/computing/MonteCarlo/MonteCarlo.html

[83] DØ Trigger Simulation Homepage, http://www-d0.fnal.gov/computing/trigsim/trigsim.html

[84] T. Sjostrand *et al.*, Comp. Phys. Comm. 135, 238 (2001); hep-ph/0010017,

[85] The CTEQ collaboration, H. Lai, *et al.*, Eur.Phys.J. C 12 375 (2000); hep-ph/9903282

[86] G. Altarelli and G. Parisi, *Asymptotic freedom in parton language*, Nucl. Phys. B, 126:298, 1977; V. Gribov and L. Lipatov, Sov. J. Nucl. Phys., 15:438, 1972; Y.Dokshitzer, Sov. J. Phys. JETP, 46:641, 1977.

[87] M. Mangano *et al.*, JHEP 0307 001 (2003); hep-ph/0206293

[88] M. Mangano, http://cepa.fnal.gov/patriot/mc4run2/MCTuning/061104/mlm.pdf (11 Jun. 2004).

[89] Standard Model Higgs Prodcution Cross Sections, http://www.physics.ucdavis.edu/∼conway/research/higgs/smhiggs-tev.html

[90] John Campbell, Keith Ellis, Monte Carlo for FeMtobarn processes http://mcfm.fnal.gov/

[91] Private talk with Kazu Hanagaki.

[92] MCFM Cross Sections, http://www-clued0.fnal.gov/∼nunne/cross-sections/mcfm_cross-sections.html,

[93] MCFM Cross Section for CAPS Production, http://www-clued0.fnal.gov/∼nunne/cross-sections/caps_xsect.html

[94] Ph.D thesis of Y. D. Mutaf, Measurement of the Ratio of Inclusive Cross Sections $\sigma(p\bar{p} \to Z + b\text{-jet})/\sigma(p\bar{p} \to Z + \text{jet})$ at $\sqrt{s} = 1.96$ TeV, p153.

[95] Counting Signed IP b-tagging certification page, http://www-d0.fnal.gov/phys_id/bid/d0_private/certification/p14/CSIP/CSIP_v2.html

[96] Secondary Vertex b-tagging certification page for p14 pass2, http://www-d0.fnal.gov/phys_id/bid/d0_private/certification/p14Pass2/SVT/secvertex_v4_frames.html

[97] D. Bloch, B. Clement, *Update of the JLIP b-tagger Performance in p14/pass2 with Jes5.3*, DØ note in preparation

[98] ALEPH Collab., D. Buskulic *et al.*, Phys. Lett. B313 (1993) 535; G. Borisove and C. Mariotti, Nucl. Instr. & Meth. A372 (1996) 181

[99] S. Tower, *Optimization of b-tag Operation Points*, DØ Note 4086.

[100] DØ common sample group p14 pass2 data set page, http://www-d0.fnal.gov/Run2Physics/cs/skimming/pass2.html

[101] M. Klute, L. Phaf, D. Whiteson, *TopAnalyze–A Framework Analze Package For Top Group Analyses*, DØ note 4122

[102] http://d0-france.fnal.gov/Run2Physics/cs/index.html

[103] http://www-d0.fnal.gov/d0dist/dist/packages/lm_tools/devel/doc/

[104] Particle Data, Phys. Lett. B Vol.592/1-4(2004) 1-1110

[105] http://www-d0.fnal.gov/∼d0upgrade/d0_private/software/jetid/jetid.html

[106] F. Deliot, E. Nurse, muo_cert package, http://www-d0.fnal.gov/d0dist/dist/releases/development/muo_cert

[107] The p14-pass2 muo_cert sample skimmed from the 1MUloose by Gavin. See http://www-d0.fnal.gov/computing/algorithms/muon/data2.html sample 1

[108] Private communication with John Hobbs.

[109] V.Buescher *et al. Recommendation of the Ad-Hoc Committee on Limit-Setting Procedure to be used by DØ in RunII*, DØ note 4629

[110] John Hobbs, Simple Limit Calculator. http://www-clued0.fnal.gov/∼hobbs/limit_calc/limit_calc.html

[111] B. Gregorio, *Search for the SM Higgs boson at the Tevatron*, ICHEP, 2006. hep-ex/0612046, Dec. 20 2006